GDAŃSK UNIVERSITY
OF TECHNOLOGY

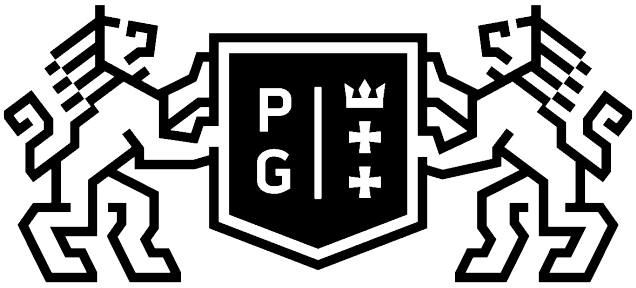

GDAŃSK UNIVERSITY
OF TECHNOLOGY

NUMERICAL ANALYSIS OF PILE INSTALLATION EFFECTS IN COHESIVE SOILS

A dissertation presented by

Jakub Konkol

submitted to
The Gdańsk University of Technology,
Faculty of Civil and Environmental Engineering

in partial fulfilment of the requirements
for the degree of
Doctor of Philosophy
in the subject of

Civil Engineering

Supervisor:	**Lech Bałachowski, PhD DSc**
Reviewers:	**prof. Marek Lefik, PhD DSc**
	prof. Dariusz Łydżba, PhD DSc

Gdańsk University of Technology
Faculty of Civil and Environmental Engineering
Department of Geotechnics, Geology and Marine Civil Engineering

Gdańsk, May 2017

Keywords: Cohesive soil, Finite Element Method, Installation effects, Lagrangian-Eulerian coupling, Large deformations, Pile jacking

“With great processing power comes great responsibility”
(in: HACKERMAN'S HACKING TUTORIALS
- How To Hack Time: https://youtu.be/KEkrWRHCDQU)

“Success is the ability to move from one failure
to another without loss of enthusiasm”
(Sir Winston Churchill)

Page intentionally left blank

Preface

Writing this PhD thesis was a challenging and tough task that has been successfully completed in February 2017. However, this scientific journey has started around March 2014 during the talk with my supervisor prof. Lech Bałachowski about the possibilities on pile installation simulations via Finite Element Method. In next year we established the subject of my PhD which finally became the topic of this thesis: “Numerical Analysis of Pile Installation Effects in Cohesive Soils”. The motivation and aim for such research is the attempt to incorporate the so-called “installation effects” into pile design process. Finally, this thesis concerns mainly the evolution of the radial effective stress on the pile shaft after pile installation and following soil consolidation as major influencing factors in the long term pile bearing capacity. I am profoundly grateful for possibility to work on this issue.

I was always interesting in computational and theoretical mechanics. Therefore, working on my PhD was a great pleasure despite a large number of pitfalls. Every time I lost my interest, I could always rely on my supervisor and departments colleagues who kept me further motivated. Thank you!

I hope you enjoy your reading.

Jakub Konkol
Gdynia, May 2017

Page intentionally left blank

Acknowledgements

Firstly, I would like to thank my advisor and supervisor Prof. Lech Bałachowski for all support and guidelines he provided me during PhD study and related research. I deeply grateful for his patience, knowledge and the way he guided my doctorate.

Besides my supervisor, I would like to thank all my Department colleagues. Special thanks to geotechnical laboratory team at Faculty of Civil and Environmental Engineering: Tomasz Kusio, Mateusz Wiszniewski, Adam Krasiński, and Jerzy Zamkiewicz. Without you, this thesis would not be the same.

I also thank organizations: General Directorate for National Roads and Motorways in Poland for providing field and laboratory test data for Koszalin clay, Menard Polska Sp. z o.o. for providing geotechnical documentation and static load test results for Poznań Łacina Commercial Centre and the Academic Computer Centre in Gdańsk (CI TASK) where calculations have been carried out.

This thesis was partially supported by the National Centre for Research and Development grant PBS3/B2/18/2015 and Young Scientists grant: edition 2015/2016 obtained from Faculty of Civil and Environmental Engineering at Gdańsk University of Technology.

Last but not the least, I would also like to thank my family and friends for all support and help they gave in last four years.

Jakub Konkol

Gdynia, May 2017

Page intentionally left blank

Statement of originality

Declaration

This is to certify that to the best of my knowledge, the content of this thesis is the result of my own research effort except where otherwise indicated. All the assistance received in preparing this thesis and sources have been acknowledged in the list of references.

This thesis has not been submitted elsewhere for any degree or other purposes.

Jakub Konkol
Gdynia, May 2017

Page intentionally left blank

Publications developed during this research

Journal Papers

1. Konkol, J., 2014. Numerical solutions for large deformation problems in geotechnical engineering, PhD Interdisciplinary Journal, 1, 49-55

2. Konkol, J., 2015. Numerical estimation of the pile toe and shaft unit resistances during the installation process in sands. Studia Geotechnica et Mechanica, 37, 37–44. doi:10.1515/sgem-2015-0005

3. Konkol, J., Bałachowski, L., 2016. Large deformation finite element analysis of undrained pile installation. Studia Geotechnica et Mechanica, 38, 45–54. doi: 10.1515/sgem-2016-0005

4. Konkol, J., Bałachowski, L., 2017. Influence of Installation Effects on Pile Bearing Capacity in Cohesive Soils - Large Deformation Analysis Via Finite Element Method. Studia Geotechnica et Mechanica 39, 27–38. doi:10.1515/sgem-2017-0003

Conference Papers

1. Kurek, N., Konkol, J., Bałachowski, L., 2016. Design of Concrete Columns with CPTu and Data Registered by Drilling Rig. XVII-ème Colloque Franco-Polonais de la Mécanique des Sols et des Roches Appliquée, Łódź, 28÷30 Novembre 2016.

2. Konkol, J., Bałachowski, L., 2017. Numerical Modeling of Cone Penetration Test in Slightly Overconsolidated Clay with Arbitrary Lagrangian-Eulerian Formulation. Procedia Engineering, 175, 273–278, doi: 10.1016/j.proeng.2017.01.023

Page intentionally left blank

Abstract

In this thesis the empirical equation for radial effective stress calculation after displacement pile installation and following consolidation phase has been proposed. The equation is based on the numerical studies performed with Updated Lagrangian, Arbitrary Lagrangian-Eulerian and Coupled Eulerian-Lagrangian formulations as well as the calibration procedure with database containing world-wide 30 pile static loading tests in cohesive soils. The empirical formula has been validated with 10 pile static load tests performed in Poznań clay and its reliability has been compared with 7 pile design methods. In this thesis, the description of research methodology and brief review of Finite Element Method with emphasis on large deformation formulations have been given. The key soil parameters which influence the radial stresses after pile installation and subsoil consolidation, both modelled numerically, have been identified. Next, the numerical methods have been validated with a high quality instrumented pile installation test in London clay and simulations of CPT and CPT-u soundings in Koszalin and Poznań clays, respectively. As a consequence of numerical tests interpretation, the general form of the empirical relation for radial effective stress has been provided. This relation has been calibrated with high quality, 30 pile static load tests. Next, the reliability of pile bearing capacity prediction with the proposed empirical formula has been checked using the database of all 75 piles and reference piles in Poznań site. Besides the validation of the author's equation for radial effective stress after installation and subsequent consolidation, the numerical calculation for the reference pile in Poznań site has been carried out. Numerical calculations include large deformation analysis where all pile construction steps have been taken into account and simplified finite element model where author's empirical formula have been adopted to predict the load-settlement response of the reference pile. Finally, the limitations of the proposed formula are provided and the further possible research directions due to pile installation effects are pointed out.

Page intentionally left blank

Streszczenie

W niniejszej pracy przedstawiono empiryczne równanie opisujące efektywne naprężenia radialne po instalacji pala przemieszczeniowego i konsolidacji podłoża gruntowego wokół niego. Propozycja została sformułowana na podstawie analiz numerycznych przeprowadzonych Metodą Elementów Skończonych i sformułowań: Zaktualizowanego sformułowania Lagrange'a, Arbitralnego sformułowania Lagrange'a-Eulera oraz Sprzężonego sformułowania Eulera-Lagrange'a. Zaproponowane równanie zostało skalibrowane na podstawie bazy danych zawierającej wyniki 30 próbnych obciążeń statycznych pali przemieszczeniowych wykonanych w depozytach gruntów spoistych na całym świecie. Propozycję autora zwalidowano na podstawie wyników 10 próbnych obciążeń statycznych pali CMC na poletkach badawczych w Poznaniu. Ponadto, własną propozycję porównano z 7 innymi, szeroko stosowanymi metodami projektowania pali w gruntach spoistych. W pracy przedstawiono metodologię badawczą oraz krótkie streszczenie Metody Elementów Skończonych (MES) z naciskiem na sformułowania przeznaczone do analizy dużych deformacji. Dokonano numerycznej identyfikacji parametrów materiałowych, które wpływają na naprężenia radialne po instalacji pala i konsolidacji podłoża gruntowego wokół niego. Następnie zweryfikowano stosowane metody numeryczne i modele konstytutywne na podstawie badań polowych na poletkach w iłach londyńskich, sondowań CPT w iłach koszalińskich oraz sondowań CPT-u w iłach poznańskich. Interpretacja testów numerycznych pozwoliła na sformułowanie zależności opisującej efektywne naprężenia radialne po instalacji pala i konsolidacji podłoża gruntowego wokół niego. Kalibracja równania została wykonana na podstawie wysokiej jakości bazy danych obejmującej 30 próbnych obciążeń statycznych. Niezawodność rozwiązania przebadano na podstawie całej bazy danych zawierającej 75 pali przemieszczeniowych wykonanych w gruntach spoistych. Oprócz walidacji propozycji autora wykonano także obliczenia numeryczne Metodą Elementów Skończonych dla reprezentatywnego pala. Obliczenia obejmowały analizę dużych przemieszczeń, w których uwzględniono wszystkie etapy konstrukcji i obciążenia wybranego pala oraz uproszczony model MES pala referencyjnego z wykorzystaniem proponowanej formuły na naprężenia radialne w celu wyznaczenia krzywej obciążenie-osiadanie. W podsumowaniu określono ograniczenia w wykorzystaniu propozycji autora oraz kierunki i możliwości przyszłych badań związanych z efektami instalacji.

Page intentionally left blank

Contents

Page intentionally left blank

List of figures

List of Tables

Notation

All symbols and abrevations used in this thesis are provided and defined directly in text, figures or they are enclosed to the equations. Here, the full notation is additionally submitted.

Symbols

Latin Letters

a	– Yield surface size
a	– Cone area ratio (only in Appendix C)
a_0	– Initial yield surface size
a'_{0c}	– Yield surface size corresponding to the p_c'
a'_{0u}	– Yield surface size corresponding to the p_u'
$\boldsymbol{b}$	– Body force tensor
$\boldsymbol{c}$	– Convective velocity vector
c'	– Effective cohesion
c_b'	– Effective cohesion at pile toe
c_d	– Dilatational wave speed
$\boldsymbol{c}_{j+1}^{\boldsymbol{M}}$	– Difference between exact and approximated M^{th} variable in $j+1$ iteration
c_s	– Cohesion corresponding to best fit envelope (σ-τ plane)
c_u	– Undrained shear strength of soil
$\overline{c_u}$	– Average undrained shear strength of soil
$\boldsymbol{d}$	– Actual displacement on n^k node in CEL formulation
$\boldsymbol{d_e}$	– Displacement vector of nodes within element in local coordinate system
$\ddot{\boldsymbol{d}}_{\boldsymbol{e}}$	– Acceleration vector of nodes within element in local coordinate system
d_i	– Penetration length on i direction
δd_i	– Virtual displacement on i direction
$\boldsymbol{d_n}$	– Normal component of penalty displacement in CEL formulation
$\boldsymbol{d_p}$	– Penalty displacement in CEL formulation

$\boldsymbol{d_t}$ – Tangential component of penalty displacement in CEL formulation

e – Void ratio

e_c – Void ratio corresponding to the p_c'

$\boldsymbol{e^{el}}$ – Deviatoric part of elastic strain tensor

e^{el} – Elastic void ratio

e_u – Void ratio corresponding to the p_u'

e_0 – Initial void ratio (corresponding to p_0')

f (or f_i) – Yield function

$\boldsymbol{f}$ (or $F(x)$) – Field variable

$\boldsymbol{f_e}$ – Vector of external forces acting on element nodes in local coordinate system

f_{j+1} – Penalty force applied on node in time $j+1$

f_s – Shaft resistance (Sleeve resistance)

g (or g_i) – Plastic potential

h – Distance from the pile toe (height above pile tip)

h – Interpenetration of the surfaces called “overclosure” (only in section 4.5)

i – subscript indicates number of variables

j – Iteration number (increment number)

$j\pm½$ – Mid-increment

k – Soil permeability coefficient

$\boldsymbol{k_e}$ – Element stiffness matrix in local coordinate system

k_i – Penalty stiffness on i direction

k_p – Penalty stiffness in CEL formulation

k_1 – Correction coefficient in Almeida's method

l – Drainage length

l_e – Finite element dimension

l_i – Characteristic contact surface length in i direction

m – Minimal of the Lagrangian and the Eulerian mass in CEL formulation

$\boldsymbol{m_e}$ – Element mass matrix in local coordinate system

n – Porosity

$\boldsymbol{n}$ – Outward normal vector to the Lagrangian surface at n^k node in CEL

$\boldsymbol{n_c}$ – Matrix of cosines of the outwards unit normal on the boundary surface

n^k – k node

n_t – Volume of the trapped fluid per current volume

p – Mean stress (equivalent pressure stress)

p – Pressure acting on the surface (only in section 4.5)

p_a – Atmospheric pressure (100kPa)

p' – Effective mean stress

p_c – Initial preconsolidation mean stress

p_c' – Initial effective preconsolidation mean stress

p_f' – Effective mean stress at failure

p_t^{el} – Tensile strength

p_0 – Initial mean stress

p_0' – Initial effective mean stress

$p_{u'}$ – Effective mean stress corresponding to the c_u

q – Mises equivalent stress (deviatoric stress)

q_b – Base (toe) resistance

q_c – Cone resistance

q_f – Ultimate pile toe resistance

q_f^{ALE} – Ultimate pile toe resistance from ALE solution

q_f^{UL} – Ultimate pile toe resistance from UL solution

$q_f^{UL,eq}$ – Ultimate pile toe resistance from UL solution after equalization

$q_f^{UL,inst}$ – Ultimate pile toe resistance from UL solution after installation

q_t – Corrected cone resistance

r – Distance from the pile axis of symmetry

r – Third stress invariant (only in chapter 3)

s – Displacement or settlement

s_r – Degree of saturation

t – Time

$\boldsymbol{t}$ – True stress at a point on surface S tensor

$\bar{\boldsymbol{t}}$ – Vector of traction imposed on surface

t_{eq} – Equalization time

t^q – Measure of equivalent deviatoric stress

t_0 – Reference (or initial) time

Δt – Time difference (Time increment)

Δt_{max} – Maximum allowable time increment

Δt_{min} – Minimum allowable time increment

u – Pore water pressure

u^{CEM} – Pore water pressure from CEM solution

u_{inst} – Pore water pressure after installation
$\boldsymbol{u}_j^{\boldsymbol{M}}$ – value of M^{th} variable in j iteration
$\boldsymbol{u}^{\boldsymbol{M}}$ – value of M^{th} variable
u_{max}^{UL} – Maximum pore water pressure from UL solution
u_{oct} – Octaherdal component of pore water pressure
u_{shear} – Shear component of pore water pressure
u^{UL} – Pore water pressure from UL solution
u_0 – Initial pore water pressure
u_2 – Pore pressure measured directly behind the cone
$\delta \boldsymbol{u}_w$ – Virtual pore water pressure field
Δu – Excess pore water pressure
Δu_{inst} – Excess pore water pressure after installation
Δu_{oct} – Octaherdal component of excess pore water pressure
Δu_{shear} – Shear component of excess pore water pressure
$\boldsymbol{v}$ – Velocity field (material velocity field)
$\check{\boldsymbol{v}}$ – Mesh velocity
$\boldsymbol{v}_w$ – Seepage velocity
$\delta \boldsymbol{v}$ – Virtual field velocity vector
w – Water content
w_L – Liquid limit
w_P – Plastic limit
x – Variable
$\boldsymbol{x}$ – Coordinates vector (only in section 4.2.2)
$\boldsymbol{x}$ – Spatial coordinates
x_i – Displacement (or rotation) according to the degree of freedom i
$\bar{x}_i$ – Prescribed displacement (or rotation) according to the degree of freedom i
$|_x$ – Spatial coordinates fixed
$z_{borehole}$ – Borehole depth
z_{head} – Pile head depth
z_{toe} – Pile toe depth

A – Skov and Denver empirical coefficient (only in chapter 2)
A – Pore pressure parameter A
A_{shaft} *(or* A_s*)* – Pile shaft area

A_{toe} *(or* A_b*)* – Pile toe area

B – Pore pressure parameter B

$\boldsymbol{C}$ – Matrix of damping coefficients

C_c – Current configuration

C_c – Compression index (only in chapter 8)

C_f – Compressibility of fluid

C_m – Compressibility of porous material

C_r – Reference configuration

C_r^t – Reference configuration in time t

$C_r^{t-\Delta t}$ – Reference configuration in time t-Δt

C_s – Compressibility of solid material (grains)

$C(t)$ – Configuration in time t

$C(t+\Delta t)$ – Configuration in time $t+\Delta t$

C_x – Spatial configuration

C_X – Material configuration

C_χ – Reference configuration in ALE formulation

C_0 – Base configuration

D – Pile diameter (external diameter)

$\boldsymbol{D}$ – All nodes displacement vector

$\dot{\boldsymbol{D}}$ – All nodes velocity vector

$\ddot{\boldsymbol{D}}$ – All nodes acceleration vector

$\boldsymbol{D_e}$ – Displacement vector of nodes within element in global coordinate system

$\ddot{\boldsymbol{D}}_{\boldsymbol{e}}$ – Acceleration vector of nodes within element in global coordinate system

$\boldsymbol{D^{el}}$ – Material stiffness matrix

D_i – Pile internal diameter

E – Elastic modulus

E' – Effective elastic modulus of soil skeleton

E_D – Dilatometer modulus

$E_{internal}$ – Internal energy

$E_k^{(t)}$ – Kinetic energy in time t

E_{oed} – Oedometric modulus

E_{total} – Total energy

$E_{tot}^{(t)}$ – Total energy in time t

$E_{tot}^{(0)}$ – Initial total energy

E_u – Undrained elastic modulus

F – Function

$\boldsymbol{F}$ – Deformation gradient (only in section 4.1.5.1)

$\boldsymbol{F}$ – Vector of external forces acting on all nodes.

$\boldsymbol{F_e}$ – Vector of external forces acting on element nodes in global coordinate system

$\boldsymbol{F^{el}}$ – Plastic part of deformation gradient

$\boldsymbol{F_{E,i}}$ – Forces applied on Eulerian element nodes in CEL formulation

F_i – Slip tolerance in i direction

$\boldsymbol{F_L}$ – Force applied on Lagrangian node in CEL formulation

$\boldsymbol{F^N}$ – Force component conjugate to the N^{th} variable

$\boldsymbol{F_p}$ – Penalty force in CEL formulation

$\boldsymbol{F^{pl}}$ – Elastic part of deformation gradient

$F_{shaft,t}$ – Total vertical force acting on pile shaft in time t

F_{toe} – Total vertical force acting on pile toe

$F(x)$ *(or* $\boldsymbol{f}$*)* – Field variable

G $(\text{or } \bar{\mu})$ – Shear modulus

G' – Effective shear modulus

G_{max} – Maximum (initial) shear modulus

G_u – Undrained shear modulus

$\boldsymbol{I}$ – Identity matrix

I_D – Material Index

I_p – Soil plasticity

I_{vr} – Measure of clay sensitivity

J – Ratio of volume in current configuration to the volume in reference configuration

J^{el} – Elastic volume change

J^{pl} – Plastic volume change

J^T – Jacobian of transformation

K – Bulk modulus

$\boldsymbol{K}$ – Global stiffness matrix

K_c – Artificial stress index after installation and equalization

K_D – Horizontal stress index

$\boldsymbol{K_e}$ – Element stiffness matrix in global coordinate system

K_0 – Lateral earth at rest pressure coefficient

K_0^{NC} – Earth pressure at rest coefficient of normally consolidated soil

K_0^{OC} – Earth pressure at rest coefficient of preconsolidated soil

K^{Π} – Parameter, that defines Cam-Clay surface in deviatoric plane

L – Embedded pile length

$\boldsymbol{L}$ – Rate of deformation (velocity gradient)

M – Slope of the critical state line in p-q plane

$\boldsymbol{M}$ – Global mass matrix

M_{DMT} – Vertical drained constrained modulus

$\boldsymbol{M_e}$ – Element mass matrix in global coordinate system

N_c, N_q – Terzaghi's bearing capacity coefficients

N_i – Eulerian basis function (includes Lagrangian node location) in CEL

N_{kt} – Cone factor

P_0 – Contact stress (DMT measurement)

P_1 – Stress to expand membrane 1mm into soil

Q – Pile capacity after time t

Q_{add} – Additional force in tension static loading test (e.g. pile self-weight)

Q_{base} (Q_b) – Pile base capacity

Q_c – Calculated pile capacity

Q_m – Measured pile capacity

Q_{shaft} – Pile shaft capacity

Q_{SLT} – Pile capacity obtained from static loading test

Q_0 – Reference capacity in time t_0

R – Pile radius

R_{mc} – Mohr-Coulomb deviatoric stress measure

S – Surface of the element

$\boldsymbol{S}$ – Deviatoric stress tensor

$\boldsymbol{S_f}$ – Source term

S_t – Soil sensitivity

T_v – Time factor

U – Elastic strain density potential or internal energy per unit mass (here equal because of adiabatic process)

U_0 – Initial internal energy per unit mass

V – Volume of the element

$W_{ext}^{(t)}$ – External work in time t

$\boldsymbol{X}$ – Material coordinates

$|_x$ – Material coordinates fixed

Greek Letters

α – Biot's effective stress coefficient

α – Adhesion coefficient (only in chapter 9)

β – Beta coefficient (only in chapter 9)

β – Constant used for wet surface size modification

β_i – Weight functions (includes influence Eulerian domain material at each nodes) in CEL formulation

γ – Shear strain

γ_i – Small allowable elastic slip in *i* direction

$\dot{\gamma}_{eq}$ – Slip rate equivalent to the critical shear stresses

$\dot{\gamma}_i$ – Slip rate in *i* direction

γ_{rv} – Shear strain in *r*-*v* plane (axisymmetric model)

γ_w – Unit weight of water

δ – Angle of interface friction

δ' – Angle of interface friction in drained conditions

δ_f – Angle of interface friction at failure

δ_{fR} – Residual angle of interface friction during fast shearing (related to total stress)

δ^{peak} – Peak angle of interface friction

δ_r – Radial displacement of the soil

δ^{rez} – Residual angle of interface friction

δ'_{sR} – Residual angle of interface friction during slow shearing (related to effective stress)

δ^{tot} – Angle of interface friction during undrained conditions

$\boldsymbol{\varepsilon}$ – Total strain tensor

$\dot{\boldsymbol{\varepsilon}}$ – Total strain rate

ε_a – Axial strain

$\boldsymbol{\varepsilon}^{\boldsymbol{el}}$ – Elastic strain tensor

$\dot{\boldsymbol{\varepsilon}}^{\boldsymbol{el}}$ – Elastic strain rate

$\varepsilon^{el}{}_{vol}$ – Elastic volumetric strain

$\dot{\boldsymbol{\varepsilon}}^{\boldsymbol{pl}}$ – Plastic strain rate

$\varepsilon^{pl}{}_{vol}$ – Plastic volumetric strain

$\delta\,\dot{\boldsymbol{\varepsilon}}$ – Virtual strain rate

ϵ – Small multiplier

η – Angle which defines shear surface under pile toe

θ – Deviatoric polar angle (Lode angle)

κ – Logarithmic elastic bulk modulus

λ – Logarithmic plastic bulk modulus

$\bar{\lambda}$ – Lamé's first parameter

λ_i – Hardening parameter depending on i number of variables

μ – Coulomb coefficient of friction

$\mu_{equalization}$ – Coefficient of friction durig equalization of pore water pressures and SLTs

$\mu_{jacking}$ – Coefficient of friction during jacking

υ – Poisson's ratio

υ' – Effective Poisson's ratio

υ_u – Undrained Poisson's ratio

ρ – Material density

ρ' – Effective soil density

ρ_d – Dry soil density

ρ_{sr} – Saturated soil density (total soil density)

ρ_w – Water density

$\boldsymbol{\sigma}$ – Stress tensor

σ – Total stress

σ_h – Horizontal total stress

$\sigma_{h,0}$ – Initial horizontal total stress

σ_v – Vertical total stress

$\sigma_{v,0}$ – Initial vertical total stress

σ' – Effective stress

$\dot{\boldsymbol{\sigma}}$ – Stress rate

σ_a – Axial stress

σ'_h – Effective horizontal stress

$\sigma'_{h,0}$ – Initial effective horizontal stress

σ_h^{ALE} – Total horizontal stress from ALE solution

σ_h^{CEM} – Total horizontal stress from CEM solution

$\sigma_h'^{CEM}$ – Effective horizontal stress from CEM solution

σ_h^{UL} – Total horizontal stress from UL solution

$\sigma_h'^{UL}$ – Effective horizontal stress from UL solution

σ_n – Normal stress

σ_r – Radial stress

σ_{ri} – Total radial stress during installation

σ'_{rf} – Radial effective stress at failure

σ'_{rr} – Radial effective stress

$\sigma'_{rr,eq}$ – Radial effective stress after equalization

$\sigma'_{rr,inst}$ – Radial effective stress after installation

$\sigma'_{rr,inst}{}^{UL\ Avg}$ – Average radial effective stress after installation from UL solution

$\sigma'_{rr,SLT}$ – Radial effective stress obtained from static loading test

σ_{rr}^{tot} – Radial total stress

$\sigma_{rr,0}^{tot}$ – Initial radial total stress

σ_t – Tension cut-off

σ'_v – Effective vertical stress

σ'_{vi} – Vertical effective geostatic stresses

$\sigma'_{v,p}$ – Effective vertical stress at pile base

σ'_{v0} $(\sigma'_{v,0})$ – Initial effective vertical stress

$\overline{\sigma_{v,0}}'$ – Average initial effective vertical stress

σ_1 – Major effective principal stress

σ_3 – Minor effective principal stress

$\Delta\sigma^{tot}$ – Total stress change

$\Delta\sigma_1$ – Change in major principal stress

$\Delta\sigma_3$ – Change in minor principal stress

τ – Shear stress

τ_{crit} – Critical shear stresses at the interfaces (only in section 4.5)

τ_f – Skin friction (unit pile shaft resistance)

$\tau_{f.max}$ – Skin friction (unit pile shaft resistance) at failure

τ_i – Shear stresses in *i* direction

τ_{rv}^{tot} – Total shear stresses in *r*-*v* plane (axisymmetric model)

ϕ' – Effective angle of internal friction

ϕ'_{cs} – Critical state angle of internal friction

ϕ_s' – Angle of internal friction corresponding to best fit envelope (σ_n-τ plane)

$\boldsymbol{\varphi}$ – Transformation function between material and spatial coordinates

$\boldsymbol{\chi}$ – Reference coordinates

$|_{\chi}$ – Reference coordinates fixed

Γ – Surface contact area

Λ – Plastic volumetric strain ratio

$\delta\Pi$ – Virtual work by contact forces

Φ – Piezometric head

$\boldsymbol{\Phi}$ – Transformation function between reference and spatial coordinates

$\Phi(x)$ – Probability density function

$\boldsymbol{\Psi}$ – Transformation function between reference and material coordinates

Abbreviations

ALE – Arbitrary Lagrangian Eulerian

API – American Petroleum Institute

AVG (Avg.) – Average value

C – Close-ended pile

CEL – Coupled Eulerian Lagrangian

CEM – Cavity Expansion Method

CFD – Computational Fluid Dynamics

Ci – Circural Pile

Cl – Clay

CMC – Controlled Modulus Column

COV – Coefficient of variation

CPT – Cone Penetration Test

CPTu – Cone Penetration Test with pore water pressure measurement

Cr – Concrete pile

CSL – Critical State Line

CU – Consolidated Undrained

C/T – Compresion/Tension

dev – Deviation

DMT – Dilatometer Test

DPL – Dynamic Probe Light

Dr – Driven pile

FDP – Full displacement pile

FE – Finite Element

FEM – Finite Element Method

FHWA	– Federal Highway Administration
Gr	– Gravel
IC	– Imperial College
ICP	– Imperial College Pile
IEC	– Installation Effect Coefficient
J	– Jacked pile
LCPC	– Laboratoire Central des Ponts et Chaussées
LDFEM	– Large Deformation Finite Element Method
MCC	– Modified Cam-Clay
MIT	– Massachusetts Institute of Technology
MPM	– Material Point Method
NC	– Normally consolidated
NCL	– Normal Consolidation Line
NGI	– Norwegian Geotechnical Institute
O	– Open-ended pile
OCR	– Overconsoliation ratio
PFEM	– Particle Finite Element Method
Q-s	– Load-settlement curve
S	– Steel
sasiCl	– sandy silty clay
SCEM	– Spherical Cavity Expansion Method
siCl	– silty clay
SLT	– Static Loading Test
SPH	– Smoothed Particle Hydrodynamics
SPM	– Strain Path Method
Sq	– Square pile
SSPM	– Shallow Strain Path Method
TL	– Total Lagrangian
TX	– Triaxial Test
UL	– Updated Lagrangian
UU	– Unconsolidated Undrained
YSR	– Yielding stress ratio

Chapter 1
Introduction

1.1 Background

Pile foundations are widespread design solution in geotechnical engineering involving soft soils and the common trend in pile designing is to use in-situ state of soil, including its physical and strength parameters. However, when installation of piles proceeds the soil state changes as well. The combination of soil physical and strength properties change during pile installation induces variation in pile bearing capacity compared with calculations based on in-situ conditions. Depending on the applied piling technology and site conditions the increase or decrease of pile bearing capacity can be observed (Samson and Authier, 1986). However, the gain of capacity is reported more often (Komurka et al., 2003), which makes this phenomenon very attractive for building industry. Its application may cause the reduction of piles length or diameters and, thereby, upgrading of existing system of foundations may bring the investment cost down.

The increase in pile bearing capacity with time was first observed by Wendel (1900) and now it is known as a set-up effect. The more general term related to all, immediate and time-depended changes is called installation effects. This phenomenon is generally related to all "displacement" piles, where large radial soil displacements occur during installation. As a consequence of this process a remoulded area around the pile is created where the physical and strength properties of the soil have been changed, see figure 1.1.

In terms of soil mechanics the set-up phenomenon can be framed in mechanism contained the following steps (Komurka et al., 2003; Lied, 2010; Long et al., 1999):

1. Generation of excess pore water pressure and soil "reorganization".
2. Dissipation of excess pore water pressure.
3. Ageing of soil structure.

Generation of excess pore water pressures as well as effective stress changes in the surrounding soil are observed during pile installation. The initial soil structure is being destroyed and the soil particles start "reorganizing" themselves (step 1) and, as the result, the new bonds between soil grains are build up. When the pile is finally placed on the design depth, the excess pore water pressures dissipate and consolidation proceeds (step 2). With or

shortly after beginning of consolidation the ageing of soil is progressing (step 3) and the creeping of soil structure appears. Also, some chemical bonding between the pile material and the soil particles may take place. Consequently, the mechanism described above induces different stress state of soil after installation.

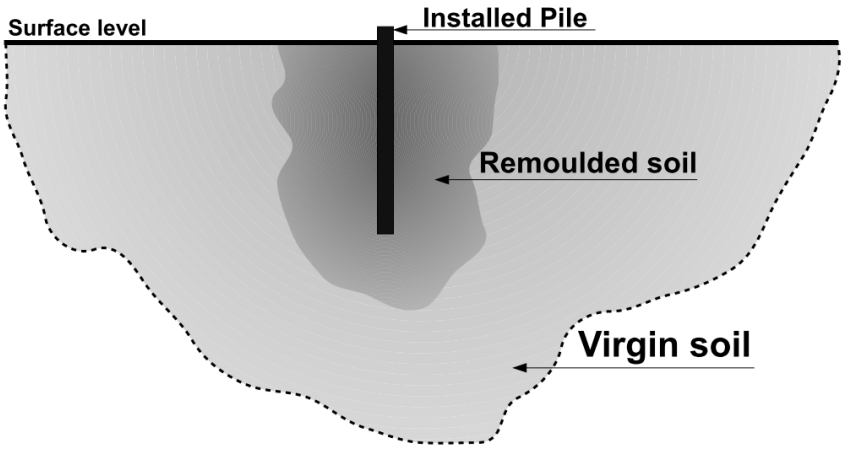

Figure 1.1. Installation effects schematically presented.

Installation effects occur in almost all kind of soils. Some exception are coarse sands, gravels (Walton and Borg, 1998) and very silty, low-plasticity soils (Holloway and Beddard, 1995). In cohesive soils such as clays the excess pore water pressure generation and dissipation as well as the soil "reorganization" become major set-up effects. Ageing is problematic phase, that can be relatively small part of whole process (Komurka et al., 2003; Schmertmann, 1991) or it can be very evident, but spread on a very long time period (Doherty and Gavin, 2013). On the other hand, in silts and fine sands major part of set-up is correlated with ageing and soil "reorganization" during installation. Generation and dissipation of excess pore water pressure seems to have minor effect (Axelsson, 2000).

1.2 Objectives of the study

The main objective of this study is to investigate numerically influence of the installation effects on the piles jacked into cohesive soil. As the influence of soil ageing in clays is ambiguous, the creep effects are omitted and only the stress and deformation fields are investigated. These include effective stress change along the pile shaft after the installation and consolidation phases in particular. The changes in excess pore water pressures are examined as far as it was possible. The presented numerical study contains pile jacking tests for different initial conditions and soil parameters. The Abaqus software suit with its powerful numerical capabilities is used to create the Large Deformation Finite Element Method (LDFEM) models.

The secondary objective of this work is to verify effectiveness and accuracy of numerical methodology proposed in this thesis. Firstly, the field tests in London clay with instrumented model piles are modelled numerically. Secondly, the results of the numerical CPT/CPT-u

probing are compared with the corresponding in-situ soundings done in Koszalin and Poznań sites. Consequently, the numerical solutions reliability is estimated.

Finally, the empirical correlation between basic soil strength parameters and radial effective stress after installation and subsequent consolidation is provided. Then, it is validated with static loading tests in Poznań site where also the LDFEM model of reference CMC column has been presented.

1.3 Thesis layout

This thesis is subdivided in ten chapters including **Introduction**. The current state of knowledge in respect to installation effects in cohesive soils is presented in **chapter 2**. The review of numerical, field and laboratory studies is shown. The large deformation finite element methods and the analytical methods for large deformations problems are listed and briefly discussed. A summary concerning recent attempts to describe installation effects is presented.

The formulation of a methodology involving combined numerical analysis used in this thesis is presented in **chapter 3**. Capabilities of Updated Lagrangian formulation and combined Lagrangian-Eulerian methods in terms of geotechnical applications are pointed out. The basic assumptions of total and effective stress approaches are described and the correlation between total and effective stress parameters is derived. The application of different numerical methods and techniques for analysis of the pile jacking in clayey soil is presented. The constitutive laws and contact formulations used in numerical models are described in details. Assumptions and limitations related to the constitutive and contact modelling are also discussed.

The large deformation Finite Elements Methods including Updated Lagrangian (UL), Arbitrary Lagrangian-Eulerian (ALE) and Coupled Eulerian-Lagrangian (CEL) are the subject of **chapter 4**. Overview and background of traditional finite element method is made. The most important aspects of UL formulation are presented. Overview of ALE and CEL methods with emphasis on the capabilities, governing equation and calculation procedure is made. Weak and strong points of all numerical methods used in this study are discussed.

Chapter 5 concerns on preliminary tests for pile jacking simulation. Effectiveness of adopted methodology is tested on a benchmark pile jacking model. The convergence and sensitivity studies for UL, ALE and CEL methods are introduced and the most influential factors affecting the numerical solutions are recognized and discussed.

Chapter 6 contains numerical models for instrumented pile tests performed in London clay in late eighties and early nineties. The chosen test site was localized in Canons Park in London, UK and the numerical model is build on the basis of available literature data. The numerical simulations results are compared with the field data which include shaft friction and pore water pressure and radial effective stresses distributions during installation and following consolidation phase.

Developing the numerical models of CPT/CPTu soundings is presented in **chapter 7**. The in-situ field measurements has been performed in cohesive soil deposits near Koszalin and

Poznań, Poland. The soil parameters are estimated on the basis of laboratory test data and with CPT/CPTu and DMT correlations. Detailed description of numerical CPT/CPT-u analysis, applied assumptions and discussion of uncertainties is presented. The results are compared with the field measurement of cone resistance, sleeve friction and the pore water pressures where available. The discussion of obtained results is carried out.

The numerical model of pile jacking in homogeneous soil is the subject of **chapter 8**. The chapter summarizes the numerical studies from chapters 5, 6, 7 and introduces additional parametric studies which focus on undrained shear strength and initial stress conditions. The combination of parameters used in chapter 8 is determined after the convergence and sensitivity test results performed in chapter 5. The installation effects due to pile jacking in different soil conditions are shown. Finally, the formulation of the empirical equation describing the radial effective stresses after installation and following consolidation is based on the conducted numerical tests.

The calibration of the empirical formula for radial effective stress calculation is presented in **chapter 9**, where the database of 75 piles is used. The proposed equation is validated with 10 static loading tests of CMC piles drilled in cohesive soil in Poznań site. The results of large deformation Finite Element (LDFE) modelling of reference pile are presented and the additional combined empirical and FEM approach is shown. Consequently, the possibility of using the proposed formula in the design practice is described.

Conclusions and remarks about presented and further research are briefly discussed in **chapter 10**. Author's proposition for radial effective stress calculation due to installation effects is summarized and possible application of proposed correlation is presented. The large deformation methods reliability is discussed and their applicability in geotechnical engineering are pointed out.

Chapter 2

From past research to this study

After the first observation of set-up by Wendel (1900) many field, laboratory and numerical studies of this phenomenon were carried out. Among the first researchers who provided the observation of installation effects in clays were Housel and Burkey (1948) and Cummings et al (1950). They measured water content and shear strength of the soil before and after pile installation. More detailed review of historical research focusing installation effects have been made by Hunt (2000). Generally speaking, in cohesive soils the set-up studies have been concentrated on strength parameters change in remoulded soil (e.g., Holtz and Lowitz, 1965), area that is affected by pile installation (e.g., Cooke and Price, 1973; Randolph et al., 1979b), stress state change around the pile (e.g., Bond and Jardine, 1991) and pore water pressures variations during the set-up and consolidation phases (e.g., Pestana et al., 2002). Many attempts have been also made to correlate installation effects with material properties of the cohesive soil (e.g., Randolph et al., 1979a). The long term increase in pile bearing capacity induced by consolidation (e.g., Gavin et al., 2010) and soil structure ageing has been also studied (e.g., Karlsrud, 2012; Skov and Denver, 1988). Those research has been undertaken to find empirical correlations of installation effects that could be applied in pile design practice. As a result, the total pile length could be reduced and building cost decreased.

Along with the field tests the analytical methods have been developed for installation phase modelling (e.g., Baligh, 1975; Randolph et al., 1979a). These solutions are generally intended to be used for the design purposes (Randolph, 2003). They are also widely coupled with FEM methods to obtain better prediction of stress state in soil structure (e.g., Randolph et al., 1979a). However, when more advanced numerical methods were implemented in commercial software in last years, new possibilities in pile set-up modelling have occurred (e.g., Beuth, 2012; Sabetamal et al., 2014; Sheng et al., 2005).

2.1 Disturbance zones around the pile

The first physical effect of pile installation in cohesive soil is the radial and vertical displacement of the surrounding soil. As a result of this process the soil becomes mechanically disturbed and the disturbance zones which depends on distance from the pile

can be specified. This is schematically presented in figure 2.1 where three main zones are distinguished: the remoulded one, the transition one and the undisturbed one (Chen et al., 1999). The range in lateral direction of each zone is described by A, B and C distances respectively. The range of zones in vertical direction, from pile toe, is represented by I, II and III values, respectively. The transition between each zones could be highly continuous due to soil granularity. Anyway, some estimated values of each zone's ranges can be found in the research studies that had begun already in 1950s.

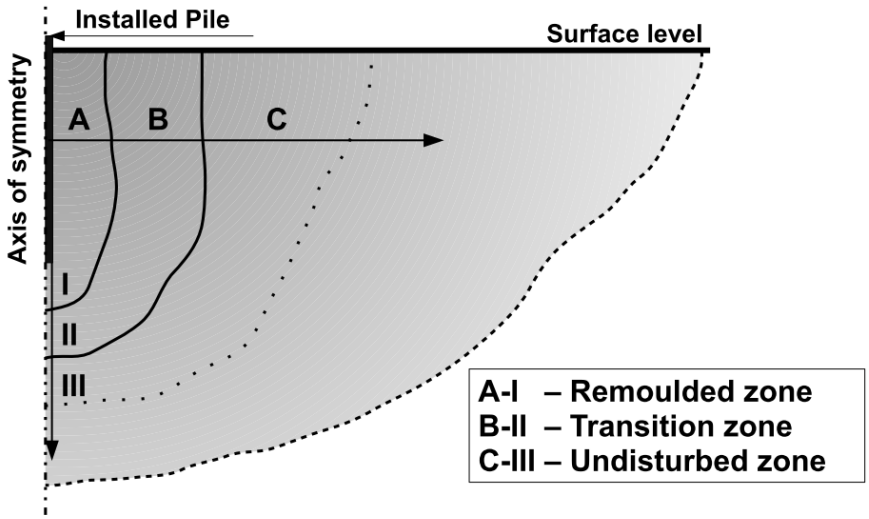

Figure 2.1. Disturbance zones due to pile set-up

In the radial direction, the remoulded zone (A distance) is usually defined as from 1 to 2 pile diameters wide outwards the pile wall (e.g., Bond and Jardine, 1991; Cooke and Price, 1973; Pestana et al., 2002; Randolph et al., 1979b). Some authors reported that total zone affected by pile installation (A and B distances summed up) can range between 1,5 and 4 pile diameters wide (e.g., Bond and Jardine, 1991; Fellenius and Samson, 1976; Holtz and Lowitz, 1965; Randolph et al., 1979b). The undisturbed zone (C distance) usually extends from 3 to 4 pile diameters wide outwards the pile wall (e.g., Bond and Jardine, 1991; Holtz and Lowitz, 1965), but value of 8 pile diameters was also reported (Roy et al., 1981).

Affected zone beneath the pile toe has been determined mainly by laboratory studies. In the vertical direction the highly remoulded area (I) is reported as a distance of 2 to 2,5 pile radius depth. In that zone the stationary soil core movement below the pile toe called 'nose cone' can be also observed (e.g., Ni et al., 2010). Total disturbance zone (I and II distances summed up) underneath the pile toe can affect the range of 3 to 5 pile diameters depth (e.g., Li and Li, 2009; Ni et al., 2010).

2.2 Mechanical changes in soil structure during pile installation

Pile installation induces two main mechanical changes in soil structure. They are related to variation in radial total stresses and pore water pressures. The common observation

is the increase in radial total stresses with depth (e.g., Bond and Jardine, 1991; Chow, 1997; Lehane and Jardine, 1994a, 1994b). However, it has been also seen that for a given depth mobilization of the total stresses depends on pile penetration depth. During jacking, the mobilized radial total stresses decrease with pile penetration. Such penetration depth dependent behaviour or length effects have been reported by Cooke et. al. (1979). Similar effects were observed during field tests performed by Bond and Jardine (1991), Lehane and Jardine (1994a, 1994b), Chow (1997) and Gavin et al. (2010). Consequently, the shear stresses on soil-pile interface are length dependent and to describe such phenomenon Heerema (1980) introduced term “friction fatigue”. The progressive failure on pile-soil interface was proposed by Kraft et al. (1981) and Randolph (1983) as possible mechanism that controls “friction fatigue” behaviour. This was schematically presented in figure 2.2 where the largest skin friction is mobilized near the pile toe are pointed out.

The field measurements during pile installation also have shown that the increase of the horizontal stresses is the highest near the pile wall and decreases outwards the pile surface (Suleiman et al., 2015).

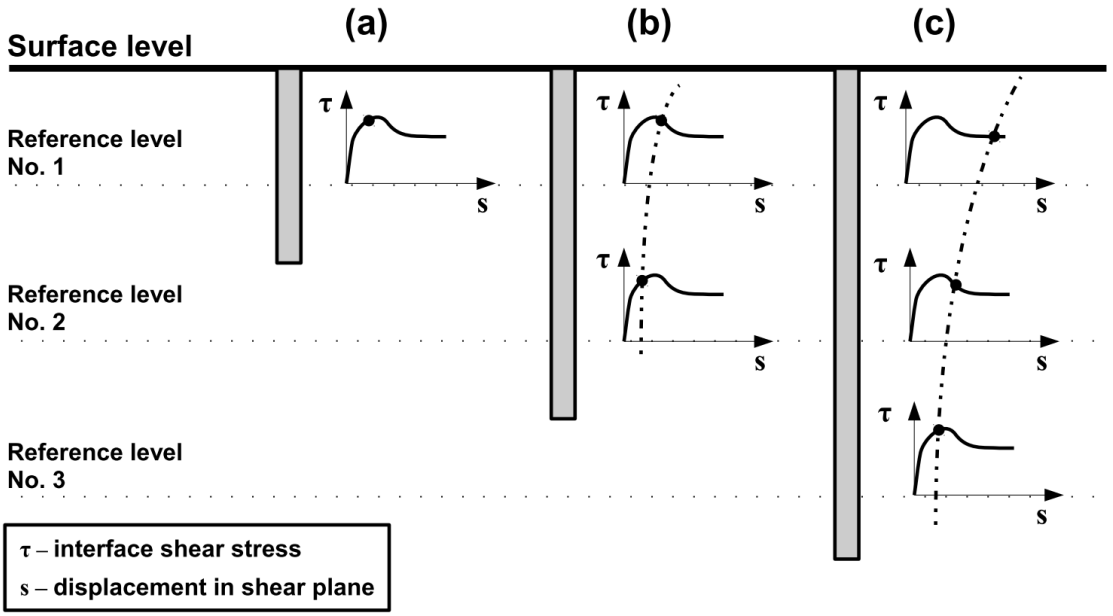

Figure 2.2. Progressive failure mechanism induced by pile installation (modified from Kraft et al. (1981) and Doherty and Gavin (2011))

The changes in pore water pressure are more complex and they are associated with ground distortions in shearing zone and with the changes in radial total stresses. Lehane and Jardine (1994a) observed that during each jacking stroke the pore-water pressures reduce instantly, which can be related to the dilatant response of the soil structure in narrow pile vicinity. When pile is in rest, the pore water pressures are increasing, which induces the radial water flow toward the pile surface. Similar effect has been noted during instrumented piles jacking in London clay (Bond and Jardine, 1991). It is also worth to mention, that the pile toe resistance measured during each jacking stage was almost equal to the CPT cone resistance (Lehane and Jardine, 1994b).

2.3 Consolidation effects

In pore water pressure equalization phase, relaxation of the total stresses occurs. This is common effect observed, for instance, in all Imperial College Pile (ICP) tests in clays (e.g., Bond and Jardine, 1991; Lehane and Jardine, 1994a). This effect is additionally combined with dissipation of the pore water pressures. However, in short time after placing pile on design depth, the pore water pressures increase rapidly (e.g., Gavin et al., 2010; Lehane and Jardine, 1994a). This implies water flow towards the pile surface, which is similar to the phenomenon observed during each jacking stroke. When the maximum pore water pressures are developed, the consolidation phase starts. The rate of pore water pressure equalization is the highest near the pile toe and it is reduced towards the soil surface (Gavin et al., 2010).

The changes in radial effective stress during equalization phase are also observed with an initial decrease and subsequent increase (e.g., Bond and Jardine, 1991; Lehane and Jardine, 1994a). At the end of consolidation the significant increase in radial effective stress against the geostatic values was measured (e.g., Gavin et al., 2010). The increase is sharp with depth (e.g., Bond and Jardine, 1991) and appears to be unaffected by jacked pile installation procedure (Gavin et al., 2010). The ratio between equalized radial effective stresses and geostatic ones is the highest near pile toe and reduces toward soil surface (e.g., Lehane and Jardine, 1994b). The phenomenon is usually related to the OCR (Lehane, 1992), because the direct correlation between initial undrained shear strength of soil and the equalized radial effective stresses has not been found (e.g., Bond and Jardine, 1991).

2.4 Ageing in cohesive soils

The phenomenon of increase in pile axial bearing capacity with time is called ageing or “time effects”. These effects are usually observed after pore water pressure equalization phase (e.g., Doherty and Gavin, 2013; Huang, 1988; Karlsrud and Haugen, 1985) and the physical background behind them is not fully understand (Komurka et al., 2003). The empirical formulas developed in last decades usually include combined consolidation and ageing effects (e.g., Huang, 1988; Skov and Denver, 1988). Based on Skov and Denver (1988) proposition Doherty and Gavin (2013) have presented empirical correlation for pile ageing in cohesive soil that can be used in design:

$$\frac{Q}{Q_0} = 1 + 0{,}25 \cdot \log\left(\frac{t}{100}\right) \tag{2.1}$$

where: Q_0 – reference capacity after time equal to 100 days, Q – pile capacity after time t, t – time.

Equation (2.1) is based on field investigation that was conducted over a 10 years period in Belfast clay on concrete driven piles. The reference time was chosen to ensure that the end of consolidation phase is achieved and the increase in axial capacity over 10 years was reported as 40% of reference value (Doherty and Gavin, 2013).

2.5 Analytical methods for installation effects prediction

Several analytical methods for taking into account pile installation has been developed. The most popular include the Cavity Expansion Method (CEM) and Strain Path Method (SPM). In the CEM, the installation process is modelled by expansion of cylindrical cavity in soil structure (Randolph et al., 1979a). The radial displacement of the soil δ_r induces by installation of the close-ended pile can be calculated by formula (e.g., Doherty and Gavin, 2011):

$$\frac{\delta_r}{R} = \sqrt{1 + \left(\frac{r}{R}\right)^2} - \frac{r}{R} \tag{2.2}$$

where: δ_r – radial displacement of the soil, R – pile radius, r – distance from the centre.

The biggest disadvantage of CEM is lack of taking into account such phenomena as the vertical deformation near the pile or shearing on the pile shaft. However, in this technique proper estimation of radial displacement is provided (Lehane and Gill, 2004). The stress state in soil structure can be calculated by the closed form solutions (Randolph and Wroth, 1979) or thorough FEM analysis (Randolph et al., 1979a). However the past studies have shown that CEM is not be well suited for the set-up modelling, especially in highly overconsolidated clays (e.g., Bond and Jardine, 1991).

The SPM is based on assumption that soil deformations and stresses in soil are decoupled (Baligh, 1985). Hence, the cone which penetrates the soil structure is similar to the viscous flow around the rigid element. As a result, the deformations and strains along the streamlines can be calculated. After constitutive law incorporation the stresses can be recovered as well. The theory of SPM has been firstly developed by Baligh (1975) and it was used for close-ended piles (Baligh, 1985). The SPM provides more accurate solutions in the close-pile region than CEM and enables better modelling of friction fatigue (e.g, Bond and Jardine, 1991). Sagaseta and Whittle (2001) have updated SPM model to the Shallow Strain Path method (SSPM). The aim was to achieve better prediction of the soil displacement during shallow penetration. Ni et al. (2010) has shown, that SSPM can provide acceptable solutions. However, the prediction becomes less accurate with increasing OCR (Whittle and Sutabutr, 1999).

2.6 Large deformation finite element (LDFE) modelling

The earliest attempts to model complex pile installation process with Finite Element Method (FEM) have already been made in 1980s (e.g., DeBorst and Vermeer, 1984; Kiousis et al., 1988). Review of methods and their limitations that were used in late 1990s was presented by Yu and Mitchell (1998). In that period a few cone penetration studies in cohesive soils have been performed. For instance, Sheng et al. (1997) has investigated pore water pressure development during penetration at different rates while van den Berg (1994) studied cone penetration in homogeneous clay in undrained conditions and compared results with other theoretical solutions.

In modern-days, rapid development in IT branch has opened new possibilities in numerical modelling and computational geomechanics. These include especially large deformation problems which are difficult to model with traditional FEM and pure Lagrangian formulation. Many numerical methods that provide accurate solutions with large deformations issues have been developed in previous decades, beginning from early 1960s. Moreover, increasing computing capabilities and necessity for large deformation analysis in engineering and science community have led to presence of these methods in commercial software packages such as ABAQUS, LS-DYNA or PLAXIS. The most popular numerical formulations for large deformation problems include combined Eulerian-Lagrangian methods such as Arbitrary Lagrangian-Eulerian (ALE) (Donea et al., 1982) and Coupled Eulerian Lagrangian (CEL) (Noh, 1963), the meshless methods such as Smoothed Particle Hydrodynamics (SPH) (Gingold and Monaghan, 1977), mesh-based particle methods such as Material Point Method (MPM) (Sulsky and Schreyer, 1996) and Particle Finite Element Method (PFEM) (Oñate et al., 2004). However, only ALE, CEL and MPM have found wider application in pile penetration problems due to their effectiveness and implementation in commercial software suits.

Currently, simulation of pile jacking process is mainly modelled in sandy soils. For example, application of CEL was presented by Hamann et al. (2015), while Phuong et al. (2014) show accurate solutions with MPM and Sheng et al. (2005) with Updated Lagrangian (UL) formulation. Installation problems in clays are widely considered in offshore structure design with special care to the jack-up foundations (e.g., Bienen et al., 2015), where CEL method is more widely used. FEM pile installation modelling in cohesive soils has become secondary concern in last years. For example, ALE formulation was used by Walker and Yu (2006) to model cone installation in clay. Sabetamal et al. (2014) used ALE to model Torpedo anchor installation in cohesive soil while Liyanapathirana (2009) used this formulation to model cone penetration in soft clay deposit. Zhou et al. (2013) have analysed excess pore water pressure generation caused by pressed pile installation and following consolidation phase in Modified Cam-Clay material in terms of UL formulation. The same method was used by Sheng et al. (2013) to perform full penetration of CPT cone in undrained conditions. Application of MPM to the penetration process in saturated clays has been presented, for instance, by Beuth (2012) and Ceccato et al. (2016). The review of some, currently used large deformation numerical methods, its efficiency and possible application in geotechnical engineering is presented in Wang et al. (2015).

2.7 On possibilities of installation effects predictions based on CPT probing

Cone penetration testing (CPT) seems to be ideally suited to make the comparison with the jacked pile. Firstly, the installation procedures of both cases are the same. Secondly, data collected from CPT test are not operator dependent. These features have made CPT very useful in design practice (Tomlinson and Woodward, 2015).

However, application of CPT probing data in installation effects predictions is far more

tricky. Although Lehane and Jardine (1994b) have shown that pile toe resistance during jacking is almost equal to the CPT cone resistance, the correlation between the toe resistance and total radial stresses is not evident due to registered friction fatigue. Results from three locations where ICP piles were tested, schematically presented in figure 2.3, do not show direct correlation between normalised installation total stresses σ_{ri}/q_b and normalised distance from the pile base h/R (see: Lehane and Jardine, 1994b). Lehane (1992) related radial stresses after installation and consolidation with OCR, which was evident from ICP tests, see figure 2.3. He also proposed empirical formula for equalized radial effective stress. This concept was later extended by Jardine and co-worked in ICP pile design method (Jardine et al., 2005) and in CPT-based method provided by Lehane et al. (2013).

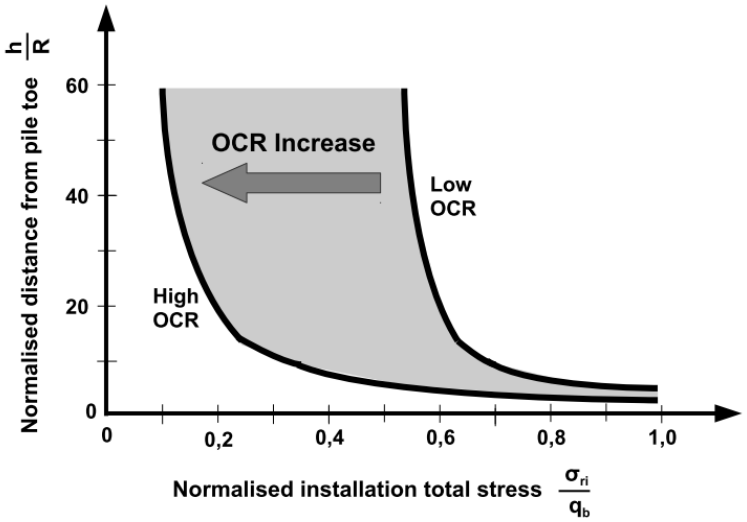

Figure 2.3 Relationship between installation radial total stress and distance from pile toe (generalised after Doherty and Gavin (2011) and Lehane and Jardine (1994b))

The observed friction fatigue seems to be also related to the contact behaviour between pile and soil and large deformation occurring on the interface (Lehane and Jardine, 1994b). Thus, the pile-soil interaction also governs the installation effects. Numerical modelling of CPT probing presented in chapter 7 of this thesis are intended to shed more light on interface problem and installation effects in cohesive soils.

2.8 Empirical formulas for installation effects based on numerical studies

One of the first empirical formulas for installation effects incorporation in pile design has been proposed by Randolph et al. (1979a), who provided the following relation:

$$\sigma'_{rr,eq} = \left(\frac{\sqrt{(3)}}{M} + 3 \right) c_u \tag{2.3}$$

where: $\sigma'_{rr,eq}$ – radial effective stress on the pile shaft after pile installation and soil

consolidation, M – stress ratio (slope of p-q plane), c_u – undrained shear strength.
However, later research have shown that radial effective stresses obtained from equation (2.3) are significantly higher than the measured ones (e.g., Bond and Jardine, 1991).

Other approaches for incorporation of installation effects in empirical formulations are based on Skov and Denver (1988) relation:

$$\frac{Q}{Q_0} = 1 + A \cdot \log\left(\frac{t}{t_0}\right) \tag{2.4}$$

where: Q_0 – reference pile capacity, Q – pile capacity after time t, A – empirical coefficient, t_0 – reference time, t – time.
The empirical A coefficient can be determined empirically (e.g., Skov and Denver, 1988) or numerically (e.g., Rosti et al., 2016).

In this thesis the emphasis is put on the determination of installation effects from laboratory soil testing rather than using the static loading test results. This is done to predict the pile capacity “a priori” and to use the static loading tests only as a verification of conducted calculations. Hence, the variation of equation (2.3) will be in terms of author's interest and similar relation will be searched.

Chapter 3

The choice of pile jacking modelling techniques

Numerical modelling of complex problem such as pile jacking using FEM requires special care. Different nature of installation and consolidation steps creates modelling problems. In installation phase, the large soil deformations in relatively short time of jacking take place. Consolidation step is quite opposite where the small deformation occurs and large times are needed for pore water pressures dissipation. These contradictory features are difficult to take into account in one numerical model. Further, even if one model for both phases can be build, a large number of simplifications is required. In this chapter the detailed discussion about numerical modelling of installation and equalization phases is considered. General remarks about FEM methods are made and the comprehensive description about physical phenomenon simplifications during pile installation is provided. Thus, analysis issues such as applied constitutive laws and contact modelling are explained. Advantages and disadvantages of numerical methods used in this study are also reported and the proposition of possible pile jacking modelling technique is presented. These include application of different numerical formulations and constitutive laws. The solution control method is also pointed out.

3.1 Numerical methods used in this study

3.1.1 General considerations

To investigate pile installation effects in cohesive soil the Finite Element Method (FEM) and Abaqus software suit is used. The FEM is a numerical method widely used to solve complex engineering problems and it is under development since 1950s (Zienkiewicz, 1995). Nowadays, it is considered as one of the most efficient methods. The basic concept of FEM is to create a meshed domain that is described by constitutive laws and other physical parameters. That built geometry contains a finite number of connected elements. Application of boundary and loading conditions enables equilibrium equations for the entire system to be solved. Consequently, approximated values of stresses, strains and displacements can be obtained. As could be noticed, the accuracy of the FEM solution depends on mesh properties, especially the element shape. If finite element starts to distort, the accuracy of the solution decreases or even can not be reached and analysis breakdowns. Thus, the mesh distortions

become the most crucial aspect in modelling large deformation problem such as pile jacking.

3.1.2 Large deformations

Large deformations are a little ambiguous term, because they depend on individual material properties. The term large deformation has different meaning for different materials. Generally speaking, it is common to accept 10% in strains as a large deformation problem (Krabbenhoft and Zhang, 2013). However, it is more clear to refer large deformation to the geometry changes of entire model. If geometry of model remains almost unchanged, the small deformations occurs. This is most often encountered civil engineering problem. In geotechnical engineering these are shallow foundation settlements or static pile loading test at small deformations. It is also consolidation problem after pile installation considered in this thesis. If the model geometry distortions becomes significant, large deformations should be considered. This kind of analysis are quite popular in mechanical engineering, for instance, in metal forming process. In soil mechanics, large deformations occur very often, for example, in slope instability, tunnelling or pile driving simulations. Where initial and final geometry of the model are completely different, as typical for failure analysis, the extreme deformation problem takes place. Examples of such events are soil liquefaction problems, underground explosions or landslides. Graphical representation of different deformations is presented in figure 3.1.

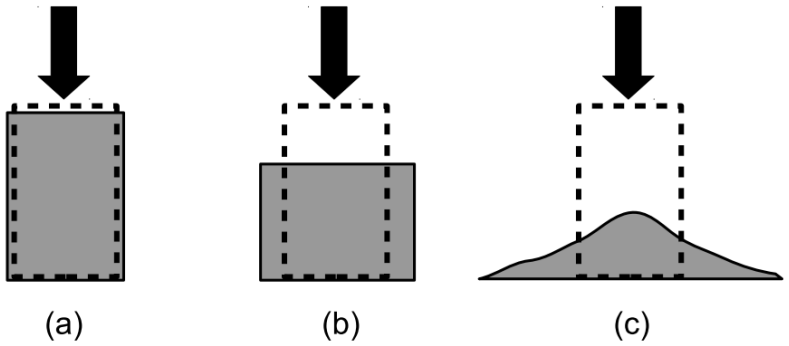

Figure 3.1. Deformation due to applied load: (a) small, (b) large (c) extreme

Deformations (small, moderate, large or extreme) introduce some problems in mechanical description. Kinematics of the material points can be express in Lagrangian or Eulerian point of view. In Lagrangian description the material points move with the mesh nodes as can be seen in figure 3.2a. In Eulerian formulation, the body movement and deformation is gathered form material points that flow through fixed mesh in space which is presented in figure 3.2b. Consequently, all the engineering problems are usually expressed in terms of Lagrangian or Eulerian formulations. Lagrangian formulation finds its wide application in solid mechanics due to possibility of single point movement tracking. It is important feature when construction deformation or settlement of the subsurface are estimated. Eulerian formulation is popular in fluid mechanics, where movement of single particles is not essential. Instead, the crucial part is the knowledge of the fluid state parameters such as velocity or temperature in single cross-section.

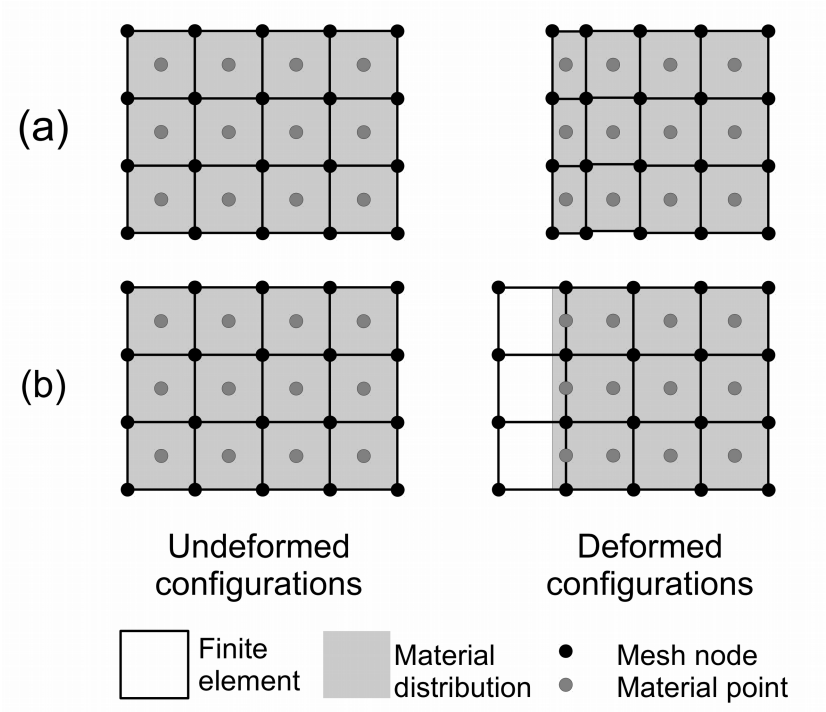

Figure 3.2. Undeformed and deformed configurations of the body in (a) Lagrangian and (b) Eulerian manner

3.1.3 Lagrangian formulation

The basic action in FEM modelling is building of undeformed model with prescribed boundary and loading conditions and other input parameters. Hence, problem is always defined in some original (initial) configuration. The aim of FEM calculations is to obtain model deformation and internal forces. Thus, all computed variables have to be referred to some configuration as can be seen in figure 3.3. The first solution is to use original (base) configuration of the system as the referential one. In this case, FEM formulation is provided in terms of Total Lagrangian (TL) description. However, progressing deformation may result in geometry change. Hence, all computed variables can be referred to the current configuration of the system which is changing with time. The FEM formulation with accordance to current configuration is called Updated Lagrangian (UL) description. The TL is dedicated to the linear analyses and small deformations problems. On the other hand, the UL is often used in non-linear analyses and large deformation problems. Both formulations have advantages and disadvantages. For example, UL is more suitable for plastic evolution process, while TL offers easier use of constitutive relations (Bathe, 1996). In pile jacking simulation the UL formulation becomes obvious choice due to large deformations and plastic strains.

Updated Lagrangian formulation, as it is implemented in FEM codes and in Abaqus in particular can be graphically presented in figure 3.4. The material points are strictly conjugated with the mesh nodes and when deformation occurs, material points move with accordance to the mesh nodes. As can be noticed, in some cases where large deformations are

appearing the extensive distortion of finite elements (FE) may occur. Consequently, the accuracy of FEM solution decreases rapidly.

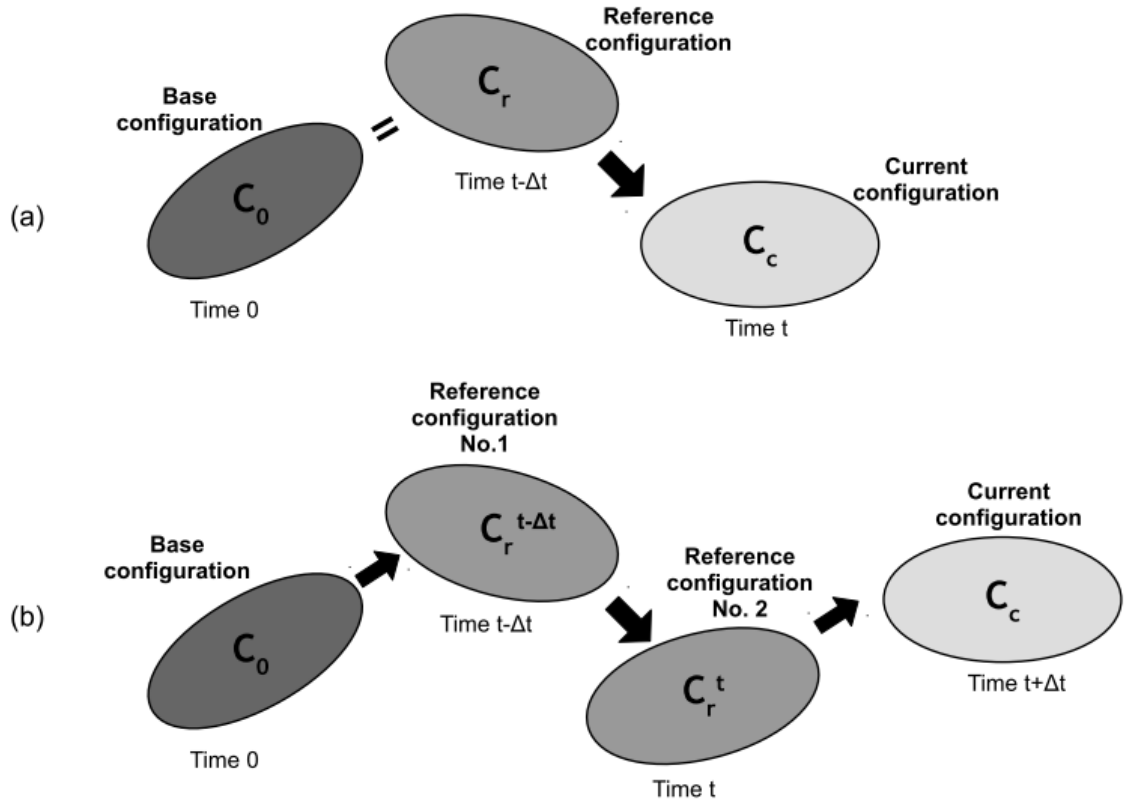

Figure 3.3. Kinematics of Lagrangian formulation in terms of (a) TL and (b) UL description (modified from (Nonlinear Finite Element Methods, 2016))

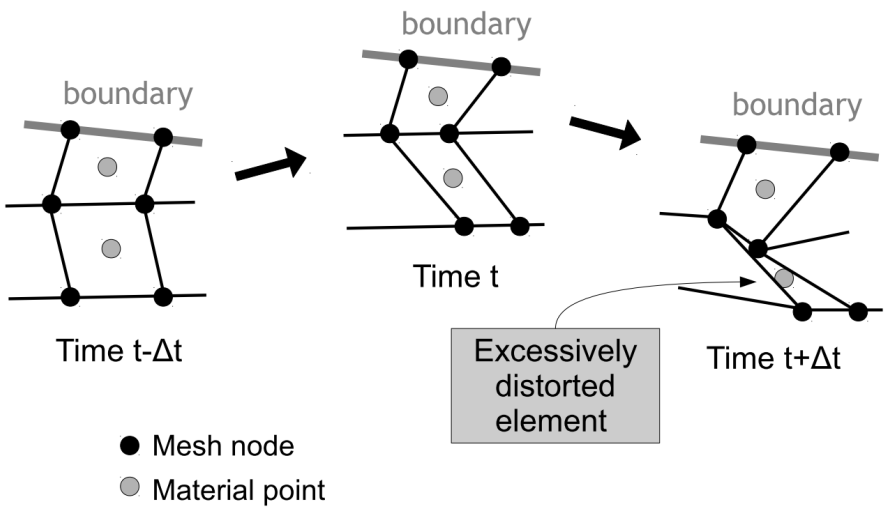

Figure 3.4. Possible progressive distortion of finite elements in UL formulation

3.1.4 Eulerian formulation

Eulerian description of FEM allows to measure the change of field variables with time in prescribed cross-sections. FEM implementation of Eulerian description is based on fixed mesh in space and material point particles which are moving through this mesh as it is presented in figure 3.5. The movement respects governing equation and prescribed boundary conditions. Hence, any finite deformation are allowed and no mesh distortion will occur. However, precise deformation calculations requires large number of small finite elements and high processing power in consequence. Moreover, free surface and interface tracking is problematic (Fedkiw et al., 1999).

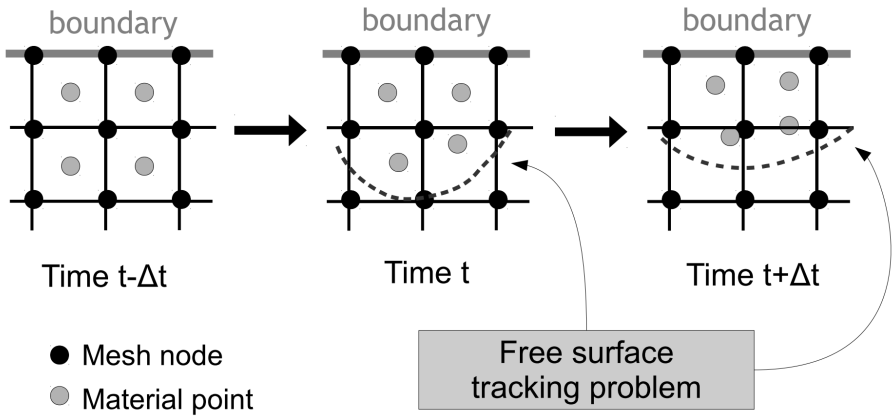

Figure 3.5. Free surface tracking problem in Eulerian FEM calculations

3.1.5 Arbitrary Lagrangian-Eulerian (ALE) formulation

The coupling between Lagrangian and Eulerian formulation has started in early 1960s in Los Alamos National Laboratory (Margolin, 2013). Arbitrary Lagrangian-Eulerian (ALE) formulation combines advantages of both Lagrangian and Eulerian formulation (Hirt et al., 1974). ALE enables the modelling of large deformation problems without extensive mesh distortions and, in contrast to pure Eulerian formulation, offers free surface tracking (Donea et al., 2004). This features makes ALE very attractive in modelling pile jacking. The basic concept of ALE assumes decoupled movement between material points and mesh nodes. Consequently, material points and mesh nodes move in arbitrary specified way (Donea et al., 1982). The calculation procedure contains three steps. In the beginning of each time increment we get deformed mesh, which becomes referential domain. Then material points are moved to new positions which are limited by boundaries nodes. This is the first step of ALE algorithm. Then, in rezone step, the new mesh in generated to obtain best fit to the existing material points and boundary nodes. Finally, the current solution is transferred from the old mesh to the rezoned one. All steps can be followed in graphical representation of the ALE calculation process in figure 3.6.

The crucial parts of ALE formulation are the rezone step and the efficiency of remapping algorithm. Frequency of the remapping also plays a key role. Although ALE offers modelling

of the large deformations, the free surface tracking may introduce some problems in numerical calculation. For example, remapping algorithm may not be able to follow complex changes in free surface shape and new rezoning techniques are still in development (e.g., Knupp et al., 2002). In terms of pile jacking, the free surface tracking problems may occur when heave of soil surface progresses.

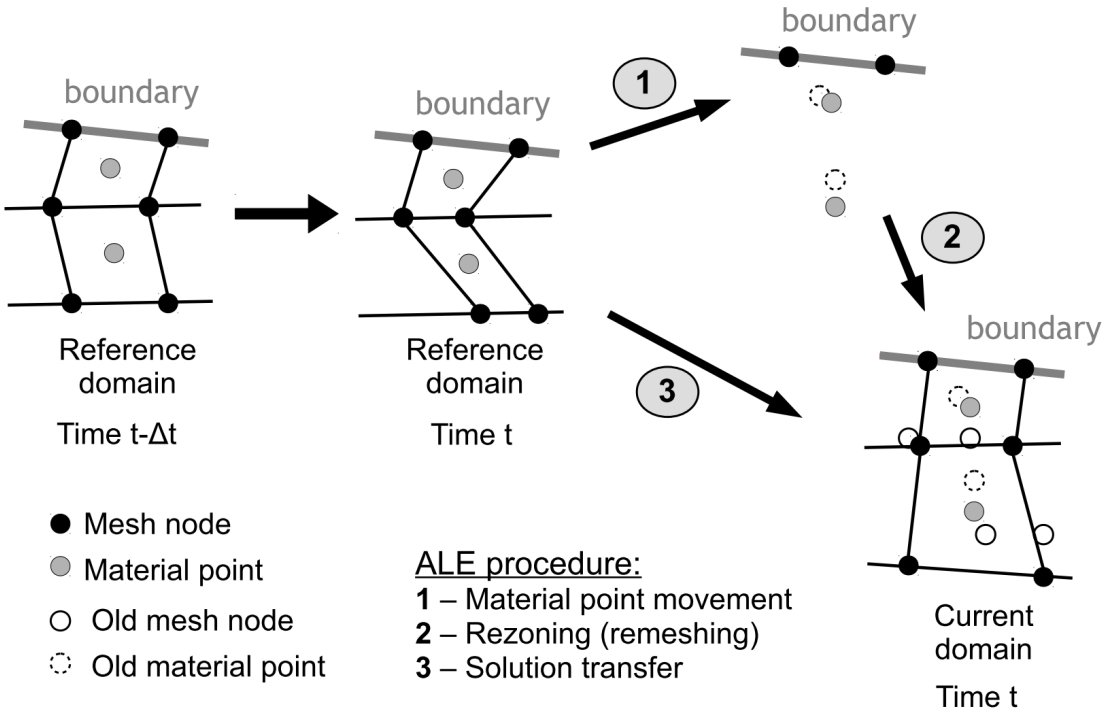

Figure 3.6. Remeshing procedure in ALE formulation

3.1.6 Coupled Eulerian-Lagrangian (CEL) formulation

Coupled Eulerian-Lagrangian (CEL) formulation was also formulated in early 1960s (e.g., Noh, 1963). CEL such as ALE also combines best features of Lagrangian and Eulerian description, but instead of remapping techniques, the contact between Eulerian and Lagrangian domain is used. Thus, each domain in CEL formulation can be discretized in Eulerian or Lagrangian manner, as it can be seen in figure 3.7. During FEM analysis the Lagrangian body penetrates the Eulerian one. In each time increment, boundary nodes from Lagrangian body are mapped into the Eulerian domain. Predefined contact algorithm enables calculation of the resistance forces that are applied on the Lagrangian boundary nodes and pressures that becomes new boundary conditions in Eulerian domain, see figure 3.7. Consequently, forces applied on the Lagrangian body induce its deformation. On the other side, new boundary conditions in form of pressures introduced to the Eulerian domain cause outflow of the material from area, where Lagrangian body is actually located.

CEL method seems to be ideally suited for engineering problem where resistance of the penetrated object is the major unknown and where the free surface deformation is not

important. This is particularly in pile jacking simulation or in offshore constructions such as spudcans. In CEL method any large finite deformation of the Eulerian domain are allowed, but similarly as in pure Eulerian description, free surface tracking is problematic and more accurate deformation calculation requires application of small finite elements.

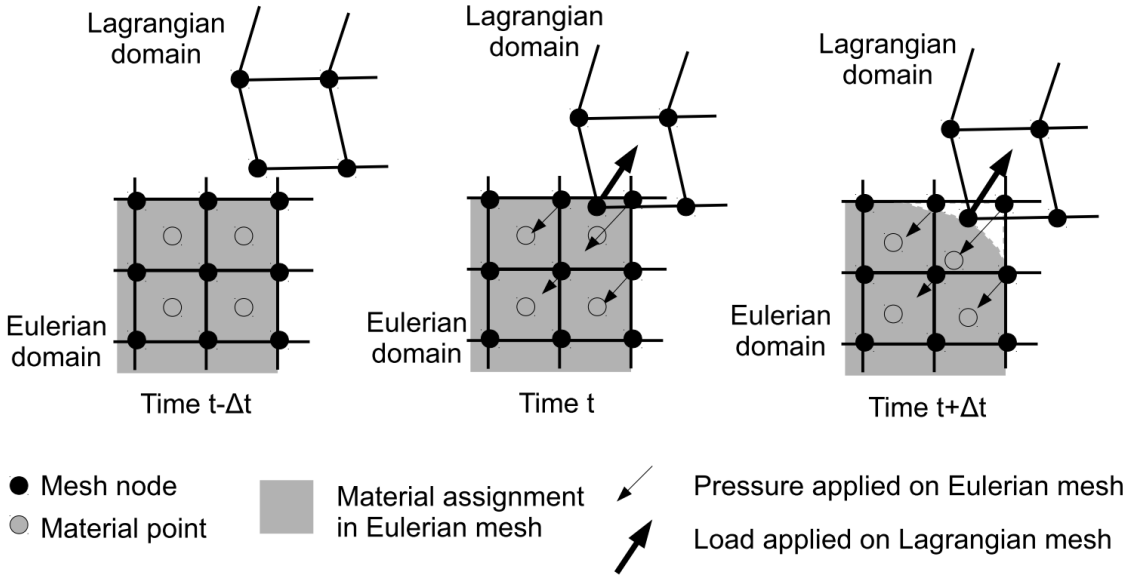

Figure 3.7. Basic concept of CEL calculation procedure

3.1.7 Implicit versus explicit analysis

To obtain numerical solution from FEM analysis one of two possible approaches have to be used. They are implicit and explicit methods, respectively. Let us assume some time depended problem, that is intended for FEM calculation, see figure 3.8. In time *t* current state of the system *C(t)* exist, which can be understand as a current or reference configuration. The state of the system in later time *t+Δt* is unknown and it is described by function *C(t+Δt)*. Implicit methods calculate state *C(t+Δt)* from both configurations, *C(t)* and *C(t+Δt)*, respectively. This can be written by equation:

$$F(C(t), C(t+\Delta t)) = 0 \tag{3.1}$$

Explicit methods used different strategy and configuration *C(t+Δt)* is found from the previous one, as described by equation:

$$C(t+\Delta t) = F(C(t)) \tag{3.2}$$

Above mathematical formulation implies significant consequences in FEM analysis. Explicit formulation is better suited for dynamic, quasi-static and short lasting events. On the other hand, implicit methods are well suited for static response of the system or long term events. Numerical formulations presented in previous sections requires the application of one of these

two described methods. ALE and CEL methods are based on incremental calculation, so explicit solver is required for them. UL formulation can work under explicit or implicit method.

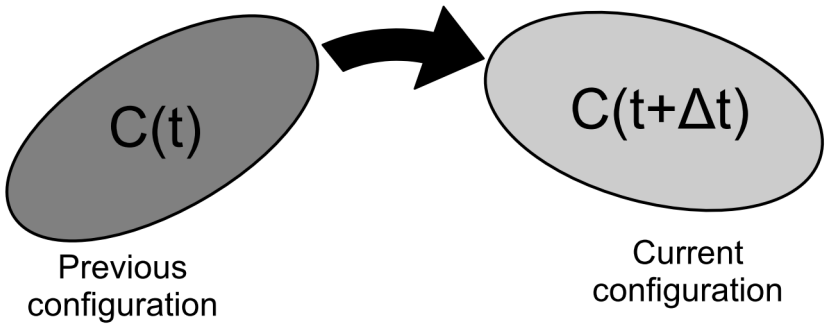

Figure 3.8. Configuration of the system at two different times

3.1.8 Numerical modelling of pile installation effects

Installation and consolidation phases that will be considered in this thesis have different physical and mechanical nature. Installation phase takes relatively small amount of time, which implies undrained conditions in cohesive soils and contains large deformation problem. Hence, explicit solver with ALE or CEL method is the best choice for this step. However, consolidation phase is small deformation problem with long time duration and drained conditions. Here, the implicit method is the only possible choice for numerically effective calculation. Some kind of compromise is to use UL formulation for both installation and consolidation phases, but large mesh distortions can make solution less accurate or even unachievable. Numerical analysis of both installation and consolidation phases for spudcan foundation in clay has been done by Yi et al. (2014). Yi et al. calculate installation phase with CEL method and then, they used external algorithm to map entire solution to the new mesh and calculate consolidation by implicit method and UL formulation. On the other hand, Zhou et al. (2013) calculate both installation and consolidation phase with UL formulation for jacked pile in cohesive soil.

Herein, another mode is proposed which is schematically presented in figure 3.9. The basic solution for undrained pile installation is UL formulation with effective stress approach. However, this solution will be controlled by independent calculation with ALE or CEL method where total stress analysis will be used. Application of ALE or CEL gives more accurate and trustworthy solution for installation phase. The comparison between ALE or CEL and UL provides information about numerically affected points in UL solution that are caused by mesh distortions for instance. Further, this kind of comparison gives a possibility to upgrade mesh shape and size in UL formulation to achieve the best possible results. The limitations of the UL formulation and theirs consequences in installation effects modelling will also be recognized. When accuracy of the implicit solution for installation phase will be satisfactory, the consolidation step in UL model will be performed. As two different analysis types (effective stress for UL and total stress for ALE or CEL) are performed in proposed approach, the correlation between constitutive laws in terms of total and effective stresses has

to be derived. This will be shown in next section.

The possibility of wider analysis of the problem make an additional advantage of using different numerical formulations and constitutive behaviours. In some cases presented in this thesis three independent solutions for single case will be given. Consequently, the reliability of analysis will be much higher.

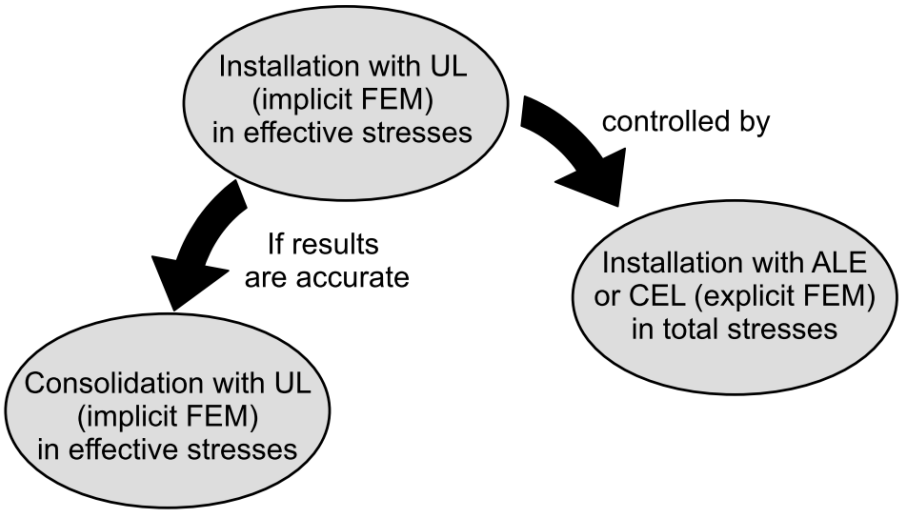

Figure 3.9. Proposed methodology for pile installation effects calculation with FEM

3.2 Total stress analysis versus effective stress analysis

3.2.1 General considerations

Abaqus software suit has significant limitations. Two-phase soil model can be built only in implicit package. Thus, the UL solution with implicit solver can be carried out with effective stress analysis. On the other hand, the default explicit package is limited only to model single-phase material. Hence, ALE and CEL solutions have to be undertaken with total stress analysis. This is why the effective and total stress approaches were assumed in the proposed methodology, as it was explained in previous section and it is shown in figure 3.9. It is possible to create user subroutine, which will take into consideration two-phase mediumin explixit solver (Hamann and Grabe, 2013), but it is not necessary. Correlation between total stress parameters with effective ones can be established in much simpler way. The additional argument for this solution is necessity of consolidation calculation in implicit solver. The fitting between effective and total stresses will be presented in the sections below. The constitutive models details with assumptions of soil simplification will be also provided.

3.2.2 Effective stress principle

Effective stress theory has been firstly developed by Terzaghi in early 1920s (Terzaghi, 1925) and has been extended by others in next years (e.g., Skempton, 1960). It states that total stresses acting on soil can be decomposed into two parts. The first one are effective stresses that represent the forces carried by the soil skeleton. The second part are the pore water

pressures. Effective stress concept for isotropic, fully saturated medium can be written by formula (Verruijt, 2016):

$$\sigma = \sigma' + \alpha u \tag{3.3}$$

where: σ – total stresses, σ' – effective stresses, α – Biot's effective stress coefficient, u – pore water pressures.

Biot's effective stress coefficient α represents the soil or rock grains connection quality and can be expressed by equation (Verruijt, 2016):

$$\alpha = 1 - \frac{C_s}{C_m} \tag{3.4}$$

where: α – Biot's effective stress coefficient, C_s – compressibility of solid material, C_m – compressibility of porous material.

Biot's effective stress coefficient α is important in rock mechanics (Segall and Fitzgerald, 1998). In terms of soil mechanics, the connection between particles is weak or does no exist. Hence, Biot's effective stress coefficient α is often assumed as equal to one and effective stress principle can be simplified to well-known formula (Verruijt, 2016):

$$\sigma = \sigma' + u \tag{3.5}$$

where: σ – total stresses, σ' – effective stresses, u – pore water pressures.

Soil is a mixture of grain particle, water, air and contaminations. The commonly accepted soil model is three-phase medium (Atkinson, 2007). These phases include air, water and solid. Numerical model of soil structure often requires more simplifications. The cohesive soils in this thesis will be considered as a two-phase, fully saturated and isotropic material. The consequences of above assumptions will be described below.

The pore water pressure changes due to loading can be estimated from Skempton's formula (Skempton, 1954):

$$\Delta u = B\left(\Delta\sigma_3 + A\left(\Delta\sigma_1 - \Delta\sigma_3\right)\right) \tag{3.6}$$

where: Δu – excess pore water pressure, $\Delta\sigma_1$ – change in major principal stress, $\Delta\sigma_3$ – change in minor principal stress, A – pore pressure parameter A, B – pore pressure parameter B.

The Skempton's pore pressure parameter A is stress dependent (Law and Holtz, 1978). Hence, it depends on constitutive law for two-phase medium. Herein, Modified Cam-Clay (MCC) model will be used to describe soil structure behaviour. Hence, value of parameter A will change with accordance to the strain changes. Pore pressure parameter B is related to the degree of saturation (Skempton, 1954). In this thesis, the fully saturated soil medium is assumed. Soils are never fully saturated, but cohesive soils shows relatively high saturation ratio. For fully saturated soil specimen B parameter is equal to one. Consequently, excess pore water pressure changes will be only strain dependent.

3.2.3 Total stress analysis

Total stress approach will be considered in CEL or ALE methods where explicit solver is used. Total stress analysis is a common approach in the cohesive soil modelling. It includes only total stresses, without taking into consideration pore water pressures. Hence, soil is modelled as a single-phase medium. It is convenient modelling technique in pile jacking analysis due to rapid loading in form of pile penetration, negligible amount of consolidation and small number of soil parameters. Herein, total stress analysis will be carried out under the following assumptions:

1. Soil is fully saturated and isotropic medium.
2. Fluid and soil grains are almost incompressible.
3. Soil can be modelled as an elastic perfectly plastic material.

The first assumption has been already stated in previous section. Soil will be described as an isotropic and elastic material by linear elastic model, which contains two soil parameters: Poisson's ratio υ_u and undrained elastic modulus E_u. The incompressibility of fluid and soil grains results in incompressible behaviour of soil medium. This assumption can be satisfied only when Poisson's ratio reaches value of υ_u=0,5. As this value can make numerical troubles (Potts and Zdravković, 1999), a little smallest number of υ_u=0,49 has to be used. The assumption of isotropic material results in separation between shear and volumetric effects, which can be written by equations (Dassault Systèmes, 2013):

$$\boldsymbol{\sigma} = 2G\,\boldsymbol{e}^{\boldsymbol{el}} + K\,\varepsilon^{el}_{vol}\,\boldsymbol{I} \tag{3.7}$$

$$\boldsymbol{\varepsilon}^{\boldsymbol{el}} = \boldsymbol{e}^{\boldsymbol{el}} + \frac{1}{3}\,\varepsilon^{el}_{vol}\,\boldsymbol{I} \tag{3.8}$$

where: $\boldsymbol{\sigma}$ – stress tensor, G – shear modulus, $\boldsymbol{e}^{\boldsymbol{el}}$ – deviatoric part of elastic strain tensor, K – bulk modulus, ε^{el}_{vol} – elastic volumetric strain, $\boldsymbol{I}$ – identity matrix, $\boldsymbol{\varepsilon}$ – elastic strain tensor.
Shear modulus and bulk modulus can be related with Poisson's ratio and elastic modulus by equations (e.g., Atkinson, 2007):

$$K = \frac{E}{3(1-2\nu)} \tag{3.9}$$

$$G = \frac{E}{2(1+\nu)} \tag{3.10}$$

where: K – bulk modulus, E – elastic modulus, υ – Poisson's ratio, G – shear modulus.
It is worth to noticed that one can derive the generalised Hooke law from equations (3.7)-(3.10), which is shown in Appendix A. In terms of total stress analysis elastic modulus E becomes undrained elastic modulus E_u and Poisson's ratio υ becomes undrained Poisson's ratio υ_u with value of 0,49. Numerical problems reported by Potts and Zdravković (1999) for

υ=0,5 can be understood taking into account (3.9). For Poisson's ratio of υ=0,5, bulk modulus K tends to infinity.

Plastic part of soil behaviour is modelled with Tresca plasticity which is well suited for undrained analysis (Potts and Zdravković, 1999). Geometrical representation of the Tresca criterion, as implemented in Abaqus, is presented in figure 3.10. Tresca plasticity consists of two governing parameters: undrained shear strength of soil c_u and tension cut-off stress σ_t. Tension cut-off is modelled with Rankine surface (Dassault Systèmes, 2013) and it is assumed that soil practically does not fail in tension. Herein, tension cut-off σ_t=1,0kPa is used to avoid numerical problems. Practically, tension stresses in pile jacking simulation are related only to the near-surface area where soil up-heave occurs. This problem will be discussed wider in chapter 5.

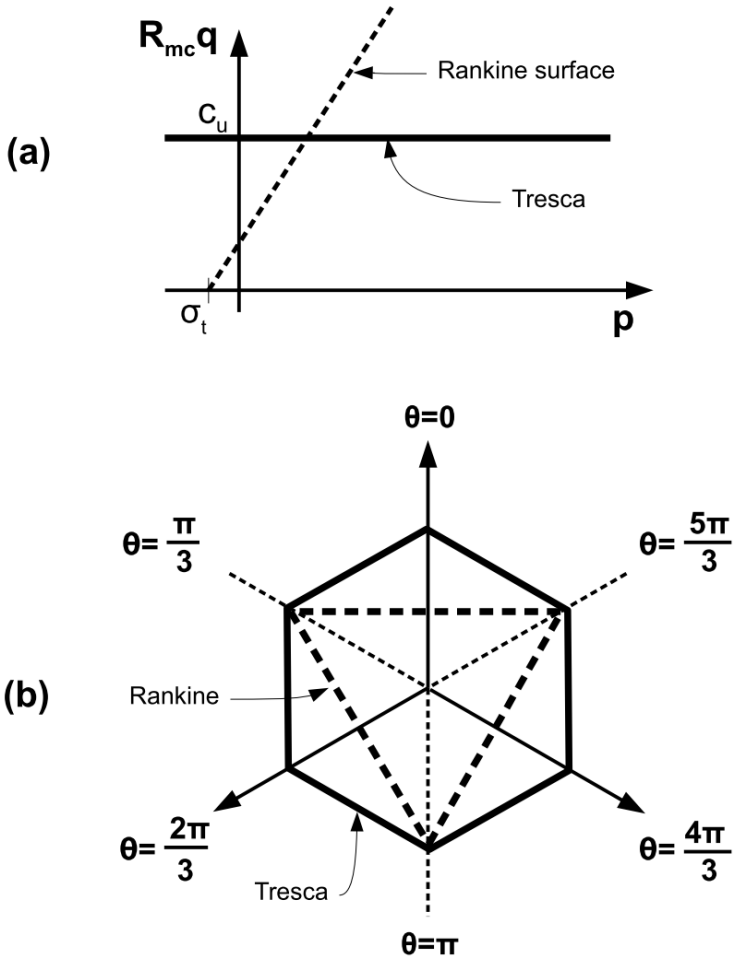

Figure 3.10. Tresca criterion in: (a) meridional and (b) deviatoric plane (modified from Dassault Systémes (2013)*)*

3.2.4 Effective stress analysis

Effective stress calculations are carried out in Abaqus implicit solver with UL formulation. Advantage of effective stress approach is the possibility of simultaneous modelling of loading

phase and following consolidation step. Consequently, installation and consolidation processes can be taken into consideration in one numerical model. Effective stress analysis is performed for two-phase soil model under the same assumption as in total stress approach:

1. Soil is fully saturated and isotropic medium.
2. Fluid and soil grains are incompressible.
3. Soil can be modelled as an elastic perfectly plastic material.

First assumption has been already stated in section 3.2.2. Modelling of soil as a two-phase, fully saturated medium enables incompressible fluid and soil to be used. Skempton's parameter B in terms of poroelasticity can be written as (Verruijt, 2016):

$$B=\frac{\Delta u}{\Delta \sigma}=\frac{C_m-C_s}{(C_m-C_s)+n(C_f-C_s)} \tag{3.11}$$

where: B – Skempton's B parameter, Δu – excess pore water pressure, $\Delta \sigma$ – total stress change, C_m – compressibility of the porous medium, C_s – compressibility of the soild particles (grains), C_f – compressibility of the fluid, n – porosity.

Assumption of incompressibility of soil grains and fluid leads to C_s=0 and C_f=0. Hence, Skempton's B parameter is equal to 1. This is consistent with engineering assumption presented in section 3.2.2 that for fully saturated soils B parameter is almost equal to one. However this assumption leads to numerical troubles. If grains and fluid are incompressible then the increase of load leads to increase in pore water pressure without any deformations. Consequently, numerical model breakdowns with an error. To avoid such situation a little compressibility of water can be introduced (Plaxis Manuals, 2015) or load can be applied in very short time with drainage permission. In pile jacking simulation the second solution is used as pile installation process requires some, still small amount of time. Moreover, the influence of drainage should be always considered in field conditions. Hence, application of the pile jacking process spread in time with permitted drainage will be more realistic. Further, pile installation time is much shorter than consolidation time, so differences between total stress analysis and effective stress analysis in pile jacking modelling will be negligible.

The Modified Cam-Clay (MCC) model will be used to model soil as a two-phase medium and elastic perfectly plastic material. Elastic part of the MCC model is modelled in Abaqus by porous elastic model. This model is based on changes in void ratio and mean stresses according to equation (Dassault Systèmes, 2013):

$$\frac{\kappa}{1+e_0}\ln\left(\frac{p+p_t^{el}}{p_0+p_t^{el}}\right)=1-J^{el} \tag{3.12}$$

where: κ – logarithmic elastic bulk modulus, e_0 – initial void ratio, p – mean stress (equivalent pressure stress), p_0 – initial mean stress, p_t^{el} – tensile strength, J^{el} – elastic volume change.

Elastic volume change can be described as (Dassault Systèmes, 2013):

$$J^{el} = \exp\left(\varepsilon_{vol}^{el}\right) = \frac{1+e^{el}}{1+e_0} \tag{3.13}$$

where: J^{el} – elastic volume change, ε^{el}_{vol} – elastic volumetric strain, e^{el} – elastic void ratio, e_0 – initial void ratio.

In original MCC model tensile strength p_t^{el} is equal to zero. Combining $p_t^{el}=0$ with equation (3.13) leads to simplification of the formula (3.13) to the following form:

$$\kappa \ln\left(\frac{p}{p_0}\right) = e^{el} - e_0 \tag{3.14}$$

where: κ – logarithmic elastic bulk modulus, p – mean stress, p_0 – initial mean stress, e^{el} – elastic void ratio, e_0 – initial void ratio.

Above formula is well known elastic part of the MCC model, and it can be directly derived from relation presented in figure 3.11. In total stress analysis decoupled volumetric and shear effects are used, so in porous elastic model the same condition needs to be stated. This is achieved by assumption of the shear modulus G and mean effective stress p independence. Thus, the deviatoric behaviour will be given as (Dassault Systèmes, 2013):

$$\boldsymbol{S} = 2G\boldsymbol{e}^{el} \tag{3.15}$$

where: $\boldsymbol{S}$ – deviatoric stress tensor, G – shear modulus, $\boldsymbol{e}^{el}$ – deviatoric part of elastic strain tensor.

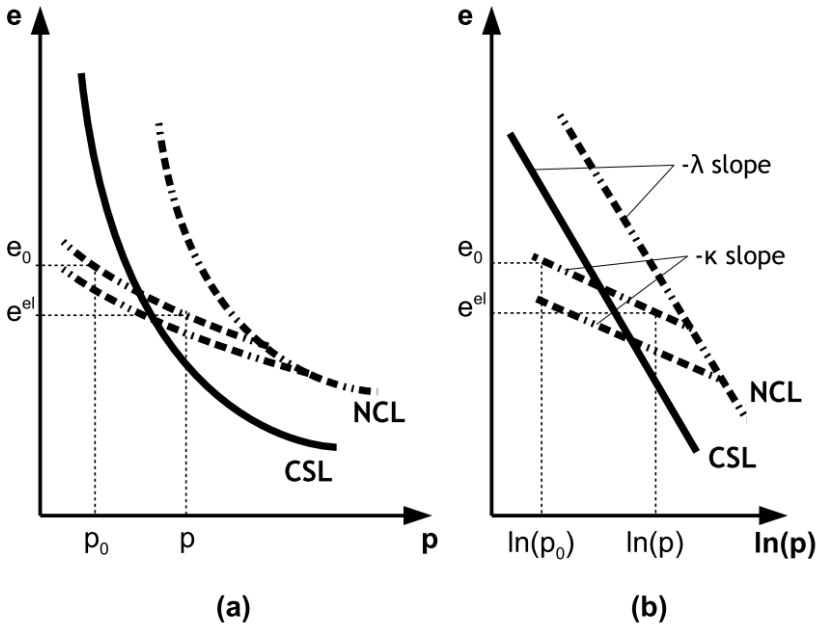

Figure 3.11. (a) e-p and (b) e-ln(p) relations used in porous elasticity and MCC model

The plastic part of the MCC will be modelled by clay plasticity model, as it is implemented in Abaqus (Dassault Systèmes, 2013). The MCC model can be introduced in *p-q-e* space as it is shown in figure 3.12. One can noticed that projection of the yield surface on *p-e* plane is presented in figure 3.11, whereas the *p-q* projection is presented in figure 3.13. Yield function is described by mean stress *p*, Mises equivalent stress *q* and third stress invariant *r* which can be written as follows (Dassault Systèmes, 2013):

$$p=\frac{1}{3}tr\,\boldsymbol{\sigma} \tag{3.16}$$

$$q=\sqrt{\frac{3}{2}\boldsymbol{S}:\boldsymbol{S}} \tag{3.17}$$

$$r=\left(\frac{9}{2}\boldsymbol{S}\cdot\boldsymbol{S}:\boldsymbol{S}\right)^{\frac{1}{3}} \tag{3.18}$$

where: p – means stress, $\boldsymbol{\sigma}$ – stress tensor, q – Mises equivalent stress or deviatoric stress, $\boldsymbol{S}$ – deviatoric stress tensor, r – third stress invariant.

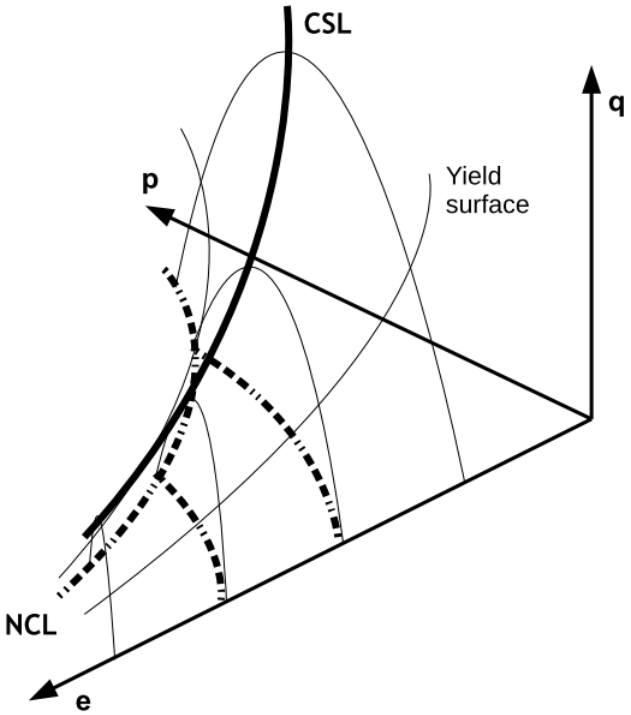

Figure 3.12. MCC model in p-q-e space

The plastic surface function in MCC plasticity is described by equation (Dassault Systèmes, 2013):

$$f(p,q,r)=\frac{1}{\beta^2}\left(\frac{p}{a}-1\right)^2+\left(\frac{t^q}{Ma}\right)^2-1=0 \tag{3.19}$$

where: p – means stress, q – Mises equivalent stress (deviatoric stress), r – third stress invariant, β – constant used for wet surface size modification (see figure 3.13), a – constant that defines yield surface size, t^q – measure of equivalent deviatoric stress, M – slope of the critical state line in p-q plane.
Measure of equivalent deviatoric stress t^q is related to the deviatoric stress q, third stress invariant r and K^π parameter by equation (Dassault Systèmes, 2013):

$$t^q = \frac{1}{2} q \left[1 + \frac{1}{K^\pi} - \left(1 - \frac{1}{K^\pi} \right) \left(\frac{r}{q} \right)^3 \right] \tag{3.20}$$

where: t^q – measure of equivalent deviatoric stress, q – deviatoric stress, K^π – parameter, that defines Cam-Clay surface in deviatoric plane (see figure 3.14), r – third stress invariant.

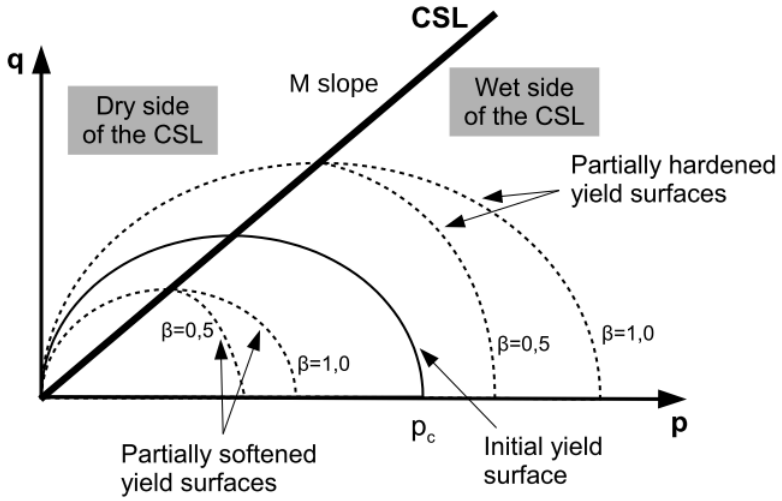

Figure 3.13. p-q projection of MCC critical state surfaces (modified from Dassault Systémes (2013)*)*

For the original MCC model the surface in deviatoric plane is a circle, so K^π is equal to one. Hence, from equation (3.20) one can see that t^q is then equal to the deriatoric stress q. The MCC model uses associated flow rule. The size of the yield surface is defined by equation (Dassault Systèmes, 2013):

$$a = a_0 \exp\left[\left(1 + e_0 \right) \frac{1 - J^{pl}}{\lambda - \kappa J^{pl}} \right] \tag{3.21}$$

where: a – size of the yield surface, a_0 – initial size of the yield surface, e_0 – initial void ratio, λ – logarithmic plastic bulk modulus (see figure 3.11), κ – logarithmic elastic bulk modulus, J^{pl} – plastic volume change, which is formulated as (Dassault Systèmes, 2013):

$$J^{pl} = \exp\left(\varepsilon_{vol}^{pl} \right) \tag{3.22}$$

where: J^{pl} – plastic volume change, ε^{pl}_{vol} – plastic volumetric strain.
Initial yield surface can be described by formula (Dassault Systèmes, 2013):

$$a_0 = \frac{p_c}{1+\beta} \tag{3.23}$$

where: a_0 – initial size of the yield surface, p_c – initial preconsolidation mean stresses, β – constant used for wet surface size modification.
In the original MCC model β=1, so:

$$a_0 = \frac{p_c}{2} \tag{3.24}$$

where: a_0 – initial size of the yield surface, p_c – initial preconsolidation mean stresses.

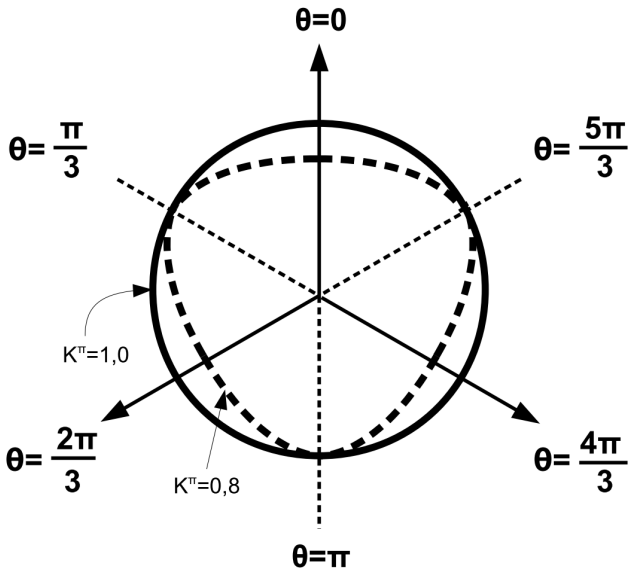

Figure 3.14. Cam-Clay surfaces in deviatoric plane (modified from Dassault Systémes (2013)*)*

3.2.5 Critical aspects of applied constitutive laws

In this thesis the isotropic material is used (see section 3.2.3 and 3.2.4). In particular, this assumption can be questionable for highly overconsolidated clays. Author is aware that for pile installation problem the anisotropy can affect the radial stresses and permeability of soil in horizontal direction. However, assuming isotropic material is practical due to often limited set of laboratory tests.

Using the MCC model for cohesive soils also can be criticized. MCC model allows for extremely large elastic part of shear stresses and it uses the Drucker-Prager failure state

instead of Mohr-Coulomb failure mode (e.g., Plaxis Manuals, 2015). While the Drucker-Prager failure state can be modified, see section 3.2.4 and Dassault Systémes (2013), the large elastic stresses remains a problem. However, in pile jacking simulation the close-pile area is plasticized, so this problem also can be neglected. The last note for MCC model is that it is rather dedicated for so-called fat-clays or low overconsolidated soils (Plaxis Manuals, 2015). In this thesis, the numerical study is intended to shed more light on the pile installation problem rather than provide highly accurate solutions. Further, as it will be shown, the MCC model also can provide acceptable and valuable results for penetration problems in highly overconsolidated soils.

3.2.6 Soil and analysis parameters

Soil parameters used in both effective and total stress analyses are presented in table 3.1. Besides the material constants, the initial conditions have to be also specified. The most important one is the lateral earth pressure at rest coefficient K_0 which has to be treated differently in total and effective stress analysis. This problem will be discussed in next section. Moreover, in effective stress analysis the soil permeability coefficient k, density of water ρ_w and initial pore water pressure distribution u_0 have to be defined.

Table 3.1. Soil parameters used in this thesis

Quantities	*Total stress analysis*	*Effective stress analysis*
Soil medium parameters	ρ_{sr};E_u; υ_u=0,49;, c_u; σ_t=1,0	ρ'; G'; e_0; κ; λ; p_c'(or a'_{0c}); M; β=1,0; K^{π}=1,0; k
Pore fluid parameters	-	ρ_w
Initial conditions	$\sigma_{h,0}/\sigma_{v,0}$	K_0; u_0

Note: all parameters are described in Notation section in the beginning of this thesis

3.2.7 Fitting between effective and total stress analysis

As it was said in previous sections, pile installation phase will be modelled in total stress approach or in effective stress one. The basic problem is to relate constitutive models used in both analyses to get similar soil response in undrained conditions. Here, the fitting between linear elastic/Tresca plasticity and the MCC has been done. Firstly, let us consider elastic parts of both constitutive laws. In total stress analysis as well as in effective one, the decoupling between shearing and volumetric effects is assumed. This leads to correlation (Atkinson, 2007):

$$G_u = G' = G \tag{3.25}$$

where: G_u – shear modulus in undrained conditions, G' – shear modulus in drained conditions, G – shear modulus of soil.

The shear modulus can be described in terms of elastic modulus and Poisson's ratio (see equation (3.10). The elastic part of MCC is described by shear modulus G and logarithmic

elastic modulus κ. Thus, the undrained elastic modulus can be written as:

$$E_u = 2G(1+\nu_u) \tag{3.26}$$

where: E_u – undrained elastic modulus, G – shear modulus, ν_u – undrained Poisson's ratio.
As Poission's ratio is assumed as ν_u=0,49 (see section 3.2.3), the undrained elastic modulus is equal to:

$$E_u \approx 3G \tag{3.27}$$

where: E_u – undrained elastic modulus, G – shear modulus.
Fitting between plastic part of MCC model and Tresca plasticity is more complex, because the undrained shear strengh of soil c_u needs to be correlated with the MCC parameters. Relation between undrained shear strength of soil with MCC parameters has been presented by Potts & Zdravković (1999):

$$c_u = OCR\,\sigma'_{vi}\; g(\theta)\cos\theta\,\frac{(1+2K_0^{NC})}{6}(1+B^2)\left[\frac{2(1+2K_0^{OC})}{(1+2K_0^{NC})\,OCR\,(1+B^2)}\right]^{\kappa/\lambda} \tag{3.28}$$

where:

$$B = \frac{\sqrt{3}(1-K_0^{NC})}{g(-30)(1+2K_0^{NC})} \tag{3.29}$$

$$g(\theta) = \frac{\sin\phi'}{\cos\theta + \frac{\sin\theta\sin\phi'}{\sqrt{3}}} \tag{3.30}$$

where in equations (3.28)-(3.30): c_u – undrained shear strength, OCR – overconsolidation ratio, σ'_{vi} – vertical effective geostatic stresses, K_0^{OC} – earth pressure at rest coefficient of preconsolidated soil, K_0^{NC} – earth pressure at rest coefficient of normally consolidated soil, κ – logarithmic elastic modulus, λ – logarithmic plastic modulus, θ – Lode angle, ϕ' – angle of internal friction.
The relation between undrained shear strength of soil and the MCC parameters has been also defined by Wroth (1984):

$$\frac{c_u}{p_0'} = \frac{M}{2}\left(\frac{p_c'}{2p_0'}\right)^{(\lambda-\kappa)/\lambda} \tag{3.31}$$

where: c_u – undrained shear strength, p_0' – initial effective mean stress, M – slope of the critical state line in p-q plane, p_c' – initial effective preconsolidation mean stresses, κ – logarithmic elastic modulus, λ – logarithmic plastic modulus.

Parameters in equation (3.30) cannot be used in Abaqus software. Proposition described with equation (3.31) is a better choice, but it only presents the switch from MCC parameters to undrained shear strength of soil. Opposite relation is also required and, consequently, equation (3.31) can be transformed to the following form:

$$p_c' = \left(\frac{4 c_u}{M} (2 p_0')^{-\kappa/\lambda} \right)^{\frac{\lambda}{\lambda-\kappa}} \tag{3.32}$$

where: p_c' – initial effective preconsolidation mean stresses, c_u – undrained shear strength, p_0' – initial effective mean stress, M – slope of the critical state line in p-q plane, κ – logarithmic elastic modulus, λ – logarithmic plastic modulus.
However, equation (3.32) is valid only for the dry side of the CSL and for the wet side of CSL with β=1. Generalised form of equation (3.32) for the wet site of the CSL is as follows:

$$p_c' = \left(\frac{2(1+\beta) c_u}{M} ((1+\beta) p_0')^{-\kappa/\lambda} \right)^{\frac{\lambda}{\lambda-\kappa}} \tag{3.33}$$

where: p_c' – initial effective preconsolidation mean stresses, β – constant used for wet surface size modification, c_u – undrained shear strength, p_0' – initial effective mean stress, M – slope of the critical state line in p-q plane, κ – logarithmic elastic modulus, λ – logarithmic plastic modulus.

Full derivation of equations (3.31)-(3.33) is shown in Appendix B. The constitutive laws parameters correlation shown by equations (3.31) to (3.33) provides similar response of the soil. This is important in installation phase, where analysis will be performed in effective and total stress. The second advantage of such approach is the possibility of verification of the undrained parameters from the drained ones. This will be important in CPT modelling (without pore water pressure measurement) with ALE, when only the installation phase will be considered. Preliminary studies considering the accuracy of above correlations will be presented in chapter 5.

The fitting between constitutive laws is the only one part of the total and effective stress analysis fitting problem. The initial conditions also have to be adjusted in both approaches. The geostatic stress consists of two components: the vertical stress and horizontal one. The vertical effective and total stress can be related with the assumption of full soil saturation:

$$\rho_{sr} = \rho' + \rho_w \tag{3.34}$$

where: ρ_{sr} – total soil density (saturated soil density), ρ' – effective soil density, ρ_w – water density.
The horizontal stresses are calculated using earth et rest pressure coefficient which is defined in terms of effective stresses:

$$K_0 = \frac{\sigma'_{h,0}}{\sigma'_{v,0}} \tag{3.35}$$

where: K_0 – lateral earth et rest pressure coefficient, $\sigma'_{h,0}$ – initial effective horizontal stress, $\sigma'_{v,0}$ – initial effective vertical stress.
The first approach to calculate the total stress ratio σ_h/σ_v is to use relation from theory of elasticity (e.g., Thomsen, 1986):

$$\frac{\sigma_h}{\sigma_v}=\frac{\nu_u}{1-\nu_u} \tag{3.36}$$

where: σ_h – total horizontal stress, σ_v – total vertical stress, ν_u – undrained Poisson's ratio.
Using the undrained Poisson's ratio of ν_u=0,49, the equation (3.36) returns value almost equal to one, which is typical for water. However, equation (3.36) does not represent realistically the initial state of the soils, especially the highly preconsolidated ones. The alternative approach is to define undrained stress ratio with Terzaghi's theorem and effective stress principle:

$$\frac{\sigma_{h,0}}{\sigma_{v,0}}=\frac{\sigma'_{h,0}+u_0}{\sigma'_{v,0}+u_0}=\frac{K_0\sigma'_{v,0}+u_0}{\sigma'_{v,0}+u_0} \tag{3.37}$$

where: $\sigma_{h,0}$ – initial horizontal total stress, $\sigma_{v,0}$ – initial vertical total stress, $\sigma'_{h,0}$ – initial effective horizontal stress, $\sigma'_{v,0}$ – initial effective vertical stress, K_0 – lateral earth pressure at rest coefficient, u_0 - initial pore water pressure.
Equation (3.37) is better formula to define the initial stress state in total stress analysis because it includes loading history and actual water table. One can noticed that for earth pressure at rest coefficient K_0=1,0 equation (3.37) also returns one.

3.3 Contact modelling

3.3.1 Pile-soil interaction

Contact between pile surface and soil is a complex interaction which depends on shearing rate, stress levels, material roughness, applied boundary conditions and total displacement (e.g., Bond and Jardine, 1991; Lehane and Jardine, 1994a; Tsubakihara et al., 1993). The description of interface behaviour is similar to the ordinary soil testing. The pile-soil interface behaviour during shearing can be described in terms of shear strain and shear stress as it is shown in figure 3.15a and there are three characteristic shear stresses defined by peak, critical and residual values. The peak and critical values can be easily measured in standard direct shear box, while residual values of interface shear strength are usually determined in ring shear apparatus which allows for arbitrary large displacement. During pile jacking different displacement on the pile wall are mobilized and consequently different shear stresses in pile shaft are generated. This problem has been already mentioned in Chapter 2, section 2.2. The interface shearing is even more complicated because, as in typical soil shearing, the influence of normal stress on the shear stresses is also observed. Hence, soil shearing against the interface can be express in normal stress versus shear stress space, as it is shown in figure 3.15b. Let us notice, that peak values are reached relatively fast and they require small

displacements, so these values are usually mobilized near pile toe. The residual strength requires large displacement to mobilize, so it will be reached on upper part of pile shaft. Both states can be approximate by straight line which lead to the Coulomb law of friction with coefficient of friction equal to (e.g, Popov, 2010):

$$\mu = \tan(\delta) \tag{3.38}$$

where: μ – Coulomb coefficient of friction, δ – angle of interface friction.

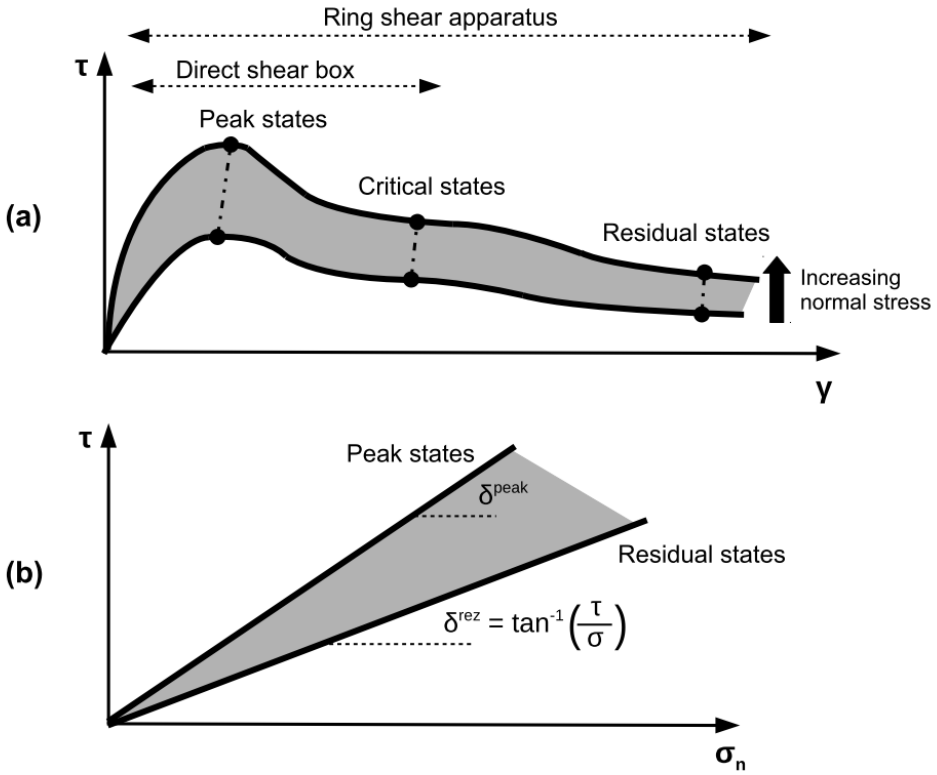

Figure 3.15. (a) Shear stress - shear strain and (b) Shear stress - normal stress relations for interface shearing

However, the most important feature that defines soil-interface behaviour in shear is the rate of shearing. Pile is typically pressed into subsoil with high velocity in undrained conditions. Then, consolidation follows where drainage is allowed and small movement of the soil around the pile can occurs. The same happens when pile is loaded. Consequently, there are two periods in pile history that affect the interface behaviour: the fast shearing during installation and slow shearing during consolidation and loading. The fast shearing (undrained conditions) and slow shearing (drained conditions) can be distinguished using the following formula (e.g., Vermeer and Meier, 1998):

$$T_v = \frac{kE_{oed}}{\gamma_w l^2} t \tag{3.39}$$

where: T_v – time factor, k – permeability coefficient, E_{oed} – oedometric modulus, γ_w – unit

weight of water, *l* – drainage length, *t* – construction time.
According to Vermeer and Meier (1998) the undrained conditions can be recognised when T_v<0,1 and the drained conditions when T_v>0,4. The fast and slow shearing are reflected in mobilized angle of interface friction. The relation between angle of interface friction and rate of shearing in terms of total stresses (undrained conditions) is presented in figure 3.16a. As can be seen, when the interface shear rate is extremely slow, maximum and minimum values of friction angle are almost the same. However, when the rate of shearing starts to increase, the peak and residual values are increasing in different manner. This is common observation from research studies (e.g., Lehane and Jardine, 1994a). After the fast shearing the slow one follows, see figure 3.16b. Here, effective values of friction angle are used and the influence of shearing rate in previous phase is observed.

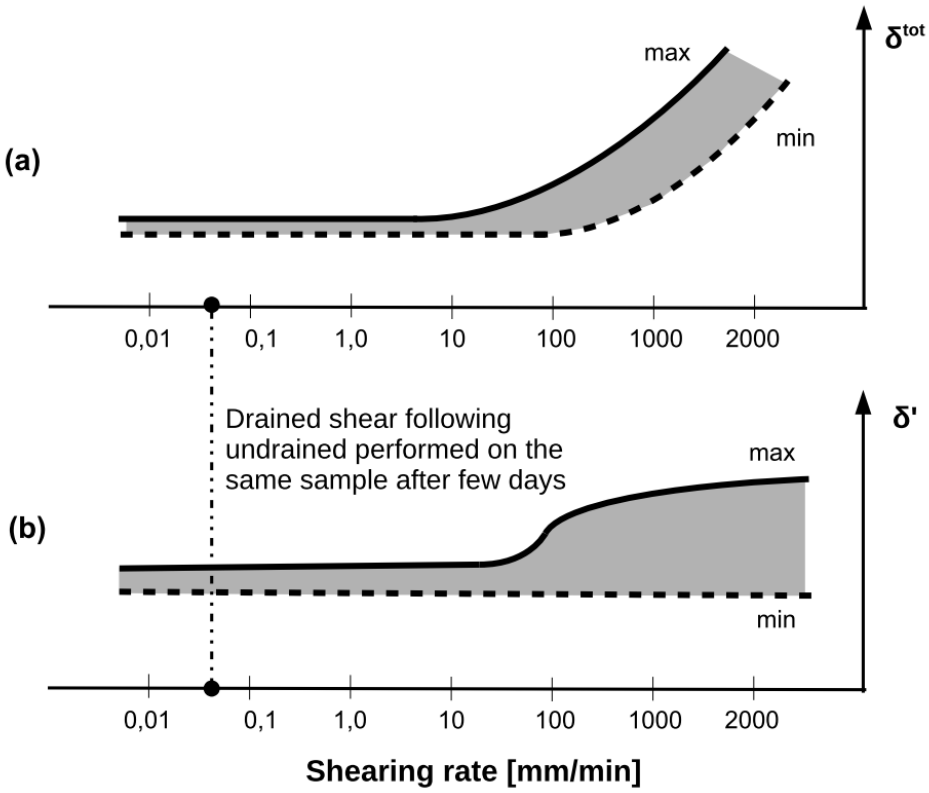

Figure 3.16. (a) Angle of interface friction mobilized during undrained shearing and (b) drained shearing following fast (generalised after Bond and Jardine (1991) and Lehane and Jardine (1994a))

3.3.2 Contact model for numerical studies

The contact modelling in FEM is divided into two concepts. In total stress analysis the adhesion is applied while in the effective stress approach the frictional contact is used. The adhesion is defined as a fraction of undrained shear strength (e.g., Potyondy, 1961). On the other hand, the friction coefficient is used in frictional contact and effective stress analysis (e.g., Tsubakihara et al., 1993). However, using the adhesion in total stress approach and friction coefficient in effective stress analysis does not permit to get the same response at the

interface. In contact modelling with Abaqus the total load is transferred from one body to another (Dassault Systèmes, 2013). Hence, analysis type is not significant and the same friction coefficient can be used in total and effective stress models. This facilitates the contact problem at the interface and enables to compare the results. Consequently, in this thesis the same friction coefficient will be used in total and effective stress approaches.

Pile will be jacked into subsoil with a prescribed velocity. Thus, we can estimate the total range of friction angle. The complex softening behaviour of interface is not possible to model with default Abaqus settings (Dassault Systèmes, 2013). Moreover, the past research has shown that interface behaviour can be ambiguous in practical application due to high variability (Geotechdata.info, 2013). Hence, the residual value of friction angle will be used for jacking phase. Consequently, friction fatigue will not occur in numerical model and obtained results may be less accurate especially near the pile toe. The advantage of such approach is relatively safe solution which gives more control in numerical modelling. In consolidation phase, carried out after installation, the coefficient of friction will be switched to the residual value with accordance to the slow shearing following fast mode. This will be done only where information about residual angle of interface friction will be provided. The contact model is schematically summarized in figure 3.17. As can be seen, pile-soil interface behaviour will be modelled with two coefficients of friction depending on current analysis phase.

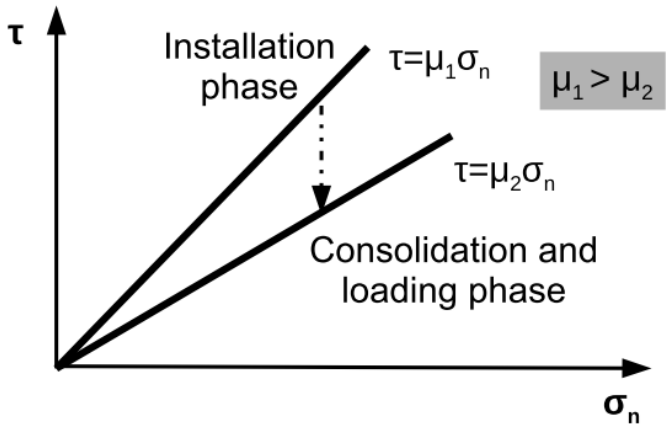

Figure 3.17. Pile-Soil contact model used in this thesis

Chapter 4

Finite Element Method (FEM) overview

The origins of FEM can be found in aerospace industry and the four pioneers of this method can be pointed out. All of them were linked with aircraft industry in some part of theirs professional career as tutors and engineers. This was mainly caused by computational cost of FEM in those times and as a result, only the large industrial companies like Boeing or government institutions were able to posses computers in early 1950s (*Introduction to Finite Element Methods*, 2015). The first of the pioneers was M.J. Turner, an Aircraft engineer at Boeing (Bjorhus, 1995). He refined and improved Direct Stiffness Method and he supervised the development of first finite element in early 1950s (Zienkiewicz, 1995). B.M. Irons, next of the FEM pioneers, invented isoparametric models and shape function. R.J. Melosh made systematization of variational derivation of stiffness matrix and E.L. Wilson developed first open source FEM software called SAP (*Introduction to Finite Element Methods*, 2015).

Simultaneously, there were a large group of founders and popularizers of FEM in 1960s. R.W. Clough, H.C Martin with M.J. Turner and L.C. Topp (1956) in paper entitled “Stiffness and deflection analysis of complex structures” have started the present computational methods and FEM in particular. J.H. Argyris, consultant in Beoing in 1950s, developed the continuum based finite element (*Introduction to Finite Element Methods*, 2015). O.C. Zienkiewicz has became probably the most recognised FEM popularizer because of first FEM textbook (with Y.K. Cheung) entitled: “The Finite Element Method in Continuum and Structural Mechanics” (Zienkiewicz and Cheung, 1967) and his further contribution in this computational method. It is worth to noticed that Zienkiewicz was inspired by another FEM pioneer named R.W. Clough who was the first who used the “finite element” name. The next great contribution has came in 1970s when Ted Belytschko introduced large displacement dynamic behaviour to the FEM calculations (Belytschko et al., 1976).

The large deformation FEM, which is widely used nowadays, finds its origins in Computational Fluid Dynamics (CFD) and in the Los Alamos National Laboratory in New Mexico where T3 group under lead of F. Harlow, the pioneer of CFD, has began research on ALE framework in early 1960s (Margolin, 2013). As a result of those research the publication entitled: “An arbitrary Lagrangian-Eulerian computing method for all flow speeds” was presented in 1974 (Hirt et al., 1974). Another strategy for Lagrangian-Eulerian coupling has

been presented by Noh in 1963 at the university of California in Berkeley and denoted as Coupled Eulerian Lagrangian formulation (Noh, 1963). This method was lately refined by Benson (1992) and Olovsson (2000).

All mentioned pioneers and popularizers of FEM were structural engineers, so it is not coincidence, that FEM has been used in Civil Engineering since 1960s. Developed a little separately from the FEM mainstream the ALE and CEL methods have found its application in structural mechanics in 1980s (e.g., Donea et al., 1982; Kennedy and Belytschko, 1982). Anyway, during next decades FEM established its position as a common numerical tool in both engineering and scientific applications.

4.1 Finite Element Method concept

Generally speaking FEM is a method that enables to find approximated solution of field variables. To achieve this the domain is divided into finite number of elements. Consequently, the approximated distribution of the field variable is calculated. The example how FEM works is presented on simple curve approximation, see figure 4.1. While the exact solution of the field variable F(x) is a parabolic curve the FEM solution is a poly-line.

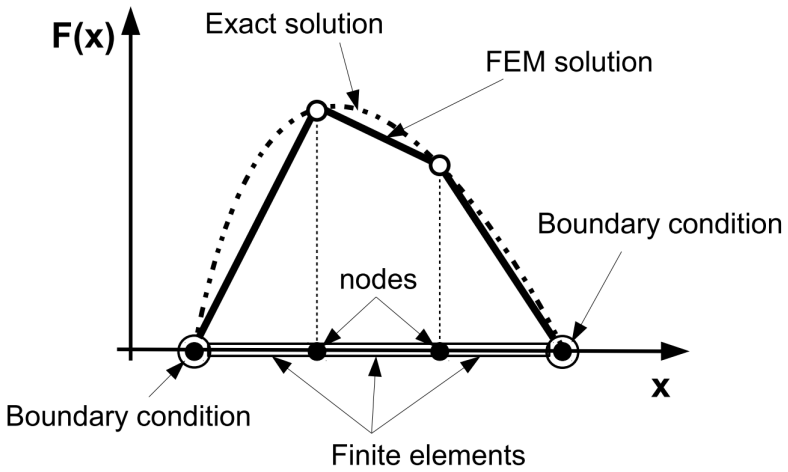

Figure 4.1. The FEM approximation of the field variable F(x)

The FEM modelling consists of several steps. These include idealization of geometry, descretization of domains, specification of material properties, attribution of boundary, initial and loading conditions, calculation procedure and results visualization and interpretation (Liu and Quek, 2013). All these steps are shortly described in sections below.

4.1.1 Idealization

The real structures are complex, so the first challenge in FEM analysis is the simplification of the object geometry to the basic shapes. This is usually done in two levels. Firstly, analyst has to keep in mind, that created geometry will be meshed and accuracy of the solution is mainly governed by the element size. On the other hand, large number of elements increases computational time. The compromise between the mentioned features results in omitting

some details, especially, when they are not important for the analysis. The second level of geometry simplification results from mechanical representation of designed domain. For example, pile can be modelled as a rigid element, because its stiffness is significantly higher than the stiffness of surrounding soil. However, if analyst pays attention to pile compressibility and its deformation, the pile needs to be discretized with continuum elements. Herein, in pile jacking simulation, deformations of pile itself are not important and they will be neglected. Hence, pile will be considered as a rigid body. Further, to provide fluent flow around the pile toe (or CPT cone), the smooth rounded transition between toe and shaft (or sleeve) is designed. Geometry details and description of this solution will be provided in chapter 5.

4.1.2 Meshing

Idealized geometry needs to be discretized into the small finite elements. This process is called meshing. Any engineering problem, which will be calculated with FEM, requires some element type, described with Lagrangian or Eulerian formulation. In Lagrangian formulation elements deform with material, while in Eulerian description material flows through them. In FEM the numerical integration is used to obtain various quantities over the element volume. Isoparametric formulation of the elements allows to converge FEM approximation to the exact solution for refined mesh (*Introduction to Finite Element Methods*, 2015). In research presented in this thesis the quadrilateral and hexahedral elements will be used. They offer better convergence rate than triangles and tetrahedra and they are not sensitive to the mesh orientation. However, they are more susceptible to the initial element shape and can be less accurate when the initial shape is not approximately rectangular (Dassault Systèmes, 2013). Elements are provided with first-order or second-order interpolation. Second-order (quadratic) elements capture stress concentration more accurately then first-order (linear) elements. However, linear elements are better for models containing nearly incompressible materials (Poisson's ratio higher than 0,48) and large deformation problems (Dassault Systèmes, 2013). Pile jacking simulation is a large deformation problem where stress concentration around pile toe occurs. Moreover, undrained conditions during installation means that material is almost incompressible (see section 2, chapter 3). Hence, some compromise should be found.

Material response in element is achieved with Gaussian quadrature in each integration points. Finite elements can use reduced or full integration scheme. Fully-integrated elements provide more accurate results, but they are time consuming and they can be affected by shear and volumetric locking. “Shear locking” is numerical generation of the shear strains that do not really exist. “Volumetric locking” affects almost incompressible materials and induces untrue deformations. Reduced-integrated elements do not lock with incompressible material and do not suffer from shear locking. However, these elements are affected by “hourglassing” (Dassault Systèmes, 2013). It is result of stress and strain calculation in the locations that provide optimal accuracy (Barlov, 1976). “Hourglassing” is a deformation of the element that leads to mesh distortion, when the zero strains are calculated in the integration point. “Hurglassing” is usually omitted by introduction of artificial stiffness based on initial shear modulus during material definition (Dassault Systèmes, 2013). In contact modelling, first

order elements perform better than quadratic ones. Three-dimensional second-order elements should be avoided in “hard” contact interaction with node-surface formulation because of equivalent nodal forces distribution when pressure is applied on the element face (Dassault Systèmes, 2013). Herein, the surface to surface contact formulation will be used to avoid such problems (see section 4.5 of this chapter). Advantages and disadvantages of fully and reduced integrated, linear and quadratic elements with short summary is presented in figure 4.2. As can be seen, universal and perfect finite element does not exist. Each element has advantages and disadvantages, so choosing element type is crucial for the effectiveness and accuracy of the FEM solution. The FE choice for pile jacking problem will be presented in chapter 5.

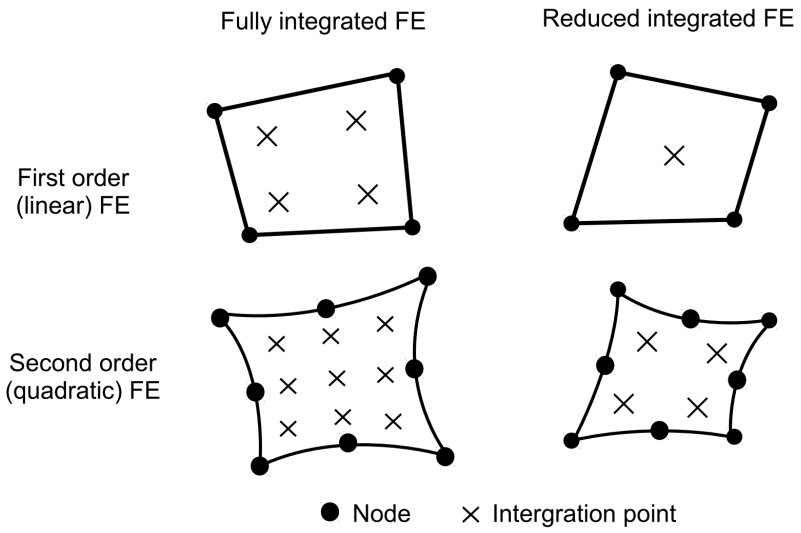

	Fully integrated FE	Reduced integrated FE
First order (linear) FE	☑ incompressible materials ☑ contact modelling ⚠ Shear locking	☑ Incompressible materials ☑ Contact modelling ☑ Large deformation ☑ Large mesh distortions ⚠ Hourglassing
Second order (quadratic) FE	☑ Stress concentration ⚠ Volumetric locking ⚠ Contact modelling	☑ Nonlinear problems ☑ Incompressible materials ⚠ Contact modelling

Figure 4.2. Advantages and disadvantages of different element formulations (based on Dassault Systémes *(2013))*

4.1.3 Material properties definition

The FEM method is well suited to multi-material analysis. Herein, the four material models will be used: linear elastic, Tresca plasticity, porous elastic and clay plasticity (combination of porous elastic and clay plasticity gives MCC model). All four models as well as the correlations between theirs parameters have been described in details in section 3.2. The parameters are listed in table 3.1 in section 3.2.5.

4.1.4 Initial, boundary and loading conditions definition

Initial, loading and boundary conditions are different according to the analysed problem. In total stress analysis initial conditions consist of prescribed geostatic stresses and contact on pile-soil interface. In effective stress analysis, initial conditions include geostatic stresses, contact properties on pile-soil interface, initial pore water pressures and void ratio distributions. In some cases, the surface load is also used as an initial condition. Boundary conditions in both analyses contains fixed appropriate degrees of freedom in soil and pile domain, while loading consist of prescribed jacking velocity.

4.1.5 Calculation procedure

In this section the basic FEM procedure with accordance to the Lagrangian formulation has been described. Mechanics problem are governed by set of partial differential equations. The FEM procedure consists of few steps. Firstly, simple form of displacement field is assumed in each finite element. Then, the equations from all FEM domain are assembled to the one global equation and the global displacement field can be calculated. Finally, stress and strain fields can be obtained with other output variables. Here, the very basic algorithm for above procedure will be shown.

4.1.5.1 Fundamental equations and general considerations

The elasto-plastic models are usually used to describe response of the material due to applied loading. The most visible effect of applied load is the deformation of the body. The basic assumption of elasto-plastic models is decomposition of the deformation gradient in elastic and plastic part (Dassault Systèmes, 2013):

$$\boldsymbol{F} = \boldsymbol{F}^{el} \cdot \boldsymbol{F}^{pl} \tag{4.1}$$

where: $\boldsymbol{F}$ – deformation gradient, $\boldsymbol{F}^{el}$ – elastic part of deformation gradient, $\boldsymbol{F}^{pl}$ – plastic part of deformation gradient.
Deformation can be related with the strains, which can be express as (Dassault Systèmes, 2013):

$$\boldsymbol{\varepsilon} = \frac{1}{2}\left(\boldsymbol{F} \cdot \boldsymbol{F}^{T} - \boldsymbol{I}\right) \tag{4.2}$$

where: $\boldsymbol{\varepsilon}$ – total strain, $\boldsymbol{F}$ – deformation gradient, $\boldsymbol{I}$ – identity matrix.
Strains described by equation (4.2) are often called Green strains ((Dassault Systèmes, 2013). However, all constitutive laws used in popular FEM packages are formulated in terms of rates due to its general applicability and the ease of implementation, so equation (4.2) can be rewritten as (Dassault Systèmes, 2013):

$$\dot{\boldsymbol{\varepsilon}} = \frac{1}{2}\left(\boldsymbol{L} + \boldsymbol{L}^{T}\right) \tag{4.3}$$

where: $\dot{\boldsymbol{\varepsilon}}$ – total strain rate, $\boldsymbol{L}$ – rate of deformation (velocity gradient), which can be defined as (Dassault Systèmes, 2013):

$$\boldsymbol{L}=\frac{\partial \boldsymbol{F}}{\partial t}\cdot\boldsymbol{F}^{-1} \tag{4.4}$$

where: $\boldsymbol{L}$ – rate of deformation, $\boldsymbol{F}$ – deformation gradient, t – time.
Total strain, similar as deformation gradient, can be decomposed in elastic and plastic part (Dassault Systèmes, 2013):

$$\dot{\boldsymbol{\varepsilon}}=\dot{\boldsymbol{\varepsilon}}^{el}+\dot{\boldsymbol{\varepsilon}}^{pl} \tag{4.5}$$

where: $\dot{\boldsymbol{\varepsilon}}$ – total strain rate, $\dot{\boldsymbol{\varepsilon}}^{el}$ – elastic strain rate, $\dot{\boldsymbol{\varepsilon}}^{pl}$ – plastic strain rate.
Firstly, let us consider the elastic part of material response. The general description of elasticity can be formulated as follows (Dassault Systèmes, 2013):

$$\dot{\boldsymbol{\sigma}}=\boldsymbol{D}^{el}:\dot{\boldsymbol{\varepsilon}}^{el} \tag{4.6}$$

where: $\dot{\boldsymbol{\sigma}}$ – stress rate, $\boldsymbol{D}^{el}$ – material stiffness matrix, $\dot{\boldsymbol{\varepsilon}}^{el}$ – elastic strain rate.
When plastic flow occurs, the stress can be derived from elastic strain density potential (Dassault Systèmes, 2013):

$$\boldsymbol{\sigma}=\frac{\partial U}{\partial \boldsymbol{\varepsilon}^{el}} \tag{4.7}$$

where: $\boldsymbol{\sigma}$ – stress tensor, U – elastic strain density potential, $\boldsymbol{\varepsilon}^{pl}$ – plastic strain tensor.
Plasticity is defined by the yield function in general form (Dassault Systèmes, 2013):

$$f_i=0 \tag{4.8}$$

where: f_i – yield function, i – subscript indicates number of variables.
It is clear that for elastic region the yield function f is lower than zero. Plastic strains can be calculated from flow potential function (Dassault Systèmes, 2013):

$$d\boldsymbol{\varepsilon}^{pl}=\sum_i d\lambda_i\frac{\partial g_i}{\partial \boldsymbol{\sigma}} \tag{4.9}$$

where: $\boldsymbol{\varepsilon}^{pl}$ – plastic strain tensor, λ – hardening parameter, i – subscript indicates number of variables, g – plastic potential, $\boldsymbol{\sigma}$ – stress tensor.
Now, let us take a closer look in flow potential function. When plastic potential is equal to the yield function which can be written as (Dassault Systèmes, 2013):

$$f_i = g_i \tag{4.10}$$

where: f – yield function, g – plastic potential, i – subscript indicates number of variables, the associated plasticity occurs. For instance, the MCC model and Tresca model use associated plasticity. However, when plastic potential is different than the yield function (Dassault Systèmes, 2013):

$$f_i \neq g_i \tag{4.11}$$

the non-associated flow occurs. This rule is valid for Mohr-Coulomb model when angle of internal friction differs from angle of dilation.

In above equations one can find that strains are related to deformations (equations (4.2) or (4.3)) and stresses are related to strains (equations (4.6),(4.7),(4.9)). The last part of fundamental continuum equations are the conservation equations. These include conservation of mass, momentum and energy which can be written in Lagrangian formulation in following form (Donea et al., 2004):

(mass equilibrium)
$$\frac{d\rho}{dt} = -\rho \nabla \boldsymbol{v} \tag{4.12}$$

(momentum equilibrium)
$$\nabla \boldsymbol{\sigma} + \rho \boldsymbol{b} = \rho \frac{d\boldsymbol{v}}{dt} \tag{4.13}$$

(energy equilibrium)
$$\rho \frac{dE_{total}}{dt} = \nabla(\boldsymbol{\sigma}\,\boldsymbol{v}) + \boldsymbol{v}\,\rho\,\boldsymbol{b} \tag{4.14}$$

where: ρ – material density, t – time, $\boldsymbol{v}$ – velocity field, $\boldsymbol{\sigma}$ – stress tensor, $\boldsymbol{b}$ – body force tensor, E_{total} – total energy.

Summing up, in this section the fundamental background of mechanics have been presented as the essential part of FEM calculation procedure.

4.1.5.2 Boundary conditions

Theory presented in section 4.1.5.1 shall be applied to the discretized FEM domain. As it was mentioned before, the FEM domain requires specification of the boundary conditions which are necessary to derive equilibrium equations in the single element and whole domain. Consequently, the first boundary condition is the displacement one also called essential one. It can be written as (Liu and Quek, 2013):

$$x_i = \bar{x}_i \tag{4.15}$$

where: x – displacement (or rotation), $\bar{x}$ – prescribed displacement (or rotation), i – subscript indicates degree of freedom.

Physical interpretation of the equation (4.15) is fixing of freedom degrees (displacement and

rotations on prescribed directions). The second type of boundary conditions are force/stress ones also called natural ones. They can be written as (Liu and Quek, 2013):

$$\boldsymbol{n}_c \boldsymbol{\sigma} = \bar{\boldsymbol{t}} \tag{4.16}$$

where: $\boldsymbol{\sigma}$ – stress tensor, $\boldsymbol{n}_c$ – matrix of cosines of the outwards unit normal on the boundary surface, $\bar{\boldsymbol{t}}$ – vector of traction imposed on surface.
The force/stress conditions are applied by prescribed stresses (e.g., surface pressure) or by forces defined in the mesh nodes.

4.1.5.3 Equilibrium and energy balance equations

In each FE of discretized domain the equilibrium which implies balance between external and internal forces acting within FE has to be fullfilled. As a consequence of this statement the momentum conservation described by equation (4.13) is provided. Using Gauss theorem and definition of Cauchy stresses one can formulate the virtual work equation as (Dassault Systèmes, 2013):

$$\int_V \boldsymbol{\sigma} : \delta \dot{\boldsymbol{\varepsilon}} \, dV + \int_v \rho \frac{d\boldsymbol{v}}{dt} \delta \boldsymbol{v} \, dV = \int_S \delta \boldsymbol{v} \boldsymbol{t} \, dS + \int_V \delta \boldsymbol{v} \boldsymbol{b} \, dV \tag{4.17}$$

where: $\boldsymbol{\sigma}$ – stress tensor, $\delta \dot{\boldsymbol{\varepsilon}}$ – virtual strain rate, ρ – material density, $\delta \boldsymbol{v}$ – virtual field velocity vector, $\boldsymbol{t}$ – true stress at a point on surface S tensor, $\boldsymbol{b}$ – body force tensor, V – volume of the element, S – surface of the element, t – time.
Equation (4.17) is a “weak form” of the equilibrium equations that facilitates application in computation (Liu and Quek, 2013). Thus, it is the basic equation in FEM analysis in many software packages. Similar analysis can be done for energy conservation equation. Change rate of kinetic and internal energy is equal to the work done by surface and body forces (Dassault Systèmes, 2013):

$$\frac{d}{dt} \int_V \left(\frac{1}{2} \rho \boldsymbol{v} \cdot \boldsymbol{v} + \rho U \right) dV = \int_S \boldsymbol{v} \cdot \boldsymbol{t} \, dS + \int_V \boldsymbol{v} \cdot \boldsymbol{b} \, dV \tag{4.18}$$

where: ρ – material density, $\boldsymbol{v}$ – velocity field vector, U – internal energy per unit mass (here equal to elastic strain density potential because of adiabatic process (Wu, 2005), $\boldsymbol{t}$ – true stress at a point on surface S tensor, $\boldsymbol{b}$ – body force tensor, V – volume of the element, S – surface of the element, t – time.
Equation (4.18) can be rewritten to the following form (Dassault Systèmes, 2013):

$$\int_V \frac{1}{2} \rho \boldsymbol{v} \cdot \boldsymbol{v} \, dV + \int_V \rho U \, dV = \int_0^t \left(\int_S \boldsymbol{v} \cdot \boldsymbol{t} \, dS + \int_V \boldsymbol{v} \cdot \boldsymbol{b} \, dV \right) dt + constant \tag{4.19}$$

where: ρ – material density, $\boldsymbol{v}$ – velocity field vector, U – internal energy per unit mass, $\boldsymbol{t}$ – true stress at a point on surface S tensor, $\boldsymbol{b}$ – body force tensor, V – volume of the element,

S – surface of the element, t – time.
Internal energy $E_{internal}$ is defined as (Dassault Systèmes, 2013):

$$E_{internal} = \int_V \rho U \, dV = \int_0^t \left(\int_V \boldsymbol{\sigma} : \dot{\boldsymbol{\varepsilon}} \, dV \right) dt - U_0 \tag{4.20}$$

where: $E_{internal}$ – internal energy, ρ – material density, U – internal energy per unit mass, $\boldsymbol{\sigma}$ – stress tensor, $\dot{\boldsymbol{\varepsilon}}$ – strain rate tensor, U_0 – initial internal energy per unit mass, V – volume of the element, t – time.
Although the virtual work principle is commonly used in FEM formulation, energy balance equations enables to control the solution. Total energy should be constant, but in numerical simulations difference of 1% is commonly accepted (Dassault Systèmes, 2013). Evaluation of the energies in FEM analysis gives more detailed look in correctness of analysis and allows for error detection.

4.1.5.4 From single FE to global domain

Principle of virtual work represented by equation (4.17) is used in each finite element, so the displacements can be calculated. The displacement within the FE can be interpolated from the nodal displacements (Liu and Quek, 2013):

$$\boldsymbol{u} = \boldsymbol{N}\boldsymbol{d}_e \tag{4.21}$$

where: $\boldsymbol{u}$ – displacement within the element (approximated), $\boldsymbol{N}$ – matrix of shape functions, $\boldsymbol{d}_e$ – displacement vector of nodes within element.
Linear shape functions are used in first-order elements, while the quadratic functions are used in second-order ones. Shape function has to fulfil some conditions to provide acceptable estimation of displacement. Procedure of shape function construction can be fund in many textbooks (e.g., Liu and Quek, 2013). Once the shape functions are constructed, the virtual work equation can be transformed into the following discrete form (Liu and Quek, 2013):

$$\boldsymbol{k}_e \boldsymbol{d}_e + \boldsymbol{m}_e \ddot{\boldsymbol{d}}_e = \boldsymbol{f}_e \tag{4.22}$$

where: $\boldsymbol{k}_e$ – element stiffness matrix, $\boldsymbol{d}_e$ – displacement vector of nodes within element, $\boldsymbol{m}_e$ – element mass matrix, $\ddot{\boldsymbol{d}}_e$ – acceleration vector of nodes within element, $\boldsymbol{f}_e$ – vector of external forces acting on element nodes; all in local coordinate system.
Equation (4.22) represents the displacement finite element analysis which is widely used in FEM software packagets. Next, the relation described with equation (4.22) has to be transformed to the global coordinate system. This is done as follows (Liu and Quek, 2013):

$$\boldsymbol{K}_e \boldsymbol{D}_e + \boldsymbol{M}_e \ddot{\boldsymbol{D}}_e = \boldsymbol{F}_e \tag{4.23}$$

where: $\boldsymbol{K}_e$ – element stiffness matrix, $\boldsymbol{D}_e$ – displacement vector of nodes within element, $\boldsymbol{M}_e$ – element mass matrix, $\ddot{\boldsymbol{D}}_e$ – acceleration vector of nodes within element, $\boldsymbol{F}_e$ – vector of external forces acting on element nodes; all in global coordinate system.

Then, equations for all elements in domain can be assembled to the one global equation (Liu and Quek, 2013):

$$\boldsymbol{K}\,\boldsymbol{D}+\boldsymbol{M}\,\ddot{\boldsymbol{D}}=\boldsymbol{F} \tag{4.24}$$

where: $\boldsymbol{K}$ – global stiffness matrix, $\boldsymbol{D}$ – all nodes displacement vector, $\boldsymbol{M}$ – global mass matrix, $\ddot{\boldsymbol{D}}$ – all nodes acceleration vector, $\boldsymbol{F}$ – vector of external forces acting on all nodes.
Equation (4.24) can be extended to the general form with transient response of the system included (Liu and Quek, 2013):

$$\boldsymbol{K}\,\boldsymbol{D}+\boldsymbol{C}\,\dot{\boldsymbol{D}}+\boldsymbol{M}\,\ddot{\boldsymbol{D}}=\boldsymbol{F} \tag{4.25}$$

where: $\boldsymbol{K}$ – global stiffness matrix, $\boldsymbol{D}$ – all nodes displacement vector, $\boldsymbol{C}$ – matrix of damping coefficients, $\dot{\boldsymbol{D}}$ – all nodes velocity vector, $\boldsymbol{M}$ – global mass matrix, $\ddot{\boldsymbol{D}}$ – all nodes acceleration vector, $\boldsymbol{F}$ – vector of external forces acting on all nodes.
The last step is to solve equation (4.25) to find global displacement vector. Then, the process is reversed: nodal displacement can be calculated from equations presented in this section. Finally, the stress and strain fields can be recovered from equations introduced in previous sections of this chapter.

4.1.5.5 Implicit solver

Implicit solver is generally used for static or quasi static problems (short review of implicit and explicit methods has been mentioned in section 3.1.7). Thus, it is also used in effective stress analysis. To solve equation implicitly the Newton method (Dassault Systèmes, 2013) in Abaqus is used and it will be described below. Lets write the static system of FEM equations (Liu and Quek, 2013):

$$\boldsymbol{K}\,\boldsymbol{D}=\boldsymbol{F} \tag{4.26}$$

where: $\boldsymbol{K}$ – global stiffness matrix, $\boldsymbol{D}$ – all nodes displacement vector $\boldsymbol{F}$ – vector of external forces acting on all nodes.
Equation (4.26) can be rewritten in more general form (Dassault Systèmes, 2013):

$$\boldsymbol{F}^{N}\left(\boldsymbol{u}^{M}\right)=0 \tag{4.27}$$

where: $\boldsymbol{F}^{N}$ – force component conjugate to the N^{th} variable, $\boldsymbol{u}^{M}$ – value of M^{th} variable.
The aim is to find $\boldsymbol{u}^{M}$. One can assume that after iteration j, the value of $\boldsymbol{u}_{j}^{M}$ is obtained. The difference between exact and approximated solution is $\boldsymbol{c}_{j+1}^{M}$. Then (Dassault Systèmes, 2013):

$$\boldsymbol{F}^{N}\left(\boldsymbol{u}_{j}^{M}+\boldsymbol{c}_{j+1}^{M}\right)=0 \tag{4.28}$$

where: $\boldsymbol{F}^{N}$ – force component conjugate to the N^{th} variable, $\boldsymbol{u}_{j}^{M}$ – value of M^{th} variable in j iteration, $\boldsymbol{c}_{j+1}^{M}$ – difference between exact and approximated M^{th} variable in $j+1$ iteration.

Using Taylor series to expand left-hand side of the equation leads to (Dassault Systèmes, 2013):

$$\boldsymbol{F}^{N}\left(\boldsymbol{u}_{j}^{M}\right)+\frac{\partial \boldsymbol{F}^{N}}{\partial \boldsymbol{u}^{P}}\left(\boldsymbol{u}_{j}^{M}\right)\boldsymbol{c}_{j+1}^{P}+\frac{\partial^{2} \boldsymbol{F}^{N}}{\partial \boldsymbol{u}^{P}\partial \boldsymbol{u}^{Q}}\left(\boldsymbol{u}_{j}^{M}\right)\boldsymbol{c}_{j+1}^{P}\boldsymbol{c}_{j+1}^{Q}+\ldots=0 \tag{4.29}$$

If approximated value $\boldsymbol{u}_{j}^{M}$ is close to the exact solution $\boldsymbol{u}^{M}$ then $\boldsymbol{c}_{j+1}{}^{M}$ has to be very small. Hence, only two first terms in equation (4.29) will be significant (Dassault Systèmes, 2013):

$$\boldsymbol{F}^{N}\left(\boldsymbol{u}_{j}^{M}\right)+\frac{\partial \boldsymbol{F}^{N}}{\partial \boldsymbol{u}^{P}}\left(\boldsymbol{u}_{j}^{M}\right)\boldsymbol{c}_{j+1}^{P}=0 \tag{4.30}$$

As a result of above considerations the linear system of equation is obtained. The following approximation of the solution can be made (Dassault Systèmes, 2013):

$$\boldsymbol{u}_{j+1}^{M}=\boldsymbol{u}_{j}^{M}+\boldsymbol{c}_{j+1}^{M} \tag{4.31}$$

where: $\boldsymbol{u}_{j+1}{}^{M}$ – next approximation of the solution, $\boldsymbol{u}_{j}^{M}$ – current approximation of the solution, $\mathbf{c}_{\mathbf{j+1}}{}^{\mathbf{M}}$ – difference between exact and approximated M^{th} variable in $j+1$ iteration.
Presented Newton method is clearly implicit. The solution is obtained from current and previous configurations of the system (see section 3.1.7). The limitations are the number of iterations and prescribed small value of difference between exact and approximated solution $\boldsymbol{c}_{i+1}{}^{M}$. As a result, convergence may not be achieved for highly non-linear problems. Further, small time steps are usually required to achieved the solution convergence which often makes implicit solver ineffective and time consuming in non-linear prolems.

4.1.5.6 Explicit solver

Explicit solver is usually applied to calculate dynamic and highly non-linear problems. In Abaqus, central difference method is used to find solutions in next time step (Dassault Systèmes, 2013) and it will be presented in this section. The global system of FEM equations have been derived in section 4.1.5.4 and it is presented by equation (4.25). One can transform equation (4.25) to the following form (Liu and Quek, 2013):

$$\ddot{\boldsymbol{D}}=\boldsymbol{M}^{-1}\left(\boldsymbol{F}-\boldsymbol{K}\,\boldsymbol{D}-\boldsymbol{C}\,\dot{\boldsymbol{D}}\right) \tag{4.32}$$

where: $\ddot{\boldsymbol{D}}$ – all nodes acceleration vector, $\boldsymbol{K}$ – global stiffness matrix, $\boldsymbol{D}$ – all nodes displacement vector, $\boldsymbol{C}$ – matrix of damping coefficients, $\boldsymbol{M}$ – global mass matrix, $\boldsymbol{F}$ – vector of external forces acting on all nodes, $\dot{\boldsymbol{D}}$ – all nodes velocity vector.
The all nodes velocity vector $\dot{\boldsymbol{D}}$ and displacement vector $\boldsymbol{D}$ can be calculated with central difference rule (Liu and Quek, 2013):

$$\dot{\boldsymbol{D}}^{\left(j+\frac{1}{2}\right)}=\dot{\boldsymbol{D}}^{\left(j-\frac{1}{2}\right)}+\frac{\Delta t^{(j+1)}+\Delta t^{(j)}}{2}\ddot{\boldsymbol{D}}^{(j)} \tag{4.33}$$

$$\boldsymbol{D}^{(j+1)} = \boldsymbol{D}^{(j)} + \Delta t^{(j+1)} \dot{\boldsymbol{D}}^{\left(j+\frac{1}{2}\right)} \tag{4.34}$$

where: $\boldsymbol{D}$ – all nodes displacement vector, $\dot{\boldsymbol{D}}$ – all nodes velocity vector, $\ddot{\boldsymbol{D}}$ – all nodes acceleration vector, Δt – time increment, j – increment number, $j\pm½$ – mid-increment.
As can be seen, at time t=0 the initial values of displacement, velocity and acceleration vector are known. Then, the application of the prescribed time increment in next time steps allows the solution to be easy proceeded. Explicit method does not require iteration procedure and inversion of global mass matrix at the beginning of analysis. Application of following repetition of equations (4.32)-(4.34) provides computational effectiveness. The crucial part of the analysis is stable time increment. This is achieved by stability principle formulated as (Dassault Systèmes, 2013):

$$\Delta t = min\left(\frac{l_e}{c_d}\right) \tag{4.35}$$

where: Δt_{max} – maximum allowable time increment, l_e- finite element dimension, c_d – dilatational wave speed (which is function of material density and elastic properties).

4.1.6 Results visualization and interpretation

The last step in FEM analysis is the visualization of the results which helps in evaluation of the solution and post-processing of the data. Advanced display options are also useful in graphical presentation of the results. Interpretation of the data should be carefully checked, for instance, the energy plots can be investigated or mesh distortion studied. Interpretation is probably the most important step in FEM modelling due to analyst decision if solution is acceptable or not. It is worth to noticed that results is FEM solution are usually averaged to provide one value in node or in entire finite element.

4.2 Updated Lagrangian formulation

4.2.1 General description

As it has been explained in sections 4.1.5.5. and 4.1.5.6, both implicit and explicit solvers use time steps to calculate deformed configuration of the system. While the implicit solver uses incremental method to calculate solution in the current step, explicit method provides direct results. One of the possible approaches of kinematic description of deformation are Total Lagrangian (TL) formulation and the Updated Lagrangian (UL) formulation. TL description uses the base configuration from the beginning of the analysis as the referential one (see section 3.1.3). Hence, the virtual work equation in TL description can be written as (Bathe, 1996):

$$\int_{V^0} \boldsymbol{\sigma}^{\mathbf{0}} : \delta\, \dot{\boldsymbol{\varepsilon}}^{\mathbf{0}} dV^0 + \int_{v^0} \rho \frac{d\,\boldsymbol{v}^{\mathbf{0}}}{dt} \delta\, \boldsymbol{v}^{\mathbf{0}} dV^0 = \int_{S^0} \delta\, \boldsymbol{v}^{\mathbf{0}} \boldsymbol{t}^{\mathbf{0}} dS^0 + \int_{V^0} \delta\, \boldsymbol{v}^{\mathbf{0}} \boldsymbol{b}^{\mathbf{0}} dV^0 \tag{4.36}$$

where: $\boldsymbol{\sigma}$ – stress tensor, $\delta \dot{\boldsymbol{\varepsilon}}$ – virtual strain rate, ρ – material density, $\delta \boldsymbol{v}$ – virtual field velocity vector, $\boldsymbol{t}$ – true stress at a point on surface S tensor, $\boldsymbol{b}$ – body force tensor, V – volume of the element, S – surface of the element, t – time, superscript *0* reefers to the base configuration at the beginning of analysis.

As one can noticed from equation (4.36), when large deformation occurs the error of field variables computed in every time step is getting higher. To avoid this the UL formulation can be used where in each time step the current configuration is used as the referential one (see section 3.1.3). Consequently, the more accurate results can be obtained. The virtual work equation in terms of UL can be written as (Bathe, 1996):

$$\int_{V^{t+\Delta t}} \boldsymbol{\sigma}^{t+\Delta t} : \delta \dot{\boldsymbol{\varepsilon}}^{t+\Delta t} dV^{t+\Delta t} + \int_{V^{t+\Delta t}} \rho \frac{d\,\boldsymbol{v}^{t+\Delta t}}{dt} \delta \boldsymbol{v}^{t+\Delta t} dV^{t+\Delta t} = \\ = \int_{S^{t+\Delta t}} \delta \boldsymbol{v}^{t+\Delta t} \boldsymbol{t}^{t+\Delta t} dS^{t+\Delta t} + \int_{V^{t+\Delta t}} \delta \boldsymbol{v}^{t+\Delta t} \boldsymbol{b}^{t+\Delta t} dV^{t+\Delta t} \qquad (4.37)$$

where: $\boldsymbol{\sigma}$ – stress tensor, $\delta \dot{\boldsymbol{\varepsilon}}$ – virtual strain rate, ρ – material density, $\delta \boldsymbol{v}$ – virtual field velocity vector, $\boldsymbol{t}$ – internal traction action on surface S tensor, $\boldsymbol{b}$ – body force tensor, V – volume of the element, S – surface of the element, t – time, superscript $t+\Delta t$ refers to the current configuration at the time $t+\Delta t$.

UL is more suited to the large deformation problems, but large mesh distortions still may produce inaccurate results. The graphical representation of TL and UL formulations has been given in figure 3.3. in this thesis.

4.2.2 Governing equations

The coupled pore fluid diffusion and stress analysis is used in Abaqus software for effective stress analysis conducted with UL formulation. In this section the governing equations in the "weak form" for effective stress approach will be presented and solution technique will be briefly described. Equilibrium equation for the effective stress analysis has to be written in virtual work principle (Dassault Systèmes, 2013):

$$\int_V \boldsymbol{\sigma} : \delta \dot{\boldsymbol{\varepsilon}}\, dV + \int_v \rho \frac{d\,\boldsymbol{v}}{dt} \delta \boldsymbol{v}\, dV = \int_S \delta \boldsymbol{v}\, \boldsymbol{t}\, dS + \int_V \delta \boldsymbol{v}\, \boldsymbol{b}\, dV + \int_V \left(s_r n + n_t\right) \rho_w \boldsymbol{g}\, \delta \boldsymbol{v}\, \boldsymbol{dV} \qquad (4.38)$$

where: $\boldsymbol{\sigma}$ – stress tensor, $\delta \dot{\boldsymbol{\varepsilon}}$ – virtual strain rate, ρ – material density, $\delta \boldsymbol{v}$ – virtual field velocity vector, $\boldsymbol{t}$ – true stress at a point on surface S tensor, $\boldsymbol{b}$ – body force except the fluid weight tensor, s_r – degree of saturation, n – porosity, n_t – volume of the trapped fluid per current volume, $\boldsymbol{g}$ – gravitational acceleration, ρ_w – fluid density, V – volume of the element, S – surface of the element, t – time.

In analysis presented in this section fully saturated medium is considered (see section 3.2.4) and no fluid is assumed to be trapped in closed pores. Hence, the equation (4.38) can be simplified to the following form:

$$\int_V \boldsymbol{\sigma} : \delta \dot{\boldsymbol{\varepsilon}}\, dV + \int_v \rho \frac{d\boldsymbol{v}}{dt} \delta \boldsymbol{v}\, dV = \int_S \delta \boldsymbol{v}\, \boldsymbol{t}\, dS + \int_V \delta \boldsymbol{v}\, \boldsymbol{b}\, dV + \int_V n \rho_w \boldsymbol{g}\, \delta \boldsymbol{v}\, \boldsymbol{dV} \tag{4.39}$$

where: $\boldsymbol{\sigma}$ – stress tensor, $\delta \boldsymbol{D}$ – virtual strain rate, ρ – material density, $\delta \boldsymbol{v}$ – virtual field velocity vector, $\boldsymbol{t}$ – true stress at a point on surface S tensor, $\boldsymbol{b}$ – body force except the fluid weight tensor, n – porosity, $\boldsymbol{g}$ – gravitational acceleration, ρ_w – fluid density, V – volume of the element, S – surface of the element, t – time.

The last equation describing effective stress analysis is the continuity statement for liquid phase in porous medium. This formula describes equilibrium in fluid inflow (or outflow) within the finite element. Continuity equation is based on the mass conservation equation (see equation (4.12) in section 4.1.5.1) and can be written as (Dassault Systèmes, 2013):

$$\int_V \delta \boldsymbol{u}_w \frac{1}{J} \frac{d}{dt} \left(J \rho_w (s_r n + n_t) \right) dV + \int_v \delta \boldsymbol{u}_w \frac{\partial}{\partial \boldsymbol{x}} \left(\rho_w s_r n \boldsymbol{v}_w \right) dV = 0 \tag{4.40}$$

where: $\delta \boldsymbol{u}_w$ – virtual pore water pressure field, J – ratio of volume in current configuration to the volume in reference configuration, ρ_w – fluid density, s_r – degree of saturation, n – porosity, n_t – volume of the trapped fluid per current volume, $\boldsymbol{x}$ – coordinates vector, $\boldsymbol{v}_w$ – seepage velocity, V – volume, t – time.

Due to assumption of fully saturation, the equation (4.40) can be transform to:

$$\int_V \delta \boldsymbol{u}_w \frac{1}{J} \frac{d}{dt} \left(J \rho_w n \right) dV + \int_v \delta \boldsymbol{u}_w \frac{\partial}{\partial \boldsymbol{x}} \left(\rho_w n \boldsymbol{v}_w \right) dV = 0 \tag{4.41}$$

where: $\delta \boldsymbol{u}_w$ – virtual pore water pressure field, J – ratio of volume in current configuration to the volume in reference configuration, ρ_w – fluid density, n – porosity, $\boldsymbol{x}$ – coordinates vector, $\boldsymbol{v}_w$ – seepage velocity, V – volume, t – time.

The pore fluid flow is governed by the Darcy law (Dassault Systèmes, 2013):

$$n \boldsymbol{v}_w = -k \frac{\partial \boldsymbol{\Phi}}{\partial \boldsymbol{x}} \tag{4.42}$$

where: n – porosity, $\boldsymbol{v}_w$ – seepage velocity, k – permeability coefficient, $\boldsymbol{\Phi}$ – piezometric head, $\boldsymbol{x}$ – coordinates vector.

4.2.3 Calculation procedure

The solution procedure is similar to this presented in section 4.1.5.4. The coupled system of equations described by equilibrium equation (4.39) and pore fluid flow equation (4.41) is solved directly by Abaqus/Standard (Dassault Systèmes, 2013). Analyst chooses the allowable pore fluid pressure change in each time increment. Then, calculations proceed in time steps and Newton method is used (see section 4.1.5.5).

The crucial part is the minimum allowable time increment Δt_{min} to obtain solution without

pore water pressure "overshoot", see figure 4.3. When the times used in numerical integration are lower then Δt_{min}, significant decrease of accuracy in pore water pressure may occur.

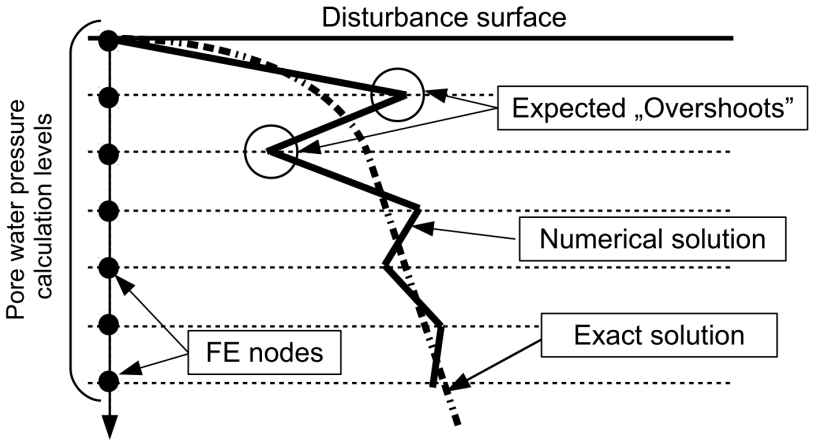

Figure 4.3. Possible pore water pressure overshoot in effective stress analysis

This problem was firstly presented for one-dimensional consolidation and fully saturated flow by Vermeer and Verruijt (1981) who proposed following criteria for the time increment:

$$\Delta t_{min} = \frac{\gamma_w \cdot (l_e)^2}{6\,Ek} \tag{4.43}$$

where: γ_w – unit weight of water, l_e – element length, E – elastic modulus, k – coefficient of permeability.

Choosing the appropriate mesh size, soil material and physical parameters allows for estimation of minimum allowable time increment in disturbance zone, where rapid change of pore water pressure occurs (e.g., pile shaft or near surface level). Thus, the stable time increments obtained in analysis should be monitored additionally with values calculated from equation (4.43).

4.3 Arbitrary Lagrangian-Eulerian (ALE) formulation

4.3.1 General description

Arbitrary Lagrangian–Eulerian (ALE) formulation combines features of pure Lagrangian and Eulerian descriptions and it has been briefly introduced in section 3.1.5. Herein, more theoretical background will be provided. Firstly, one can introduce pure Lagrangian and Eulerian description of motion. Let us assume material and spatial configurations as it can be seen in figure 4.4. The transformation between material configuration and spatial configuration denoted by $\boldsymbol{\varphi}$ is the following function (Donea et al., 2004):

$$\boldsymbol{\varphi}(\boldsymbol{X}, t) = (\boldsymbol{x}, t) \tag{4.44}$$

where: $\boldsymbol{\varphi}$ – transformation function, $\boldsymbol{X}$ – material coordinates, $\boldsymbol{x}$ – spatial coordinates, t – time.

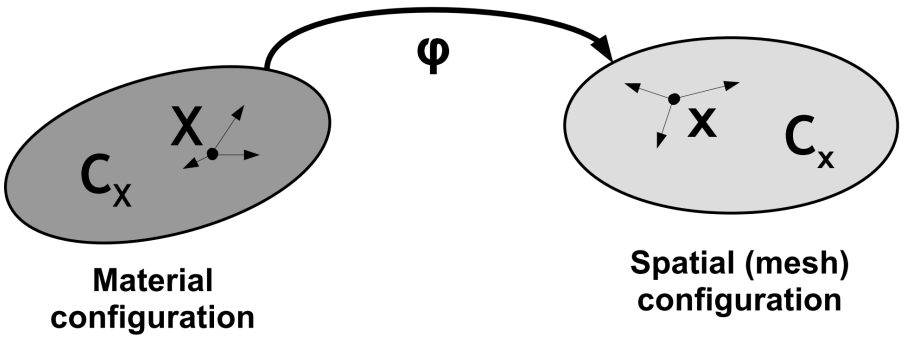

Figure 4.4. Material and spatial configurations

The Lagrangian description of motion can be written as (Donea et al., 2004):

$$\boldsymbol{x}=\boldsymbol{x}(\boldsymbol{X},t) \tag{4.45}$$

where: $\boldsymbol{X}$ – material coordinates, $\boldsymbol{x}$ – spatial coordinates, t – time.
Equation (4.45) represents the material which deforms with the mesh. The Eulerian viewpoint can be formulated as (Donea et al., 2004):

$$\boldsymbol{X}=\boldsymbol{X}(\boldsymbol{x},t) \tag{4.46}$$

where: $\boldsymbol{X}$ – material coordinates, $\boldsymbol{x}$ – spatial coordinates, t – time.
Here, the material flows through the mesh. The Jacobian of transformation is (Donea et al., 2004):

$$J^T=\left|\frac{\partial \boldsymbol{x}}{\partial \boldsymbol{X}}\right| \tag{4.47}$$

where: J^T – Jacobian of transformation, $\boldsymbol{X}$ – material coordinates, $\boldsymbol{x}$ – spatial coordinates, t – time.
In ALE description of motion, the third configuration also called reference one denoted as $\boldsymbol{C\chi}$ is introduced as it can be seen in figure 4.5. The relations between material, spatial and referential configurations are described by transformations: $\boldsymbol{\varphi}$, $\boldsymbol{\Psi}$ and $\boldsymbol{\Phi}$. Now, one can write equation describing mesh velocity and material velocity in terms of ALE formulation (Donea et al., 2004):

$$\boldsymbol{v}(\boldsymbol{X},t)=\frac{\partial \boldsymbol{x}}{\partial t}|_X \tag{4.48}$$

$$\check{\boldsymbol{v}}(\boldsymbol{\chi},t)=\frac{\partial \boldsymbol{x}}{\partial t}|_{\chi} \tag{4.49}$$

where: $\boldsymbol{v}$ – material velocity vector, $\check{\boldsymbol{v}}$ – mesh velocity vector, $\boldsymbol{X}$ – material coordinates, $\boldsymbol{x}$ – spatial coordinates, $\boldsymbol{\chi}$ – reference coordinates, t – time, $|_X$ – in reference to material configuration (material coordinates are fixed), $|_\chi$ – in reference to the referential domain (reference coordinates are fixed).

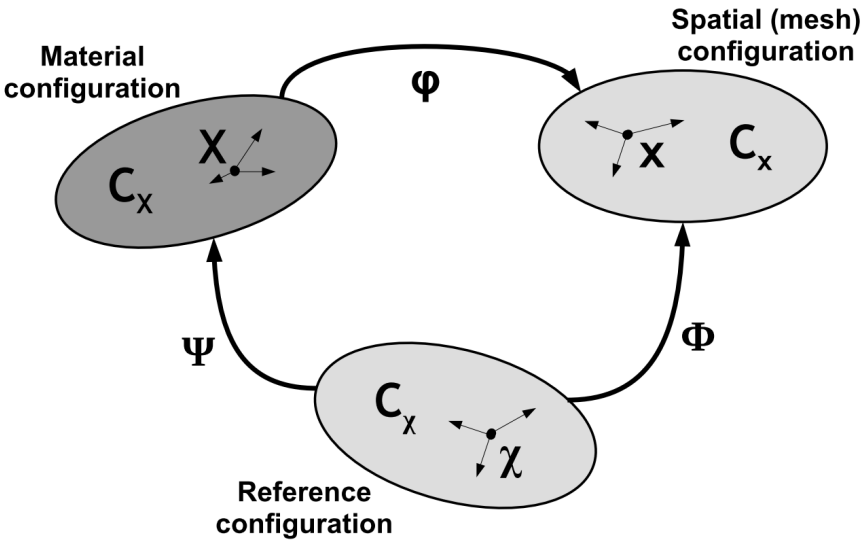

Figure 4.5. ALE kinematics (modified from (Donea et al., 2004))

The connective velocity $\boldsymbol{c}$ represents relative motion between material and spatial domains and it can be written as (Donea et al., 2004):

$$\boldsymbol{c}=\boldsymbol{v}-\check{\boldsymbol{v}} \tag{4.50}$$

where: $\boldsymbol{v}$ – material velocity vector, $\check{\boldsymbol{v}}$ – mesh velocity vector, $\boldsymbol{c}$ – convective velocity vector. Equation (4.50) describes fundamental ALE concept where some velocity $\boldsymbol{c}$ exists which relates in arbitrary way movement between material and spatial configurations.

One can notice that ALE is the generalized description of motion. Let us assume situation where $\boldsymbol{\Phi}=\boldsymbol{I}$ ($\boldsymbol{I}$ is identity matrix). In such case the reference configuration is the same as the spatial one:

$$\boldsymbol{x}\equiv\boldsymbol{\chi} \tag{4.51}$$

where: $\boldsymbol{x}$ – spatial coordinates, $\boldsymbol{\chi}$ – reference coordinates.
As the result the Eulerian description is obtained, see figure 4.6. Consequently, mesh and material velocities are described as:

$$\boldsymbol{v}(\boldsymbol{X},t)=\frac{\partial \boldsymbol{x}}{\partial t}|_X \Leftrightarrow \boldsymbol{v}(\boldsymbol{X},t)=\frac{\partial \boldsymbol{\chi}}{\partial t}|_X \tag{4.52}$$

$$\check{\boldsymbol{v}}(\boldsymbol{\chi},t)=\frac{\partial \boldsymbol{x}}{\partial t}|_\chi \Leftrightarrow \check{\boldsymbol{v}}(\boldsymbol{x},t)=\frac{\partial \boldsymbol{x}}{\partial t}|_x=0 \tag{4.53}$$

where: $\boldsymbol{v}$ – material velocity vector, $\check{\boldsymbol{v}}$ – mesh velocity vector, $\boldsymbol{X}$ – material coordinates, $\boldsymbol{x}$ – spatial coordinates, $\boldsymbol{\chi}$ – reference coordinates, t – time, $|_X$ – material coordinates are fixed, $|_\chi$ – reference coordinates fixed, $|_x$ – spatial coordinates are fixed.

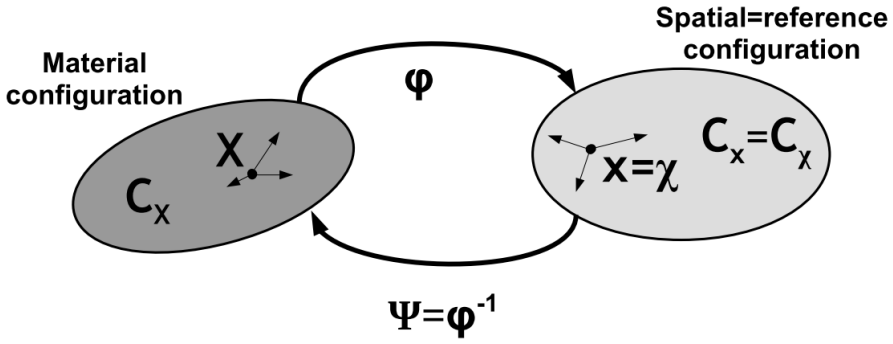

Figure 4.6. Eulerian description obtained from ALE formulation

In this case convective velocity $\boldsymbol{c}$ is equal to $\boldsymbol{v}$ as the result of equation (4.51). Mesh is fixed in space and only material flows through it. When $\boldsymbol{\Psi}=\boldsymbol{I}$ the reference domain is the material one and Lagrangian description is obtained as it is presented in figure 4.7. In this case:

$$\boldsymbol{X}\equiv\boldsymbol{\chi} \tag{4.54}$$

where: $\boldsymbol{X}$ – material coordinates, $\boldsymbol{\chi}$ – reference coordinates.
Thus, the mesh and material velocities are described as:

$$\boldsymbol{v}(\boldsymbol{X},t)=\frac{\partial \boldsymbol{x}}{\partial t}|_X \Leftrightarrow \boldsymbol{v}(\boldsymbol{\chi},t)=\frac{\partial \boldsymbol{x}}{\partial t}|_\chi \tag{4.55}$$

$$\check{\boldsymbol{v}}(\boldsymbol{\chi},t)=\frac{\partial \boldsymbol{x}}{\partial t}|_\chi \Leftrightarrow \check{\boldsymbol{v}}(\boldsymbol{\chi},t)=\boldsymbol{v}(\boldsymbol{X},t) \tag{4.56}$$

where: $\boldsymbol{v}$ – material velocity vector, $\check{\boldsymbol{v}}$ – mesh velocity vector, $\boldsymbol{X}$ – material coordinates, $\boldsymbol{x}$ – spatial coordinates, $\boldsymbol{\chi}$ – reference coordinates, t – time, $|_X$ – material coordinates are fixed, $|_\chi$ – reference coordinates are fixed.

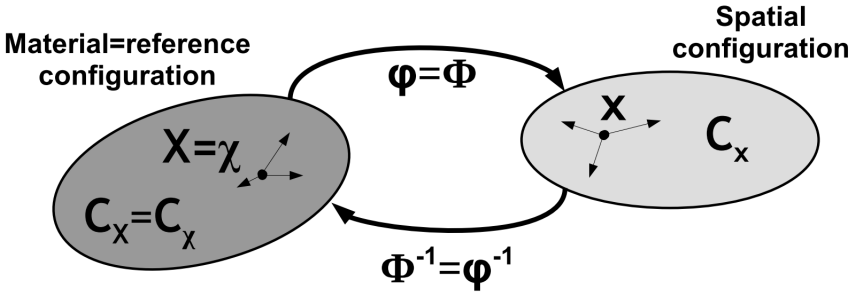

Figure 4.7. Lagrangian description obtained from ALE formulation

One can see that mesh velocity and material velocity are the same. This implies a material

trapped in the spatial mesh, which can be observed in classical Lagrangian FEM formulation.

Field variables in terms of ALE can be written in general form as (Donea et al., 2004):

$$\frac{\partial \boldsymbol{f}}{\partial t}|_{x}=\frac{\partial \boldsymbol{f}}{\partial t}|_{\boldsymbol{\chi}}+\frac{\partial \boldsymbol{f}}{\partial x}\cdot\boldsymbol{c}=\frac{\partial \boldsymbol{f}}{\partial t}|_{\boldsymbol{\chi}}+\boldsymbol{c}\cdot\nabla \boldsymbol{f} \tag{4.57}$$

where: $\boldsymbol{f}$ – field variable, $\boldsymbol{x}$ -spatial coordinates, t – time, $|_x$ – material coordinates fixed, $|_{\chi}$ – reference coordinates fixed, $\boldsymbol{c}$ – convective velocity vector.

Equation (4.57) can be easily rewritten into the pure Lagrangian or Eulerian formulation. When $\boldsymbol{c}$=0 and $\boldsymbol{X}\equiv\boldsymbol{\chi}$ Lagrangian formulation occurs and equation is formulated as:

$$\frac{\partial \boldsymbol{f}}{\partial t}|_{\boldsymbol{\chi}}=\frac{\partial \boldsymbol{f}}{\partial t}|_{x}\Leftrightarrow\frac{\partial \boldsymbol{f}}{\partial t}|_{x}=\frac{df}{dt} \tag{4.58}$$

where: $\boldsymbol{f}$ – field variable, t – time, $|_x$ – material coordinates are fixed, $|_{\chi}$ – reference coordinates fixed.

When $\boldsymbol{c}$=$\boldsymbol{v}$ and $\boldsymbol{x}\equiv\boldsymbol{\chi}$ the Eulerian formulation occurs and equation can be rewritten in following form:

$$\frac{\partial \boldsymbol{f}}{\partial t}|_{x}=\frac{\partial \boldsymbol{f}}{\partial t}|_{x}+\frac{\partial \boldsymbol{f}}{\partial x}\cdot\boldsymbol{v}\Leftrightarrow\frac{df}{dt}=\frac{\partial \boldsymbol{f}}{\partial t}+\boldsymbol{v}\cdot\nabla \boldsymbol{f} \tag{4.59}$$

where: $\boldsymbol{f}$ – field variable, t – time, $|_x$ – material coordinates are fixed, $|_x$ – spatial coordinates fixed, $\boldsymbol{x}$ – spatial coordinates vector, $\boldsymbol{v}$ – material velocity vector.

Equation (4.59) is well-known formula for relation between spatial and material time derivatives (e.g., Benson and Okazawa, 2004).

4.3.2 Governing equations

Conservation of mass, momentum and energy in ALE formulation can be written in following form (Donea et al., 2004):

(mass equilibrium)
$$\frac{\partial \rho}{\partial t}|_{\boldsymbol{\chi}}+\boldsymbol{c}\cdot\nabla\rho=-\rho\nabla\boldsymbol{v} \tag{4.60}$$

(momentum equilibrium)
$$\rho\left(\frac{\partial \boldsymbol{v}}{\partial t}|_{\boldsymbol{\chi}}+(\boldsymbol{c}\cdot\nabla)\boldsymbol{v}\right)=\nabla\cdot\boldsymbol{\sigma}+\rho\,\boldsymbol{b} \tag{4.61}$$

(energy equilibrium)
$$\rho\left(\frac{\partial E_{total}}{\partial t}|_{\boldsymbol{\chi}}+\boldsymbol{c}\cdot\nabla E_{total}\right)=\nabla\cdot(\boldsymbol{\sigma}\cdot\boldsymbol{v})+\boldsymbol{v}\cdot\rho\,\boldsymbol{b} \tag{4.62}$$

where: ρ – material density, t – time, $\boldsymbol{c}$ – convective velocity vector, $\boldsymbol{v}$ – material velocity vector, $\boldsymbol{\sigma}$ – stress tensor, $\boldsymbol{b}$ – body force vector, E_{total} – total energy, $|_{\chi}$ – reference coordinates fixed.

One can notice that Lagrangian conservation equation can be simply obtained from

equations (4.60)-(4.62) with assumption presented in equation (4.54) in section 4.3.1 and with application of convective velocity $\boldsymbol{c}$=0. The similar methodology can be applied to recover Eulerian conservation equations.

4.3.3 Calculation procedure

ALE adaptive meshing procedure is implemented in Abaqus/Explicit package. In this case, incremental calculation procedure (see section 4.1.5.6) is advantage, because mesh up-date process can be invoked every prescribed number of increments. The procedure consists of three steps: material points movement, new mesh generation and solution transfer. All steps have been described and illustrated in section 3.1.5 and here only the numerical background is provided. In ALE formulation the operator split method is used and the solution strategy is similar to the pure Eulerian calculation (Benson and Okazawa, 2004). The general form of conservation equation can be written as (Donea et al., 2004):

$$\frac{\partial \boldsymbol{f}}{\partial t}|_{\chi} + \boldsymbol{c} \cdot \nabla \boldsymbol{f} = \boldsymbol{S}_f \tag{4.63}$$

where: $\boldsymbol{f}$ – field variable, t – time, $|_{\chi}$ – reference coordinates fixed, $\boldsymbol{c}$ – convective velocity, $\boldsymbol{S}_f$ – source.

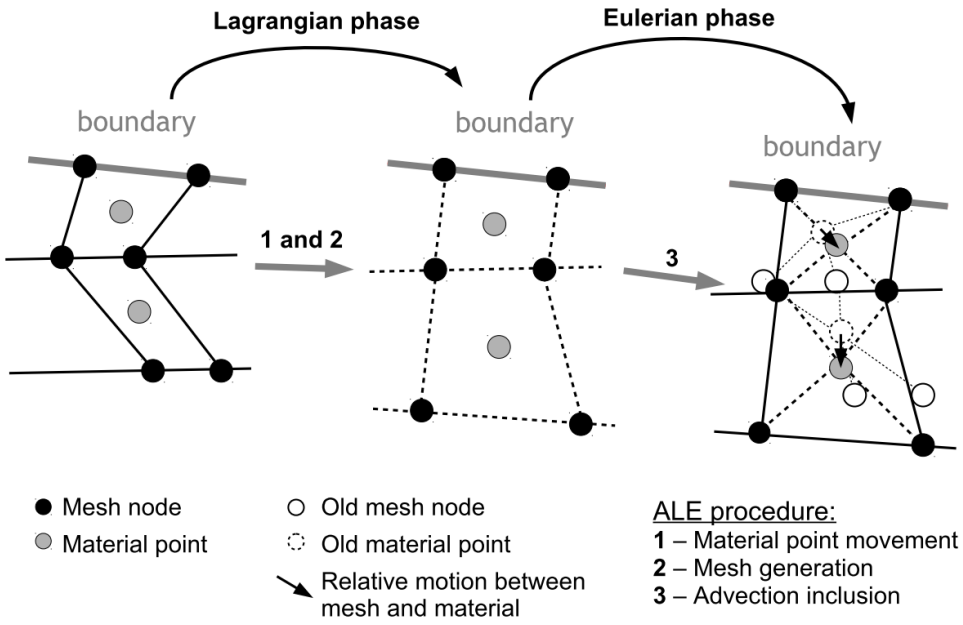

Figure 4.8. Split Operator for ALE formulation

Using split operator the equation (4.63) is divided into two separate parts. Firstly, Lagrangian phase is calculated (Donea et al., 2004):

$$\frac{\partial \boldsymbol{f}}{\partial t}|_{\chi} = \boldsymbol{S}_f \tag{4.64}$$

where: $\boldsymbol{f}$ – field variable, t – time, $|_{\chi}$ – reference coordinates fixed, $\boldsymbol{S}_f$ – source.

Then, the Eulerian part is solved (Donea et al., 2004):

$$\frac{\partial \boldsymbol{f}}{\partial t}|_{\chi} + \boldsymbol{c} \cdot \nabla \boldsymbol{f} = 0 \tag{4.65}$$

where: $\boldsymbol{f}$ – field variable, t – time, $|_{\chi}$ – reference coordinates fixed, $\boldsymbol{c}$ – convective velocity. The interpretation of using Split operator is as follows. First, the material points movement is calculated, see equation (4.64). Here, the boundary, loading, contact conditions, etc., are carried out and new mesh is generated. Then, the relative motion between material and mesh nodes is included during performance of the advection sweep, see equation (4.65). Graphical interpretation of Split operation usage is presented in figure 4.8.

4.4 Coupled Eulerian-Lagrangian (CEL) formulation

4.4.1 General description

Coupled Eulerian–Lagrangian (CEL) formulation usually uses Lagrangian viewpoint for penetrating object (e.g., pile) and the Eulerian viewpoint for target (e.g., soil structure). The essential part of CEL formulation is the application of boundary conditions on Lagrangian and Eulerian parts in each time step (Brown et al., 2002). In Abaqus, CEL method is based on Immersed Boundary Method developed initially by Peskin (1972). In this method, Lagrangian mesh is used for interface while Eulerian mesh is used for domain as it is presented in figure 4.9a. Force in n^k node is transferred on the surrounding Eulerian nodes with accordance to prescribed function, see figure 4.9b. The transition between Lagrangian and Eulerian mesh can be easily done with application of transformation function (see section 4.3.1 and equation (4.47)).

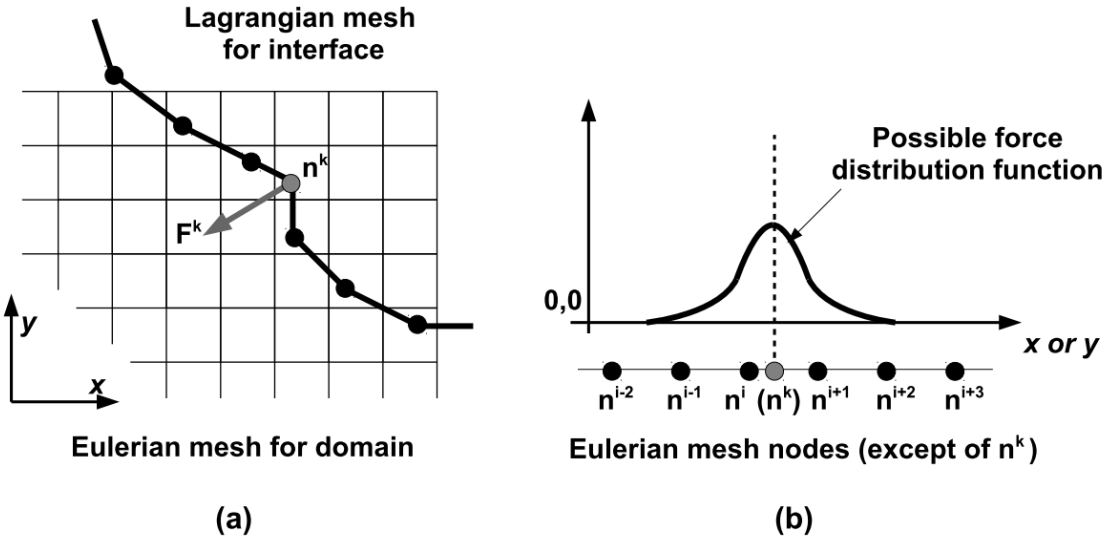

Figure 4.9. The immersed Boundary method concept (modified from Mittal and Iaccarino (2005))

The contact constrains between Lagrangian and Eulerian parts are modelled by penalty contact method (Dassault Systèmes, 2013). This method consists of two steps in every time

increment. Firstly, the motion of the Lagrangian part and the Eulerian material is calculated from interface forces obtained in previous time increment. Thus, the relative displacements between the Lagrangian nodes and the Eulerian material points are obtained and the interface forces can be calculated again. The penalty method developed by Olovsson (2000) will be described here due to its generality. As it was said, the motion of the Lagrangian element can be calculated from the force obtained in previous increment which is graphically presented in figure 4.10. The penalty force can be described by equation (Brown et al., 2002):

$$\boldsymbol{F_p} = k_p \boldsymbol{d_p} \tag{4.66}$$

where: $\boldsymbol{F_p}$ – penalty force, k_p – penalty stiffness, $\boldsymbol{d_p}$ – penalty displacement.

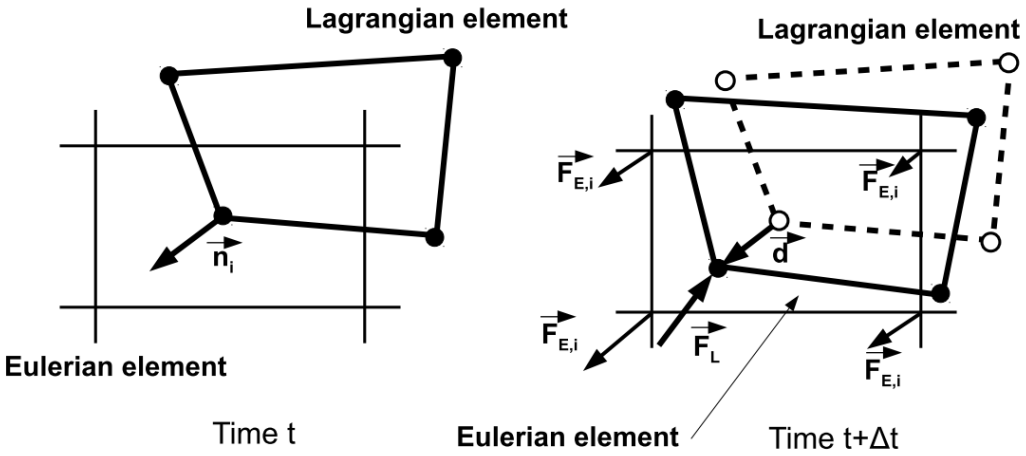

Figure 4.10. The penalty contact method for CEL formulation (modified from Brown et al. (2002)

Penalty displacement $\boldsymbol{d_p}$ can be calculated by formula (Brown et al., 2002):

$$\boldsymbol{d}_p = \begin{cases} \boldsymbol{d}_n & \mu = 0 \\ \boldsymbol{d}_n + \mu \left| \dfrac{\boldsymbol{d}_t}{\boldsymbol{d}_n} \right| \boldsymbol{d}_t & \boldsymbol{d}_n < \mu \boldsymbol{d}_t \\ \boldsymbol{d} & \boldsymbol{d}_n > \mu \boldsymbol{d}_f \end{cases} \tag{4.67}$$

where:

$$\boldsymbol{d_n} = (\boldsymbol{d} \cdot \boldsymbol{n}) \cdot \boldsymbol{n} \tag{4.68}$$

$$\boldsymbol{d_t} = \boldsymbol{d} - \boldsymbol{d_n} \tag{4.69}$$

where: $\boldsymbol{d_p}$ – penalty displacement, $\boldsymbol{d_t}$ – tangential component of penalty displacement, $\boldsymbol{d_n}$ – normal component of penalty displacement, $\boldsymbol{d}$ – actual displacement (see figure 4.10), μ – friction coefficient, $\boldsymbol{n}$ – outward normal vector to the Lagrangian surface at n^k node.
The penalty stiffness is defined as (Brown et al., 2002):

$$k_p = \epsilon \frac{m}{\Delta t^2} \tag{4.70}$$

where: k_p – penalty stiffness, m – minimal of the Lagrangian and the Eulerian mass, Δt – time increment, ϵ – small multiplier.
As a consequence, the forces applied on Eulerian nodes that will enforce material outflow can be described as (Brown et al., 2002):

$$\boldsymbol{F}_{\boldsymbol{E},\boldsymbol{i}} = N_i \beta_i \boldsymbol{F}_{\boldsymbol{p}} \tag{4.71}$$

where: $\boldsymbol{F}_{\boldsymbol{E,i}}$ – forces applied on Eulerian element nodes, N_i – Eulerian basis function (includes Lagrangian node location), β_i – weight functions (includes influence of Eulerian domain material at each node), $\boldsymbol{F}_{\boldsymbol{p}}$ – penalty force.
The force acting on the Lagrangian node is described as (Brown et al., 2002):

$$\boldsymbol{F}_{\boldsymbol{L}} = -\sum_i \boldsymbol{F}_{\boldsymbol{E},\boldsymbol{i}} \tag{4.72}$$

where: $\boldsymbol{F}_{\boldsymbol{L}}$ – force applied on Lagrangian node, $\boldsymbol{F}_{\boldsymbol{E,i}}$ – forces applied on Eulerian element nodes.

As one can notice, the most crucial problem in penalty contact method is difference between Lagrangian and Eulerian mesh size. The Lagrangian mesh size should be smaller than Eulerian one. Otherwise, the leakage of the Eulerian material through the Lagrangian mesh may occur.

4.4.2 Governing equation and calculation procedure

The Lagrangian part in CEL formulation is calculated using the procedure described in section 4.1.5. The Eulerian part uses conservation of mass, momentum and energy described in Eulerian form (Benson and Okazawa, 2004):

(mass equilibrium)
$$\frac{\partial \rho}{\partial t} + \boldsymbol{v} \cdot \nabla \rho = -\rho \nabla \boldsymbol{v} \tag{4.73}$$

(momentum equilibrium)
$$\rho \left(\frac{\partial \boldsymbol{v}}{\partial t} + (\boldsymbol{v} \cdot \nabla) \boldsymbol{v} \right) = \nabla \cdot \boldsymbol{\sigma} + \rho \boldsymbol{b} \tag{4.74}$$

(energy equilibrium)
$$\rho \left(\frac{\partial E_{total}}{\partial t} + \boldsymbol{v} \cdot \nabla E_{total} \right) = \nabla \cdot (\boldsymbol{\sigma} \cdot \boldsymbol{v}) + \boldsymbol{v} \cdot \rho \boldsymbol{b} \tag{4.75}$$

where: ρ – material density, t – time, $\boldsymbol{v}$ – material velocity vector, $\boldsymbol{\sigma}$ – stress tensor, $\boldsymbol{b}$ – body force vector, E_{total} – total energy.
The strategy of solving above set of equations is the same as in ALE method. The equations (4.73)-(4.75) have general form (Benson and Okazawa, 2004):

$$\frac{\partial \boldsymbol{f}}{\partial t} + \boldsymbol{v} \cdot \nabla \boldsymbol{f} = \boldsymbol{S}_{\boldsymbol{f}} \tag{4.76}$$

where: $\boldsymbol{f}$ – field variable, t – time, $\boldsymbol{v}$ – material velocity, $\boldsymbol{S}_f$ – source.
Using the Split Operator method the Lagrangian and Eulerian phases can be distinguished (Benson and Okazawa, 2004):

(Lagrangian phase)
$$\frac{\partial \boldsymbol{f}}{\partial t} = \boldsymbol{S}_f \tag{4.77}$$

(Eulerian phase)
$$\frac{\partial \boldsymbol{f}}{\partial t} + \boldsymbol{v} \cdot \nabla \boldsymbol{f} = 0 \tag{4.78}$$

where: $\boldsymbol{f}$ – field variable, t – time, $\boldsymbol{v}$ – material velocity, $\boldsymbol{S}_f$ – source.
The graphical interpretation of using the Split Operator in CEL or pure Eulerian formulation is presented in figure 4.11.

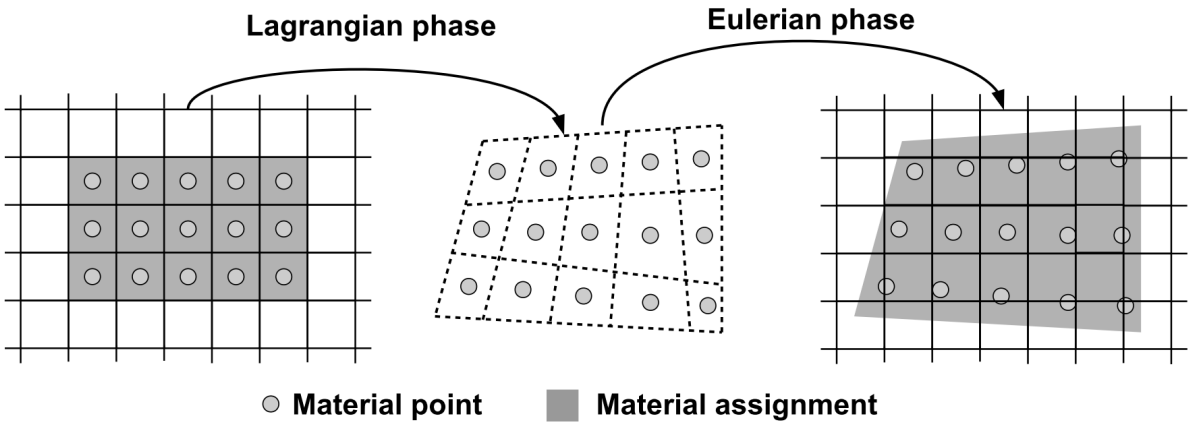

Figure 4.11. Split operator for Eulerian formulation (modified from Benson and Okazawa (2004))

4.5 Contact modelling in FEM

4.5.1 General considerations

Surfaces in FEM model are also discretized in small elements and the contact model describes the interactions between such defined surfaces. The first step is to choose master (first) surface and the slave (second) one, see figure 4.12. Nodes on the slave surface should not penetrate the master one, so to achieve this goal, slave surface should have finer mesh than the master surface. Choosing the slave surface on the domain with softer material also provides better performance of contact modelling (Dassault Systèmes, 2013).

In this thesis, the surface to surface discretization is used for contact modelling, which considers average contact conditions between surfaces and provides more accurate results (Dassault Systèmes, 2013). However, in surface to surface discretization the single slave node may penetrate into the master surface. The next issue of contact modelling is to use finite sliding formulation where the areas of surfaces that are in contact are continuously tracked by

computing algorithm. This is usually very complex calculation procedure which includes separation, sliding and rotation of the surfaces (Dassault Systèmes, 2013).

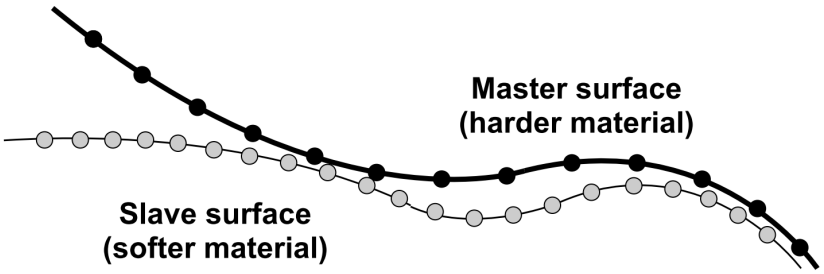

Figure 4.12. Surface discretization in FEM analysis

4.5.2 Contact contribution to FEM procedure

The basic interaction between surfaces consists of normal and tangential behaviour. Normal behaviour is modelled as a so-called "hard" contact, which is presented in figure 4.13. When surfaces are in contact (clearances close) the pressure acts on both surfaces. Otherwise (clearances open), no pressure is applied. The advantage of such approach is simplicity which can be described by equation (Dassault Systèmes, 2013):

$$\begin{array}{llll} p=0 & for & h\le 0 & (clearances \quad open) \\ h=0 & for & p>0 & (clearances \quad close) \end{array} \tag{4.79}$$

where: p – pressure acting on the surfaces, h – interpenetration of the surfaces called "overclosure".

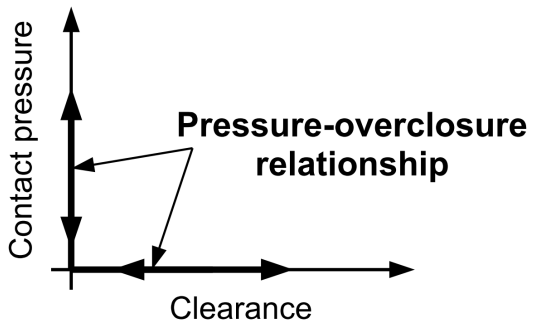

Figure 4.13. Pressure-overclosure relationship in "hard" contact model (based on Dassault Systémes (2013))

The hard contact model can provide some difficulties in numerical calculation in implicit formulation. The rapid "jump" from open to close clearances can make lack of convergence in Newton method (Dassault Systèmes, 2013).

The tangential behaviour is modelled using Coulomb friction law (see section 3.2). Thus, the shear stresses can be written as (Dassault Systèmes, 2013):

$$\tau_{crit} = \mu\, p \tag{4.80}$$

where: τ_{crit} – critical shear stresses at the interfaces, μ – friction coefficient, p – pressure acting on the surfaces.
When critical shear stresses are reached, the slip may occur. In isotropic friction the following equation can be written (Dassault Systèmes, 2013):

$$\frac{\tau_i}{\tau_{crit}} = \frac{\dot{\gamma}_i}{\dot{\gamma}_{eq}} \tag{4.81}$$

where: τ_i – shear stresses in i direction, τ_{crit} – critical shear stresses, $\dot{\gamma}_i$ – slip rate in i direction, $\dot{\gamma}_{eq}$ – slip rate equivalent to the critical shear stresses.
Here a basic problem in implicit analysis can be recognised. How to differ the states when surfaces are sticking and when they are sliding. In explicit method there is no problem in sticking or sliding, because the incremental formulation allows the surfaces in one increment to be stuck, while in the next one to be in relative motion. As one can see, the explicit formulation is well-suited for "hard" normal and tangential behaviour. In implicit formulation the "elastic slip" needs to be introduced to avoid the rapid "jump" between sticking and sliding state as it can be seen in figure 4.14. "Elastic slip" is simply reversible relative sliding between surfaces and it can be expressed as (Dassault Systèmes, 2013):

$$\gamma_i = F_i \cdot l_i \tag{4.82}$$

where: γ_i – small allowable elastic slip in i direction, F_i – slip tolerance in i direction, l_i – characteristic contact surface length in i direction, which can be described as average length of all elements in contact.
By default the slip tolerance F_i in Abaqus is assumed as 0,5%. Hence, the allowable elastic slip is usually 0,5% of the average length of elements in contact.

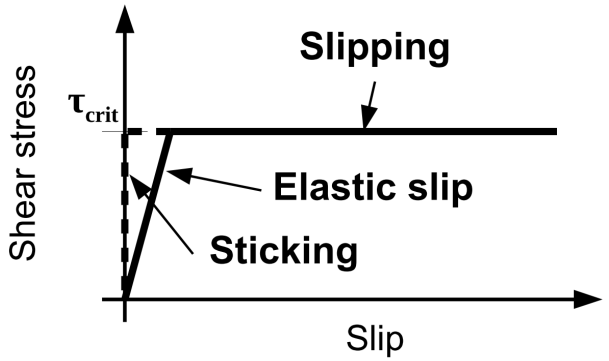

Figure 4.14. Elastic slip concept in FEM (based on Dassault Systémes (2013))

After defining the normal and tangential behaviour, the pressure acting on the surfaces can

be calculated. The penalty contact method is used in numerical studies described in this thesis and it is illustrated in figure 4.15. When the slave node penetrates the master surface in time step *j* the penalty force is applied. It can be written as (Dassault Systèmes, 2013):

$$f_{j+1} = k_i \cdot d_i \tag{4.83}$$

where: f_{j+1} – penalty force applied on node in time step *j+1*, k_i – penalty stiffness on *i* direction, d_i – penetration length on *i* direction.
In time step *j+1* the penalty force is taken into consideration in balance equations. Penalty stiffness is calculated automatically by Abaqus algorithm to provide the minimum penetration length without significant time increment reduction. The default value reduces the stable time increment by no more than 4% (Dassault Systèmes, 2013).

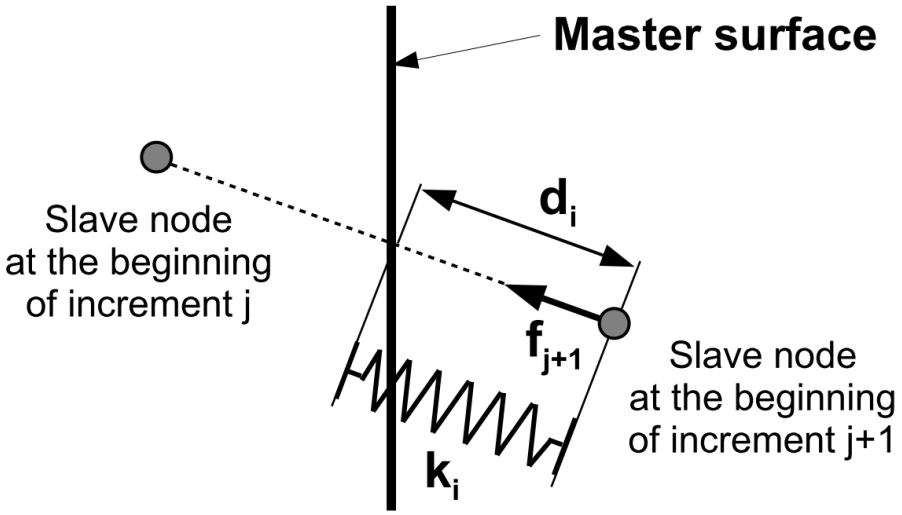

Figure 4.15. Penalty contact method (modified from Dassault Systémes *(1999))*

The contact occurrence induces additional terms to the virtual work equations. The virtual work contribution due to penalty contact method can be written as (Dassault Systèmes, 2013):

$$\delta \Pi = \int_{\Gamma} k_i d_i \delta d_i \, d\Gamma \tag{4.84}$$

where: $\delta\Pi$ – virtual work by contact forces, k_i – penalty stiffness on *i* direction, d_i – penetration length on *i* direction, Γ – surface contact area, δd_i – virtual displacement on *i* direction.

Page intentionally left blank

Chapter 5

Preliminary studies

Preliminary studies play a key role in scientific research (Woken, 2013). The understanding of possible wide range of factors which affect solution results in better performance of final models and case studies. In pile jacking simulation many simplifications have been introduced on constitutive modelling stage (see chapter 3), but there are still a lot of uncertainties, concerning friction behaviour or initial stress state, which need to be identified. The influencing factors can be divided into convergence components and sensitivity elements, see figure 5.1. The investigation of factors affecting numerical solution will be carried out in reference to radial total and/or effective stresses. Gathered information will be used in simulations presented in further chapters.

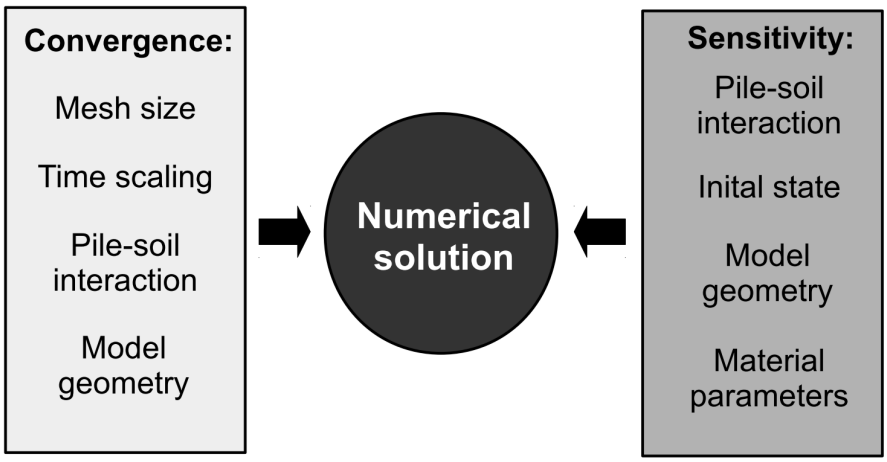

Figure 5.1. Convergence and sensitivity factors affecting numerical solution

5.1 Total versus effective stress parameters correlation

In section 3.2 the total and effective stress approaches have been presented with possible correlation between parameters occurring in both of them. The installation phase is undrained analysis which is the only one modelled by both, total and effective stress approaches (see

section 3.8.1). Hence, the validation of parameters correlation presented in section 3.2.6 will be carried out by numerical unconsolidated undrained (UU) triaxial test. Firstly, one can introduce typical soil parameters (e.g., Terzaghi et al., 1996) for total stress analysis where Tresca plasticity is used, see table 5.1. The soil in triaxial tests is assumed to be weightless and the initial loading state is isotropic (horizontal stress to vertical stress ratio is equal to one), see figure 5.2. Moreover, application σ_h/σ_v ratio equal to one is safe because it gives a uniform pressure distribution and water-like behaviour (see section 3.2.6). Tension cut-off of 1.0 is assumed to exclude tension strength of soil.

Table 5.1. Total stress analysis parameters

Parameter	ρ_{sr}	E_u	υ_u	c_u	σ_h/σ_v	σ_t
	g/cm³	*kPa*	-	*kPa*	-	*kPa*
Value	*2,2**	*2 500*	*0,49*	*80*	*1,0*	*1,0*

*Weightless soil is obtained by application of zero gravitational acceleration

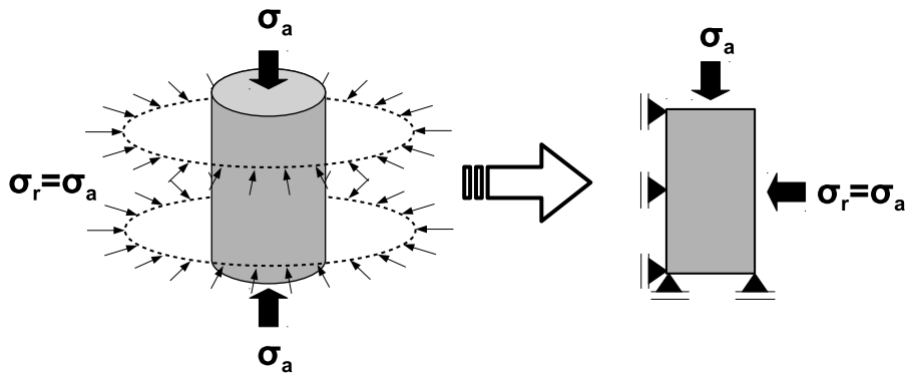

Figure 5.2. Initial axisymmetric state of the isotropically loaded soil sample with corresponding numerical model.

Next, one can correlate the effective stress parameters to the total ones for elasticity after equation (3.26) and for plasticity after equation (3.32), both derived in section 3.2.6. Effective shear modulus can be calculated directly from equation (3.27), while the MCC plasticity parameters such as stress ratio M, logarithmic elastic modulus κ, logarithmic plastic modulus λ need to be assumed (e.g., Mayne, 1988; Terzaghi et al., 1996). The initial void ratio e_0 and effective soil density ρ' are adjusted to the total soil density ρ_{sr}. One can summarize the effective stress parameters in table 5.2. Here, the weightless and isotropically loaded sample is also assumed. The preconsolidation mean stress p_c' depends on initial mean stress p_0'. For physical properties provided in tables 5.1 and 5.2 the relation between initial mean stress p_0' (or depth below surface level) and preconsolidation mean stress p_c' follows the curve plotted in figure 5.3.

Table 5.2. Effective stress parameters

Parameter	ρ'	G'	e_0	κ	λ	p_c'	M	ρ_w	K_0	k
	g/cm³	*kPa*	-	-	-	*kPa*	-	*g/cm3*	-	*m/s*
Value	*1,2**	*839*	*0,65*	*0,08*	*1,0*	*varying*	*0,835*	*1,0*	*1,0*	10^{-10}

*Weightless soil is obtained by application of zero gravitational acceleration

The numerical UU tests have been carried out for 5 different loads. The relation between deviatoric stress q with the axial strain is presented in figure 5.4. As one can see, total stress analysis represented by Tresca plasticity gives the same response, which is typical for this criterion. Quite good agreement between total and effective stress analysis was also achieved. The best agreement is observed when initial mean stresses p_0' are equal half of the yield surface size in failure (see section 3.2.4). When this condition is not fulfilled, the plastic flow occurs and plastic strains are generated. As a result the yield plastic surface can be a little bit smaller then assumed in derivation of equation (3.32).

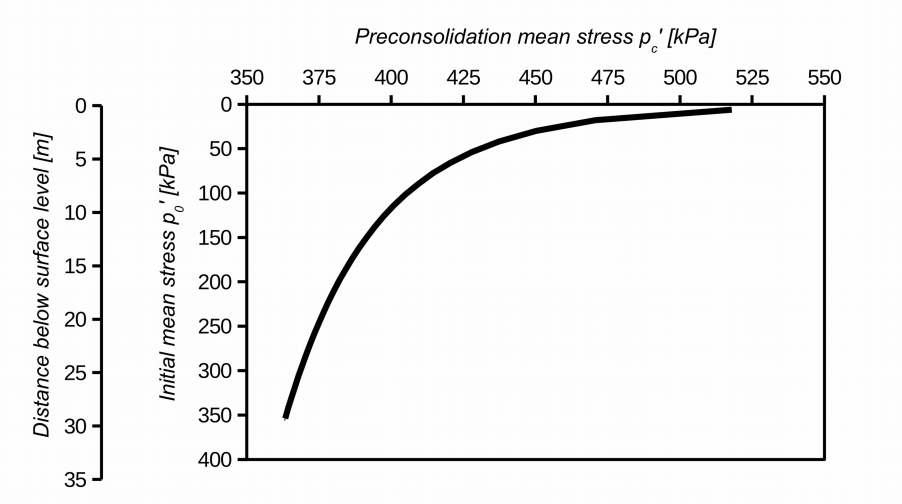

Figure 5.3. Relation between preconsolidation mean stress and initial mean stress for total-effective parameters fitting

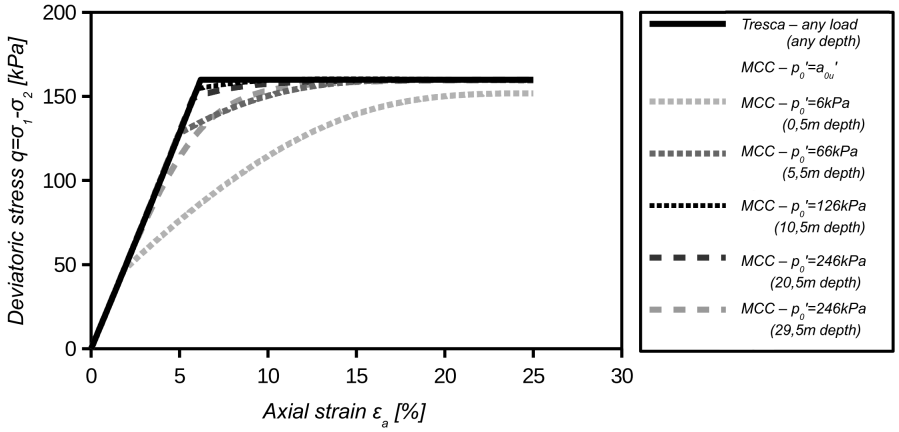

Figure 5.4. Numerical UU test for the Tresca material and correlated MCC material

5.2 Pile jacking preliminary tests

Pile jacking preliminary tests consist of 138 numerical simulations carried out with ALE, UL and CEL formulations. The aim of preliminary tests is to verify compatibility between

different formulations and to provide convergence and sensitivity studies for each method. As the result, the wide scope of guidelines about numerical model development is determined. In addition, the factors which influences the radial total stresses increase are identified and the findings obtained during preliminary studies are used in next chapters.

5.2.1 Problem description

5.2.1.1 Geometry and material properties

Preliminary pile jacking test is performed in the prescribed geometry given in figure 5.5. The width of the soil domain is equal to the twenty pile diameters and it was assumed in accordance with values used in literature (e.g., Hamann et al., 2015; Qiu et al., 2011). The domain height of 60D was adopted after author's experience (Konkol, 2015; Konkol and Bałachowski, 2016). The large amount of soil mass is intended to dump the disturbance induced by penetration process. The pile is modelled as a discrete rigid element and it is pre-installed in soil at the depth of 0,5m to avoid initial mesh distortions, which is particularly important in UL model. The same strategy has been used in previous research with ALE or UL methods where Lagrangian mesh has been used (e.g., Hamann et al., 2015). The verification of pre-instalation effect has been done by author in terms of ALE model and no significant difference has been recognised regardless the pile pre-instalation was applied or not. However, it was found that pile pre-instalation facilitates the convergence problems due to mesh distortion in UL solution. The pile pre-instalation was not used in CEL model due to lack of Lagrangian mesh. Here, the Eularian mesh has been divided on the material free area and material assignment regions and the pile was placed just above the surface level, see figure 5.5b.

The soil domain is modelled as elastic-perfectly plastic materials with parameters submitted in tables 5.1 and 5.2. Three types of analyses are carried out, which are the total stress analysis using ALE formulation, the effective stress analysis using UL formulation and total stress analysis with CEL method. All three analyses should give similar response because of mechanical parameters compatibility as it was presented in section 5.1. In ALE and UL method the pile is pressed using zipper-type technique developed by Mabsout and Tassoulas (1994). In this method the small diameter tube (1mm diameter in this study) is connected with pile and it supports the soil mass, see figure 5.5a. The tube is in frictionless contact with soil and when pile jacking progresses, the tube slides down. The roundings between toe and tube as well as between toe and shaft are designed to minimize the sudden stress change around the vertex, which was observed when sharp chamfer had been used (Sheng et al., 2009). The roundings also provide better soil flow around the toe and they facilitate the convergence of UL solutions. The pile-soil contact is modelled using finite sliding, see chapter 4 section 4.5.1. The interaction between pile shaft and soil is frictionless. Pile is jacked with the constant velocity of 1cm/s to the designed depth of 8,0m.

5.2.1.2 Stability conditions

There are two basic stability conditions in pile jacking modelling. In explicit formulation (ALE and CEL models) the numerical model has to be in equilibrium at the initial state which

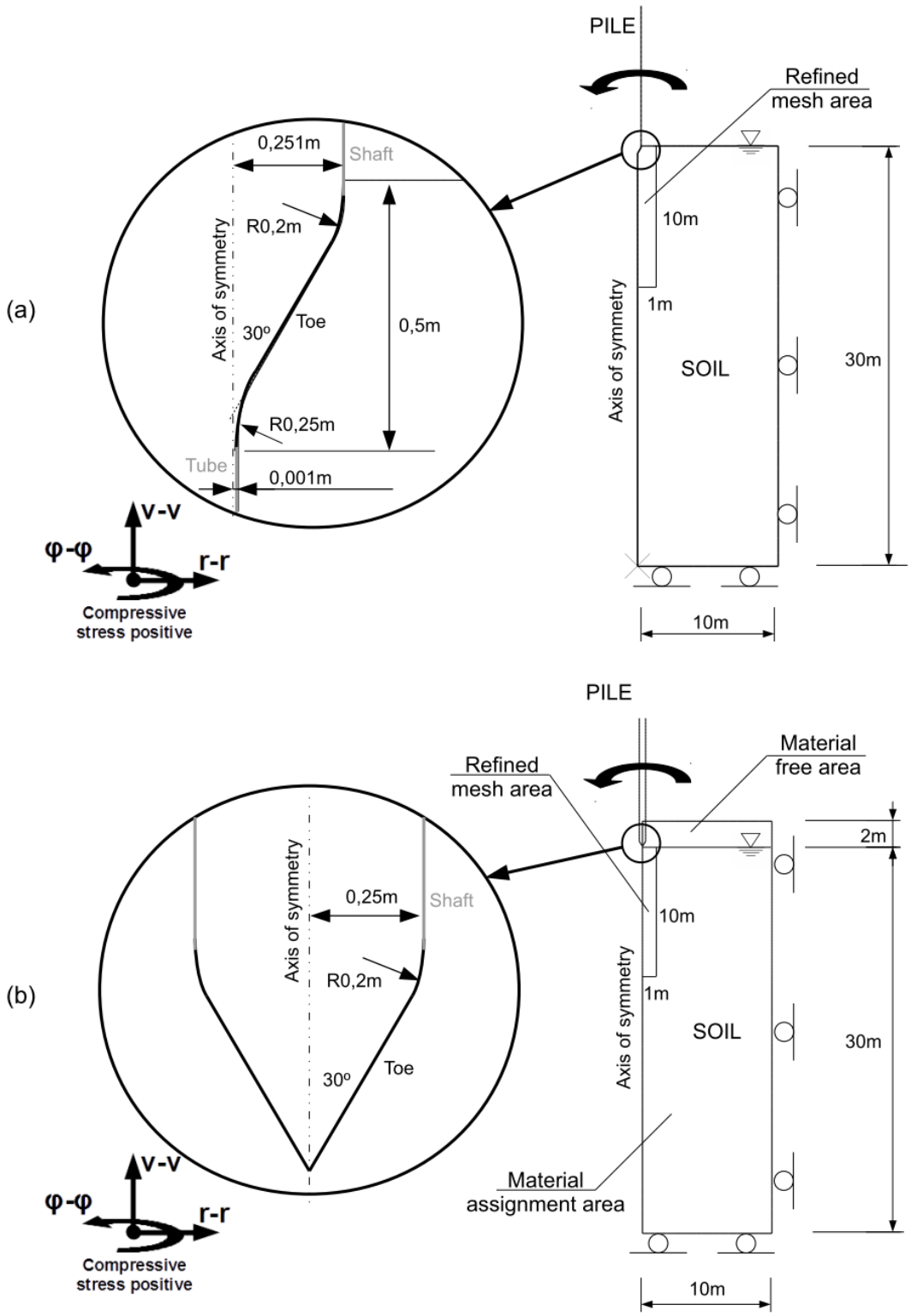

Figure 5.5. Model geometry in (a) ALE and UL formulation and (b) CEL formulation

can be problematic to achieve when the pile pre-installation is used. The "geostatic" step of 10s duration in ALE formulation has been applied to check the stress state changes. The large

soil domain and the artificial bulk viscosity of 0,12 results in acceleration dumping and almost static response of the model (stress oscillations are about 0,5kPa). Due to lack of pre-instalation in CEL model, the geostatic step duration was fixed as 1s and it also provides almost static state of the system. The state at the end of the jacking was also checked. Here also small differences in stress state were observed (about 1kPa). This implies quasi-static conditions in ALE and CEL models and it will be confirmed by energy plots in the later part of this thesis.

In UL model the geostatic step is obtained as an individual procedure. The only problem is the pore pressure "overshoot" (see equation 4.43 in secton 4.2.3) which may occur in numerical solution. The pore pressure overshot depends mainly on mesh size and permeability coefficient. This problem will be described in more details in section 5.2.5.

5.2.1.3 Solutions compatibility evaluation

The evaluation of the solutions is performed by comparison of some of field variables provided directly or indirectly from Abaqus solver. Stress and strain components, pore water pressures and displacements are provided directly and they will be shown for a cross-section in 0,5mm distance from the pile wall with averaging threshold of 100%. The pile toe and shaft resistances are provided as resistance force acting on the surface in contact. The pile toe resistance is calculated by formula:

$$q_b = \frac{F_{toe}}{A_{toe}} = \frac{F_{toe}}{\pi R^2} \tag{5.1}$$

where: q_b – toe (base) resistance, F_{toe} – total vertical force acting on pile toe, A_{toe} – pile toe area, R – pile radius.
The pile shaft resistance is calculated as an average unit resistance acting on current pile shaft area:

$$f_s = \frac{F_{shaft,t}}{A_{shaft,t}} \tag{5.2}$$

where: f_s – shaft resistance, $F_{shaft,t}$ – total vertical force acting on pile shaft in time t, $A_{shaft,t}$ – actual pile shaft area in contact with soil in time t.

5.2.2 Establishing numerical models

The initial run consists of total stress analysis with ALE and CEL formulation and effective stress analysis with UL formulation. In total stress approach (ALE model) the quadratic, 4 nodded, linear finite elements with reduced integration (CAX4R) are used with minimum size of 4,0x4,0cm in refined mesh area. In CEL model the Eulerian first order elements with reduced integration (EC3D8R) and minimum size of 5x5cm are used. The double precision analysis due to large number of increments is carried out. In UL model, the quadratic, second order elements with reduced integration (CAX8RP) and minimum size of 1,0x2,0cm in refined mesh area are applied. The element type choice has been discussed in details in

chapter 4, section 4.1.2. Three numerical models with generated meshes are presented in figure 5.6.

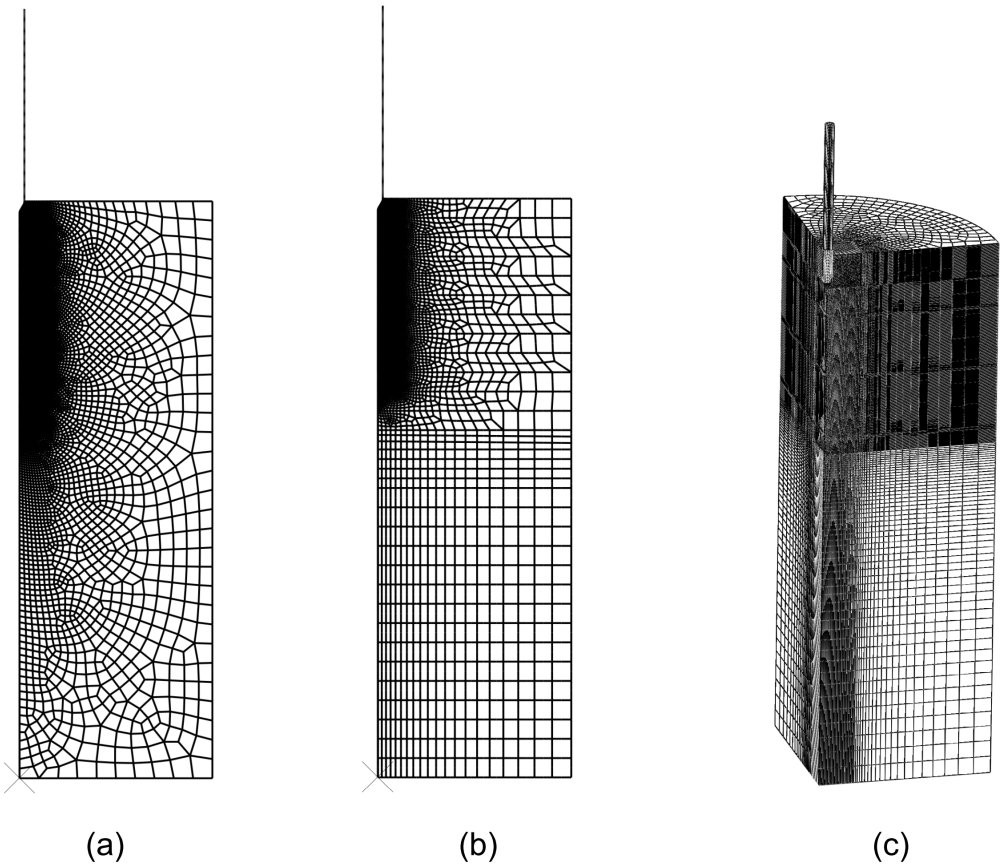

Figure 5.6. Meshed numerical models in (a) ALE (b) UL and (c) CEL method

5.2.2.1 Numerical study results

The pile toe unit resistance obtained from total and effective analysis is presented in figure 5.7a. As can be seen, a very good agreement between solutions is obtained despite different numerical formulations and constitutive behaviour and the deviation in toe resistance is approximately 7%. The radial total stress, vertical total stress, hoop total stress and shear stress distributions are presented in figure 5.7b, 5.7c, 5.7d and 5.8e, respectively. Here, the results are quite confusing. The stress distributions around the pile toe are the same which suggests a good performance of applied methods in all three cases. The shear stresses along the pile shaft are close to zero and this is also correct due to frictionless behaviour on pile-shaft interface. The similar distribution is also provided for hoop stresses. However, the radial and vertical stress distributions are quite different. The only exception is the similarity between ALE and UL solutions. The detailed discussion about each formulation is provided below.

ALE versus CEL

It has been found that CEL formulation is sensible to so-called “plough effect”. In eulerian

mesh the material is not fixed to the mesh (see chapter 3 and 4), so each element is filled with material in some percentage of total volume. This results in more rapid stress decrease near the shaft area in comparison to ALE formulation, see figure 5.8 where the total radial stresses are plotted for five different depths. The refining of the mesh does not improve the solution, but only enables to find peak stress in closer distance to the pile shaft, see figure 5.11. Similar results have been observed by Qiu et al. (2011). Thus, the CEL formulation is a good choice, when analyst is interested in total pile or structure resistance rather than in stress investigation in pile neighbourhood (e.g., Tho et al., 2013). However, mesh design correctly still allows for safe stress estimation which can be valuable in large deformation analysis in soft soils (e.g., Hamann et al., 2015; Qiu et al., 2011). In Chapters 6 the application of CEL method in stress distribution prediction is shown.

ALE versus UL

The results from ALE and UL formulations are quite similar in terms of radial, vertical and hoop total stress, see figure 5.7b and 5.8. Thus, the verification of the UL model is possible by using the referential ALE solution and the assumption presented in section 3.1.8 is fulfilled. The differences are small despite various failure surface in Π-plane where MCC is a circle while Tresca is a hexagon (see section 3.2.3). One can use Mises plasticity instead of Tresca to obtain the exact compatibility between effective and total stress constitutive laws. This was checked by the author and the same high compatibility between UL and ALE solutions has been achieved. Figure 5.8 shows that $\sigma_{rr}/\sigma_{rr,0}$ ratio decreases with the depth and the influence of pile installation is between 5 and 8 pile radii.

The radial effective stress and pore water pressure distributions obtained from UL model are presented in figure 5.9. As can be seen, the radial effective stress is constant with depth. In addition, on the pile length except the tip neighbourhood the effective stress predictions provided by the UL formulation are close to the Cavity Expansion method (CEM) derived by Randolph et al. (1979a):

$$\sigma'_{rr}=\left(\frac{\sqrt{3}}{M}+1\right)c_u \tag{5.3}$$

where: σ'_{rr}'– radial effective stress, M – stress ratio (p'-q slope), c_u – undrained shear strength. The pore water pressure predictions based on UL method is generally close to hydrostatic one except the upper part where some suction is observed and near tip where some overpressure is generated. The pore water pressure distributions are quite different in comparison to CEM prediction given by equation (Randolph et al., 1979a):

$$u=u_0+c_u\ln\left(\frac{G}{c_u}\right) \tag{5.4}$$

where: u – pore water pressure, u_o – hydrostatic pore water pressure, G – shear modulus, c_u – undrained shear strength.

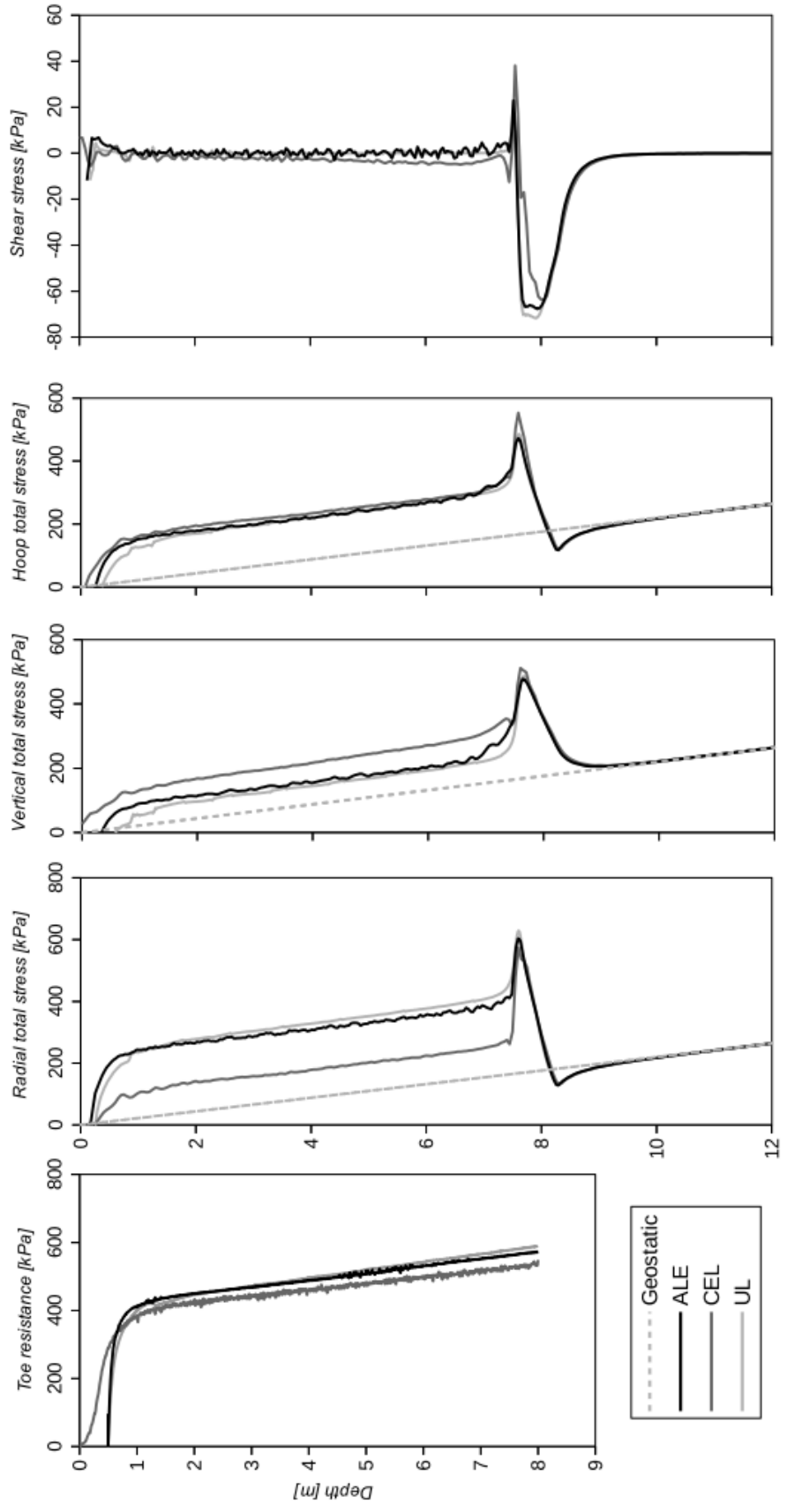

Figure 5.7. (a) Toe resistance, (b) radial total stress, (c) vertical total stress, (d) Hoop total stress and (e) shear stress obtained from UL, ALE and CEL models

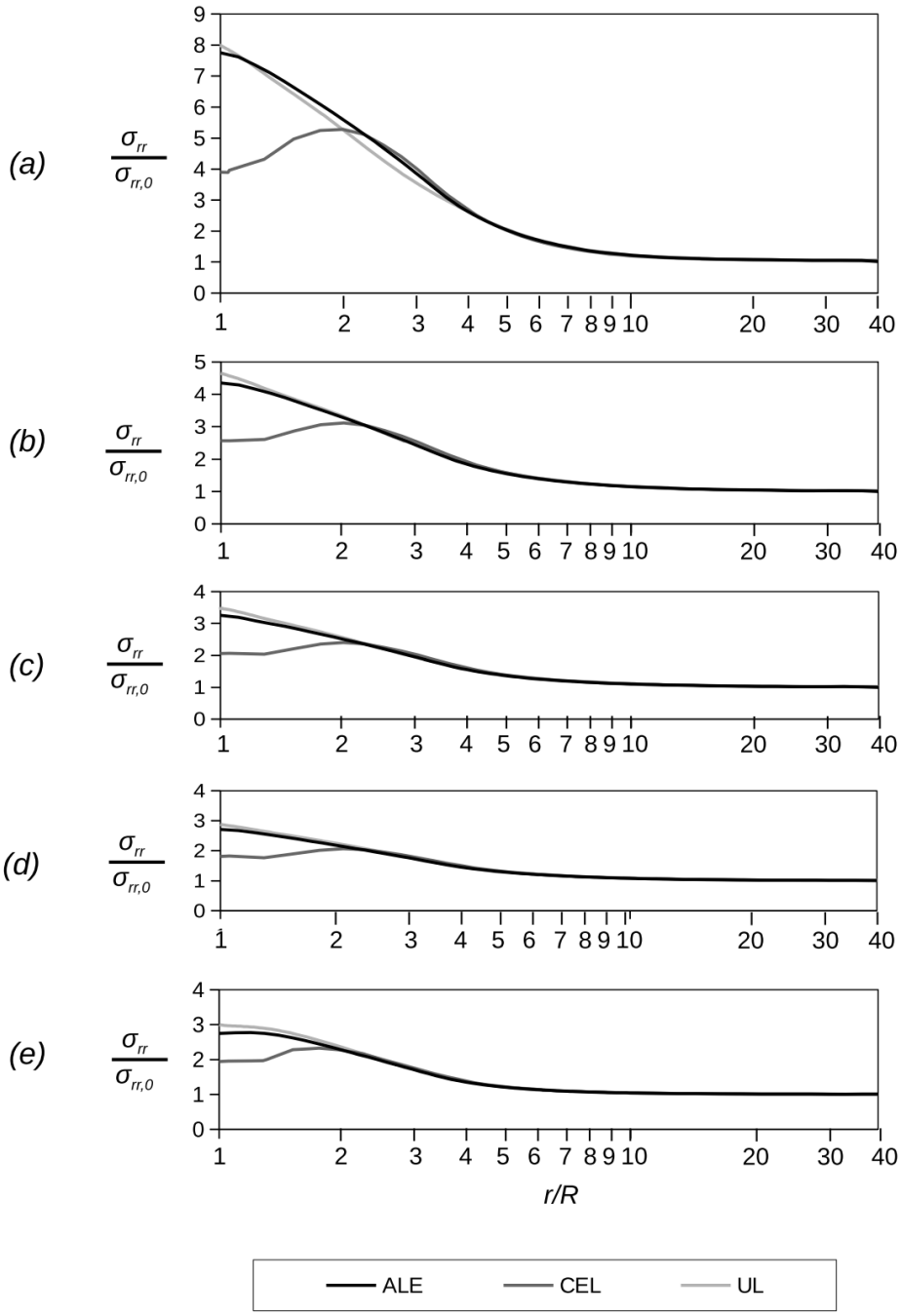

Figure 5.8. Normalized radial total stress distribution for (a) 1,5m; (b) 3,0m; (c) 4,5m; (d) 6,0m and (e) 7,5m depth

In UL method the suction in the upper part of soil structure can be noticed, while CEM provides highly overestimated pore water pressure prediction which are in agreement with UL only in pile toe region. The differences are believed to be induced by combined vertical and horizontal movement of the soil in contrast to the pure horizontal displacement in CEM method (Yu, 2000). The void ratio remained constant and it is consistent with assumption provided in section 3.2.6. about undrained analysis in effective stress approach.

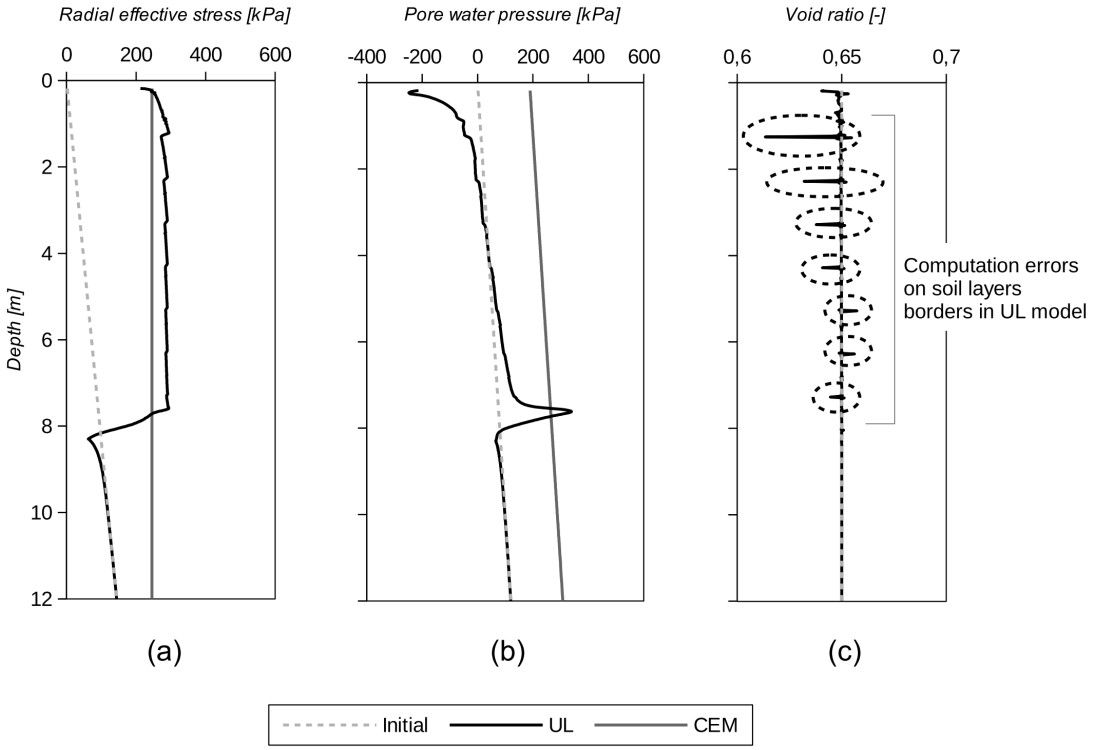

Figure 5.9. (a) Radial effective stress, (b) pore water pressure and (c) void ratio distribution obtained from UL model

The energy plots for all three models are presented in figure 5.10 as normalized values. As can be seen, the kinematic energy does not exceed 3,5% of an external work during jacking and thus, all models can be treated as a quasi-static problems. The total energy error does not exceed 1%, so all solution are numerically correct.

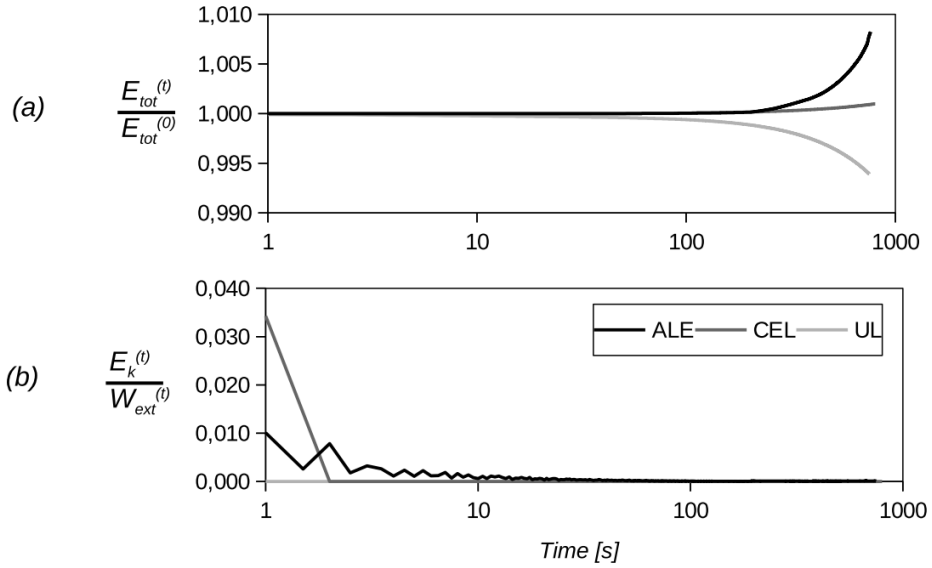

Figure 5.10. (a) Total energy error and (b) kinetic energy to external work ratio for numerical models

5.2.2.2 Mesh size

Mesh size study is standard convergence issue in FEM analysis and it has also been done in this thesis. The list of tested mesh sizes is summarized in table 5.3. Herein, the mesh size in jacking area depends on surface discretization (see section 4.5.1) and convergence accuracy. It has been found that even a coarser mesh in ALE and UL formulation can provide the same level of results accuracy, so the meshes described in section 5.2.2 are designed correctly. Consequently, it can be stated that only 6-8 finite elements per pile diameter is needed to obtain reliable and very effective solution in terms of ALE or UL, while in CEL formulation around 10 finite elements are needed per pile diameter.

Table 5.3. Mesh size convergence studies

Numerical formulation	*Mesh size [cm]*	
	Results are converging	*Results start to diverge*
ALE	*2,5x2,5* *4,0x4,0* *8,0x8,0*	-
CEL	*2,5x2,5* *5,0x5,0*	*8,0x8,0*
*UL**	*0,5x1,0* *1,0x2,0* *2,0x2,0*	-

*"trials and errors" method

Significant limitation of numerical calculations with UL formulation is related to progressive mesh distortions. Dozen numerical breakdown have been encountered during this research and it is consistent with works of other authors (e.g., Sheng et al., 2014). In addition, in UL solutions the trial and error method needs to be used to find converging meshes (Sheng et al., 2014). Application of the finer mesh in UL formulation leads also to higher solution noise, especially when friction behaviour on pile interface is applied. Observation encountered with UL method during this research are generally consistent with other authors experience (Sheng et al., 2009, e.g., 2014).

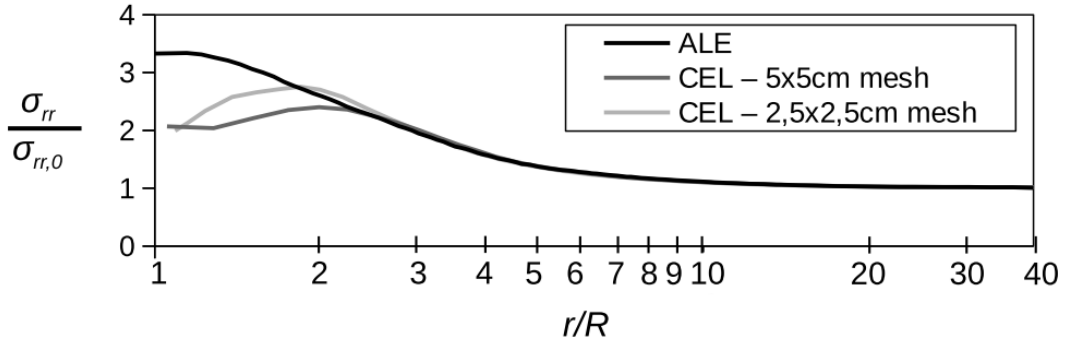

Figure 5.11. Effect of refining mesh size in CEL formulation

As it was previously said in section 5.2.2.1, in CEL formulation the accuracy of stress

prediction near pile wall is limited and the mesh refinement is ineffective. Figure 5.11 shows the total radial stress distribution at the depth of 4,5m with different meshes. As one can notice, finer mesh gives more accurate results, but computational time usually limits the effectiveness of this approach. Based on the presented example, it can be shown that total stress in CEL model is usually about 50%-80% of ALE solution, see figure 5.11.

5.2.2.3 Time scaling

Time scaling is one of the techniques that allows for computational time reduction in explicit methods such as ALE and CEL. In these models the Tresca plasticity which is insensitive to the rate effects is used. Hence, increasing loading rate involves only numerical approximation errors. The common practice is to limit the impact velocity to 1% of dilatational wave speed (e.g., Dassault Systèmes, 2013). In preliminary ALE and CEL models this speed can be calculated as:

$$c_d = \sqrt{\frac{2G(1-\nu_u)}{(1-2\nu_u)\rho_{sr}}} \tag{5.5}$$

where: c_d – dilatational wave speed, G – shear modulus, υ_u – undrained Poisson's ratio, ρ_{sr} – total soil density.

Using the parameters provided in table 5.1., the dilatational wave speed can be calculated as 139,45m/s. Hence, the maximum impact velocity should not exceed 1,39m/s and this condition is fulfilled (pile jacking velocity is fixed as 1cm/s). According to Abaqus manual (Dassault Systèmes, 2013) the time scaling can be used as long as no visible solution changes are observed. The influence of time scaling has been tested on ALE model due to computational time efficiency and no difference in stress distributions were observed until velocity of 5 cm/s was reached. Above this value the declining or increasing of local stress is noticed, whereas pile toe resistance value is preserved. Consequently, the results for 5 cm/s and higher rates may be acceptable when analyst is not interested so much in field variables but rather in cone or sleeve resistance. In that case, the combined effect of mesh size and time scaling can result in very significant computational time reduction. In numerical tests presented in this thesis the prototype loading rate will be used with some exceptions clearly pointed out. As no higher impact velocities than 7 cm/s will be used, the field variables are believed to be the accurate values.

5.2.2.4 Tension cut-off

Tension cut-off is important factor in numerical simulations in geotechnics because it eliminates tensile strength of the soil. In jacking process simulated with ALE or CEL formulation tension cut-off can provide unrealistic heave of the soil surface, as can be seen in figure 5.12. This phenomenon can even lead to the termination of calculation which has been encountered few times by author. The numerical tests performed show that lack of tension cut-off in material specification affects only the near surface area. This region is generally

difficult to analyse because of pile pre-installation and to facilitate the numerical calculations the tension cut-off will be omitted. Consequently, no extensive up-heave will occur (such as presented in figure 5.12) and calculation will proceed a little faster (9% computational time decrease is observed).

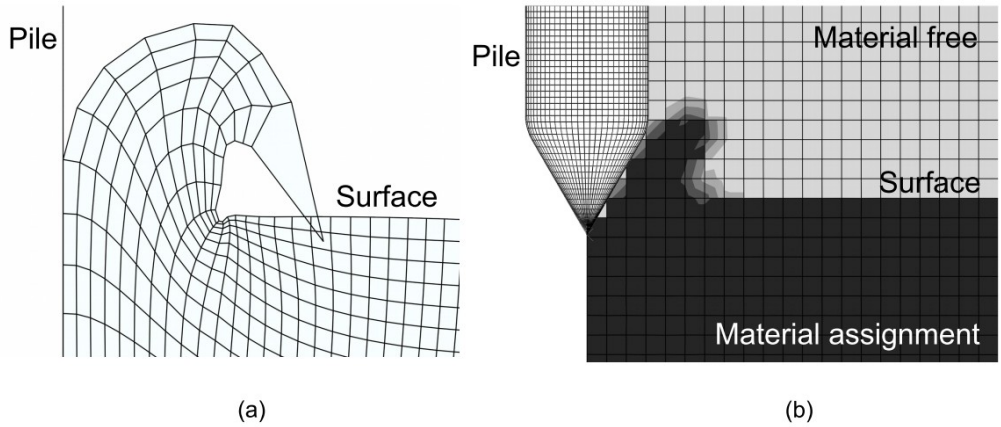

Figure 5.12. Unnatural soil up-heave induced by specification of tension cut-off in (a) ALE and (b) CEL model

5.2.2.5 Boundary effects

The reduction of the soil domain width may be desirable due to decrease of total number of elements and reduction of computational time. The three soil domain widths of dimensions of 10, 20 and 30 pile diameters has been investigated. The radial total stress increase at the boundary for 10, 20 and 30 pile diameter domain wide are 13%, 3% and 1%, respectively. The boundary effects in the range of 10% can still be acceptable for proper estimation of toe and shaft resistance as they do not influence the radial stresses generated near the pile wall. The vertical dimensions of the soil domain fixed at 60D provide a minimal stress change registered at the bottom of soil domain, so assumed dimensions are defined correctly. Summarizing, the soil domain of 20 pile diameter width is a suitable choice which enables safe calculation with minimized influence of boundary effects.

5.2.2.6 Pile diameter (roundings) effects

The only effect of pile diameter should be related to the different roundings between the toe and the shaft and the toe and the guiding tube. As it was explained in section 5.2.1.1 the roundings provide better flow of soil around the pile, but they are designed according to experience or “trials and errors” method, especially in UL formulation. However, those rundings (see figure 5.5 for instance) increase the pile toe conical area. The total pile resistance can be divided into contact pressure and frictional pressure. The increase in toe conical area does not influence the contact pressure but it increases frictional pressure (due to increased surface of friction). While this “roundings effect” is less important in large diameter piles, it can influence the calculation of toe resistance of small diameter piles. The pressure and frictional components of total toe resistance for pile diameters of 0,1m, 0,2m, 0,5m, and

0,8m in terms of ALE formulation are presented in figure 5.13. The toe resistance due to contact pressure is almost the same in all tested piles, but the significant differences can be observed in fictional part of pressure acting on pile toe. While differences in frictional pressure for large diameters piles are quite small (around 20kPa), the differences between small and large diameter piles are significant (up to 80kPa). This is direct consequence of using the same roundings radii between the toe and shaft and between toe and tube, which results in increased conical toe surface where friction acts.

Summarizing, the use of the same roundings irrespective of pile diameter influence the calculated toe resistance. They can have visible impact on pile toe resistance, but this influence is usually negligible in large diameter pile or when the frictional component of toe resistance is very small. In small diameter piles and when the frictional component of total toe resistance is high, the effects of roundings should be examined and it may be included in pile toe resistance calculation. However, when frictionless behaviour on pile toe is assumed the roundings problem fades. It has been also observed that shaft resistance is not influenced by the pile roundings and the inspection of radial total stresses has shown that pile diameter has no impact on radial total stress change.

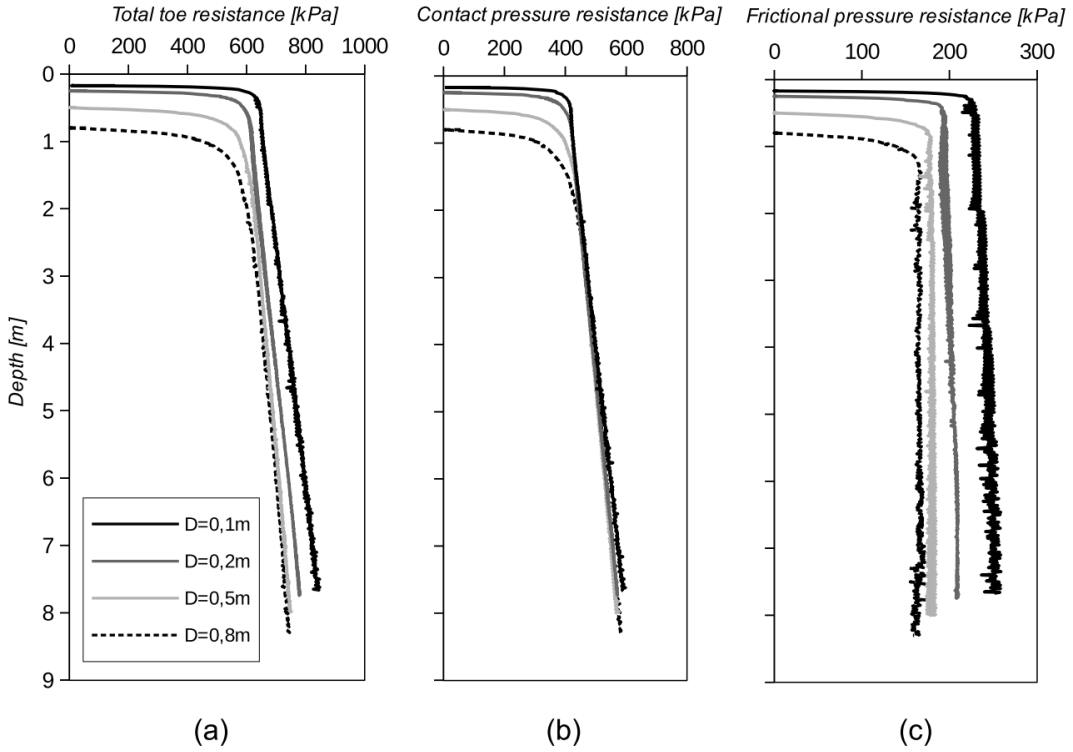

Figure 5.13. Total toe resistance divided into contact pressure and frictional pressure

5.2.3 Sensitivity studies

After establishing numerical models in section 5.2.2, the different factors influencing the solution can be recognised and their impact on radial stresses can be measured. The ALE

model is chosen for parametric study due to its computational efficiency. The investigated parameters include friction behaviour, elastic response of soil domain and initial stress state. In all presented cases total energy error does not exceed 1%.

5.2.3.1 Frictional behaviour on pile-soil interface

Behaviour of pile-soil interface is the most influential parameter that intuitively should affect numerical solution. As it has been explained in previous chapters, the Coulomb law of friction is used to describe pile-soil interface behaviour. The 2,5x2,5 mesh size is applied in order to model the friction behaviour more accurately. The first investigated problem is the toe and shaft dependency in friction terms. In figure 5.14, the frictionless toe and shaft have been compared with frictionless toe and friction shaft. As one can notice, friction conditions on the pile shaft does not influence the resistance mobilized on the pile toe.

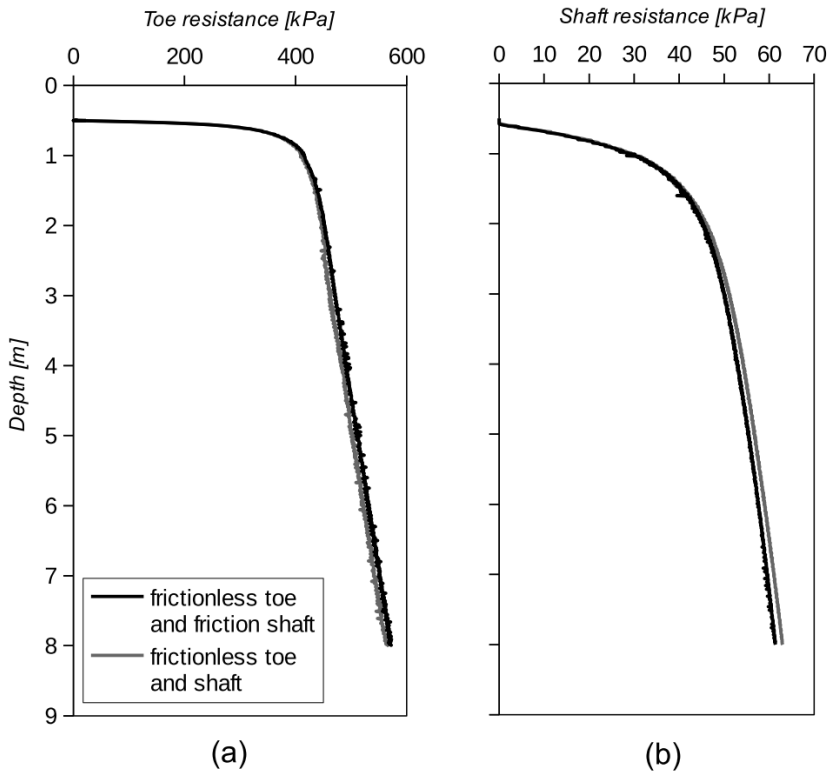

Figure 5.14. (a) Toe and (b) shaft friction independence behaviour

The results of parametric study concerning the influence friction coefficient using the five different values are presented in table 5.4. The friction coefficient impact on pile toe and shaft resistances is shown in figure 5.15. The toe resistance reaches its maximum values with angle of interface friction equal to the 0,6 of the angle of internal friction. Further increase of friction coefficient does not improve the toe resistance. Friction coefficient effect on the pile shaft is however quite different. Slow increase in shaft resistance is observed with increasing friction coefficient and $\delta=\phi'$ can be accepted as the limit angle of interface friction corresponding to the highest shaft friction.

Table 5.4. Friction coefficients used in sensitivity tests

Friction coefficient μ -	*Corresponding angle of friction δ* °	*δ/ϕ' ratio** -
0,000	*0,0*	*0*
0,114	*6,5*	*0,30*
0,231	*13,0*	*0,60*
0,354	*19,5*	*0,90*
0,488	*26,0*	*1,20*

*Effective angle of internal friction $\phi'=21,5°$ is derived from stress ratio M=(6sinϕ ')/(3-sinϕ '), where M=0,835 (see table 5.2)

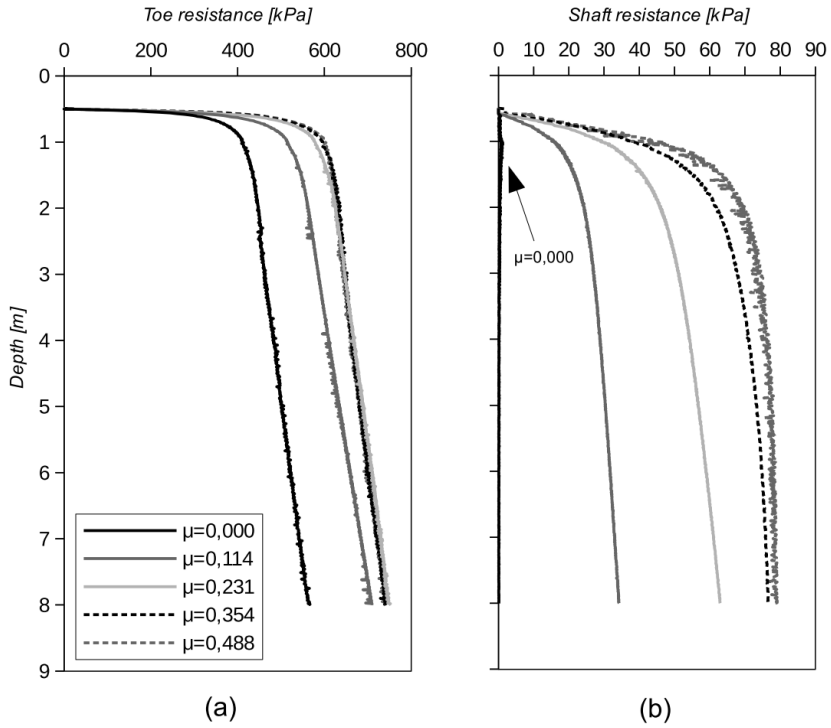

Figure 5.15. Friction influence on pile toe and shaft resistance

The friction influence on shear stress distribution in the pile neighbourhood is presented in figure 5.16 and in figure 5.18. for selected depth. Higher shear stresses are mobilized for higher friction coefficient. The application of friction angle higher than 0,6ϕ' results in shear zone partitioning, see figure 5.16. When shear zones begin to divide, no significantly increase in shaft resistance can be mobilized. The shear stresses distribution near the pile toe is almost the same with friction coefficients equal and higher than 0,231 and this observation is consistent with calculated pile toe resistance. The influence of friction coefficients on radial total stress is presented in figure 5.17 and 5.19. It can be seen that interface friction angle higher than 0,6ϕ' provides similar radial total stress distribution near pile toe, whereas the influence of friction on the pile shaft is much more visible. The increase in radial total stress is much higher with lower friction coefficient, especially at small depths, see figure 5.19. It is

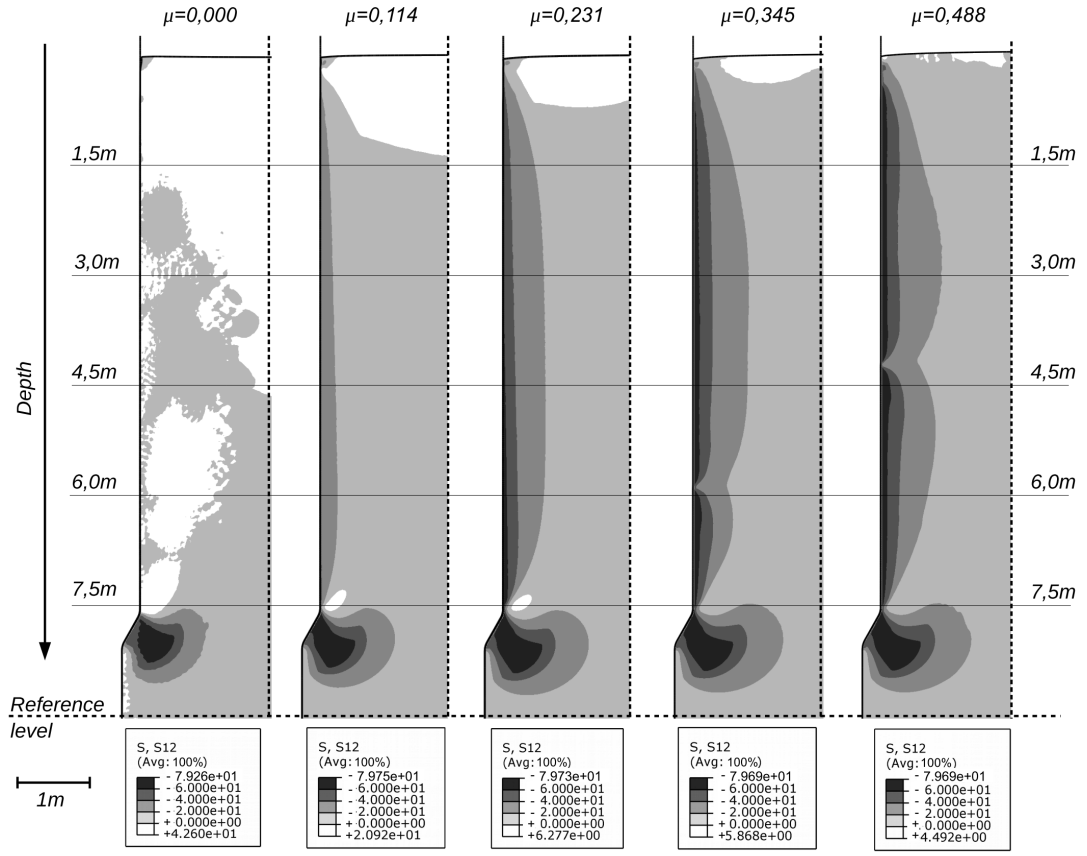

Figure 5.16. Shear stress maps due to different friction behaviour

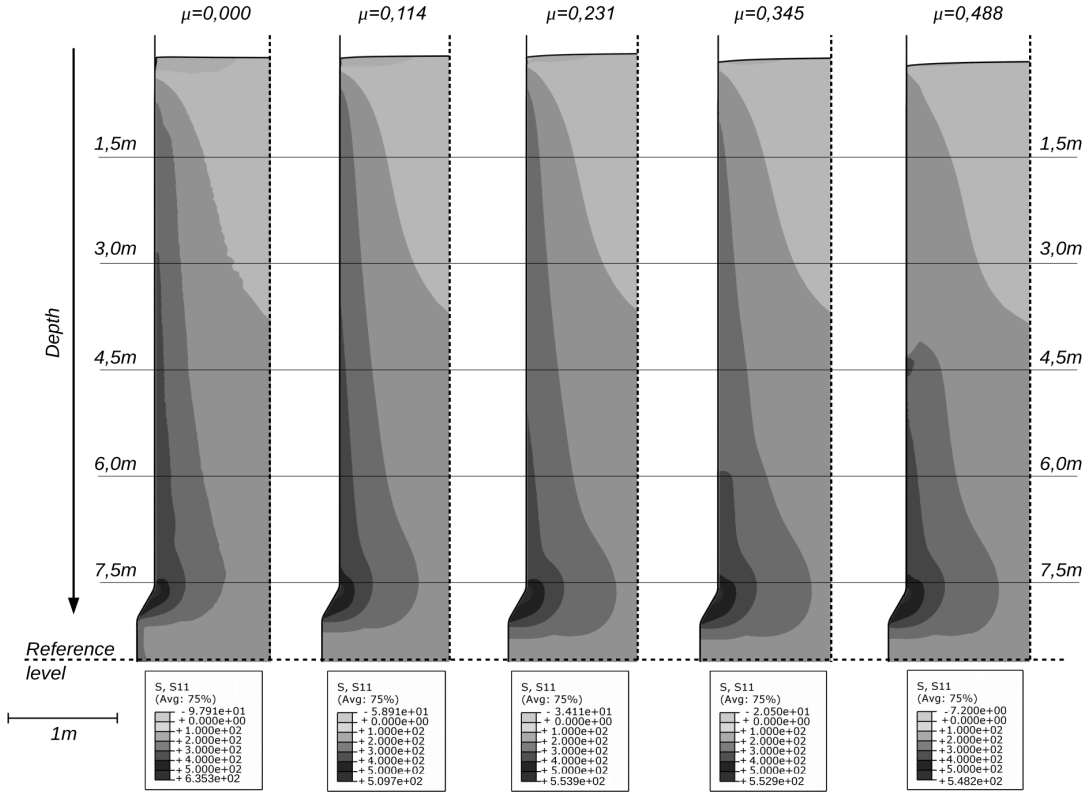

Figure 5.17. Radial total stress map due to different fiction behaviour on pile-soil interface

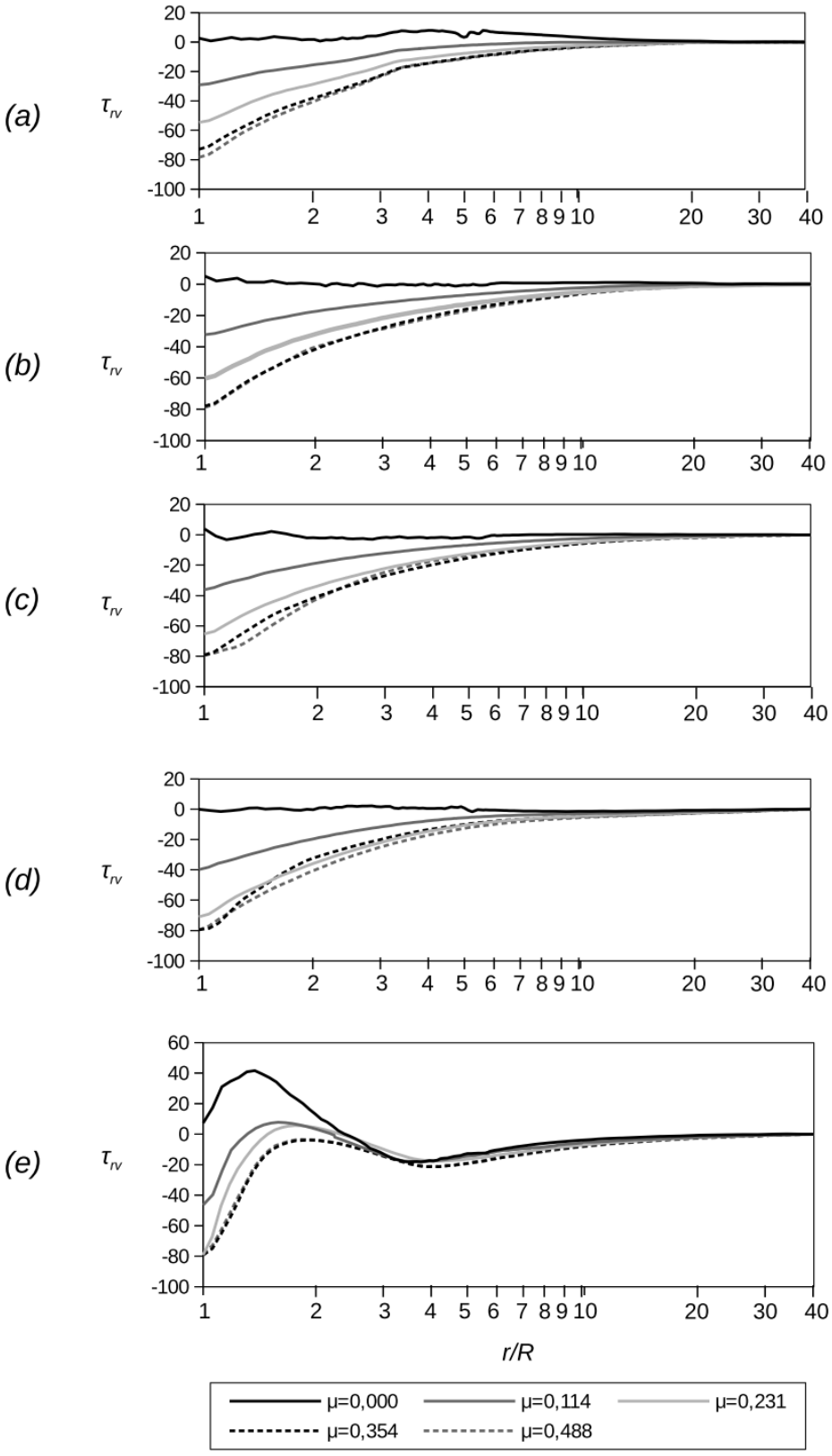

Figure 5.18. Shear stress distribution for (a) 1,5m; (b) 3,0m; (c) 4,5m; (d) 6,0m; (e) 7,5m depth due to different friction conditions

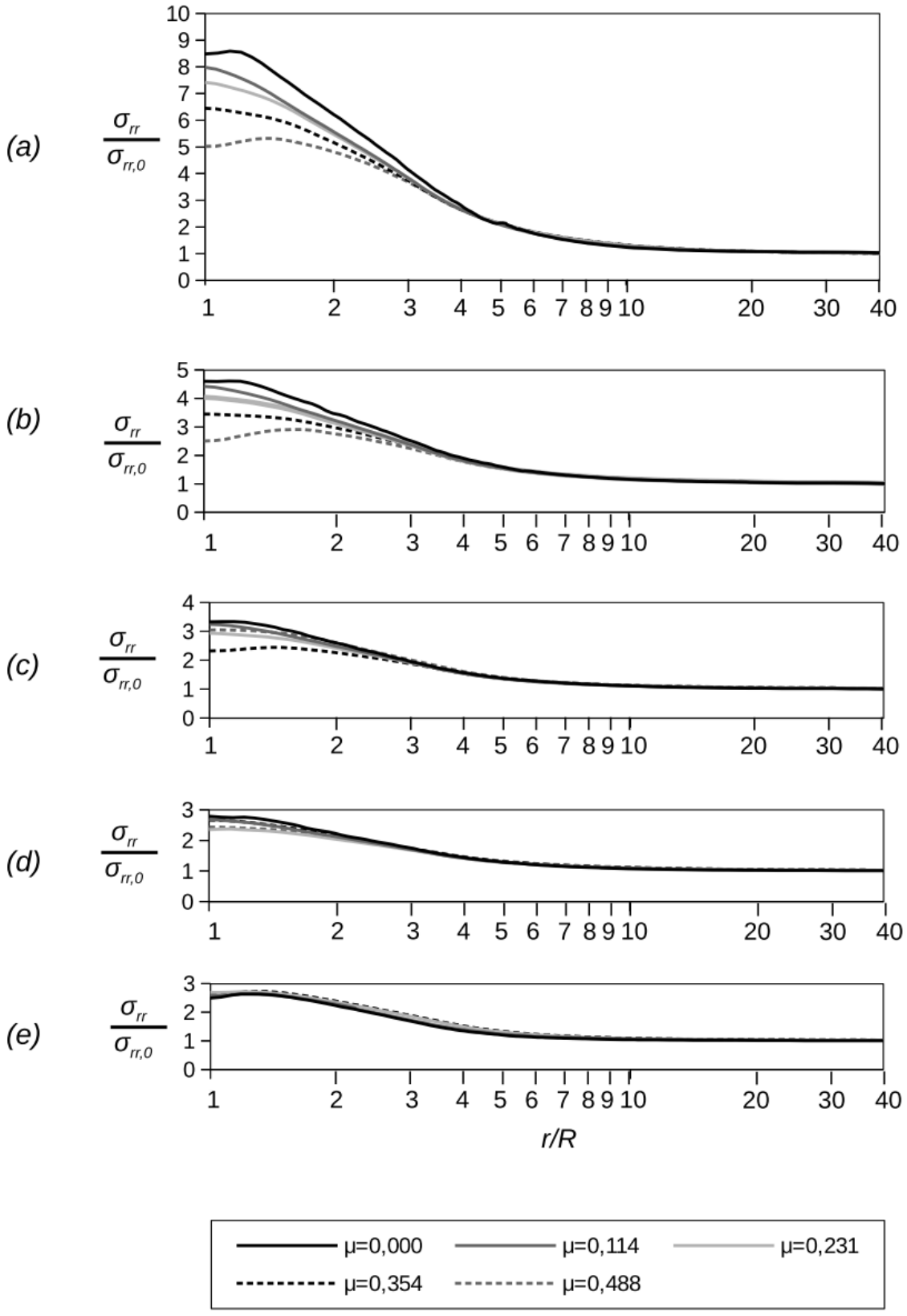

Figure 5.19. Normalized radial total stress for (a) 1,5m; (b) 3,0; (c) 4,5m; (d) 6,0m; (e) 7,5m depth

consistent with the theoretical background, because the increase in shear stress due to friction induces the decrease other stress components to fulfil the same material strength limits. The force required to install the pile on design depth increases with firction. Consequently, the large soil mass is also pushed downward and smaller radial stress are generated. If frictionless behaviour is applied, then all soil is pushed outward the pile wall and vertical movement are much smaller. Thus, the largest radial stress are generated.

The increase in radial total stresses along the pile shaft is presented in figure 5.20. The largest increase in radial total stress has been involved by the frictionless contact. The observed jumps are related to the partition of shear zone when higher coefficients of friction are applied, see figure 5.16.

Besides the ALE model, the friction coefficient fixed as 0,231 was also tested in CEL formulation. Here, pile shaft resistance was 20% lower than ALE solution. This is a consequence of total radial stress underestimation presented previously in section 5.2.2., figure 5.7.

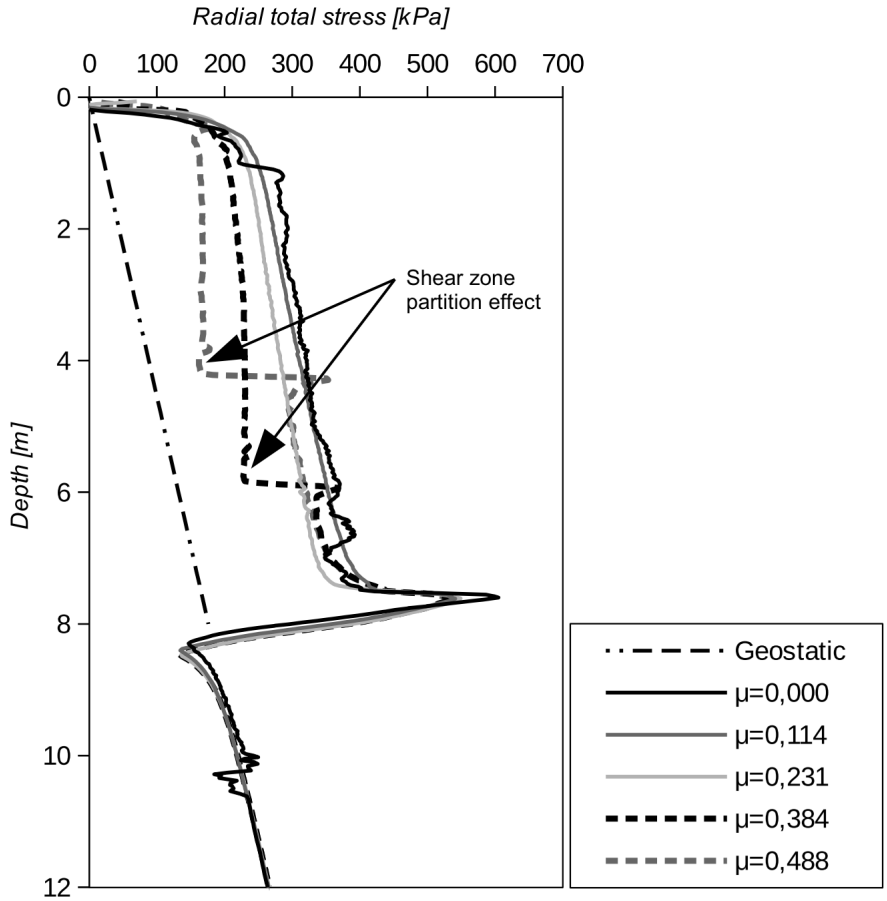

Figure 5.20. Radial total stress after pile jacking due to different friction behaviour on pile-soil interface

5.2.3.2 G/c_u ratio influence

The undrained shear strength of soil clearly influences numerically calculated pile resistance (e.g., Sheng et al., 2013). The influence of undrained elastic modulus will be investigated in this section. The five undrained elastic modulus E_u equal to 1250kPa,

2500kPa, 5000kPa, 10000kPa and 20000kPa were tested, which corresponds to the G/c_u ratio of 5,24; 10,49; 20,97; 41,95; 83,89, respectively. In all cases the G/c_u ratio is relatively small, which is in agreement with the large strain problem (e.g., Vardanega and Bolton, 2013). The pile toe resistances due to different undrained elastic moduli are plotted in figure 5.21 (the shaft resistance is omitted due to frictionless behaviour). The elastic properties influence on pile toe resistance is undeniable. When the plastic zone around the pile is observed, the rest of soil domain is in elastic state and its higher stiffness results in higher pile toe resistance. Similar observation has been noticed by Van Den Berg (1994) who model the cone penetration in clay with ALE. This observation has far reaching consequences as soil shear modulus is strain dependent. The logarithmic shear strains distributions at five levels are plotted in figure 5.22. As can be seen, in all cases the large strains (larger than 5%) are generated at normalized distance *R/r* of 4 and lower. As the soil is strain dependent material, the reliable solutions are limited to the close shaft area where large strains would be involved. Consequently, this area is generally considered as an objective of studies where reliable results can be provided.

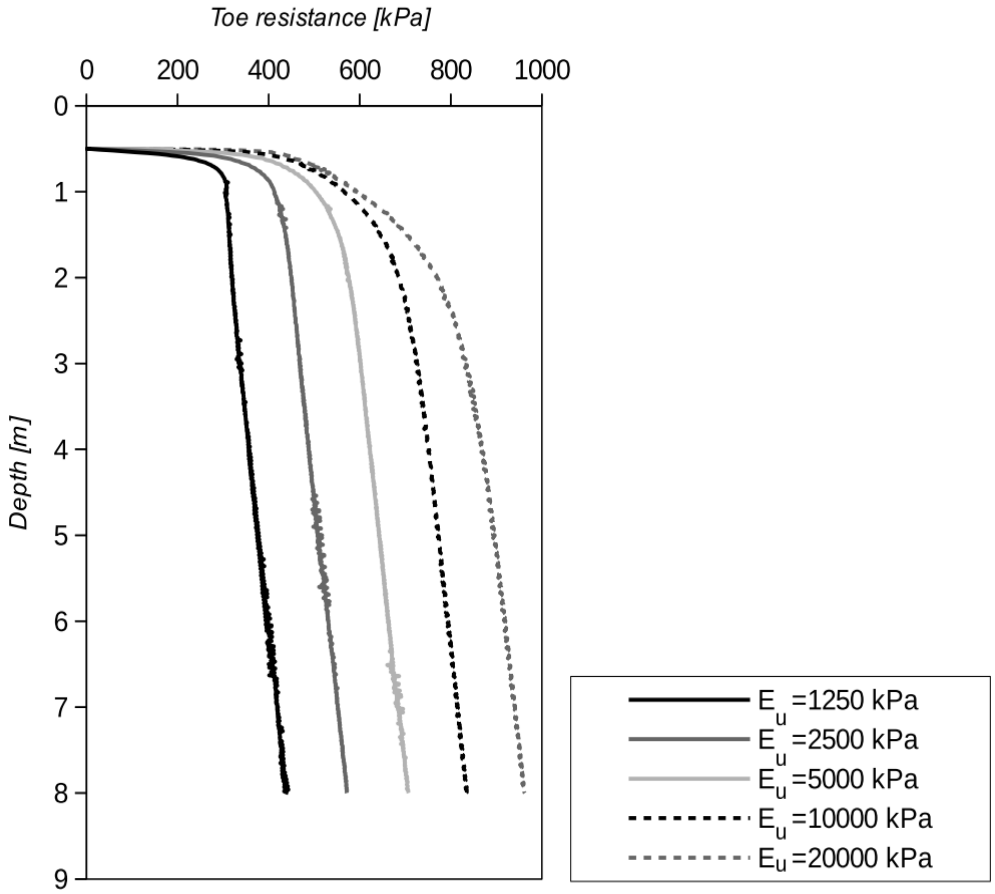

Figure 5.21. Toe resistance due to different undrained elastic modulus

The shear stress generated due to jacking process in the soil characterized by different elastic moduli are presented in figure 5.23 (stress map). The negligible shear stress remains near the pile shaft at the end of jacking, but when the pile toe penetration had proceed the large shear

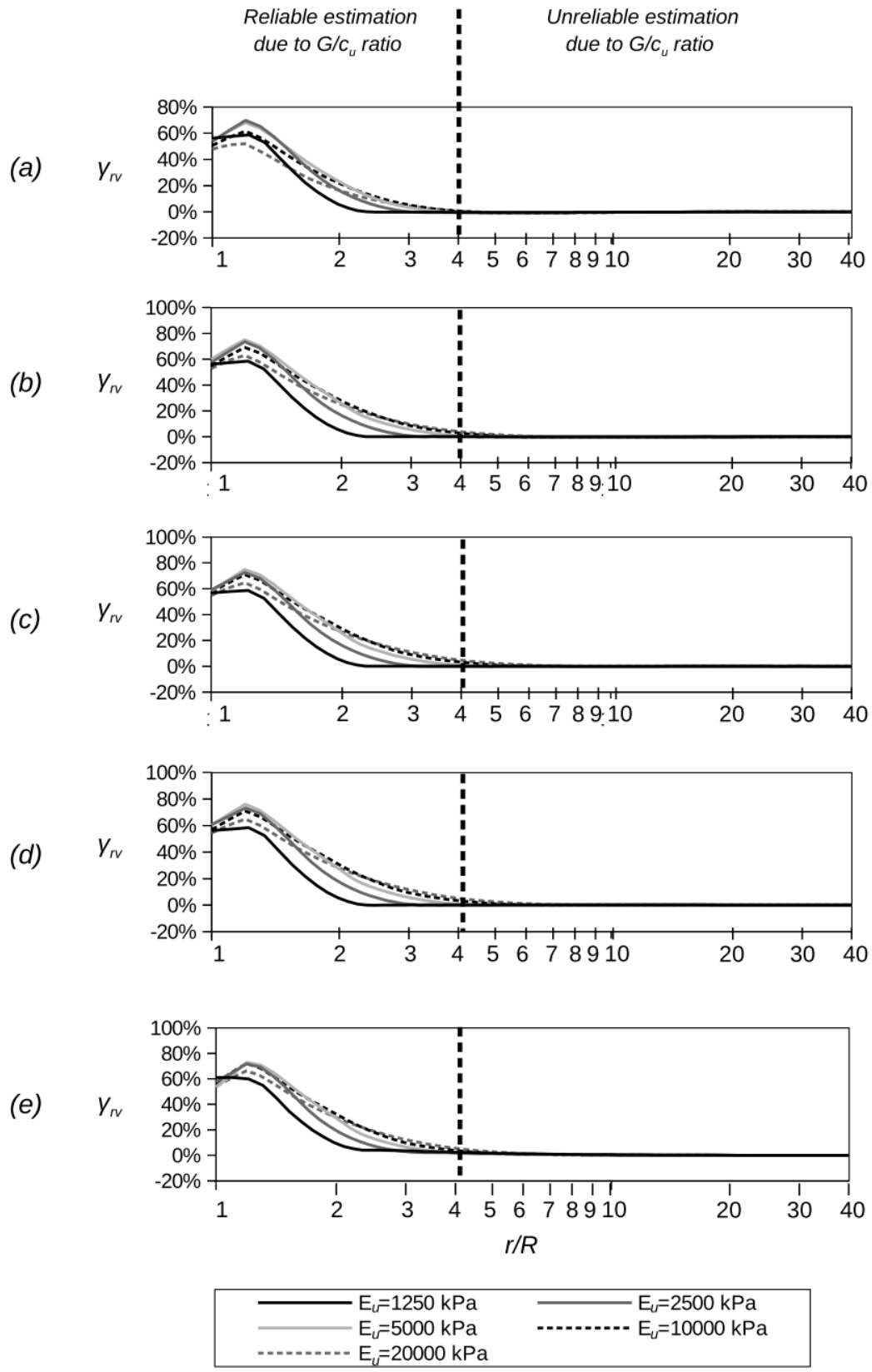

Figure 5.22. Shear strain development at (a) 1,5m; (b) 3,0m; (c) 4,5m; (d) 6,0m and (e) 7,5m depth

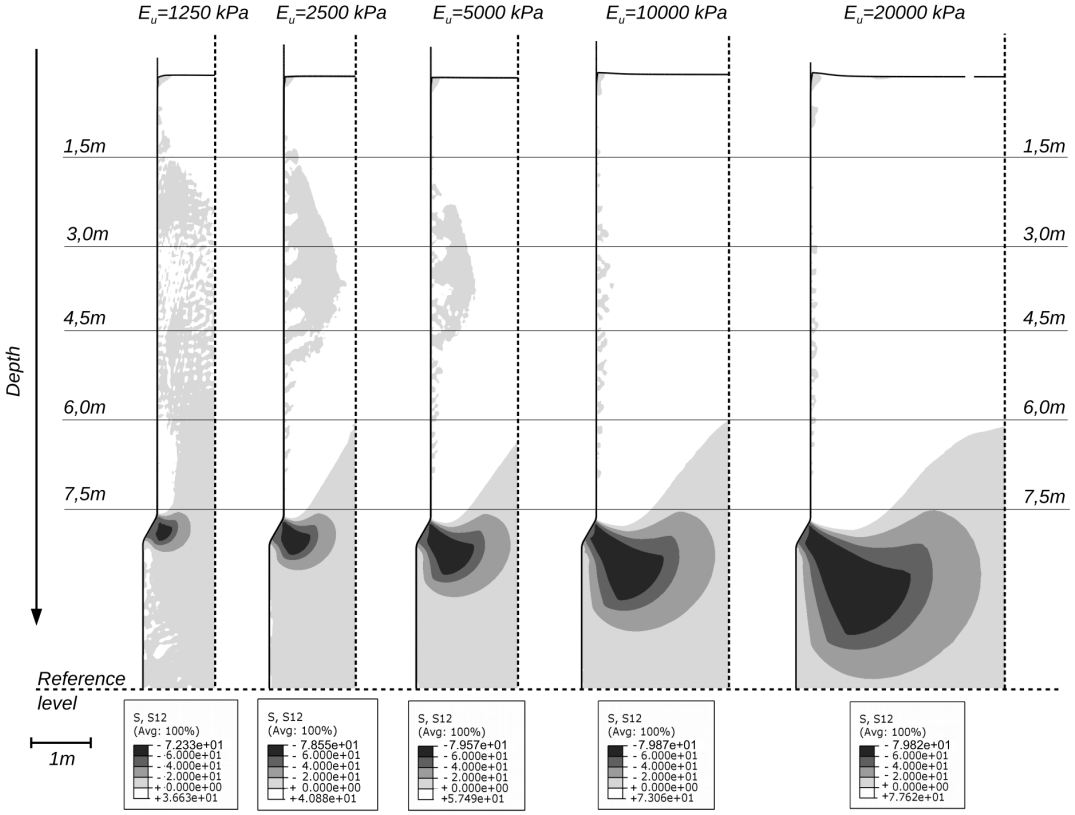

Figure 5.23. Shear stress distribution due to different undrained elastic modulus

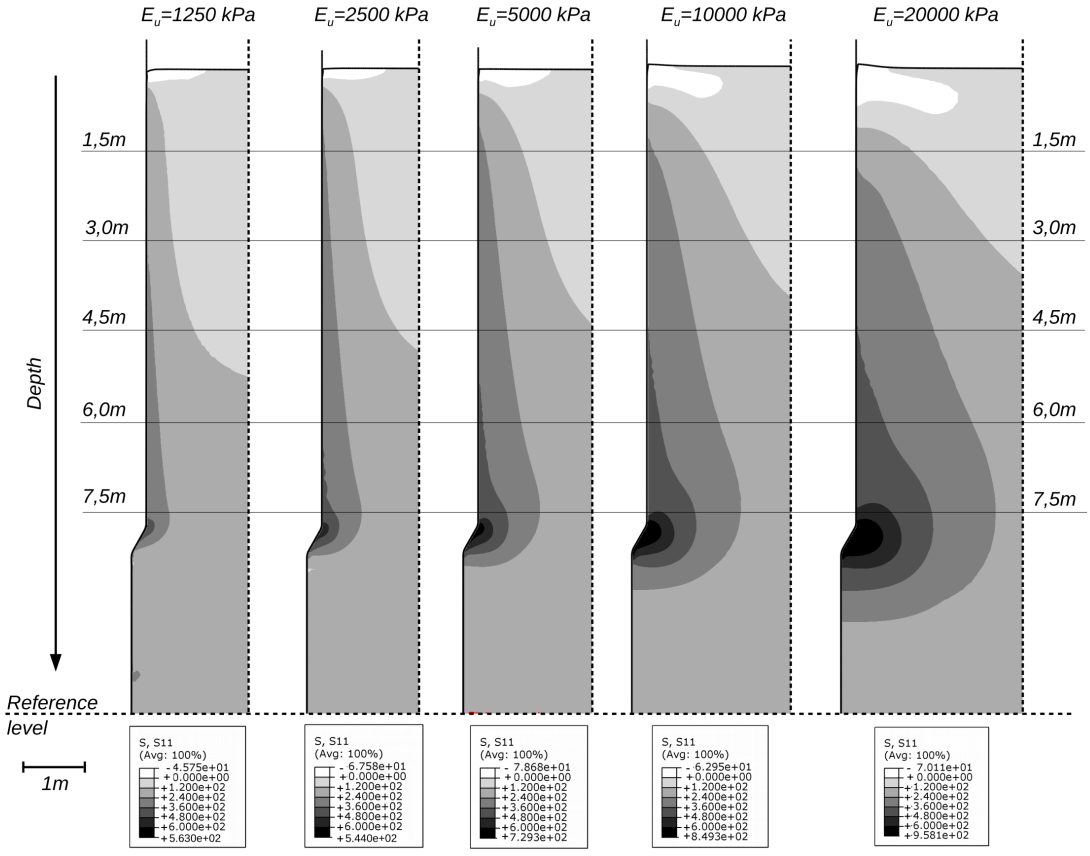

Figure 5.24. Radial total stress distribution due to different undrained shear modulus

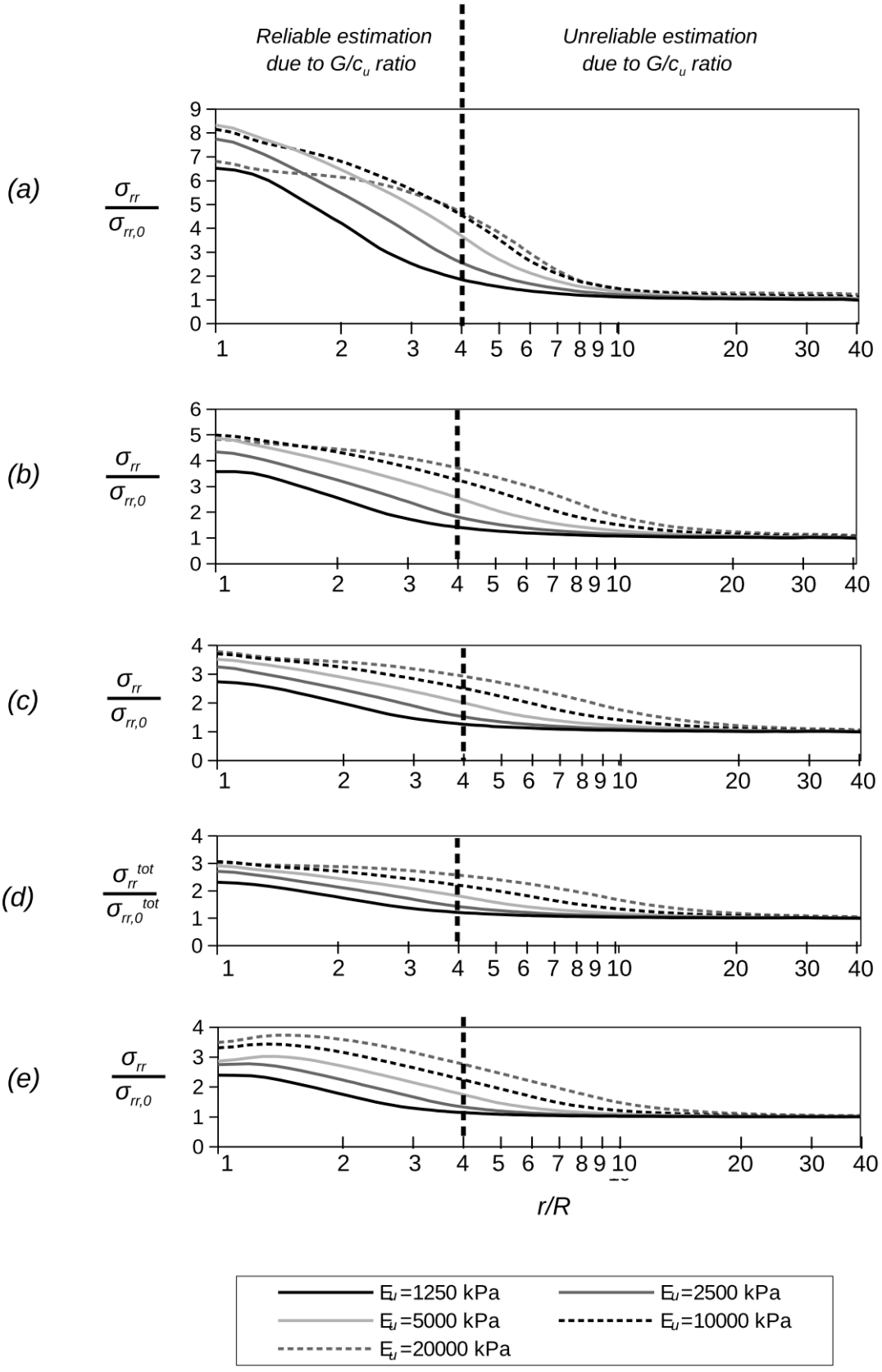

Figure 5.25. Normalized radial total stress at (a) 1,5m; (b) 3,0m; (c) 4,5m; (d) 6,0m and (e) 7,5m depth

strains have been developed near the pile toe, see figure 5.22. With different values of undrained elastic modulus the different ranges of mobilized shear stresses under pile toe can be observed as it is presented in figure 5.23. As one can see, the increase of the zone with higher shear stress results in higher mobilization of pile toe resistance. Hence, elastic modulus becomes governing factor in the pile toe resistance estimation with FEM.

The normalized radial stress distribution at 5 different depths is shown in figure 5.25 and they are also marked in figure 5.24 where the horizontal total stresses acting near the pile shaft area are presented. It can be noticed that with increasing elastic modulus, the area of increased radial stresses becomes wider from 4 pile radii when E_u=1250kPa to approximately 20 pile radii when E_u=20000kPa. This observation is also consistent with the previous studies (e.g., Randolph et al., 1979a). The radial total stress distribution due to higher undrained elastic modulus can result in boundary effects, but the generated differences in terms of normal stress at the boundary are still relatively small (up to 10%) and, based on boundary effects examination in section 5.2.2.5., the boundary impact in pile shaft area can be neglected.

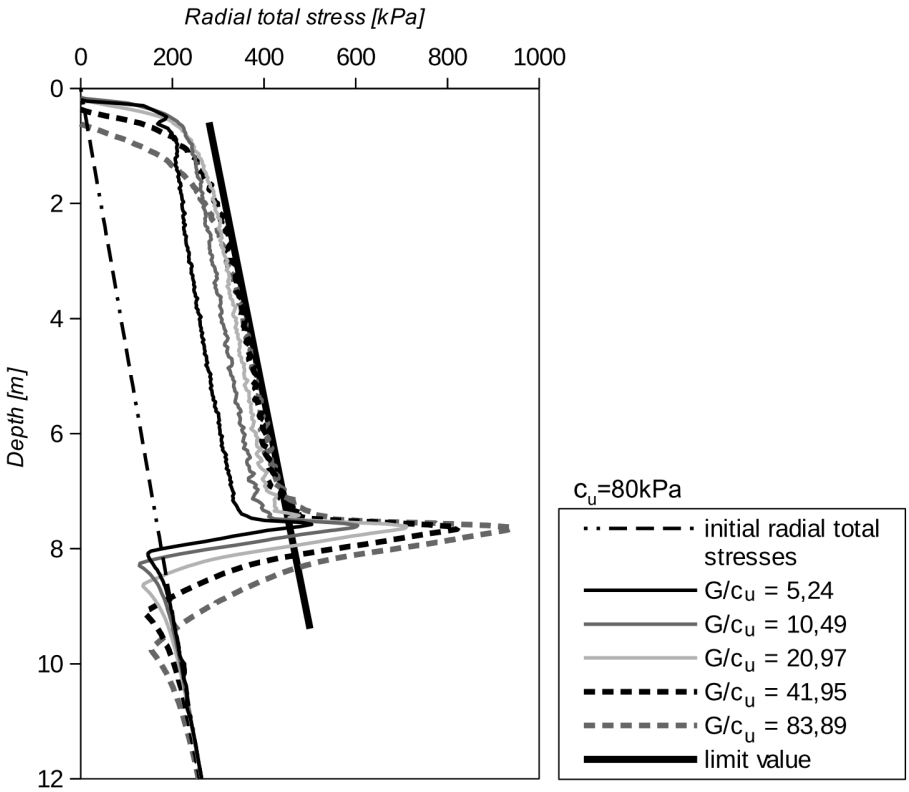

Figure 5.26. Radial total stress distribution along the pile shaft after jacking due to different G/c_u ratio

As the main objective of this thesis is the installation effects investigation and the radial stress changes in particular, the increase in radial total stress along the pile shaft is presented in figure 5.26. No significant increase in stresses on the pile shaft is observed when G/c_u ratio exceeds 40. The other observation is that around the pile toe and near the ground surface level

the significant disturbance in radial total stresses is noticed.

Sensitivity tests performed in this section show that application of appropriative elastic modulus is crucial for the cone resistance. Hence, very careful estimation of this parameter should be made to get accurate results. However, this note is not applicable to the pile shaft when G/c_u ratio is higher then 40 as it returns almost the same radial total stress increase in all tested cases. Generally speaking, soil undergoes failure at relatively steady strain values which implies constant G/c_u ratio with prescribed c_u for the same soil type. For instance, in clays the average G/c_u is 500 (Hara et al., 1974) and it is decreasing 5-10 times when large strain occurs (e.g, Vardanega and Bolton, 2013). Hence the typical G/c_u ratio for large strain problem is within 50-100. As no significant increase in radial total stress has been observed when G/c_u exceeds 40, the G/c_u equal to 50 will be assumed in tests performed in chapter 8.

5.2.3.3 Initial stress state influence

As it has been explained in section 3.2.3, in total stress analysis the ratio between horizontal total stress and vertical total stress is used as an initial condition. Herein, the influence of this ratio will be investigated. As the material properties of soil will rest the same, the ratio between horizontal stress and vertical stress has to fulfil the strength condition for applied constitutive law which is the Tresca plasticity (Potts and Zdravković, 1999):

$$\frac{|\sigma_v - \sigma_h|}{2} \leq c_u \tag{5.7}$$

where: σ_v – vertical total stress, σ_h – horizontal total stress, c_u – undrained shear strength.
If this condition is not fulfilled, the initial failure of the material will occur. To avoid this situation, the boundary values of σ_h/σ_v are equal to 0,76 and 1,24 and those initial conditions are tested.

Based on previous research the initial stress state should play a minor role due to soil plastic state around the shaft (Randolph et al., 1979a). The radial total stress increase is presented in figure 5.27. and only slight differences can be observed. Hence, the σ_h/σ_v ratio has low and rather predictable effect on radial total stress increase. As total stress approach is used here, the verification of initial state will be checked in section 5.4.2., where the effective stress approach is used.

5.2.4 Compatibility study between ALE and UL models

The compatibility between ALE and UL formulations as well as between total and effective stress analysis has been shown in section 5.2.2. In section 5.2.3. the factors affecting the total stress approach were recognised and here, the same factors will be verified by effective stress analysis. In all tests the total energy error does not exceed 1%.

5.2.4.1 Shaft friction compatibility

Incorporating the friction behaviour in UL formulation presents significant difficulties. Firstly, the friction interface on pile toe results in convergence problems that has been also

encountered by Sheng et al. (Sheng et al., 2009, 2014). Consequently the only possibility is to model friction on the pile shaft. Here however, the solution is strongly influenced by friction coefficient, coefficient of permeability and mesh size. Many "trial and errors" studies have been performed to find the most accurate UL model in comparison to referential ALE solution. As a result, the mesh size 0,5x1,0cm is chosen, the friction condition on the pile shaft is exactly the same as in ALE model (μ=0,231) and coefficient of permeability is fixed as 10^{-7}m/s. As it will be shown later, even such small value of soil permeability allows for some consolidation during pile jacking.

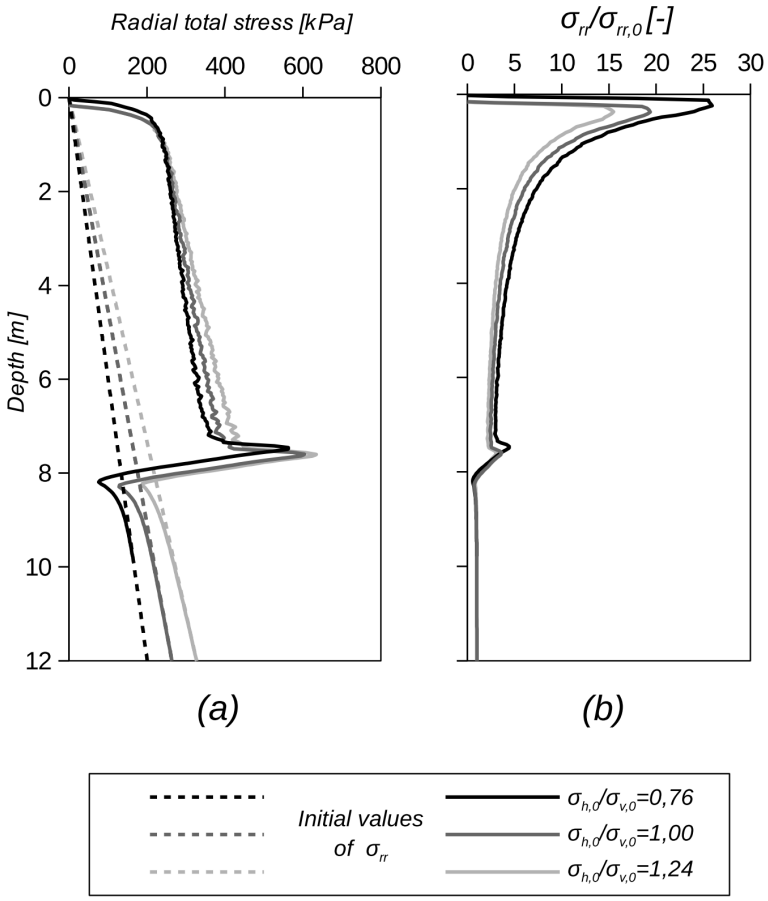

Figure 5.27. Initial stress state influence on radial total stress after installation phase

The application of friction behaviour on the pile shaft with higher friction coefficients results in convergence problem and the author's research reveals the limit value of friction interface angle δ as 0,5ϕ'. The calculation trials with friction coefficients of μ=0,354 (δ=0,75ϕ') and μ=0,488 (δ=ϕ') has ended after jacking to the depth of 0,8m, which is generally consistent with other research (e.g, Sheng et al., 2009). The comparison between toe and shaft resistances obtained with UL and ALE formulations is presented in figure 5.28a and 5.28b, respectively. As can be seen, consistent results are reached. However, the radial total stress distribution is not so satisfactory and the differences up to 15% are found, see figure 5.28c. The investigation of the shear stresses, see figure 5.28d shows almost the same response of the soil structure in both models. Figure 5.29 shows the radial total stress, radial effective

stress, pore water pressures and void ratio distributions along the pile shaft when friction and frictionless interaction is used. The results are compared with CEM method. It can be seen that no change in effective stress is observed with increasing friction coefficient. However, the change in generated pore water pressures is noticed, but it can be related to the initiated consolidation process, see figure 5.29d where a decrease of void ratio is shown. Laboratory observations (e.g., Eid et al., 2014; Tsubakihara and Kishida, 1993) and numerical studies (e.g., Bayoumi et al., 2008) on interface behaviour show that increasing roughness, and consequently friction coefficient of the interface, results in higher pore water pressure generation and lower effective stresses. Although the same mechanism is observed here, the effective stress analysis shows considerably minor influence of roughness in this process, probably due to partial consolidation. It can be also induced by mesh distortions and inadequate work of finite elements (possibility of such problem was briefly reported in section 4.1.2). The decrease in radial total stress due to frictional shaft in UL formulation is similar to the ALE solution, but much lower differences can be observed.

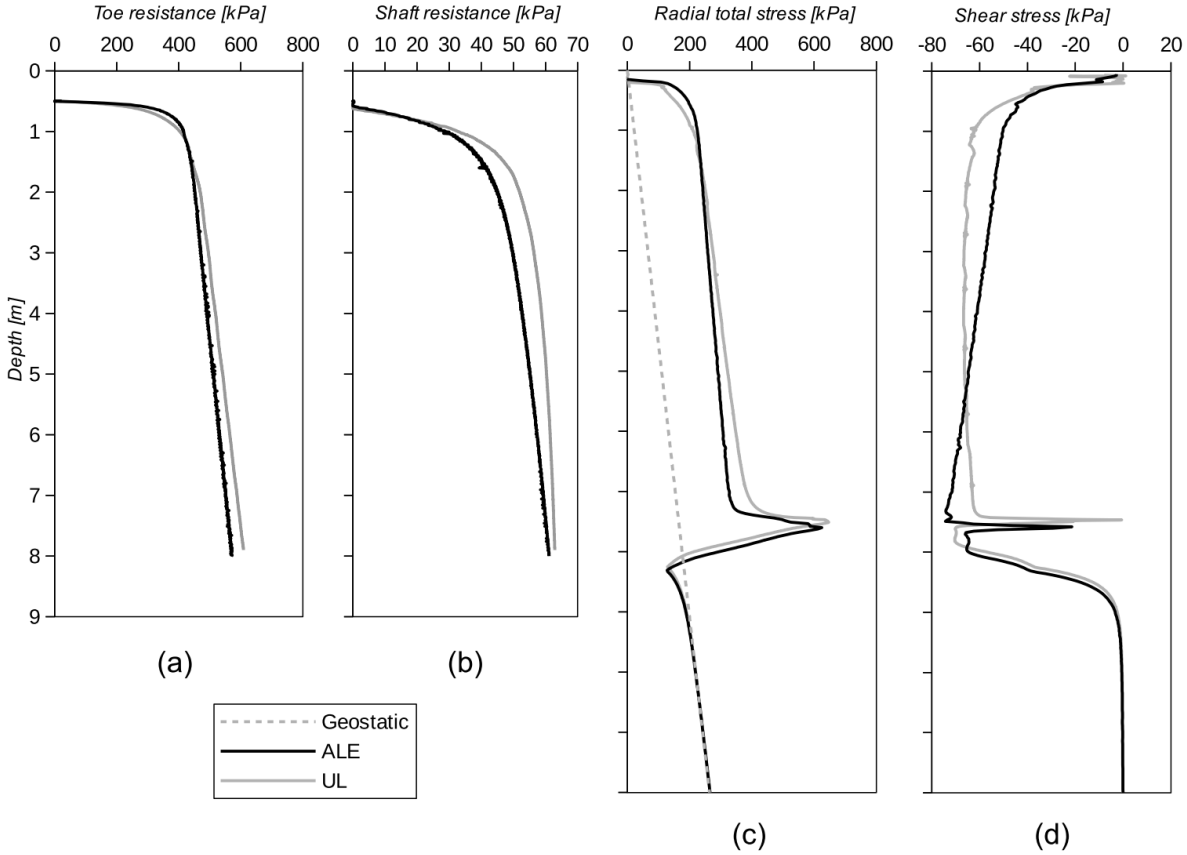

Figure 5.28. ALE versus UL in terms of (a) toe resistance, (b) shaft resistance, (c) radial total stress and (d) shear stress

Summing up, the validation of the friction influence on the radial total stress distribution along the pile shaft is hampered. The reasons of such behaviour are ambiguous and they may be referred to proper element choice or the mesh distortion in UL formulation. Due to lack of proper evaluation and convergence problems with higher friction coefficients (higher than

μ=0,231), only frictionless interface behaviour will be used in studies presented in chapter 8. However, the friction behaviour in UL still enables the proper estimation of shaft resistances when the calculation will proceed which will be shown in chapters 6 and 7.

5.2.4.2 G/c_u compatibility

The compatibility between UL and ALE in terms of G/c_u is verified for four values: 10,49; 20,97; 41,95; 83,89 which corresponds to the E_u of 2500kPa, 5000kPa, 10000kPa and 20000kPa, respectively. The frictionless interface is used and the material properties are the same as in UL models in section 5.2.2 except the shear modulus values. The radial total stress distribution is presented in figure 5.30 and almost the same response of the system was achieve as in ALE model. Hence, the G/c_u compatibility is conserved.

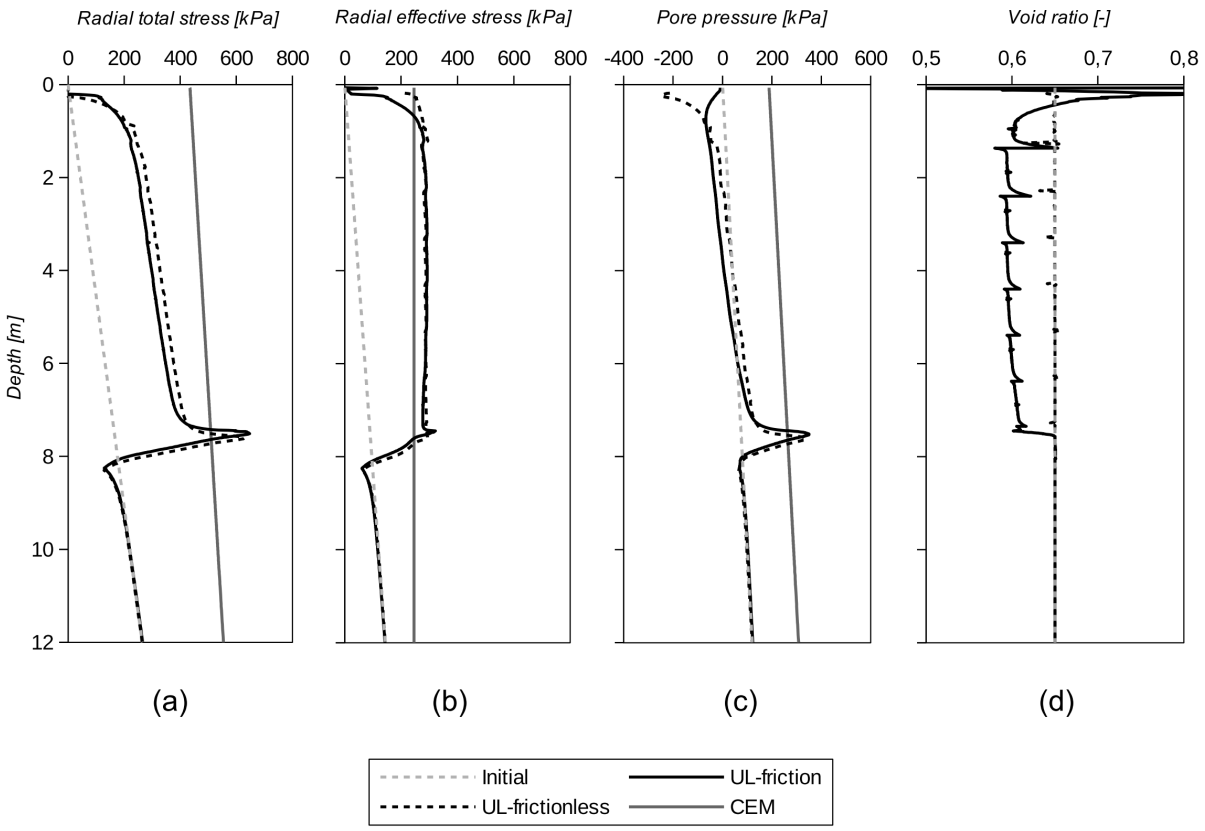

Figure 5.29. (a) Radial total stress, (b) Radial effective stress, (c) Pore water pressure and (d) void ratio in UL formulation due to different shaft friction behaviour

5.2.4.3 Initial stress state compatibility

Initial stress state in effective stress analysis is related to the initial total stress state presented in section 5.2.3.3. The assumptions and derivation of σ_h/σ_v ratio in effective and total stress approaches has been presented in chapter 3 section 3.2.6. Based on equation (3.37) the σ_h/σ_v ratio equal to 0,76 and 1,24 corresponds to the K_0 equal to 0,56 and 1,44, respectively. The increase in radial total stress due to lateral earth pressure et rest coefficient is presented in figure 5.31a. The slight influence of initial stress state is recognised as in

referential ALE models. The comparison between σ_h/σ_v ratio obtained in UL and ALE models is shown in figure 5.31b. The agreement between ALE and UL is satisfactory along the pile shaft in depth range from ~1m to ~7m. In the surface area the differences are more significant, but as it has been mentioned before, this region is difficult to analyse and it is omitted in this thesis.

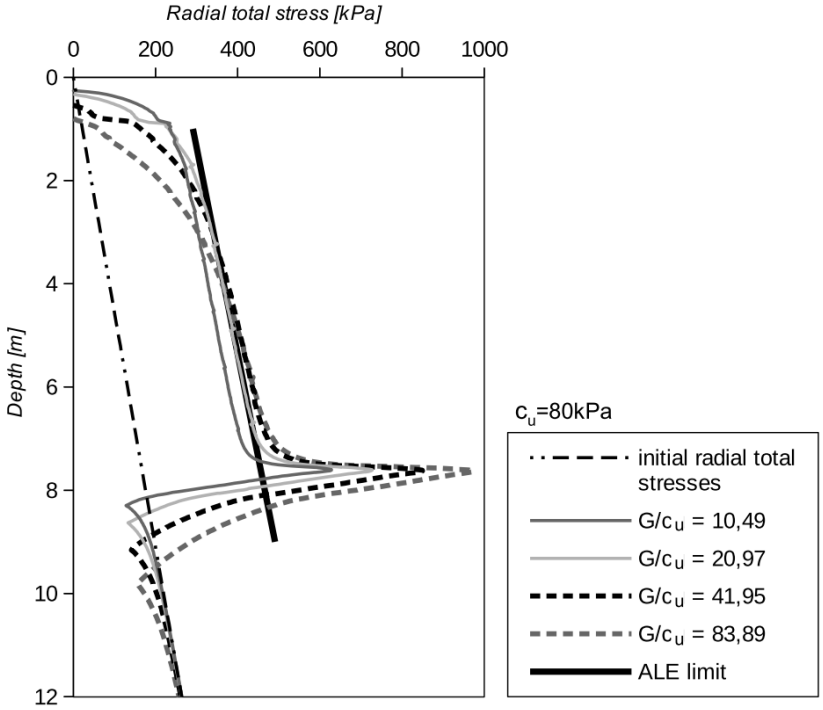

Figure 5.30. ALE and UL compatibility in terms of G/c_u ratio

5.2.5 Dissipation Tests in UL formulation

5.2.5.1 Pore water pressure "overshoot"

Pore water pressure "overshoot" can provide inaccurate pore water pressure distribution along the pile shaft and consequently the underestimated or overestimated values of total stress. The compatibility between ALE and UL shows the similar distribution of total stresses, but during consolidation phase the dissipation of pore water pressures takes place which results in effective stress change. Thus, accurate calculation of the possible "overshoot" is crucial for the accurate effective stress determination after consolidation. To check the pore water pressure overshoot the two different cases have been investigated and they are summarized in table 5.5. In the first variant the pore water pressure should be calculated accurately, because in only small number of increments the stability condition was not fulfilled, while in the second variant, the "overshoot" should certainly appear. It should be noted that coefficient of permeability in the first variant has to be much lower than the real values for clays to satisfy the condition described by equation (4.43), see section 4.2.3. However, the inspection of radial total stress reveals no impact of applied mesh and permeability coefficients, see figure 5.32a. Similar effect can be also observed after

consolidation, see figure 5.32b. Both variants result in almost the same soil response. Solution where pore water pressure "overshoot" should appear is more smooth than accurate solution which provides more noisy results. Hence, the application of Vermeer and Verruijt (1981) condition is not necessary to obtain reliable results. Further, due to "trials and error" method in UL model design it is often impossible to fulfil this condition.

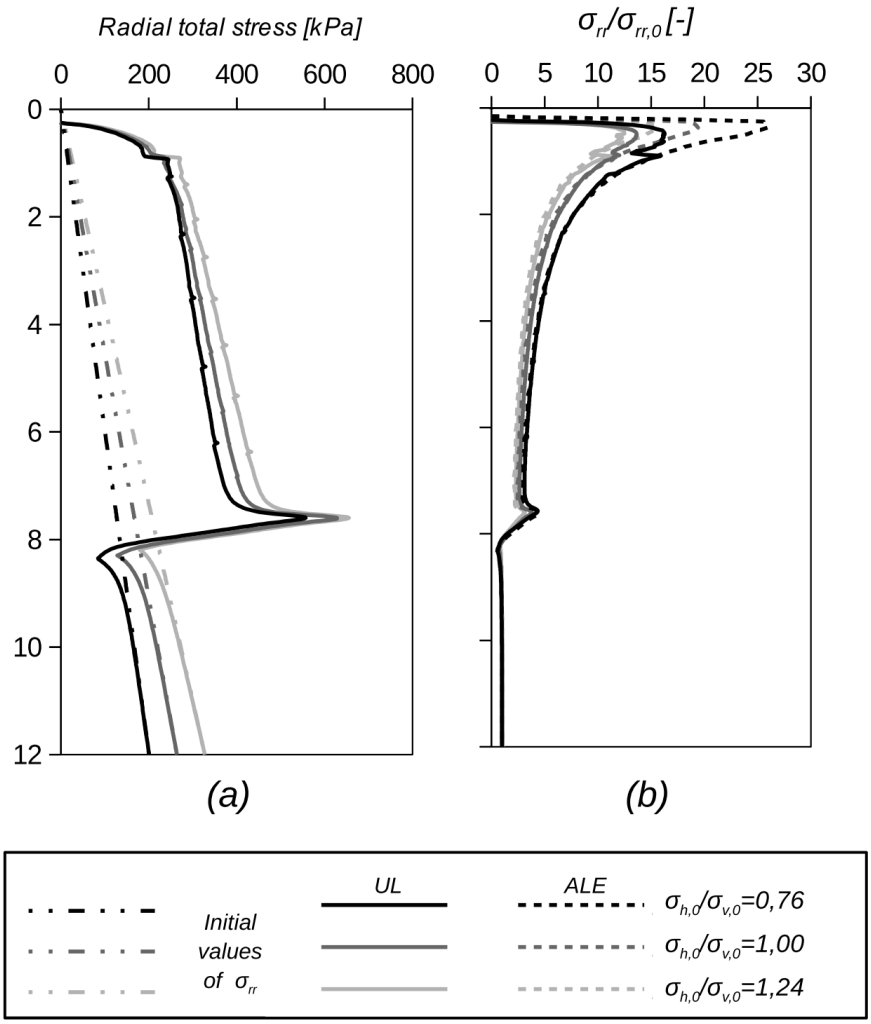

Figure 5.31. Initial stress state compatibility between ALE and UL

The second observation from the presented studies is that the soil permeability hardly influences the results after consolidation. This is intuitively correct as in all cases the same load is transferred on soil, and different soil permeabilities should result only in different consolidation time that is required.

5.2.5.2 Effective stress distributions along pile shaft

The distribution of the radial effective stress after consolidation due to influence of G/c_u ratio and initial stress state are shown in figures 5.33a and 5.33b, respectively. Here, the similar conclusion can be drawn as in sections 5.4.2.2 and 5.4.2.3. The G/c_u ratio higher than

50 does not influence radial total stresses which is significantly visible for depth between 4m to 7m below ground level. The differences in radial effective stresses due to initial stress state are more noticeable after equalization phase and thus, the influence of initial stress state is higher than CEM can predict (Randolph et al., 1979a).

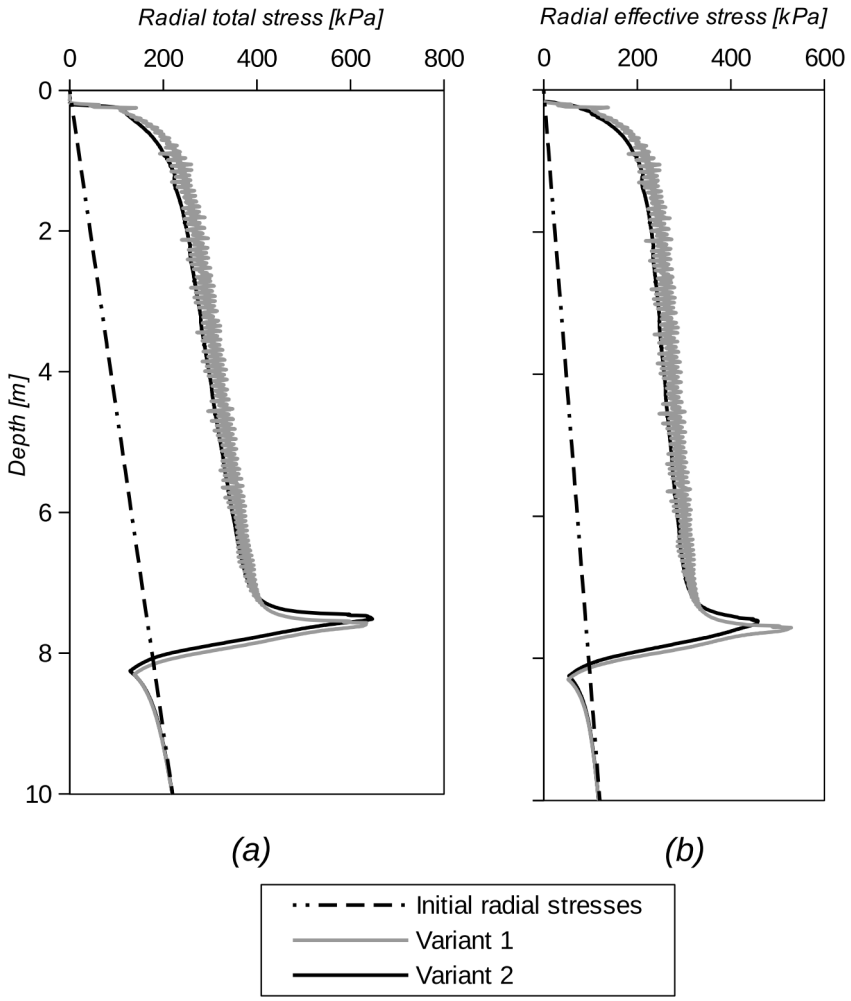

Figure 5.32. (a) Radial total stress after installation and (b) radial effective stress after consolidation distributions calculated with not-expected (variant 1) and expected (variant 2) pore pressure overshoot

Table 5.5. Details of Pore water pressure "overshoot" calculation models

Variant	*1*	*2*
Mesh size	*0,5x1,0cm*	*0,5x1,0cm*
Friction coefficient on pile shaft	*0,231*	*0,231*
Elastic modulus ($E \approx p_0'/\kappa$)	*75÷4425kPa*	*75÷4425kPa*
Permeability coefficient	*10^{-5}m/s*	*10^{-7}m/s*
Minimum usable time increment	*0,00094÷0,05555s*	*0,094÷5,555s*
Increment during calculation	*0,00195÷0,5s*	*0,00001÷0,5s*
Equation (4.43) satisfied per total increment number	*4445/4519*	*0/4266*

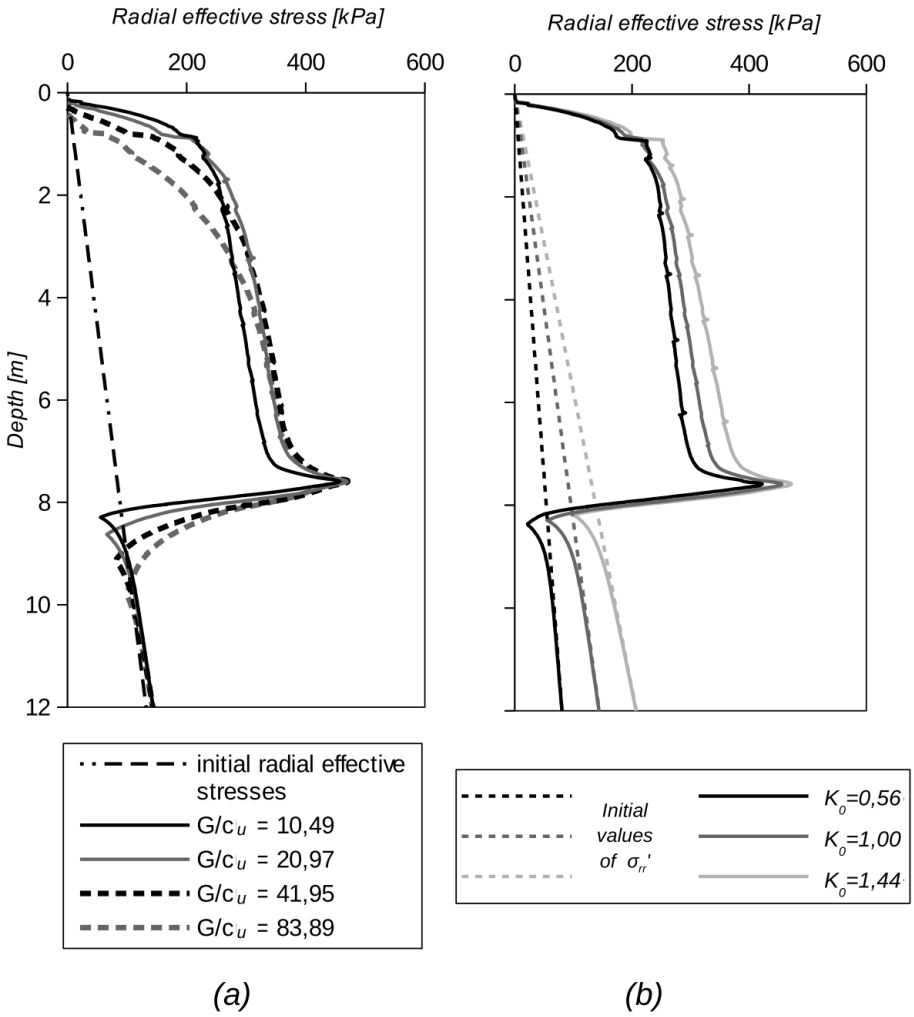

Figure 5.33. Effective stress distribution along the pile shaft due to different G/c_u ratio and K_0

5.3 Findings evaluation and discussion

5.3.1 ALE model

Numerical model developed in ALE formulation provides the most stable solution. However, due to default software configuration only the total stress analysis can be performed with ALE. Preliminary tests provide useful information about convergence and sensitivity problems which may be encountered during numerical calculations. The following findings have been recognized:

1. Six finite elements per pile diameter is the minimum number that should be used.
2. Loading rate should be limited to 5cm/s (0,05% of dilatational wave speed) to neglect the numerical effects.
3. Boundary effects are negligible when soil domain is minimum 20 pile diameters wide, but this value can be higher as it depends on elastic properties of soil.
4. Tension cut-off can be omitted in numerical models due to unnatural up-heave of soil

surface and convergence problems.

5. The reliable area for correct stress distributions due to G/c_u ratio for large deformation is usually limited to the 4 pile radius.
6. G/c_u higher than 40 does not influenced the $\sigma_{rr}/\sigma_{rr,0}$ ratio in performed tests.
7. The pile toe and shaft are independent in numerical simulations.
8. Angle of interface friction δ higher than $0{,}6\phi'$ does not influence the pile toe resistance, whereas the δ up to ϕ' strongly influences $\sigma_{rr}/\sigma_{rr,0}$ ratio.
9. Initial stress state in terms of σ_h/σ_v ratio has slight impact on toe and shaft resistance.
10. Pile diameter has no impact on results, but the roundings between pile and shaft can influence shaft friction, especially when small pile diameters are used.

Based on these findings the following recommendation to the ALE models can be formulated:

1. Using six to eight finite elements per pile diameter is the most effective.
2. Width of soil domain with 20D minimize boundary effects.
3. Loading rate will be similar as for prototype.

5.3.2 UL model

UL model needs to be developed with “trial and error” method and this has been verified independently from other researchers (e.g., Sheng et al., 2014). However, a satisfactory compatibility between UL effective stress model and ALE total stress model has been achieved. The following conclusions concerning UL preliminary studies can be written:

1. When friction interface is modelled, the medium compatibility in radial total stress between UL and ALE models is observed.
2. The higher interface friction coefficients (corresponding to δ higher than $0{,}5\phi'$) results in convergence problems and calculation termination.
3. Friction behaviour can be applied on pile shaft, whereas the pile toe needs to be in frictionless contact to perform successful deep penetration calculations.
4. The response in the pile toe and shaft average resistances are quite acceptable.
5. Good agreement in G/c_u ratio and in the initial stress state is observed between UL and ALE model.
6. The initial conditions in terms of K_0 have much more impact on radial effective stress during jacking and equalization phase than CEM prediction can provide (Randolph et al., 1979a).
7. The Vermeer and Verruijt (1981) formula described by equation (4.43) for pore pressure “overshoot” is not necessary applicable to model accurately the pile jacking problem.

5.3.3 CEL model

The CEL formulation offers the best theoretical mechanism to include large deformation problems. However, the accuracy near the pile wall is questionable and the results converge to ALE solution. The problem is also the full three dimensional model that has to be used and computational time in consequence. However, the total pile resistance is predicted accurately, especially when frictionless behaviour is applied. The following observation can be drawn

due to modelling in CEL terms:

1. The radial total stress near the pile wall and average shaft resistance are usually underestimated approx 20% in comparison with ALE and UL.
2. Application of finer mesh converge the results to the ALE solutions.
3. Application of 8-10 elements per pile diameter enables to get the reliable estimation of pile toe resistance.

5.3.4 Summary

Preliminary tests conducted in this chapter are intended to facilitate the FEM model designing. They also define factors influencing the radial effective stress distribution after consolidation such as the initial stress state and undrained shear strength of soil with G/c_u ratio higher than 40. ALE solution facilitates finding the appropriate and compatible UL solution where “trial and errors” method has to be used. The UL, ALE and CEL methods are reliable numerical solutions for pile toe resistance predictions. UL and ALE show good agreement in radial total stress calculation while CEL underestimates this variable.

All presented numerical approaches has advantages and disadvantages presented and discussed in this chapter. It will be shown in next chapters that all presented numerical methods can be satisfactory used for pile/cone penetration prediction.

Chapter 6

Numerical modelling of instrumented piles

Instrumented pile tests are powerful geotechnical research tools which introduce more detailed insight into the soil behaviour during pile installation. In the last years instrumented piles have been successfully applied in cohesive soils. Azzouz and Morrison (1988) have shown application of MIT instrumented pile tests in two Empire clay sites. Coop and Worth (1989) performed tests in overconsolidated Gault clay at Madingley site, on the outskirts of Cambridge and in the normally consolidated clay at Huntspill site, in Somerset county. Bond and Jardine (1991) performed a series of tests in London clay using Imperial College (IC) instrumented piles. The same piles have been used in field experiments in soft marine clay in Bothkennar, Scotland (Lehane and Jardine, 1994b), and in glacial clay at Cowden, north-east England (Lehane and Jardine, 1994a). More recently, Pestana et al. (2002) used full-scale, instrumented piles in uniform deposit of Young Bay Mud and Gavin et al. (2010) conducted tests at Kinnegar site, northern Ireland. In all cited tests the significant increase of radial stress has been observed.

In this chapter, the numerical modelling of the instrumented pile experiment conducted in London clay is shown. The London site (Bond and Jardine, 1991; Coop, 1987) offers a wide range of available laboratory and field database and it is well suited as a reference for the numerical simulations. The field measurement of the radial total and effective stresses is compared with FEM results and the applicability of the numerical methods to the real study of structure behaviour is shown. Finally, selected numerical methods are discussed with the obtained results.

6.1 London clay field tests

The field experiments in London clay have been performed by Imperial College research team at Canons Park, northern London (Bond and Jardine, 1991). The instrumented pile used at Canons Park was close-ended, tubular, stainless steel pile with diameter of 0,102m that was ended with 60° solid cone. The instrumented pile was equipped with three clusters, spaced at intervals of approximately 1m, each containing axial load cell, pore pressure sensors, surface stress transducers and temperature sensor (Bond and Jardine, 1991), see figure 6.1. Due to the

top layer of gravel, see figure 6.2, the pre-bored steel casing was used at the first two meters depth.

The site conditions consist of two layers of heavily overconsolidated London clay. The first one is approximately 2 meters depth, disturbed, brown silty fissured clay and it is underlaid by light brown, intact and stiff clay layer. The soil profile with CPT sounding and K_0 distribution is presented in figure 6.2. The K_0 line has been estimated from the soil's stress history (lower bound) and self-boring pressuremeter tests (upper bound). The laboratory investigation consists of Atterberg limits determination, the unconsolidated undrained triaxial tests and interface ring-shear tests. These tests are complemented by oedometer tests done by Som (1968) and triaxial tests performed by Jardine (1985) and Jardine et al. (1984). The summary of the London Clay geotechnical parameters at Canons Park is presented in table 6.1.

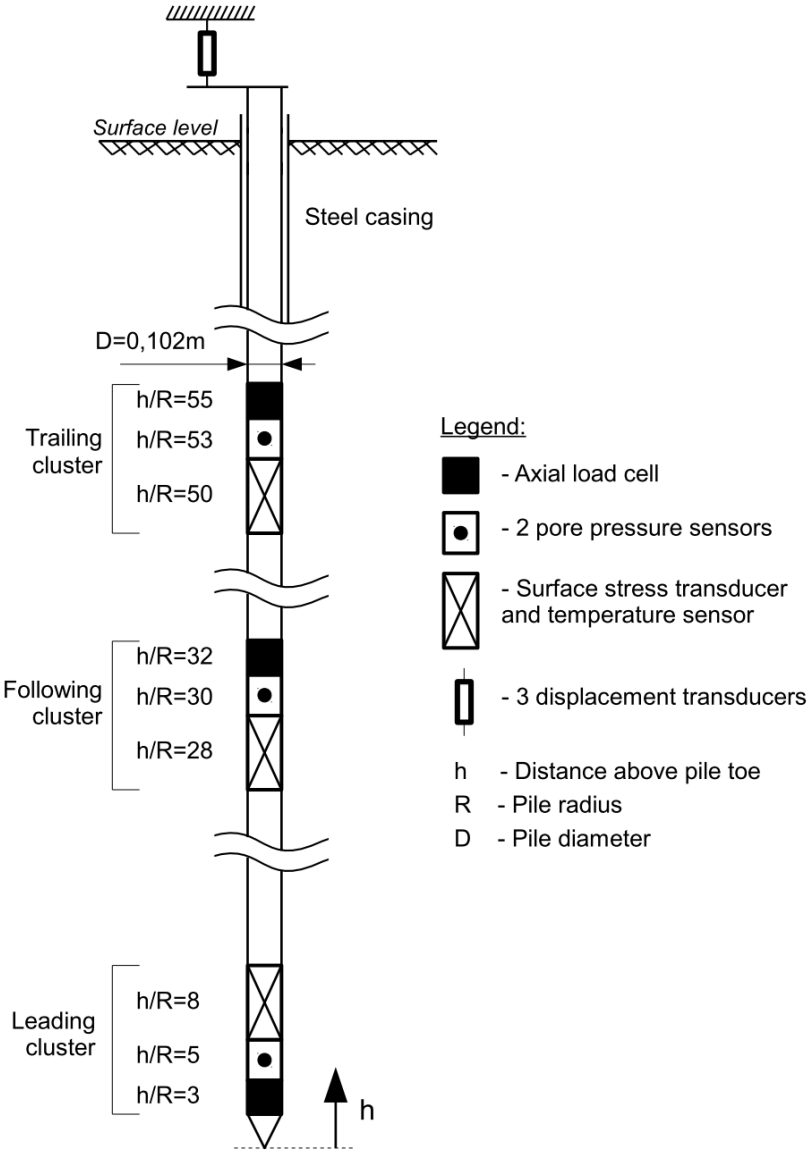

Figure 6.1. Imperial College Instrumented Pile used in Canons Park (after Bond and Jardine (1991))

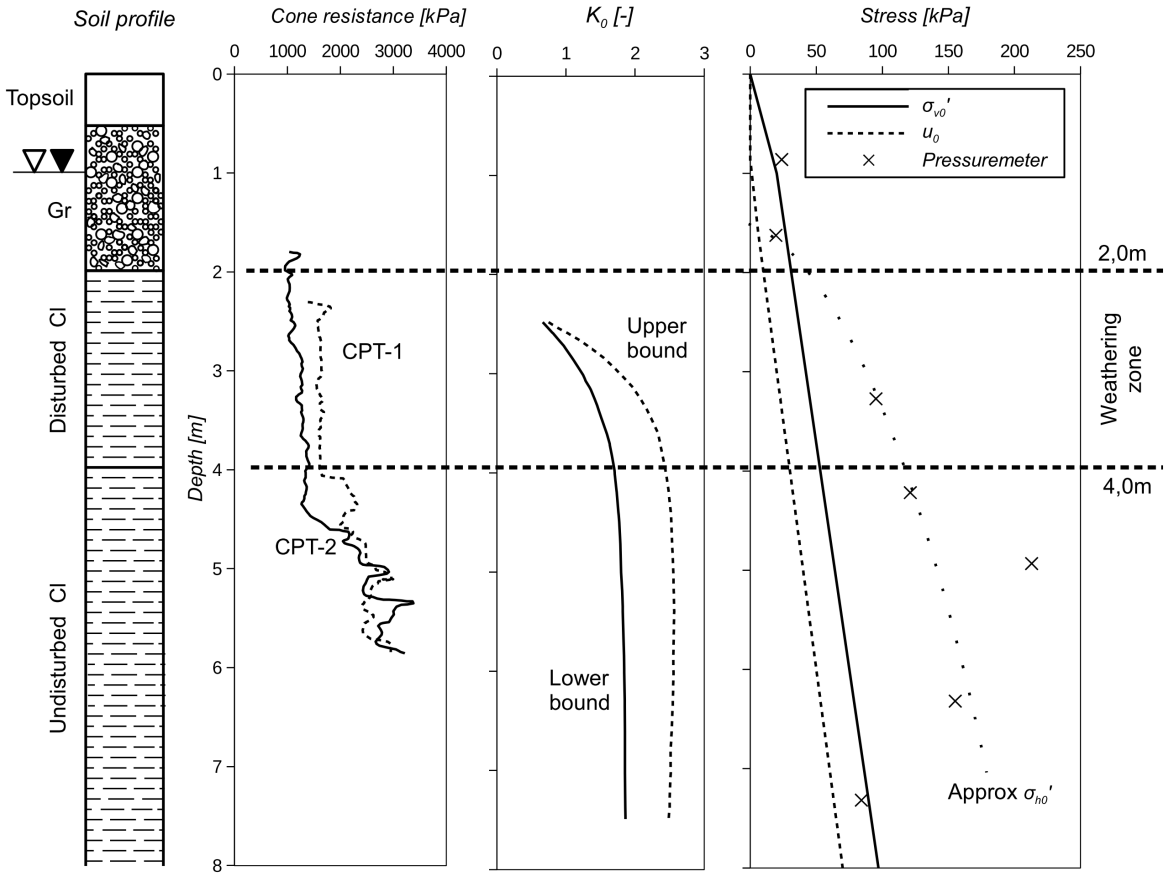

Figure 6.2. In-situ conditions for Canons Park site

Table 6.1. Canons Park Clay parameters

London clay type	*Parameter*	*Value*	*Units*	*Reference*
Disturbed brown clay	w	*~30*	*%*	*Bond and Jardine (1991)*
	w_P	*~30*	*%*	*Bond and Jardine (1991)*
	w_L	*~80*	*%*	*Bond and Jardine (1991)*
	$k^{(1)}$	$1x10^{-7}$	*m/s*	*Water Resources Board (1972)*
	c_u	*~75*	*kPa*	*Coop (1987), Bond and Jardine (1991)*
	G_{max}	*~10000*	*kPa*	*Coop (1987), Bond and Jardine (1991)*
Intact brown clay	c_u	*~120*	*kPa*	*Coop (1987) Bond and Jardine (1991)*
	G_{max}	*~25000*	*kPa*	*Coop (1987), Bond and Jardine (1991)*
	w	*~30*	*%*	*Bond and Jardine (1991)*
	w_P	*~30*	*%*	*Bond and Jardine (1991)*
	w_L	*~70*	*%*	*Bond and Jardine (1991)*
	$k^{(2)}$	$1x10^{-10}$	*m/s*	*Chandler et al. (1990)*
Common parameters	E_u/c_u (ε_a>5%)	*150*	-	*Jardine et al. (1984)*
	ρ	*2,1*	g/cm^3	*Bond and Jardine (1991)*
	ϕ'_{cs}	*22,5*	°	*Bond and Jardine (1991)*
	λ	*0,921*	-	*Som (1968), Jardine (1985)*
	κ	*0,0894*	-	*Som (1968), Jardine (1985)*
Contact parameters	δ_{fR}	*13,5*	°	*Lemos (1986), Tika (1989)*
	δ'_{sR}	*10,5*	°	*Lemos (1986), Tika (1989)*

(1)Average value for weathering zone, (2)Average value for horizontal and vertical component

6.2 Geotechnical parameters estimation

In the numerical studies, the soil is modelled as an elastic-perfectly plastic material. In the total stress analysis with ALE or CEL formulation the linear elasticity and Tresca plasticity are used, while in effective stress analysis the MCC model is applied. The geotechnical parameters and initial conditions are derived directly from laboratory tests. The shear modulus is assumed for large strain problem and it is based on TX data performed by Jardine et al. (1984). The initial preconsolidation pressure is calculated by equation (3.32) to obtain best fit to the undrained shear strength. The lateral earth pressure at rest coefficient is estimated as a mean value from oedometer data (Som, 1968) and pressuremeter tests (Jardine, 1985) while the total stress ratio σ_h/σ_v is assessed after equation (3.37). The soil parameters are varying with depth with subsoil divided into one meter thick layers and they are presented in figure 6.3. Due to incompatibility between surface level and water table the total stress ratio σ_h/σ_v has been approximated to three various values. As the insignificant influence of initial radial stress on the pile installation has been shown in section 5.2.4.3, the approximation of σ_h/σ_v ratio does not create essential errors. All parameters used in effective and total stress approach are listed in table 6.3.

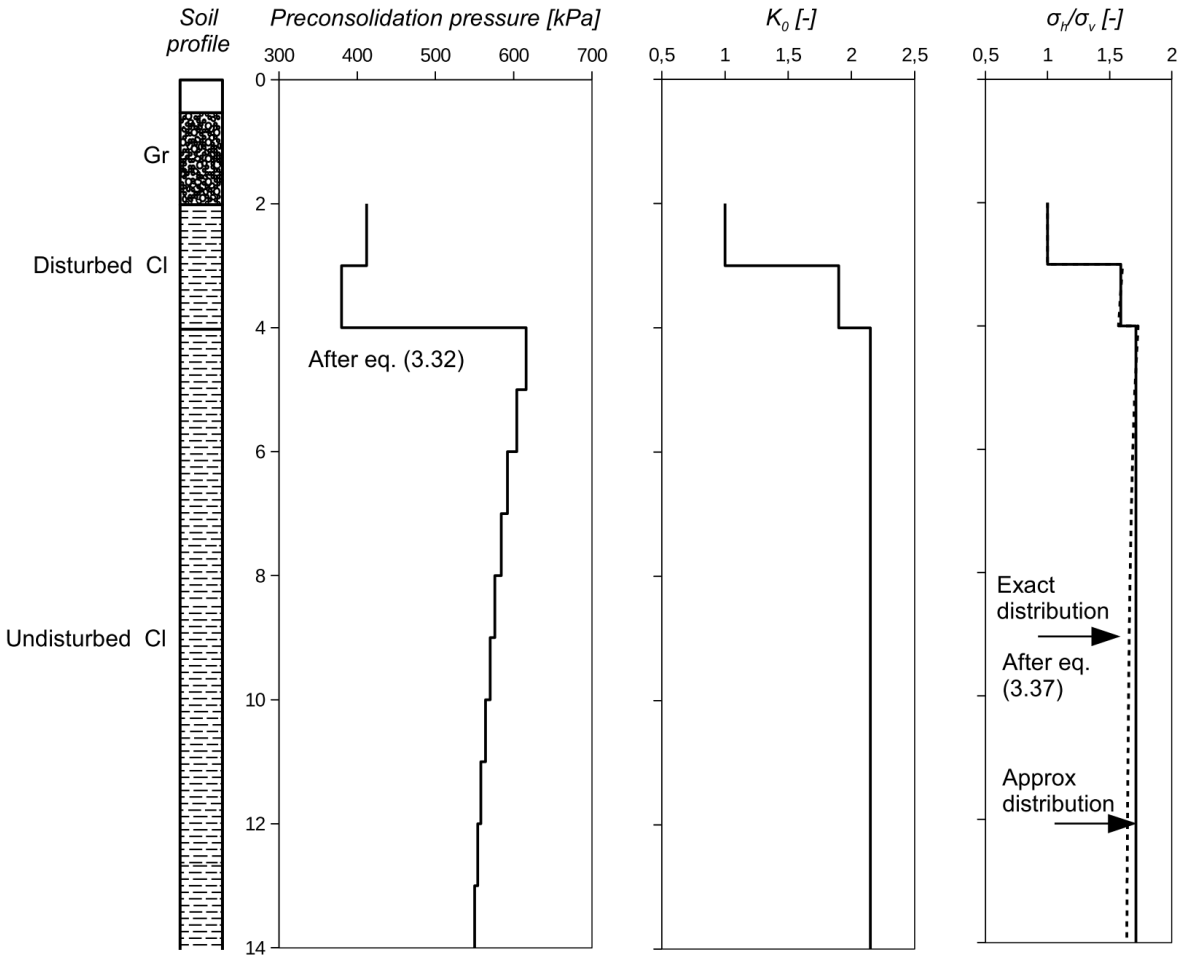

Figure 6.3. Distribution of preconsolidation pressure (left), K_0 (middle) and stress ratio (right) with depth

The validation of assumed parameters has been done by performing numerical UU triaxial test using effective stress approach and MCC model. The comparison between laboratory and numerical results is presented in figure 6.4 in terms of stress paths in *p'-q* plane. As can be seen from laboratory test data, the dilatant response of Canons Park Clay starts from axial strain equal to 1,0% and in numerical study the same criterion is applied. Consequently, relatively good agreement between laboratory and numerical test results for the peak deviator stress is reached.

Table 6.2. Geotechnical parameters used in numerical models

Analysis type	*Parameter*	*Unit*	*Disturbed London Clay*	*Undisturbed London Clay*
Effective stress analysis (MCC model)	ρ'	t/m^3	*1,1*	*1,1*
	e_0	-	*0,582*	*0,582*
	G	*kPa*	*5000*	*8000*
	κ	-	*0,0894*	*0,0894*
	λ	-	*0,921*	*0,921*
	M	-	*0,8773*	*0,8773*
	p'_c	*kPa*	*412÷380**	*625÷557**
	K_0	-	*1÷1,9**	*2,15*
	ρ_w	t/m^3	*1,0*	*1,0*
	k	*m/s*	$1x10^{-7}$	$1x10^{-10}$
Total stress analysis (linear elasticity and Tresca plasticity)	ρ_{sr}	t/m^3	*2,1*	*2,1*
	E_u	*kPa*	*15000*	*24000*
	ν_u	-	*0,49*	*0,49*
	c_u	*kPa*	*75*	*120*
	σ_h/σ_v	-	*1÷1,59**	*1,71*
Contact parameters	$\mu_{jacking}$	-	*0,240*	*0,240*
	$\mu_{equalization}$	-	*0,185*	*0,185*

* values varying with depth, see figure 2

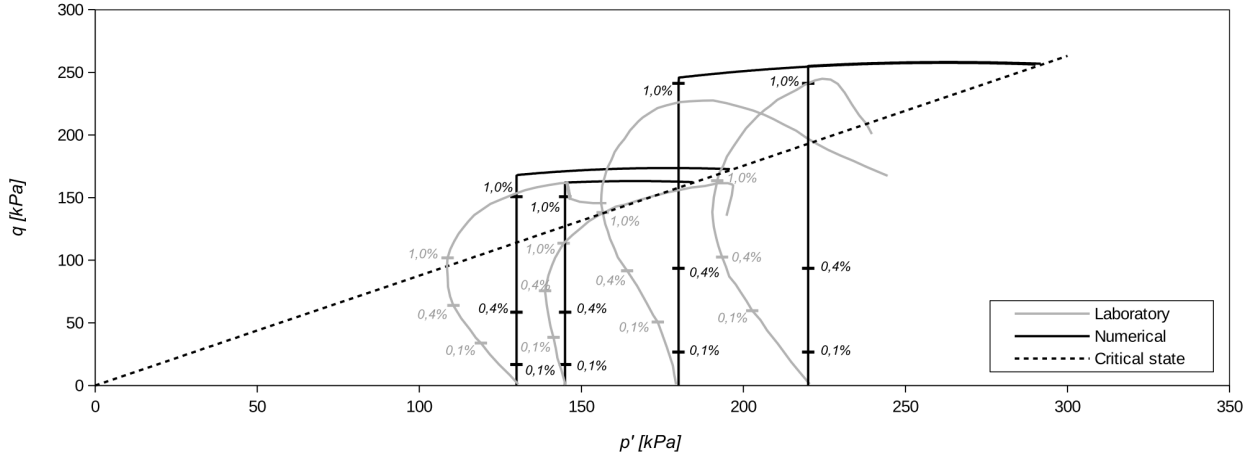

Figure 6.4. Numerical versus laboratory TX testing of Canons Park Clay

6.3 Numerical models development

The three numerical models are designed: UL model with effective stress approach, CEL and ALE models with total stress approach. The soil domain is almost 70 pile diameters wide and 280 pile diameters high and these values guarantee the lack of boundary effects. Each model consist of geostatic step to verify initial equilibrium, driving step and additional consolidation phase in UL formulation. The reference CP5f pile is chosen for numerical modelling. Pile is jacked with velocity of 445mm/min (0,74cm/s) to the depth of 5,92m below surface level (3,92m below the top of clay layers). Shaft friction, normal stresses and pore water pressures are registered at three levels with accordance to the field instrumented pile. Developing of numerical models is based on preliminary studies which have been presented in chapter 5 and more details about each model will be provided in following sections.

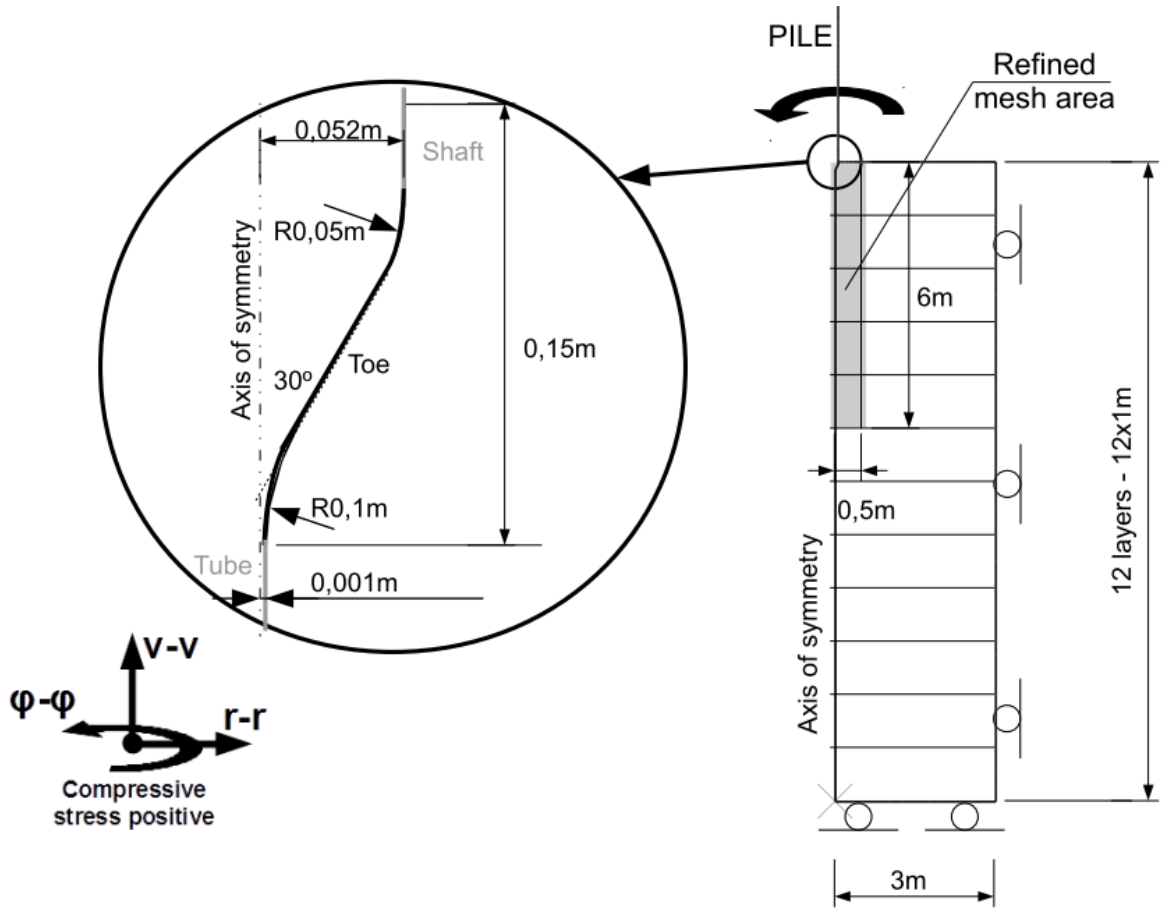

Figure 6.5. UL model geometry for Canons Park site

6.3.1 UL model

The UL model geometry is presented in figure 6.5. The overburden pressure of 30kPa is applied to take into consideration the overlaying soil weight. The boundary condition of pore

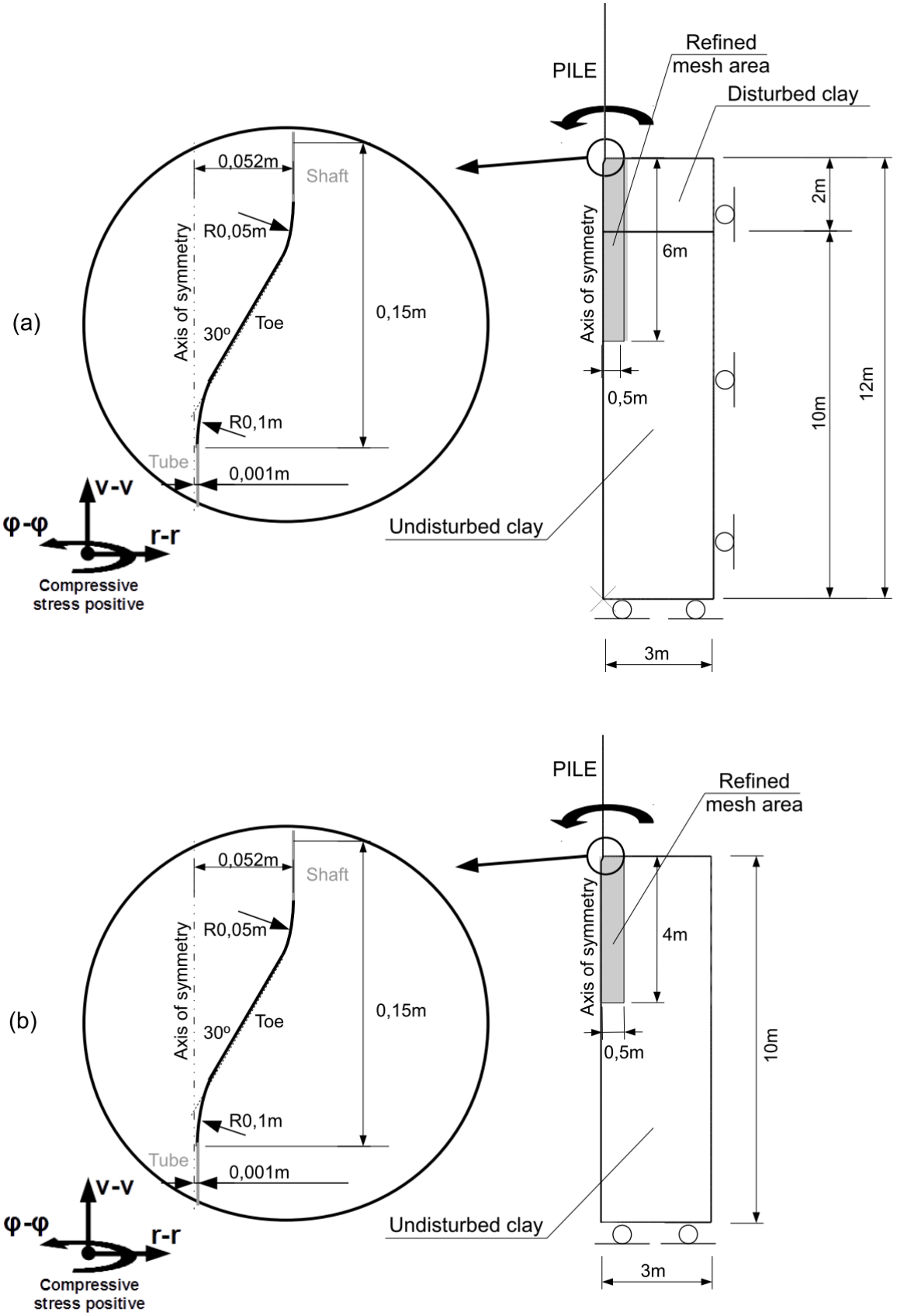

Figure 6.6. (a) DCLAY and (b) UCLAY models geometry for Canons Park site with ALE

water pressure fixed as 10kPa is modelled to include the overlaying piezometric water head. Soil domain consists of 12 soil layers in which different material parameters have been applied with accordance to the data provided in section 6.2. The numerical model is meshed with 9464, CAX8RP elements of minimum size 1,0x2cm in jacking area. Two different coefficients of interface friction between pile shaft and soil have been used in jacking phase and the following consolidation phase. This is due to results of experimental program conducted by Lemos (1986) and Tika (1989). This modelling technique is consistent with assumptions presented in chapter 3, section 3.2.2. The frictionless behaviour between pile toe and soil is used to avoid convergence problems (see section 5.2.4.1). Pile is pressed with so called zipper type technique (Mabsout and Tassoulas, 1994) and it is pre-installed in soil at the depth of 0,15m. The pile is fixed in space during the consolidation phase of duration of $3{,}6x10^{10}$s.

6.3.2 ALE model

The ALE formulation as it is implemented in Abaqus does not allow for multi-material problem calculation (Dassault Systèmes, 2013). Hence, the Canons Park problem will be considered in two stages. Firstly, penetration through the layer of disturbed London clay (model DCLAY) will be performed, see figure 6.6a. Then, the second model, called UCLAY, containing undisturbed layer will be used, see figure 6.6b. In both models, the total stress analysis is used and the cone is pre-installed in the soil at the depth of 0,15m. The overburden pressure is applied to include the overlaying soil weight. DCLAY model contains two layers of clay: disturbed and undisturbed one with parameters provided in table 6.2. In both models, the frictionless toe and friction shaft are assumed and this is done to obtain compatibility between ALE and UL formulations. In both models the zipper-type technique (Mabsout and Tassoulas, 1994), described previously in chapter 5, is used. DCLAY and UCLAY models contains 44712 and 30912 CAX4 elements with minimum size of 1x1cm in jacking area, respectively. Although in DCLAY the penetration was prescribed to total depth of 3,96m, the calculation has failed when the cone reached undisturbed clay layer. This observation is consistent with description of analysis in Abaqus manual (Dassault Systèmes, 2013) and other research (e.g., Bienen et al., 2015).

6.3.3 CEL model

The geometry and boundary conditions of CEL model are presented in figure 6.7. The CEL formulation allows for multi-material models, so three layers of soil has been assumed, see figure 6.6. The first layer represents the overlaying gravel (see figure 6.2). The next soil layers are modelled with materials provided in table 6.2. The 53352, EC3D8 elements are used in numerical model with minimum size of 1,2x1,2cm in the jacking area, see figure 6.7. The contact between discrete rigid pile and soil is modelled using general contact algorithm and penalty contact method with friction coefficient of 0,240. It should be noticed, that only the clay layers are in contact with pile. As the practical workaround, the contact between each soil layers is also assumed as frictional with friction coefficient of 0,240. The pile was jacked over 3,96m of clay with velocity of 2cm/s. In order to save computational time the jacking velocity

has been increased in comparison to the field one. Similar strategy was used by e.g., Qiu and Grabe (Qiu and Grabe, 2012) and as it was presented in chapter 5, this is allowable modification. Material mixing was observed during calculation, which hampered the results analysis. Due to high friction each soil layer tends to follow the pile shaft which results in unreliable stress distribution along the pile shaft. Combining this phenomenon with findings about underestimation of radial total stress in close shaft area (see section 5.2.2.2) results in some simplifications that are required to analyse the numerical results. Consequently, in stress analysis author assumed that the reliable horizontal stress acting on pile shaft is the largest

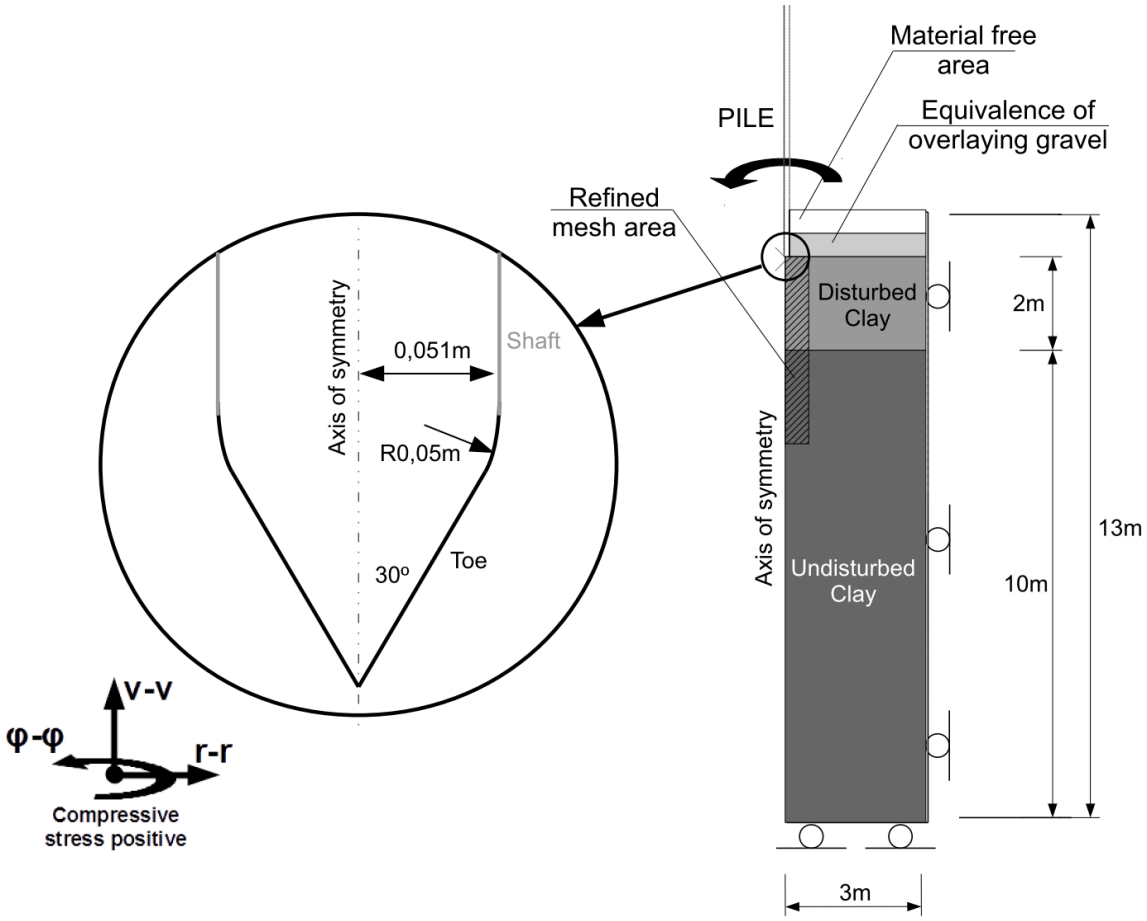

Figure 6.7. CEL model for Canons Park site

one at the distance of one pile radius pile from the shaft

6.4 Field measurements and numerical study comparison

In this section the numerical results will be compared with the field tests performed by Coop (1987) and Bond and Jardine (1991). The comparison is mainly focused on radial stress, but other elements such as shear strain development along the radial directions or mean stress distribution are also presented.

6.4.1 Installation phase

Numerical calculation have been carried out with respect to the field measurement

conditions (rate of jacking of 7,4mm/s). The radial total stresses for ALE, CEL and UL are precisely specified at the middle on each calculation layer i.e. 2,5; 3,5; 4,5; 5,5 and 6,0 meters below the surface level, because the same method has been applied in soil parameters averaging. An exception is the value for 3,0m depth instead of 2,5m for CEL formulation due to overburden soil attraction along the shaft in this region. The soil attraction is the main problem with CEL formulation where the friction on pile-soil interface induces material drag along the shaft, see figure 6.8. Consequently, the radial total stress provided by CEL formulation are selected as a maximum one at the distance of one pile radius from shaft. The radial total stress distributions for depths mentioned in this paragraph are plotted in figure 6.9 whereas the total radial stresses acting on the pile shaft are presented in figure 6.10a.

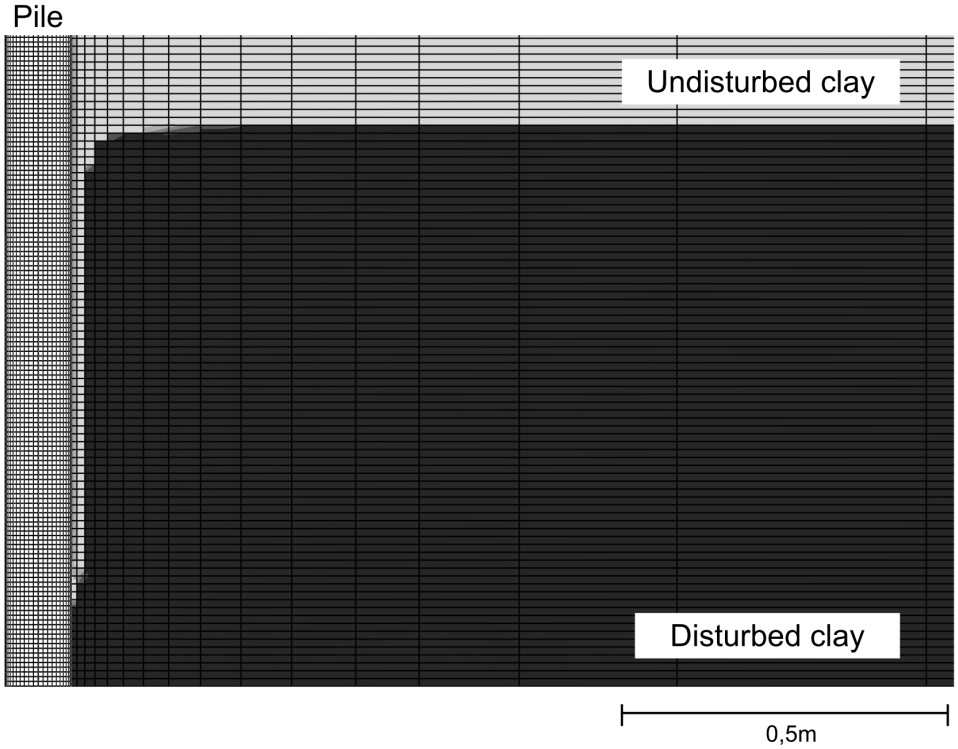

Figure 6.8. Undisturbed clay attracted along the pile shaft in CEL model

Some important features are shown in the figures 6.9 and 6.10a. ALE and UL formulation provide similar results although the ALE solution contains two separate numerical models and, by consequences, the discrepancies are a little more visible. The much more challenging problem is the analysis of CEL model results. Due to effect of soil attraction and numerical approximation in close shaft area (underestimation of results; see chapter 5, section 5.2.2.2), this region is hampered to analyse. The soil attraction problem is however less important near the pile toe, where all formulations result in the similar response, see figure 6.9e. Nevertheless, all numerical methods provide acceptable response of the soil structure due to pile jacking and the numerical results are close to the measured ones, where significant increase in radial total stress is observed. In the next section the after-consolidation state with UL formulation will be analysed.

The comparison between measured and calculated pore water pressures at the end of

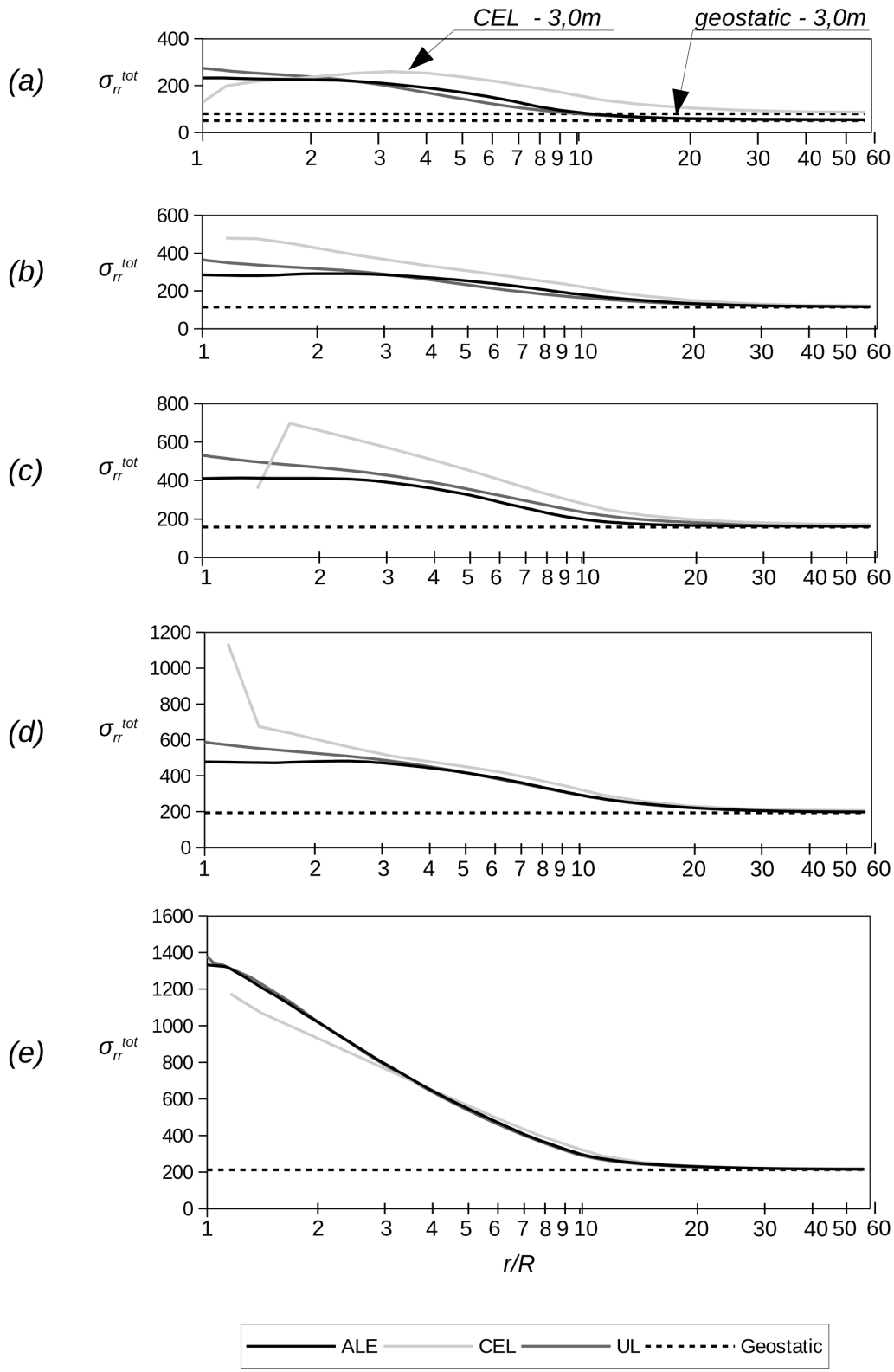

Figure 6.9. Radial total stress distribution at (a) 2,5m; (b) 3,5m; (c) 4,5m; (d) 5,5m and (e) 6,0m depth for Canons Park site

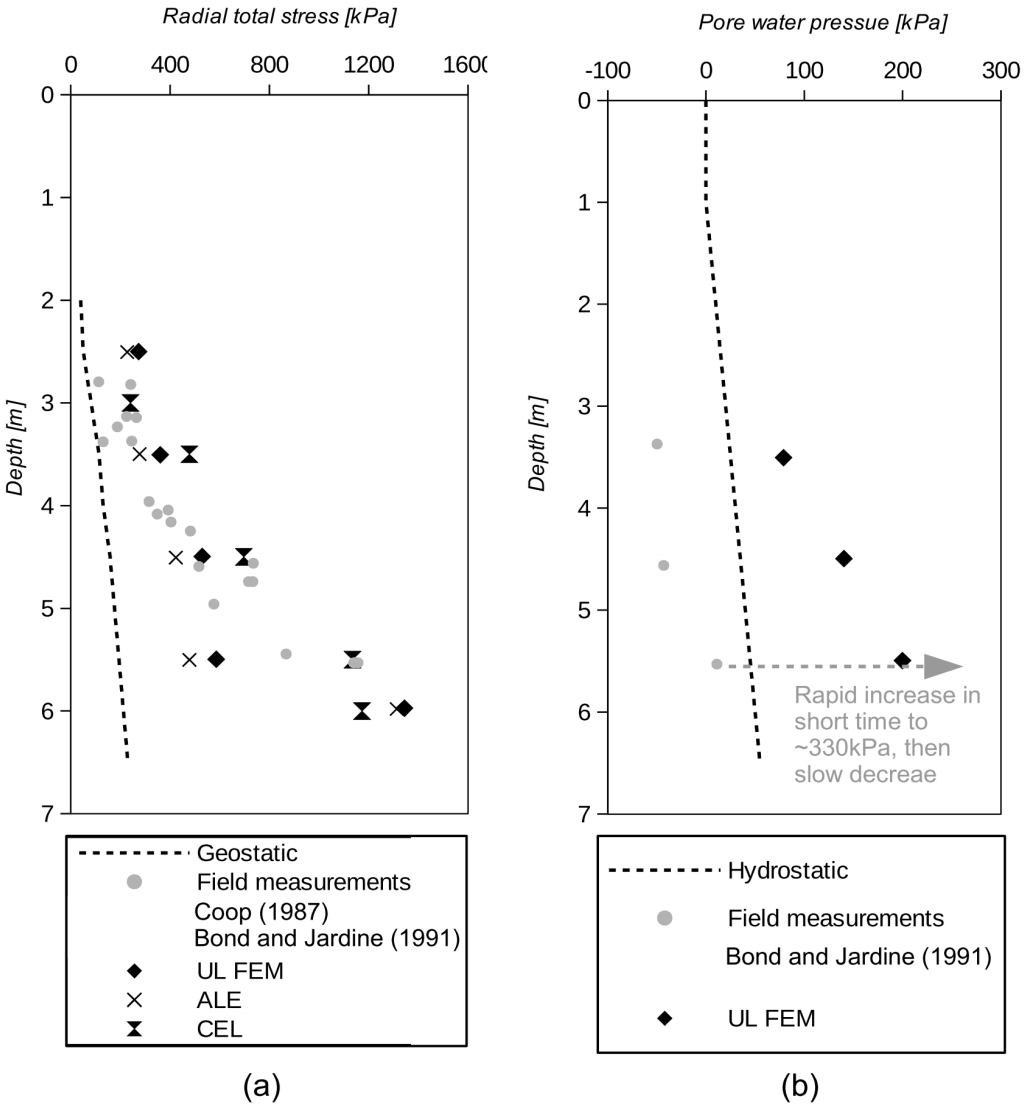

Figure 6.10. (a) Radial total stress and (b) pore water pressure distributions at the end of installation phase for Canons Park site

installation phase is presented in figure 6.10b. The negative pore pressure has been registered in the instrumented piles while the positive one is obtained in numerical calculation. The reasons for this phenomenon can be twofold: firstly, the cavitation that occurred in the field tests could bring down the reliability of pore water pressure measurement (Bond and Jardine, 1991) or secondly, the used contact or constitutive model is oversimplified. The answer to this problem remains open.

6.4.2 Consolidation phase

The radial effective stresses along the pile wall are shown in figure 6.11. The stresses are provided in the middle of each soil layer and for the pile tip. This is more correct due to simplification of continuous soil deposit to the layered one as it has been mention in previous sections. As one can see, the satisfactory agreement between field measurements and

numerical study is achieved. The discrepancies are referred to the near pile toe region and to the disturbed clay layer where slightly overestimated radial stresses are noticed. The narrow peak in radial stresses occurs around the pile toe, which has been already observed in chapter 5. Here, the same mechanism is noticed but the field measurement shows that range of toe influence on radial stress is wider than numerical predictions reveal.

The mean effective stress distribution along the radial direction for 3,1m depth below the surface level are confronted with the laboratory measurements done on samples from 3,10m and 3.86m depths (Bond and Jardine, 1991). The results are shown in figure 6.12 where good agreement can be seen for maximum mobilized stress. However, field measurements suggest narrower influence of the installation (up to 4 pile radii) than numerical results (up to 8 pile radii). Similar comparison is done for the shear strain around the jacked pile and it is presented in figure 6.13. In the field, the shear strain have been estimated by measuring the slopes of bedding planes (Bond and Jardine, 1991) denoted as γ_{rv}. Two strain measures are shown in figure 6.13. They are the octahedral shear strain which represent the total effort of shear around the pile and the logarithmic shear strain in r-z plane. As can be seen, for logarithmic shear strain γ_{rv} the agreement between numerical calculation and the field study is satisfactory from normalized radius of 1,5. In very close distance to the pile wall the shear strain calculated numerically drops suddenly, while the field measured one still increases. This problem is related to the formulation of FEM where the shearing is developed in the first

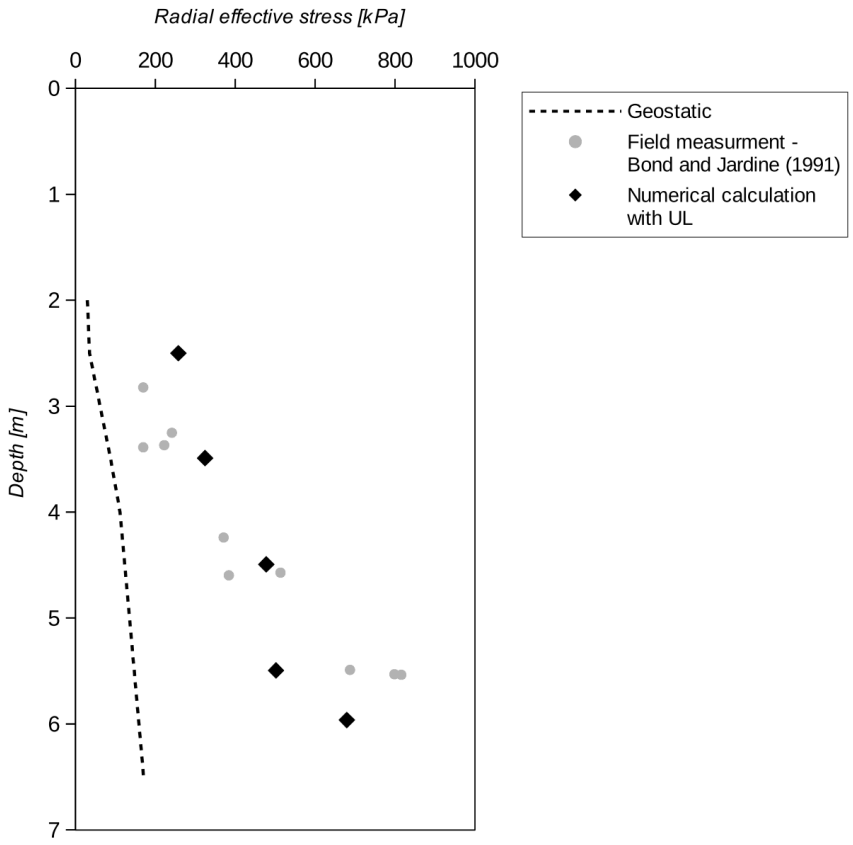

Figure 6.11. Effective stress distribution at the end of consolidation for Canons Park site

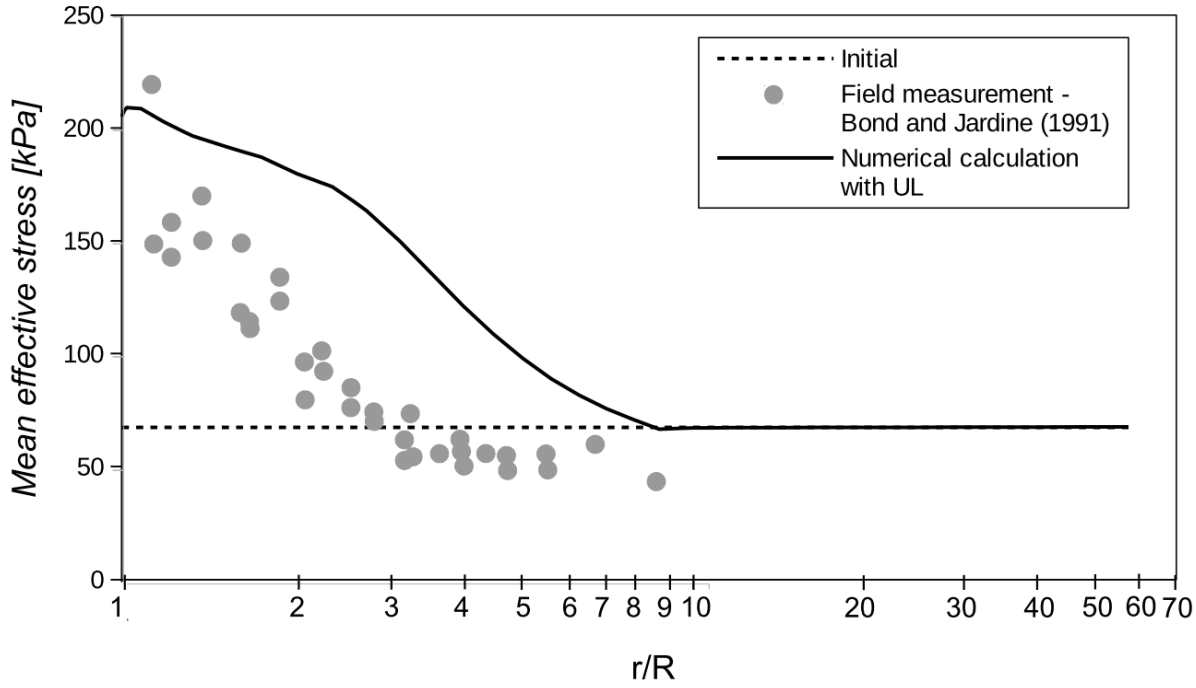

Figure 6.12. Laboratory measurement and UL calculation of mean effective stress for 3,5m depth for Canons Park site

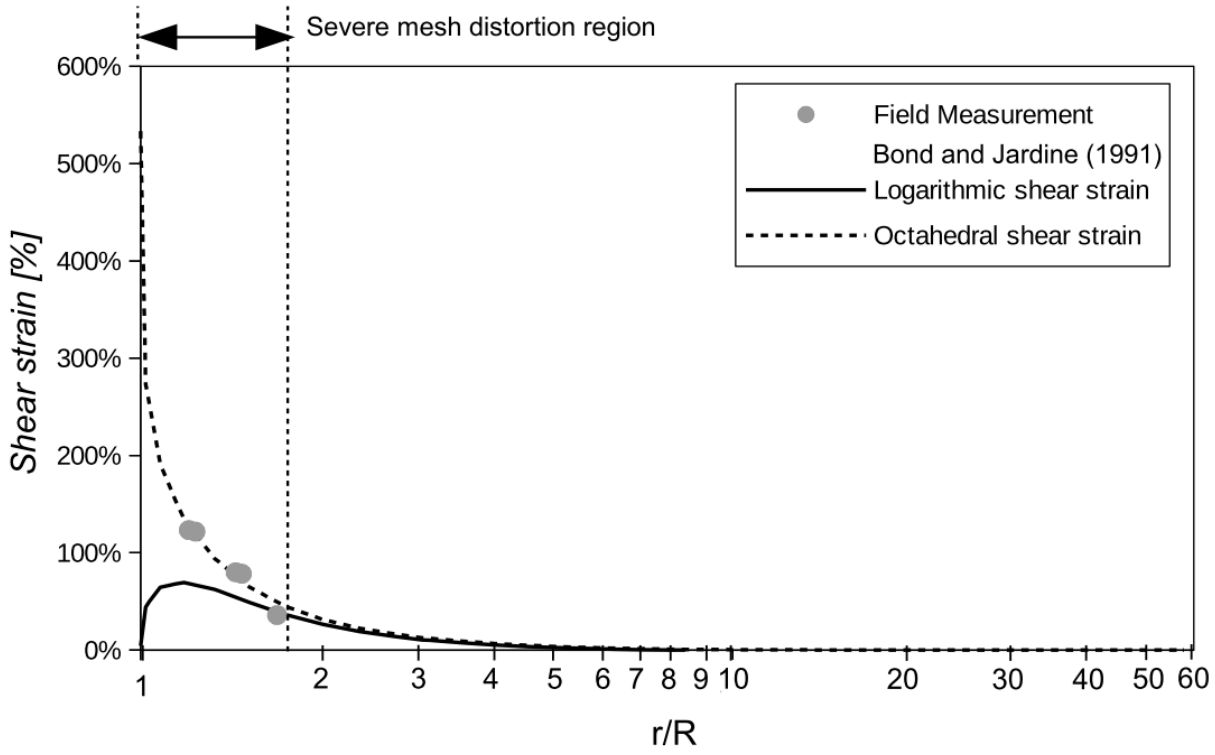

Figure 6.13. Laboratory assessment and UL calculation of shear strain development in radial direction for Canons Park site

finite elements next to the pile wall and to the severe mesh distortion in this area. Application of a very fine mesh may results in more precise results in this area, but as it was said in chapter 5, in UL formulation the mesh is design by “trial and error” method. However, the octahedral shear strain fits almost perfectly the laboratory assessment. The decision which shear measure represents better the in-situ conditions remains open.

6.5 Summary

In this chapter the reasonable radial total stress distributions along the pile shaft has been obtained during installation phase and the results suits well to the field tests in Canons Park. The CEL method provides the more accurate results, especially in the near cone area. ALE and UL formulation also return acceptable results, but with the peak in radial total stress around the pile toe. After consolidation, the calculated and measured radial effective stress distributions are also quite similar. Hence, the UL FEM can provide acceptable numerical solution in terms of jacked pile. In contrast to pure CEM method (see, Bond and Jardine, 1991), the UL method is more accurate in perditions of effective stress distributions and excess pore water pressures (see figures 6.8 and 6.9). In addition, the UL provides also more reasonable shear strain distribution in perpendicular direction form pile shaft (see figure 6.13). However the obtained radial effective stress after consolidation seems to be overestimated for disturbed clay and slightly under-predicted in undisturbed, high OCR clay.

Summing up, UL, ALE and CEL have shown its applicability in geotechnical calculation of pile installation effects. The acceptable agreement between numerical solutions and field testing of instrumented piles has been presented. Thus, the numerical method can be used to investigate the possible qualitative and quantitative mechanisms of long term increase in pile shaft capacity due to installation and consolidation phases.

Page intentionally left blank

Chapter 7

Numerical modelling of CPT probing

The cone penetration test (CPT) is widespread as geotechnical site investigations method. In recent decades many numerical investigations of cone penetration into the subsoil have been made. The main scope of the previous research has been concentrated on the cone factor (e.g., Liyanapathirana, 2009; Sheng et al., 2013; Van Den Berg, 1994; Walker and Yu, 2006) due to its importance in shear strength determination (Robertson and Cabal, 2010). The influence of partial drainage and rate effects on cone resistance has been also analysed by, among others Obrzud et al. (2011), Yi et al. (2012), Sheng et al. (2014). Verification of most of numerical studies has been done in laboratory using calibration chamber device (e.g., Abu-Farsakh et al., 2003; Wei et al., 2005). The numerical studies verification in field conditions is however not widely used (e.g., Burns and Mayne, 1998; Wei, 2004).

Historically, the CPT numerical modelling has its origins in middle 70s when the analysis of deep penetration has started (e.g., Baligh and Scott, 1976). Later, the Strain Path method has been developed by Baligh (1985) and the CEM with Critical State concepts have been used to investigate stress distributions and pore water pressures around the cone due to installation and consolidation (see, Baligh and Levadoux, 1980; Chen and Mayne, 1994; Levadoux and Baligh, 1986; Mayne, 1991, 2001).

In this chapter the verification of the numerical models is done by comparison of results from numerical solution and in-situ measurements. The soil parameters are determined in laboratory and the parameters calibration is conducted numerically with respect to the laboratory procedures. The reference localizations are Koszalin where CPT sounding with ALE is shown and Poznań where both ALE and UL methods are used. The aim of this chapter is to clarify modelling problems of CPT probing and on correlation of the numerical analysis results with the in-situ measurements.

7.1 Koszlin CPT probing area

7.1.1 Geotechnical site investigation

The 322 boreholes and 37 CPT probings have been done as a field geotechnical investigation in Koszalin area of S6 highway, section 4. The WD-102 structure has been

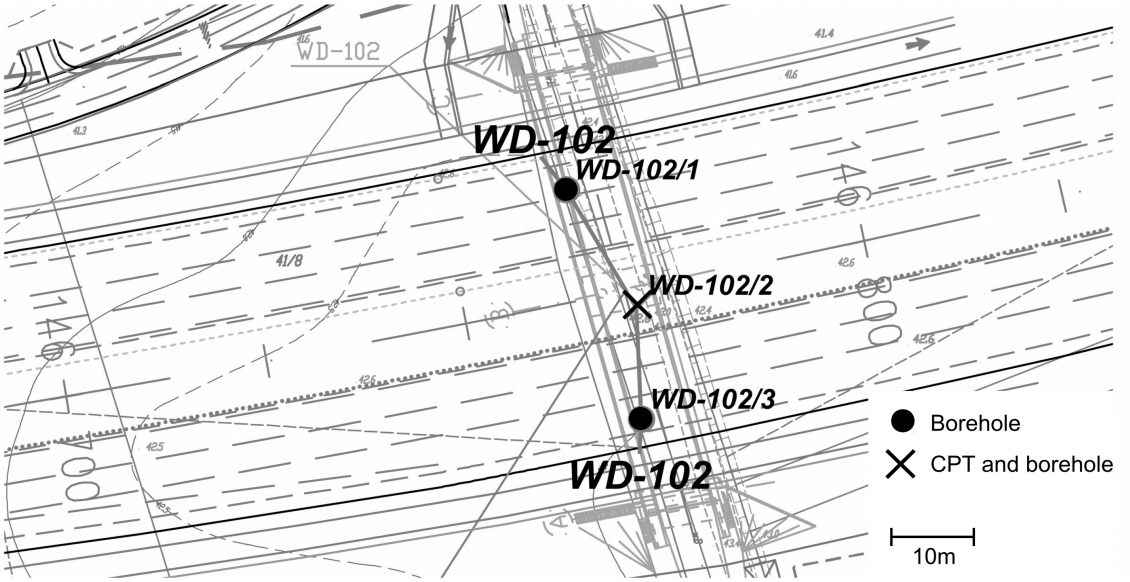

Figure 7.1. Localization of geotechnical investigation in WD-102 structure area

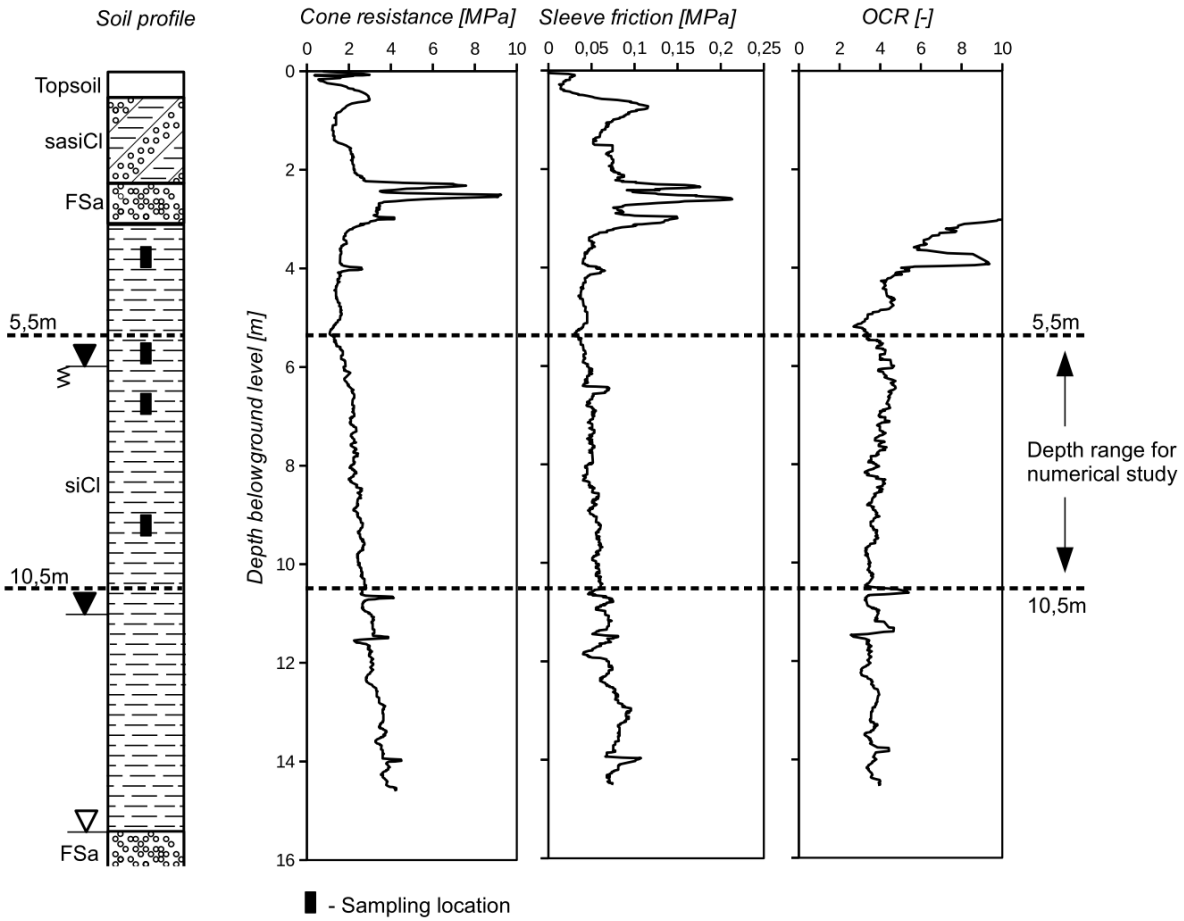

Figure 7.2. Soil and CPT profiles for WD-102 structure site

selected as a reference localization due to uniform, slightly overconsolidated clay layer and wide scope of laboratory data for this location. The geotechnical field investigation on WD-102 structure consists of one electrical CPT cone test and two boreholes drilled in approximate distance of 15m as it is shown in figure 7.1. The CPT graph with the soil profile standardized from three boreholes and OCR distribution is presented in figure 7.2. As can be seen, the grey, stiff ($I_L \approx 0,1$) clay layer is slighty overconsolidated with OCR ranging from 3,5 to 4,5 at the depth considered in numerical calculation chosen from 5,5m to 10,5m below ground level. The water table is stabilized 11,0m below surface level, but the filtering into the borehole is recognized at the depth of 6,0m. The physical and mechanical parameters determined in laboratory are summarized in table 7.1. A number of tests has been performed and they include grain size analysis, consistency limits tests, oedometer tests, direct shear tests, pocket shear vane tests and pocket penetrometer tests. Field and laboratory investigation data has been commissioned by General Directorate for National Roads and Motorways in Poland and forwarded to the author for the purpose of this research.

Table 7.1. Koszalin Clay properties

Parameter	*Value*	*Units*
w	*~13,5*	*%*
w_P	*~12,0*	*%*
w_L	*~30,5*	*%*
ρ_{sr}	*2,23*	*g/cm^3*
c_u	*95÷150*	*kPa*
ϕ_s	*19,2*	*^{o}*
c_s	*70*	*kPa*
e_0	*0,37-0,39*	-
λ	*0,023*	-
κ	*0,006*	-
K_0*	*1,0*	-

*CPT estimation

7.1.2 Geotechnical parameters estimation

The CPT probing in Koszlin clay is performed with ALE formulation and the Tresca plasticity with linear elasticity as constitutive behaviour. Although the applied constitutive behaviour requires five parameters, the lack of triaxial undrained test or direct shear box undrained test makes the reliable parameters estimation hampered. The most accurate estimation of undrained shear strength is done by application of equation (3.31). However, in equation (3.31) the effective values and MCC parameters are used. Thus, the first proceed test is to estimate the effective stress parameters based on oedometer and direct shear box. Consequently, the effective stress parameters used in MCC model are presented in table 7.2. Most of the presented values are provided directly from the laboratory tests, see table 7.1, but few are based on additional derivations. The elastic shear modulus G of 11280 kPa is obtained from equation (Atkinson, 2007):

$$G = \frac{E'}{2(1+\nu')} \tag{7.1}$$

Table 7.2. MCC Koszalin Clay parameters

Parameter	*ρ'* *g/cm³*	*G'* *kPa*	*e_0* -	*κ* -	*λ* -	*p_c'* *kPa*	*M* *kPa*	*ρ_w* *g/cm³*	*K_0* -	*k* *m/s*
Value	*1,23*	*11280*	*0,37*	*0,006*	*0,026*	*eq.(3.32)*	*Initially assumed as 0,866*	*1,0*	*1,0*	*10^{-10}*

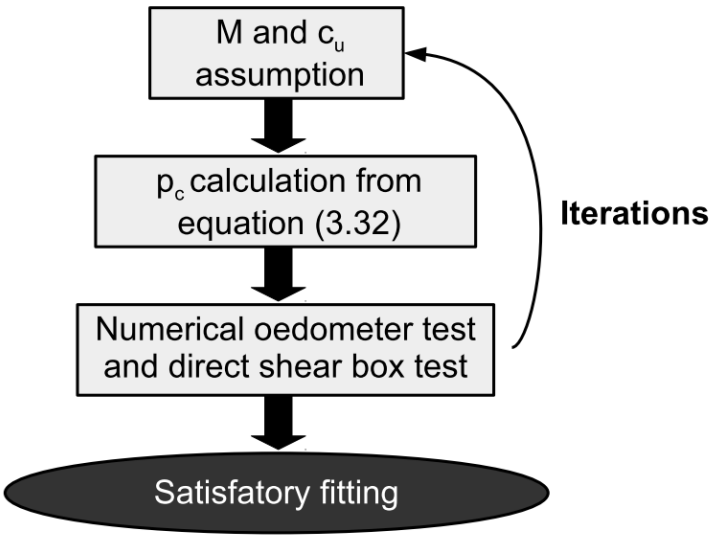

Figure 7.3. Calibration procedure for undrained shear strength estimation

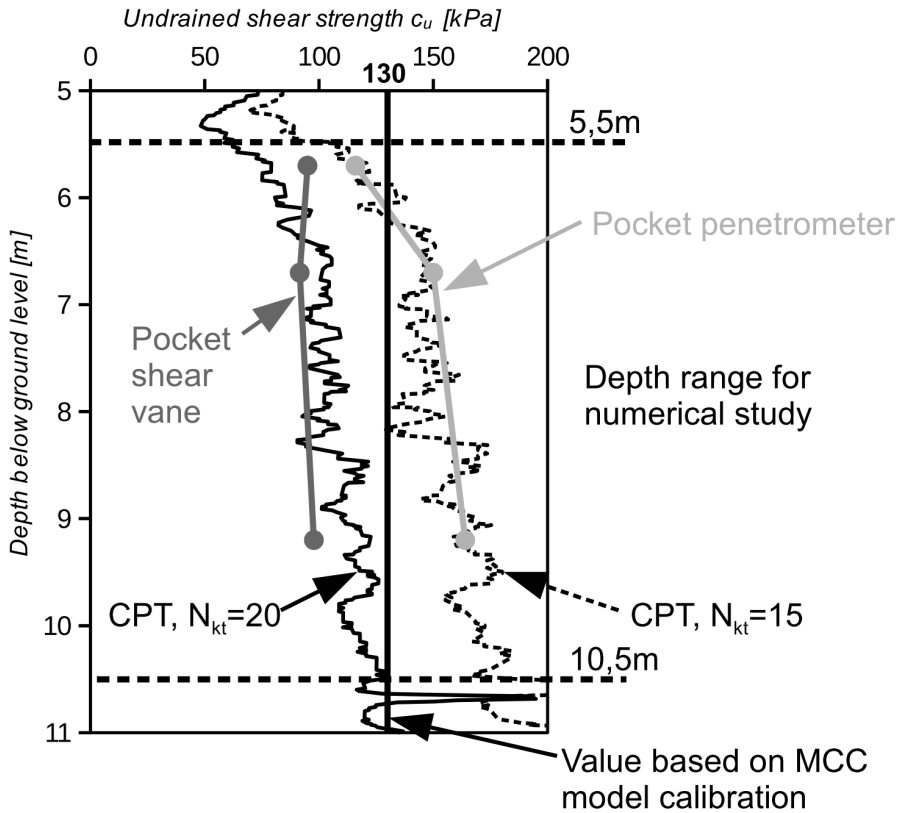

Figure 7.4. Undrained shear strength estimates

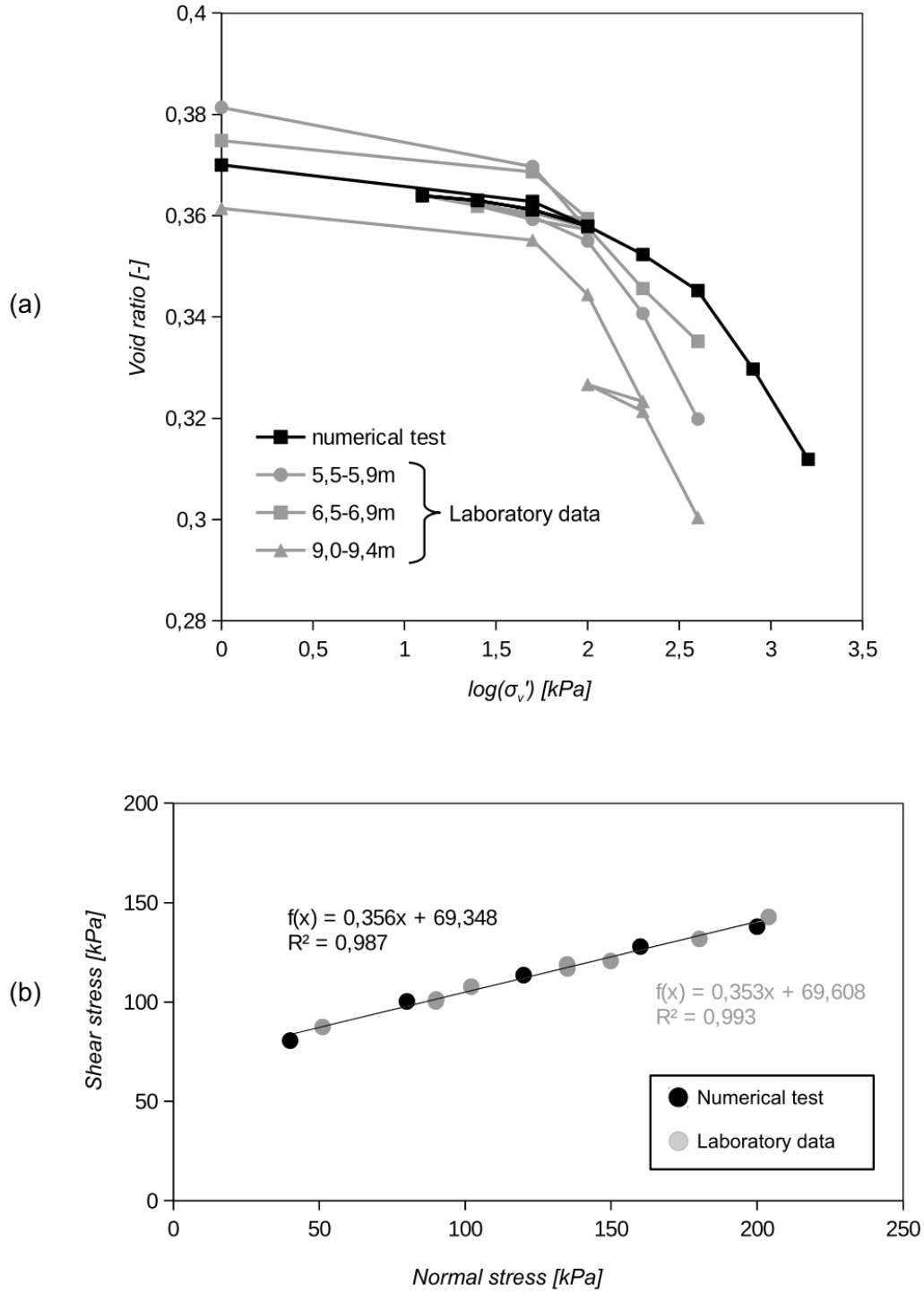

Figure 7.5. Numerical tests versus laboratory measurements: (a) oedometer and (b) direct shear test

where: E' – drained elastic modulus, here $E' \approx p_0'/\kappa$ where κ – logarithmic elastic modulus (e.g., Dai and Qin, 2013), ν' – drained Poisson's ratio, here fixed as 0,33.

As the mean initial stresses on depths range from 5,5 to 10,5m below surface level is approximately 180kPa for fully saturated clay, the shear modulus can be calculated as 11280kPa. The coefficient of permeability of 10^{-10}m/s is based on relation with plasticity

index (Benson et al., 1992). The two unknown parameters: p_c' and M are directly related to the undrained shear strength, see equation (3.31). The additional difficulty is that direct shear test conducted in laboratory have been done in partially drained conditions where the clay specimens probably have not been submerged in the water. However, the boundaries of possible undrained shear strength can be estimated from the pocket instruments, see table 7.1 and figure 7.4. The procedure described in figure 7.3 is used to find appropriate value of undrained shear strength of Koszalin clay. The numerical oedometer test as well as direct shear tests are conducted with accordance to laboratory procedures. In calibration procedure the stress ratio M is assumed as 0,866 which corresponds to the angle of internal friction of 22,2º with respect to the TX conditons or 30º in plane strain conditions. This is a typical value for clays (e.g., Terzaghi et al., 1996). The best fitting results are obtained for undrained shear strength of 130kPa and the comparison between laboratory and numerical results of calibration are provided in figure 7.5b. The figure 7.5a shows that most crucial parameter is the preconsolidation pressure. The laboratory oedometer tests suggest that p_c' is around 150kPa, but the undrained shear strength of 90÷150kPa enforces p_c' ranging between 430÷830kPa for corresponding response of MCC model. For c_u=130kPa, which suits well the direct shear test, the p_c' is 700kPa and hence, some discrepancies can be observed in oedometer numerical simulation.

The c_u estimated from oedometer test and direct shear box is also compared with the undrained shear strength of the Koszalin clay based on pocket instruments such as pocket shear vane tests and pocket penetrometer and the CPT estimation for cone factor of 15 and 20 as it is presented in figure 7.4. As one can see, the calibrated value of c_u fits well the laboratory and field estimates.

The total stress parameters used in ALE model are presented in table 7.3. The total stress ratio σ_h/σ_v is calculated using equation (3.37). The last unknown is the contact behaviour between probe and soil. The shear behaviour in cone-soil interface with total stress analysis is usually expressed as a function of undrained shear strength (Potyondy, 1961). However, this kind of contact is not directly available in Abaqus software. Consequently, the penalty contact algorithm and tangential behaviour with prescribed coefficient of friction have been applied. As a practical workaround, two numerical runs have been performed in this study with the coefficients of friction fixed as 0,129 and 0,264, corresponding to the angle of internal friction δ as $\delta=\frac{1}{3}\phi'$ and $\delta=\frac{2}{3}\phi'$, respectively.

Table 7.3. Total stress parameters for Koszalin Clay

Parameter	ρ_{sr}	E_u	υ_u	c_u	σ_h/σ_v
	g/cm³	*kPa*	-	*kPa*	-
Value	*2,23*	*33600*	*0,49*	*130*	*1,0*

7.1.3 CPT numerical modelling

In ALE solution the experience from chapter 5 is used to build effective numerical model. The geometry of ALE model is presented in figure 7.6. The cone of the standard dimension of 35,68mm is modelled as a rigid body and it is pre-installed in the soil at the depth of 6 cm. The soil domain is axisymmetric, 18m hight and 3m wide and it is discretized with 102822

quadratic, 4-nodded, linear elements with reduced integration (CAX4R) with minimum size of 4x4mm in jacking area. Cone was pressed with zipper-type technique (Mabsout and Tassoulas, 1994) from initial depth of 5,5m to the final depth of 10,5m with constant rate of 2cm/s. The overburden pressure is modelled to include the weight of overlaying soil.

7.1.4 Numerical studies results

The cone resistance and sleeve friction obtained from numerical simulation and field measurement are compared in figure 7.7a. In the test with $\delta=⅓\phi'$ the technical problem has occurred just after the cone has passed 9,5m depth and the calculation has not been restarted as the restart file was found corrupted. However, the results are still valid and they can be used for the interpretation. As one can see, the cone resistance curve calculated numerically is almost constant with depth and it is also close to this measured in the field. The constant cone resistance is consistent with other numerical studies in homogeneous soils (e.g., Liyanapathirana, 2009; Sheng et al., 2013). The improvement of the numerical model is possible, but it requires application of undrained shear strength increasing with depth. However, due to lack of undrained triaxial tests, the estimation of undrained shear strength varying with depth is hampered. As it has been reported in chapter 5, the cone roundings may

Table 7.4. Average friction ratios for cohesive soils in Koszlin area

Soil	*siCl**	*Cl*	*sasiCl*	*ALE, δ=⅓Φ'*	*ALE, δ=⅔Φ'*
R_f *[%]*	*1,5÷2,5*	*4÷6*	*2÷4*	*~4,4*	*~6,2*

*Soil modelled in numerical study

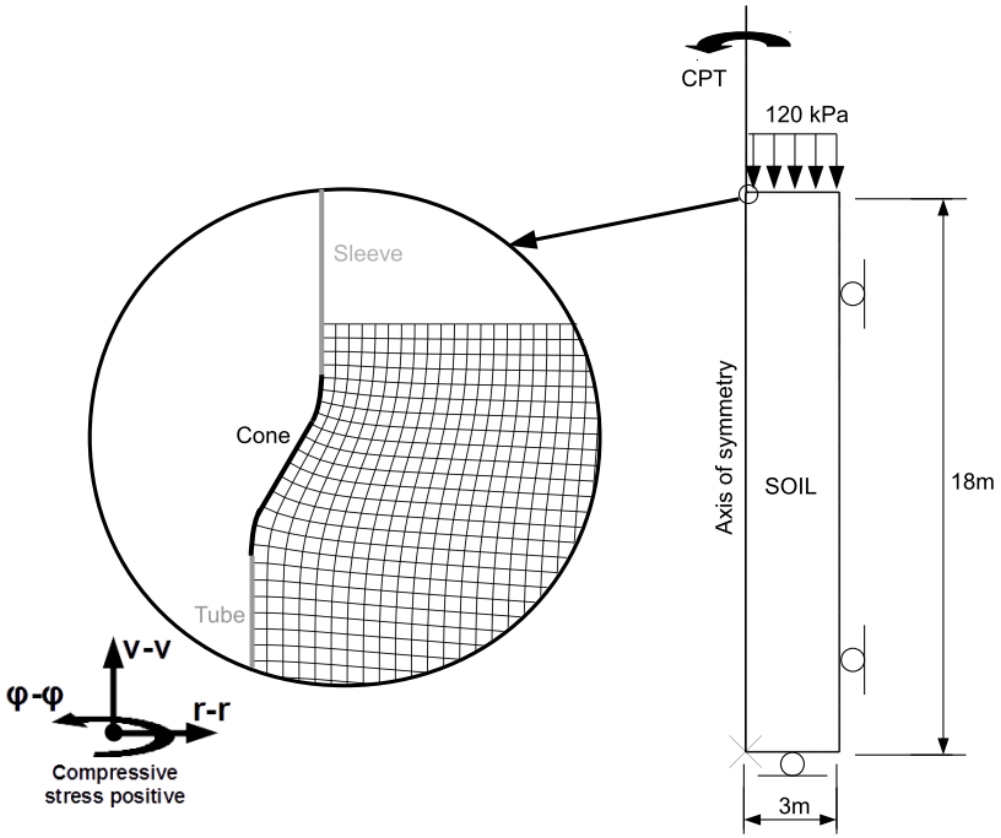

Figure 7.6. Axisymmetric CPT model with ALE formulation

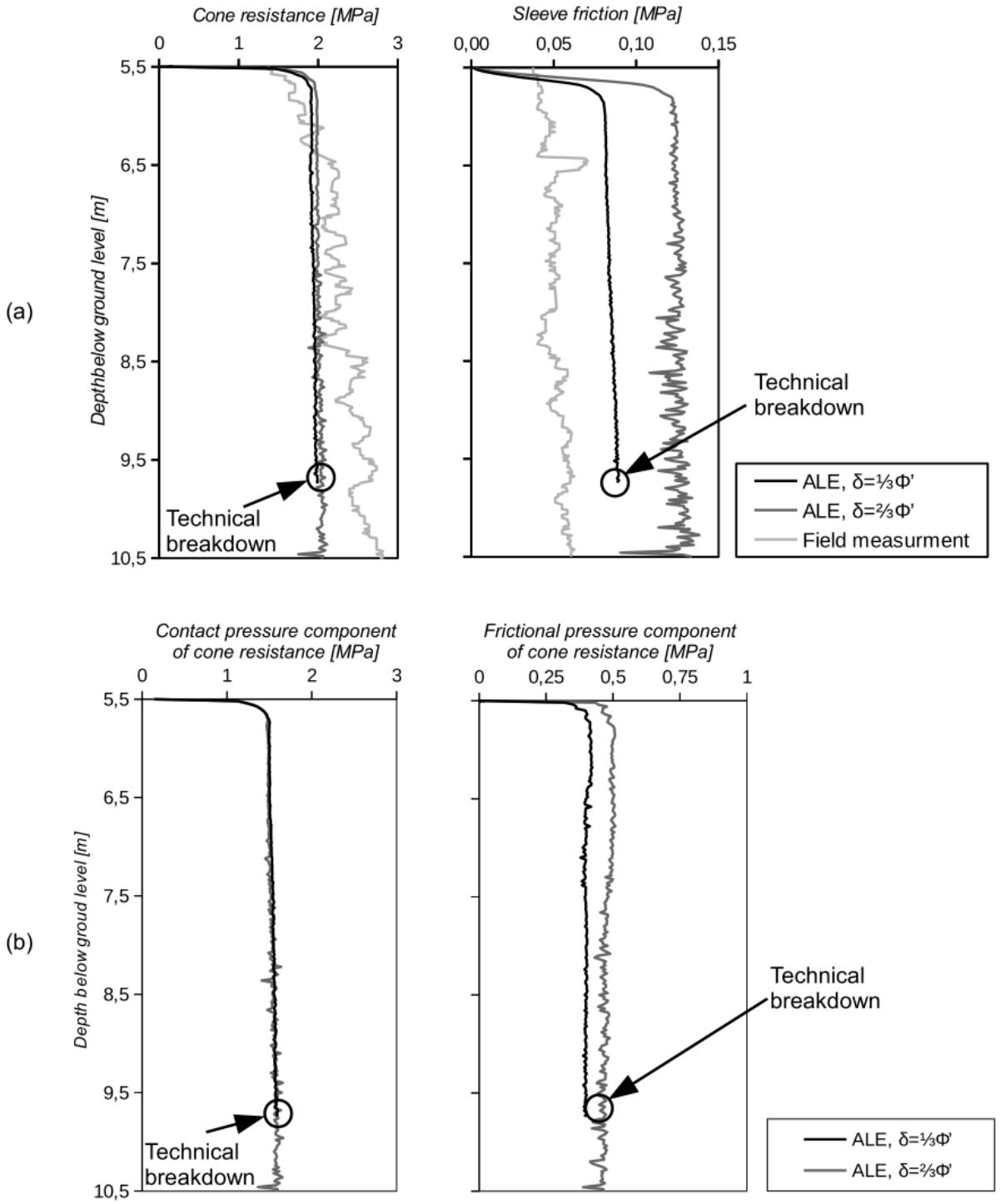

Figure 7.7. (a) Numerical results versus field measurement, (b) contact and frictional part of cone resistance

influence the total cone resistance. The detailed analyse of roundings geometry shows that its influence is less than 5% of total cone resistance. Hence, the rounding effects can be neglected. The differences in frictional component of cone resistance between $\delta=\frac{1}{3}\phi'$ and $\delta=\frac{2}{3}\phi'$ are in range of 0,1MPa, see figure 7.7.b and thus, the contact pressure component of cone resistance as a consequence of strength parameters plays a more important role in cone

resistance rather than friction behaviour. This observation is also consistent with preliminary tests where the friction behaviour on pile toe resistance was also limited.

The applied coefficients of friction return overestimated values of sleeve friction. The friction ratios for clayey soils from Koszalin area are provided in table 7.4. The calculated values overestimate 2 or 3 times the measured sleeve friction and here the influence of friction is evident. Thus, the proper definition of contact condition on cone-soil interface is crucial for successful numerical modelling.

7.2 Poznań CPT probing area

7.1.1 Geotechnical site investigation

The geotechnical documentation of commercial centre in Poznań consists of 3 independent site investigation reports. Totally, the 102 boreholes, 86 CPT/CPT-u with 22 dissipation tests, 5 dilatometer tests (DMT) and 10 Dynamic Probe Light tests (DPL) have been done. Laboratory tests include 6 series of three consolidated undrained (CU) triaxial tests, 6 oedometer tests, grain size analysis and standard classification tests. The CPT-u no. 142 has been selected as the reference localization due to close DMT probing localization and borehole no. 103 from which the samples for oedometer and triaxial tests have been taken. The map of reference localizations is presented in figure 7.8. The soil profile obtained from no. 103 borehole and the profiles of CPT-u and DMT soundings are shown in figure 7.9a and 7.9b, respectively. The water table is recognised at the depth of 0,9m. The depth range for numerical studies has been selected from 6,5m to 7,5m below ground level. The laboratory tests include oedometer tests and consolidated undrained triaxial tests with pore water pressure measurement. The field and laboratory tests have been forwarded to author by

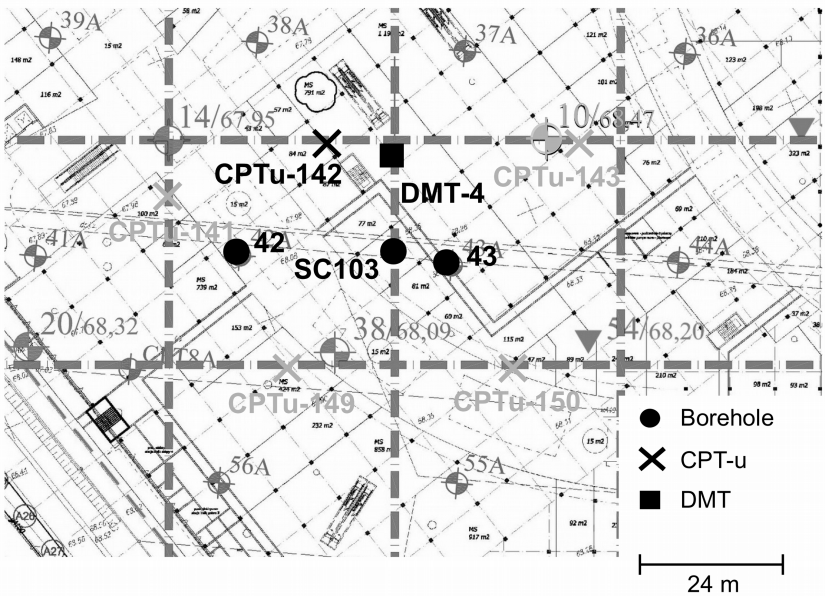

Figure 7.8. Reference CPT probing location at commercial centre "Łacina" in Poznań area.

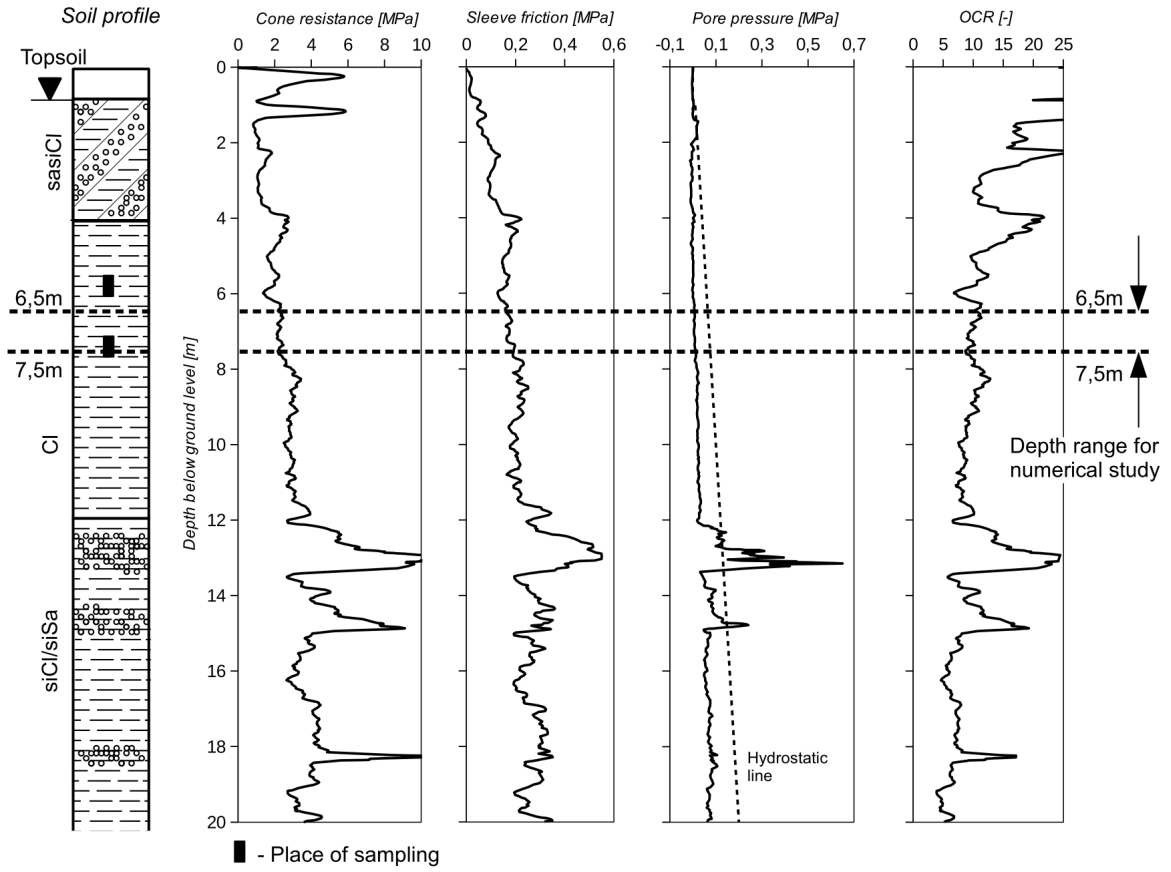

(a)

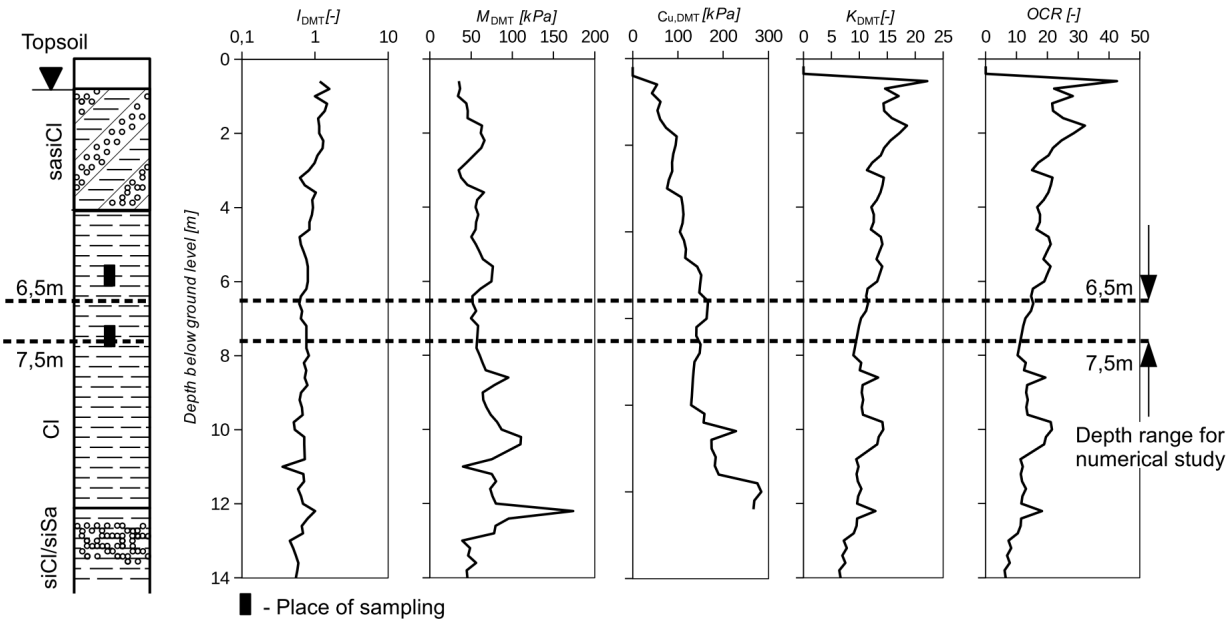

(b)

Figure 7.9. (a) CPT and (b) DMT probing results for Poznań site

Menard Polska under the cooperation in the National Centre for Research and Development grant. The geotechnical parameters obtained from the laboratory and field tests are summarized in table 7.5. The earth pressure at rest coefficient has been estimated from DMT test. The undrained shear strength is based on both CPT-u and DMT probing results (empirical equation are presented in Appendix C). Drained elastic modulus E' have been estimated from TX testing and DMT sounding.

Table 7.5. Poznań Clay parameters

Parameter	*Value*	*Units*
w	*25,7*	*%*
ρ_{sr}	*2,02*	*g/cm^3*
M	*0,601*	-
e_0	*0,67÷0,74*	-
k	*2x10^{-12}*	*m/s*
λ	*0,074*	-
κ	*0,025*	-
E'	*46 300*	*kPa*
c_u	*110÷150*	*kPa*
K_0	*2,0*	-

7.2.2 Geotechnical parameters estimation

The calibration of the geotechnical parameters has been done by numerical triaxial and oedometer tests, both performed with accordance to the effective stress approach. The effective stress parameters are presented in table 7.6. The values are in majority based on direct laboratory data, but some additional derivations are also made. The shear modulus of 17800kPa has been calculated after equation (7.1) with assumption of Poisson's ratio of 0,3 and it was confirmed with triaxial tests, see figure 7.10b. Effective elastic modulus has been estimated from dilatometer tests using equation (C.14), see Appendix C. The another problem is the assumption of initial void ratio which ranges from 0,67-0,74 depending on soil sample. Consequently, the mean value of 0,709 is considered in numerical studies. The initial preconsolidation stress has been estimated from equation (3.32) and the calibration procedure in triaxial apparatus. The coefficient of permeability of $2x10^{-10}$m/s is based on literature database for Poznań clays (Gawriuczenkow, 2005).

The comparison between numerical triaxial tests and the laboratory ones is presented in figure 7.10 and the confrontation between numerical oedometer and laboratory ones is shown in figure 7.11. One can seen that in consolidated undrained test an exceptionally good agreement has been reached in stress paths (figure 7.10a) and a little worse, but still acceptable in q-ε_a relationship (7.10b). The interpretation of numerical oedometer test is more problematic with comparison to the laboratory ones. Firstly, the relatively large differences occur in initial void ratio. Generally, the satisfactory results have been achieved in virgin consolidation line and the discrepancies are related to the low pressure ranges. However, this research is focused on the plastic state and high stresses. Hence, the oedometeric response is acceptable as long as stress paths in triaxial test are almost the same as in laboratory data.

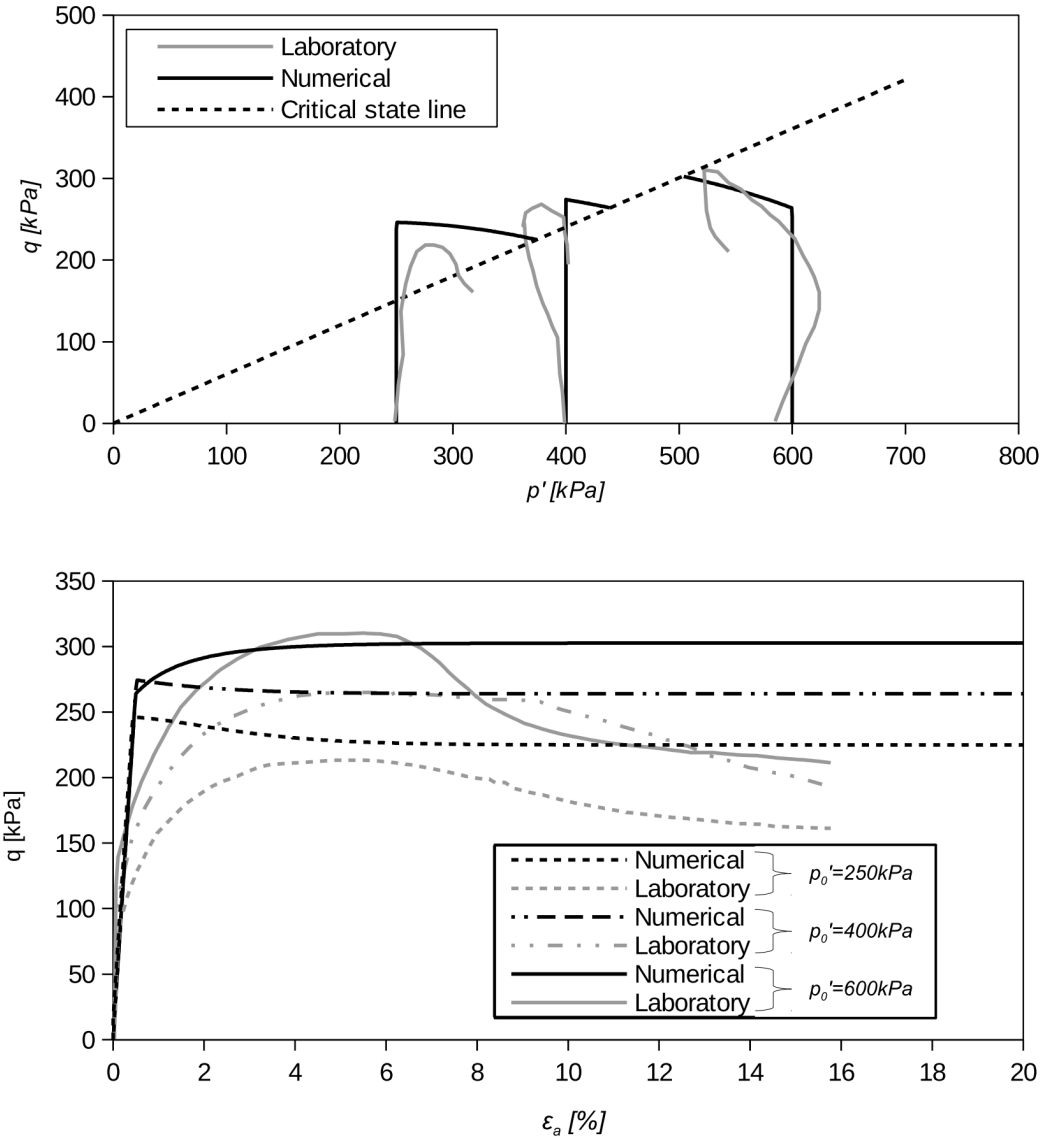

Figure 7.10. Numerical triaxial tests versus laboratory ones: (a) stress paths, (b) deviatoric stress-axial strain

Table 7.6. MCC Poznań Clay parameters

Parameter	*ρ'*	*G'*	*e_0*	*κ*	*λ*	*p_c'*	*M*	*ρ_w*	*K_0*	*k*
	g/cm^3	*kPa*	*-*	*-*	*-*	*kPa*	*kPa*	*t/m^3*	*-*	*m/s*
Value	*1,01*	*17 800*	*0,709*	*0,025*	*0,074*	*1 217*	*0,601*	*1,0*	*2,0*	*2x10^{-10}*

Table 7.7. Total stress parameters for Poznań Clay

Parameter	*ρ_{sr}*	*E_u*	*υ_u*	*c_u*	*σ_h/σ_v*
	g/cm^3	*kPa*	*-*	*kPa*	*-*
Value	*2,016*	*53 050*	*0,49*	*110*	*1,5*

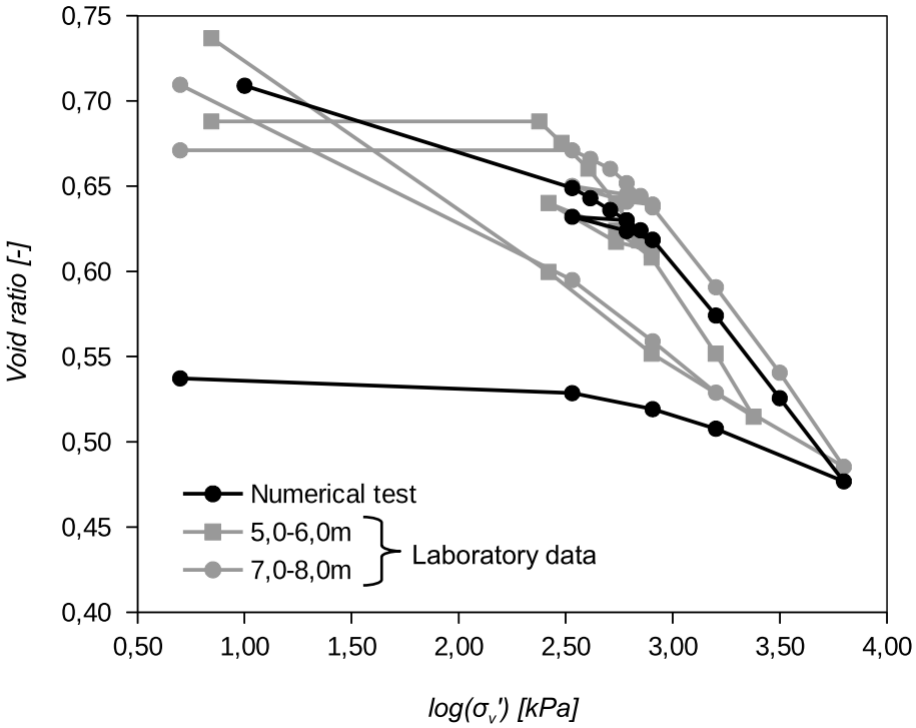

Figure 7.11. Numerical oedometer compared to the laboratory tests.

The total stress parameters have been calculated with respect to methodology given in chapter 3 and they are presented in table 7.7. The undrained elastic modulus, undrained shear strength and σ_h/σ_v ratio are calculated using equations (3.26), (3.31) and (3.37), respectively.

7.2.3 CPT numerical modelling

The CPT probing is modelled with UL and ALE formulation and in both cases, the range for numerical study has been selected as 6,5-7,5 meters below ground level due to laboratory tests available for that depth range. As the deep and long time duration CPT penetration has been shown in section 7.1. for Koszalin clay, here only 1m depths numerical sounding is carried out. The aim of this section is to present the compatibility between UL and ALE formulations in terms of CPT modelling. The soil in UL and ALE models is considered as uniform and homogeneous and the details of numerical models development will be provided in following sections.

7.2.3.1 ALE model

The geotechnical parameters used in ALE model with total stress approach are presented in table 7.7 and the model geometry is shown in figure 7.12. The standard CPT cone with diameter of 35,68mm is used and it is pre-instaled in the soil at the depth of 6cm. The soil domain is axisymmetric with dimensions of 8x3m and it is discretized with 47536 CAX4R elements with minimum size of 4x4mm. Cone is pressed with zipper-type technique (Mabsout and Tassoulas, 1994) through the 1m depths with rate of 2cm/s. The overburden pressure is applied to include overlaying soil mass. Two jobs have been submitted. In the first

one the coefficient of friction on cone-soil interface is set as 0,00 while on the sleeve it is fixed as 0,187 which corresponds to $\delta \approx \frac{2}{3}\phi'_{cs}$. This is done to fulfil the compatibility with UL model. The second job has been submitted with coefficient of friction of 0,287 which corresponds to the friction angle $\delta = \phi'_{cs}$, where ϕ'_{cs} is equal to ~16º.

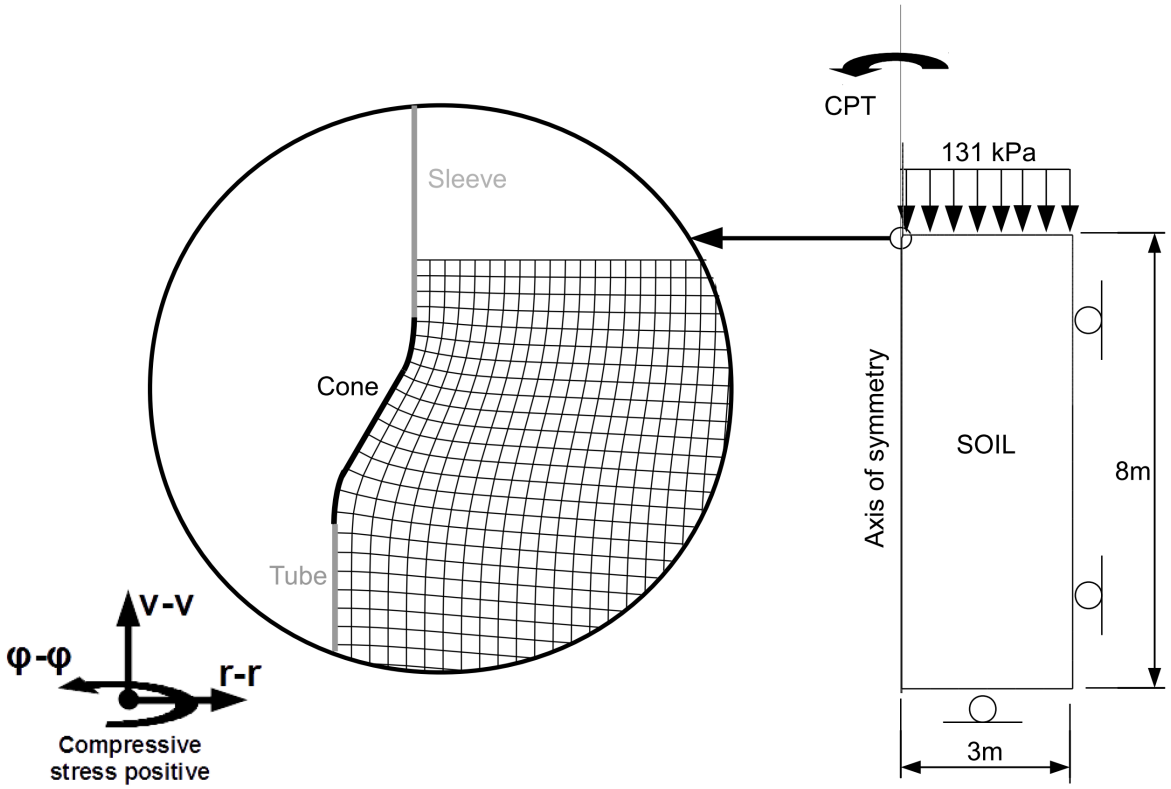

Figure 7.12. ALE model for Poznań site

7.2.3.2 UL model

The soil parameters of effective stress analysis with UL model are presented in table 7.6. The only exception is the variation of initial preconsolidation pressure p_{c0}' to satisfy the constant value of undrained shear strength with depth, see figure 7.13. Consequently, the 8 layers of soil have been developed in the domain that has dimensions of 3x8m, as it is presented in figure 7.13. The overburden pressure takes into account the overlaying soil weight and the fixed pore water pressure of 56kPa on the top of soil domain represents the current piezometric level. The soil domain is discretized with 10266 CAX8RP elements with minimum size of 4x6mm in jacking area. The interaction between cone and soil is assumed frictionless due to numerical problems presented in chapter 5. However, the friction behaviour between sleeve and soil is consistent with ALE model and, consequently, it is fixed as $\delta \approx \frac{2}{3}\phi'_{cs}$. The cone is pressed using zipper-type technique (Mabsout and Tassoulas, 1994) with rate of 2cm/s over the 1m depth. After jacking, the numerical dissipation of pore water pressure has been performed with assumption of fixed cone position.

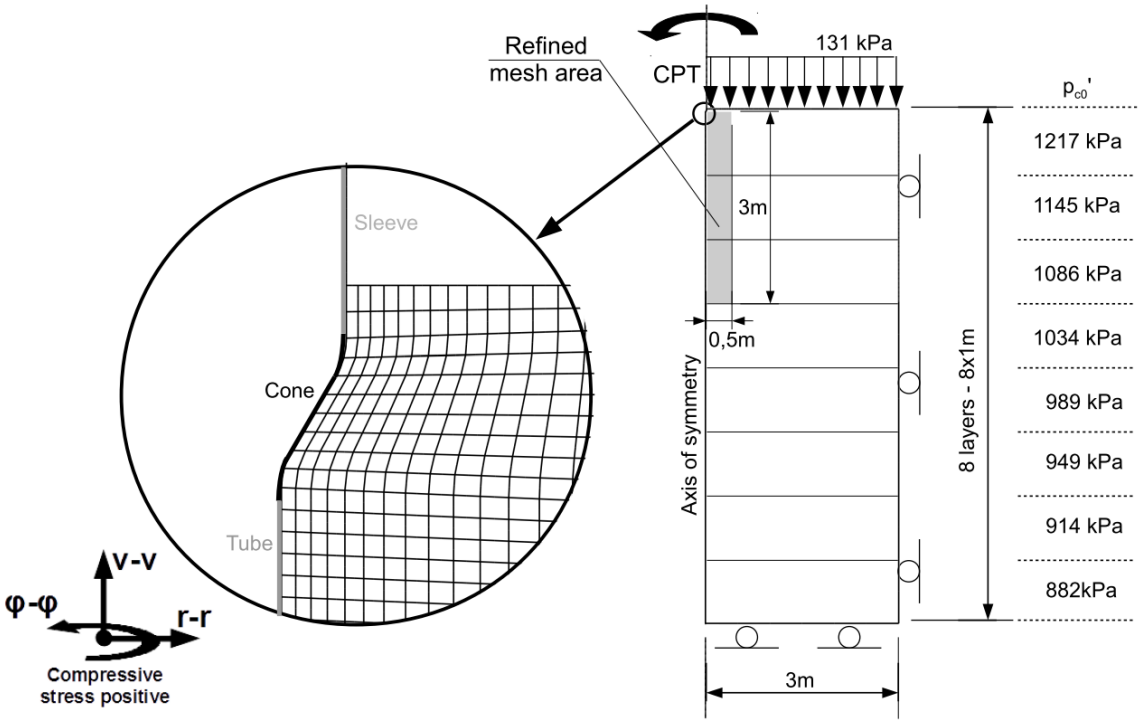

Figure 7.13. UL model for Poznań site

7.2.4 Numerical studies results

The cone resistance and sleeve friction obtained from numerical analysis and field measurement are presented in figure 7.14. Similarly as in the numerical calculations in chapter 5, the agreement between UL and ALE is quite good. Application of higher friction coefficient results in more accurate cone resistance distribution with depth in comparison to the field measurement. Although some differences exist, they can be dimmed by possible error due to mesh size. Application of friction coefficient of 0,287 which corresponds to the friction angle $\delta=\phi'_{cs}$ returns very satisfactory distribution of cone resistance in relation to the field measurement.

However, the sleeve friction is underestimated. Here, the opposite situation occurs to the CPT probing in Koszalin Clay. The dissipation test have been carried out at the depth of 7,5m and the calculation point was chosen above the connection between cone and sleeve, near the shoulder filter element localization. The results during equalization phase are summarized in figure 7.15, while the typical results for this site are presented in figure 7.16. It is worth to mention that data presented in figure 7.16 cannot be directly linked to the numerical investigation and only the general trends are valid. The field and numerical studies show the similar, approximately 33% reduction in cone resistance. The pore water dissipation curve obtained numerically is rather typical for overconsolidated soils (e.g., Bałachowski, 2006a; Sully et al., 1999). However, in Poznań area the registered u_2 pressure during field jacking was negative which is typical for highly overconsolidated soils. Consequently, in dissipation test the u_2 pressure increases to the hydrostatic value, see figure 7.16b. The opposite result has been archived numerically where high positive pressures have been observed. This implies

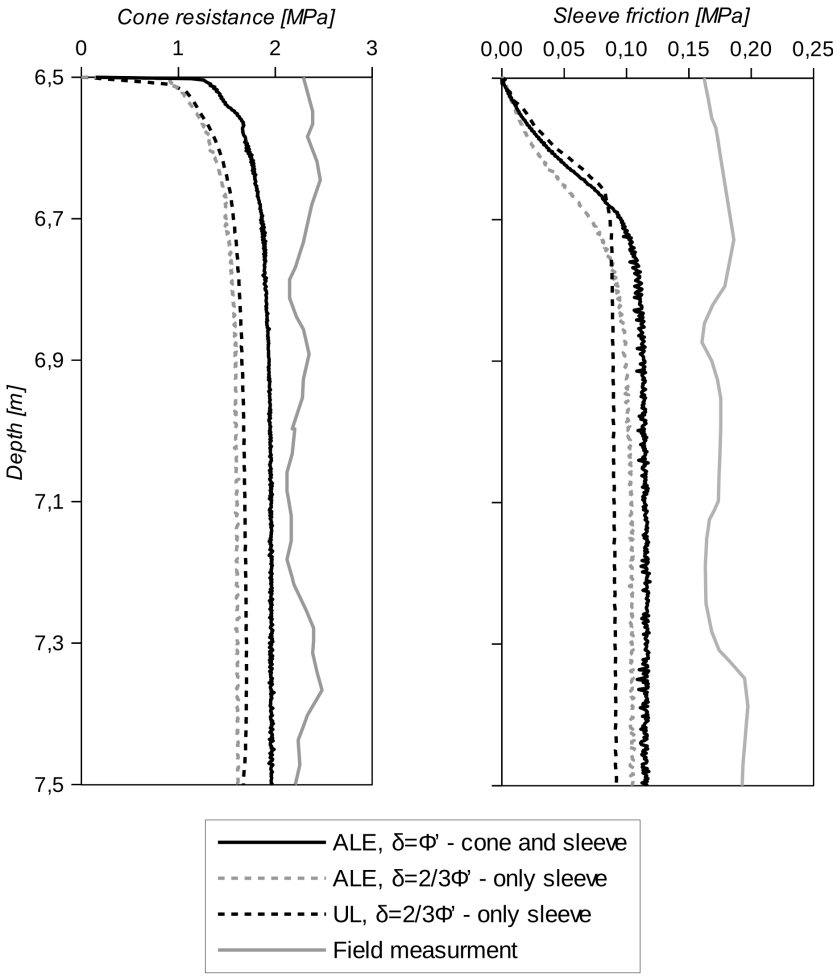

Figure 7. 14. Numerical results versus field measurement, Poznań site

(a)

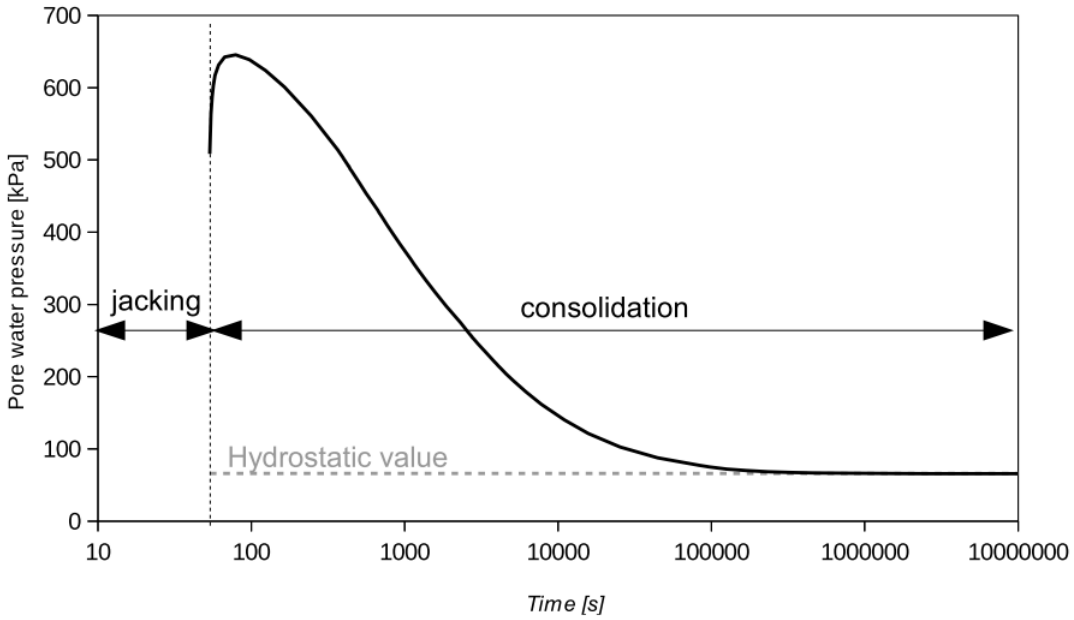

Figure 7.15. Numerical dissipation results in Poznań site: (a) pore water pressure and (b) cone resistance decays

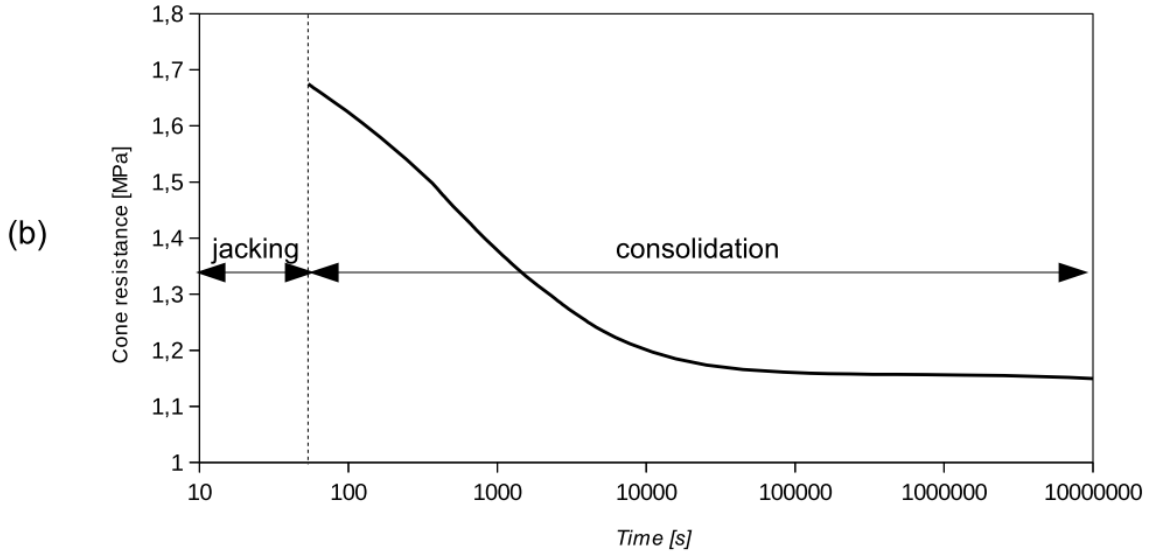

Figure 7.15. (continued)

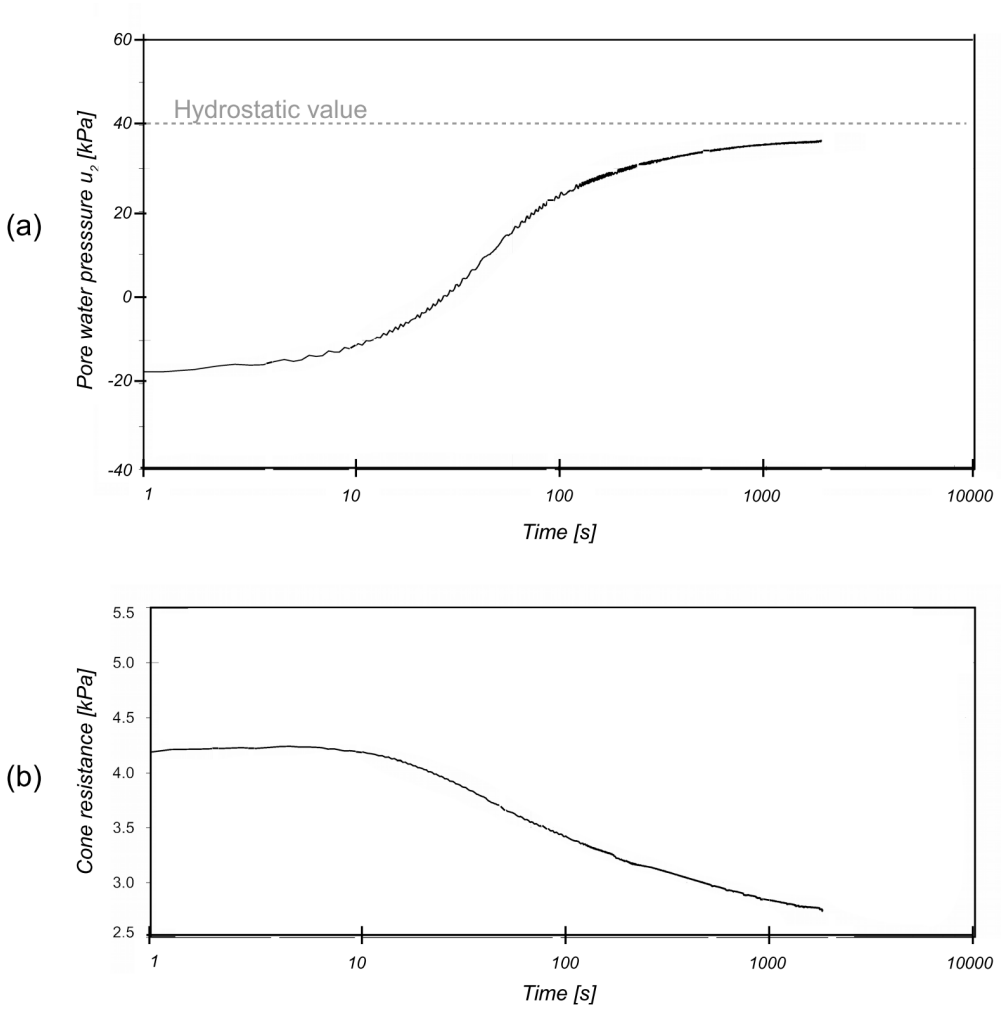

Figure 7.16. Example of typical field measurement of (a) pore water pressure and (b) cone resistance decays for clayey soil in Poznań site

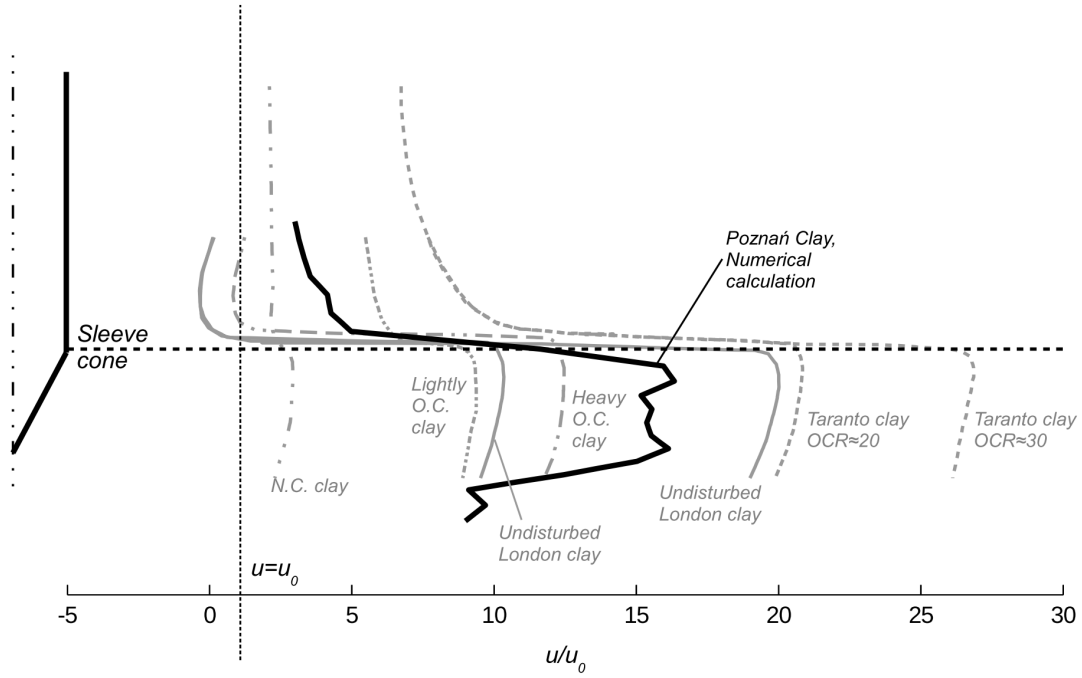

Figure 7.17. Normalized pore water pressure distributions around cone based on field measurements (after Robertson et al., 1986) and numerical study in Poznań Clay

that numerical model is not able to catch properly the drop in pore water pressure which occurs on cone face and behind the cone (Robertson et al., 1986). However, pore water pressures distributions around the cone tip respects the in-situ measured trends, see figure 7.17.

7.3 Summary

The ALE and UL methods have proved to be suitable numerical solutions for prediction of cone resistance, which confirmed previous research (e.g., Levadoux and Baligh, 1986; Sheng et al., 2013, 2014; Wei et al., 2005). However, the sleeve resistance is quite difficult to analyse. The sleeve friction was overestimated in lightly overconsolidated clay (Koszalin). On the other hand, the underestimation of f_s was observed in highly overconsolidated cohesive soil (Poznań). Sleeve friction is directly related to the radial stresses. Consequently, findings from CPT modelling correspond to the results of numerical simulation of pile installation in London clay. In London clay the underestimation of radial effective stress has been recognised in high OCR, undisturbed clay while overestimation has been seen in the disturbed clay. Numerical simulation of CPT probing conducted in this chapters seems to confirm observations made during the jacking of instrumented piles in highly overconsolidated London clay. It was also found that it is possible to numerically simulate pore water pressure distribution in the vicinity of the cone and to obtain the reasonable results.

Chapter 8

Installation effects – a numerical analysis

In this chapter the selected numerical studies from previous chapters will be extended by predefined tests to describe the stress state around the pile after installation and the consolidation phase. Firstly, the research testing program is based on preliminary studies presented in chapter 5. Secondly, the additional numerical tests are performed under prescribed assumptions. Finally, results from these tests and from tests presented in chapters 5, 6 and 7 will be combined together and they will be analysed to provide the empirical equation for horizontal stress component along the pile shaft after consolidation. The empirical formula will be focused on global soil behaviour around the central part of the pile shaft to avoid the influence of the pile toe on shaft resistance and poor reliability of numerical solutions near the surface level.

8.1 Research program description

The chapter 5 studies have provided the framework of possible factors which influence the radial effective stress as well as some limitation in compatibility between UL, ALE and CEL models. In this chapters only the UL and ALE formulations will be used due to theirs effectiveness (Wang et al., 2015) and good compatibility (see chapter 5).

8.1.1 Influencing factors

The four major factors influencing radial effective stress have been recognised in chapter 5 as: friction on pile-soil interface (δ), undrained shear strength (c_u), initial stress state (K_0) and shear modulus (G). Application of friction model on pile-soil interface results in not very accurate compatibility between ALE and UL formulation in general. Undrained shear strength is governing soil parameter that has the largest impact on radial stresses. Initial stress state represented by lateral earth pressure at rest coefficient or σ_h/σ_v ratio plays a minor role on installation effects, but it will be additionally investigated in this chapter. According to models previously tested in this thesis rigidity index (G/c_u ratio) higher than 40 does not show significant influence on radial stresses mobilized on the pile shaft.

8.1.2 Numerical testing program

Testing program consists of 7 tests selected from previous chapters and 9 tests which are conducted under assumptions presented in next section. Finally, these 16 tests are representative to analyse the installation effects in cohesive soils.

8.1.2.1 Assumption for nine additional tests

In all the 9 tests, the jacked pile 0,3m in diameter was modelled. According to preliminary studies, the soil domain is chosen as 30 diameters width and 60 diameters hight which is 9m and 18m, respectively. Jacking depth is fixed as 4,5m (15 pile diameters). The average and typical soil parameters for most clays are based on literature data and they are provided in table 8.1. The derived values of effective density and dry density are based on well-known relations (e.g., Atkinson, 2007):

$$\rho' = \rho_{sr} - \rho_w \tag{8.1}$$

$$\rho_d = \rho_{sr} - \left(\frac{e_0}{1+e_0} \right) \rho_w \tag{8.2}$$

where: ρ' – effective soil density, ρ_{sr} – total (saturated) soil density, ρ_w – density of water fixed as 1g/cm^3, ρ_d – soil dry density, e_0 – initial (virgin) soil void ratio.
The stress ratio M is calculated from effective angle of internal friction (e.g., Atkinson, 2007):

$$M = \frac{6 \sin \phi'}{3 - \sin \phi'} \tag{8.3}$$

where: M – stress ratio, ϕ' – effective angle of internal friction.
The compression index is based on empirical formula provided by Azzouz et al. (1976):

$$C_c = 0{,}4 \left(e_0 - 0{,}25 \right) \tag{8.4}$$

where: C_c – compression index, e_0 – virgin void ratio.
The plastic volumetric strain ratio is fixed as 0,8 due to its adequacy for many clays (Mayne, 1988) and it is defined as (Wroth, 1984):

$$\Lambda = 1 - \frac{\kappa}{\lambda} \tag{8.5}$$

where: Λ – plastic volumetric strain ratio, κ – elastic logarithmic bulk modulus, λ – plastic logarithmic bulk modulus.
Plastic logarithmic bulk modulus λ is related to the compression index C_c by equation (e.g, Plaxis Manuals, 2015):

$$\lambda = \frac{C_c}{2{,}3} \tag{8.6}$$

The CPT modelling in Chapter 7 and preliminary test with λ and κ used in equations (8.5) and (8.6) have revealed that very low values of plastic and elastic logarithmic moduli can provide numerical difficulties in modelling layered soil. In particular, UL and ALE solutions differ more than 20-25% in such case. Hence, λ and κ obtained from equations (8.5) and (8.6) have been multiplied by 10 and they return values equal to 0,610 and 0,122, respectively. These are still acceptable values for so-called fat clays and they will provide more accurate solution. The G/c_u ratio fixed as 50 is assumed with respect to chapter 5 findings to satisfy condition of $G/c_u \geq 40$ (see section 5.2.4.2) while the undrained shear strength is a governing parameter influencing installation effects.

Table 8.1. Typical geotechnical parameters of clay selected for the purposes of numerical tests

Parameter		Value	Units	Reference
Physical	ρ_{sr}	*2,1*	g/cm^3	*Terzaghi et al. (1996)*
	ρ'	*1,1*	g/cm^3	*derived, eq. (8.1)*
	ρ_d	1,725	g/cm^3	*derived, eq. (8.2)*
	e_0	*0,6*	-	*Terzaghi et al. (1996)*
Strength	φ'	*20*	^{o}	*Terzaghi et al. (1996)*
	M	*0,941*	-	*derived, eq. (8.3)*
	G/c_u	*50*	-	*Assumption*
	Λ	*0,8*	-	*Mayne (1988)*
	λ	*0,610*	-	*derived, eq. (8.6)*
	κ	*0,122*	-	*derived, eq. (8.5)*
Filtration	ρ_w	*1*	g/cm^3	-
	k	10^{-8}	*m/s*	*Atkinson (2007)*

Table 8.2. Numerical tests summary

No	*Pile Diameter* *m*	c_u *kPa*	G/c_u -	K_0 -	σ_h/σ_v * -	*Pile-soil behaviour*	*Conducted in chapter*
1	*0,3*	*300*	*50*	*2,0*	*1,524*	*frictionless*	*Chapter 8*
2	*0,3*	*300*	*50*	*0,5*	*0,738*	*frictionless*	*Chapter 8*
3	*0,3*	*300*	*50*	*1,0*	*1,000*	*frictionless*	*Chapter 8*
4	*0,3*	200	*50*	0,5	0,738	*frictionless*	*Chapter 8*
5	*0,3*	*200*	*50*	*1,0*	*1,000*	*frictionless*	*Chapter 8*
6	*0,3*	*200*	*50*	*2,0*	*1,524*	*frictionless*	*Chapter 8*
7	*0,3*	*100*	*50*	0,5	0,738	*frictionless*	*Chapter 8*
8	*0,3*	*100*	*50*	*1,0*	*1,000*	*frictionless*	*Chapter 8*
9	*0,3*	*100*	*50*	*2,0*	*1,524*	*frictionless*	*Chapter 8*
10	*0,5*	*80*	*~40*	*1,0*	*1,000*	*frictionless*	*Chapter 5*
11	*0,5*	*80*	*~40*	*0,56*	*0,760*	*frictionless*	*Chapter 5*
12	*0,5*	*80*	*~40*	*1,44*	*1,240*	*frictionless*	*Chapter 5*
13	*0,102*	*75*	*~67*	*1,0*	*1,000*	*friction*	*Chapter 6*
14	*0,102*	*75*	*~67*	*1,9*	*1,590*	*friction*	*Chapter 6*
15	*0,102*	*120*	*~67*	*2,15*	*1,790*	*friction*	*Chapter 6*
16	*0,03568*	*110*	*~162*	*2,0*	*1,500*	*friction*	*Chapter 7*

* Calculated by equation (3.37)

8.1.2.2 Tests summary

The 16 tests considered in installation effect estimations are summarized in table 8.2. Tests denoted by numbers 1 to 9 will be conducted in this chapter while tests from no. 10 to no. 16 are selected from previous chapters. As one can see, in summarized tests piles with different diameters are used, different soil conditions are applied and even different friction behaviour on pile-soil interface is considered. This extensive spectrum of testing conditions is chosen to shed possible wide light on installation effects that can be provided by numerical methods.

8.2 Numerical models of jacked piles

Tests performed in this section contain nine, 0,3m diameter piles jacked 4,5m into subsoil. The piles are pre-installed in soil at the depth of 0,325m. The axisymmetric soil domain has dimensions of 9m per 18m both for ALE and UL models. The details of soil models are provided in sections below.

Table 8.3. *Total stress parameters for ALE models*

Test No	ρ_{sr}	E_u	υ_u	c_u	σ_h/σ_v
	g/cm³	*kPa*	-	*kPa*	-
1		*44700*		*300*	*1,524*
2		*44700*		*300*	*0,738*
3		*44700*		*300*	*1,000*
4		*29800*		200	*0,738*
5	*2,1*	*29800*	*0,49*	*200*	*1,000*
6		*29800*		*200*	*1,524*
7		*14900*		100	*0,738*
8		*14900*		*100*	*1,000*
9		*14900*		*100*	*1,524*

Table 8.4. MCC parameters for UL models

Parameter	ρ'	G'	e_0	κ	λ	p_c'	M	ρ_w	K_0	k
	g/cm³	*kPa*	-	-	-	*kPa*	*kPa*	*g/cm³*	-	*m/s*
Value	*1,1*	*varying*	*0,6*	*0,122*	*0,610*	*varying*	*0,941*	*1,0*	*varying*	10^{-8}

8.2.1 ALE models

The soil parameters used in ALE models are presented in table 8.3. The parameters are based on data shown in tables 8.1. and 8.2 to fulfil testing program assumptions. The model geometry is illustrated in figure 8.1. The soil domain is discretized with 14490 CAX4R elements with minimum size of 3x3cm in jacking area. The pile has been jacked with zipper-type technique (Mabsout and Tassoulas, 1994) with rate of 1cm/s. No overburden pressure has been applied and frictionless behaviour on soil-pile interface has been used.

8.2.2 UL models

The UL model geometry is presented in figure 8.2 and the soil parameters are summarised in table 8.4 and in table 8.5 where constant parameters and variables are summarized. The 24 layers of soil have been created to take into account the varying preconsolidation pressure and

to provide the same undrained shear strength in the soil profile. The overburden pressure of 1kPa has been applied to sustain the stability of the solution. The pile was jacked using zipper-type technique (Mabsout and Tassoulas, 1994) to the depth of 4,5m with rate of 1cm/s. The Soil domain is discretized using CAX8RP elements and no friction behaviour was used in UL model. At the consolidation phase the pile position was fixed at the depth of 4,5m.

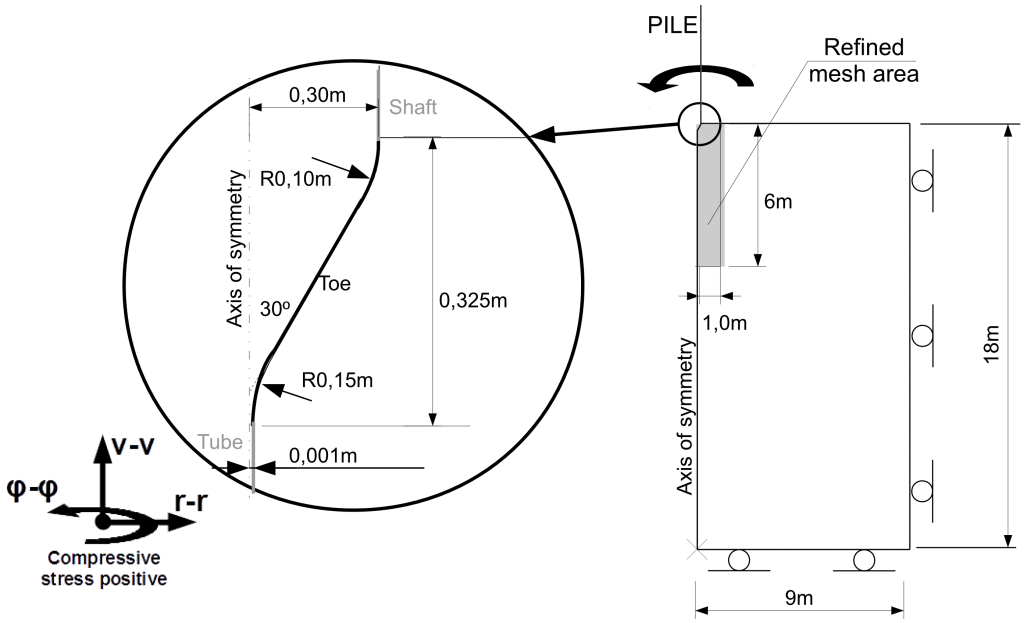

Figure 8.1. Geometry of complementary ALE models

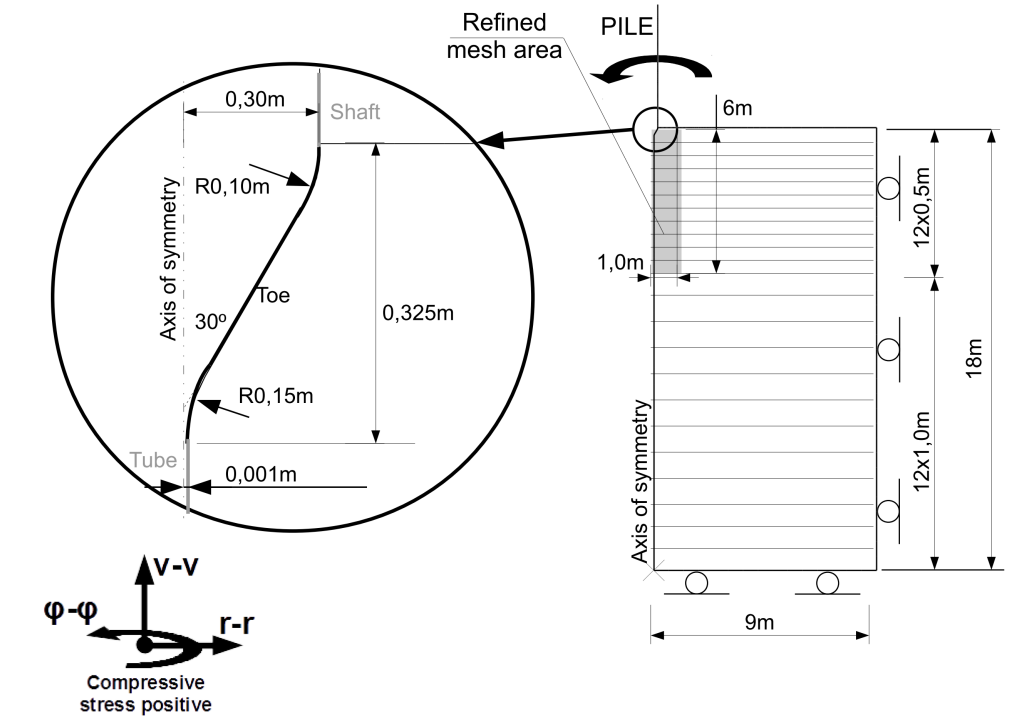

Figure 8.2. Geometry of complementary UL models

Table 8.5. UL model parameters

Test No	*G*	*p_c'*	*K_0*	*Elements number*	*Minimum element size*
	kPa	*kPa*	*-*	*-*	*cm*
1	*15000*	*4380÷1514*	*2,0*	*11813*	*2,0x2,0*
2	*15000*	*5507÷1904*	*0,5*	*7288*	*3,0x3,0*
3	*15000*	*4976÷1720*	*1,0*	*7194*	*2,0x4,0*
4	*10000*	*3317÷1147*	*0,5*	*9973*	*2,0x2,0*
5	*10000*	*2998÷1036*	*1,0*	*11968*	*2,0x2,0*
6	*10000*	*2638÷912*	*2,0*	*10373*	*2,0x2,0*
7	*5000*	*1395÷482*	*0,5*	*13372*	*1,5x2,0*
8	*5000*	*1260÷436*	*1,0*	*13175*	*1,5x2,0*
9	*5000*	*1109÷383*	*2,0*	*14077*	*1,0x2,0*

8.3 Results

The analysis of results in terms of installation effects will be mainly focused on the radial stresses and the pore water-pressures distributions along the pile shaft. However, the stresses and pore water pressures generated under the pile toe will be also analysed. The physical state around the pile after installation and consolidation will be also discussed.

8.3.1 Post-installation state

Relatively good compatibility between UL and ALE models in tests from no. 6 to no. 16. is achived. However, in tests no. 1 to no. 5 where large values of initial plastic surface have to be applied to satisfy high undrained shear strength, the UL solution is underestimated for the upper part of the pile and overestimated for the lower part. The best coincidence between UL and ALE models is observed in the middle part of the pile. Consequently, this part of pile and especially halfway of the pile length will be considered as the most reliable and it will be used for detailed analysis.

The analysis of post-installation phase starts with compatibility between ALE and UL at the end of this step. Similar studies have been made in previous chapters, but here they will be shown once again to prove that the soil condition after installation is nearly the same in ALE and UL formulations. Next, the distributions of normalized radial effective stresses and pore water pressures will be presented and the discussion of results will be made.

8.3.1.1 Pile shaft

The compatibility between radial total stresses for 16 tests are shown in table 8.6. The reference location as the halfway of the pile length has been selected for the homogeneous soil models or as a halfway of layer thickness for layered soil models (tests no. 13, no. 14 and no. 15). As can be seen, the UL formulation provides slightly overestimated solutions but the agreement between UL and ALE is relatively good with COV of 12%. The differences are caused by severe mesh distortions and application of high initial yield surface sizes in some tests.

The effective radial stress versus normalized depth plots are presented in figure 8.3. The

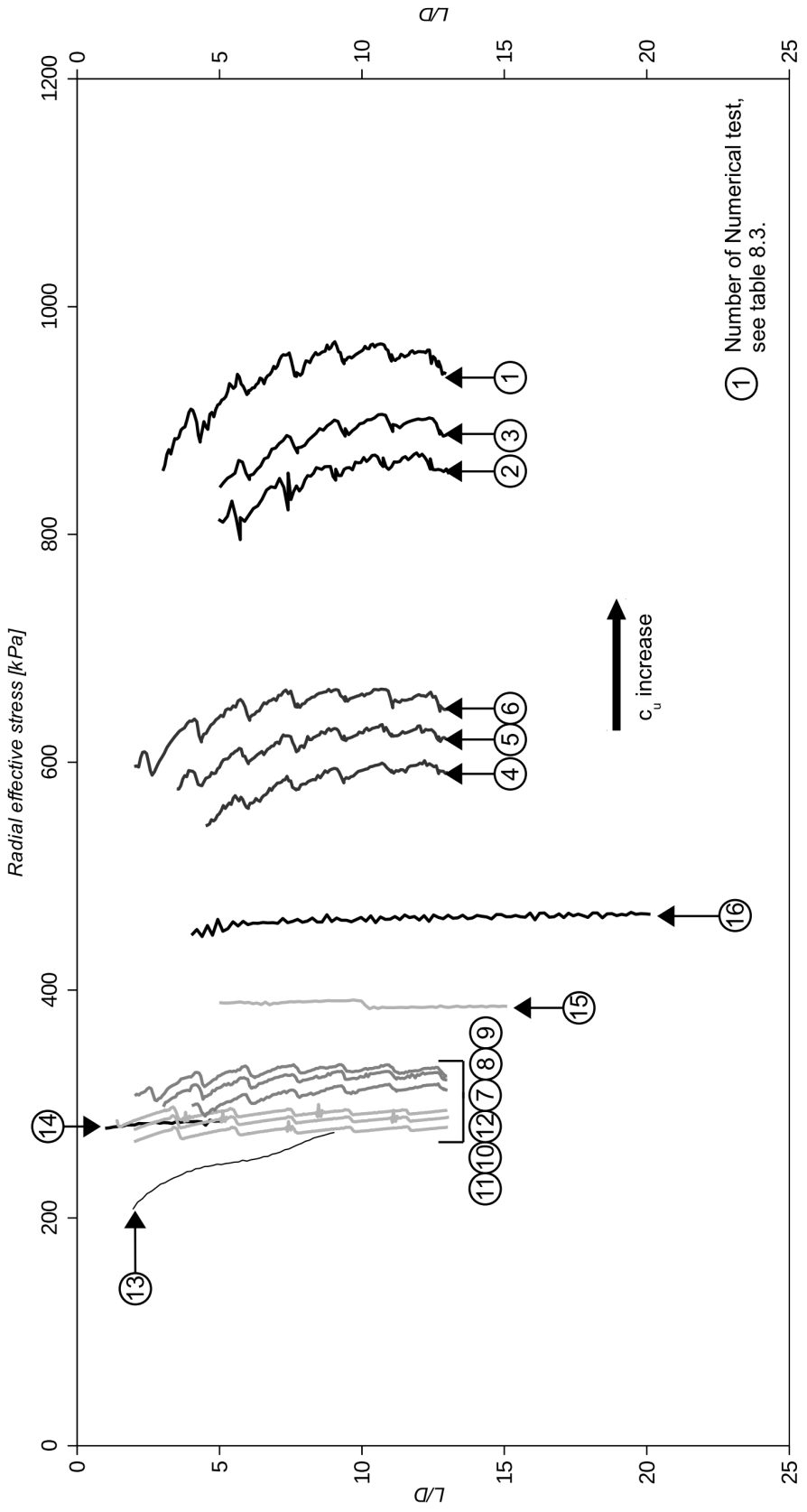

Figure 8.3. Effective stress distributions after installation phase

Table 8.6. ALE and UL models compatibility (pile half-length)

Test no	σ_h^{ALE}	σ_h^{UL}	$\sigma_h^{ALE}/\sigma_h^{UL}$
	kPa	*kPa*	-
1	*1067,93*	*1011,55*	*1,06*
2	*1038,76*	*895,15*	*1,16*
3	*1040,57*	*897,11*	*1,16*
4	*698,74*	*603,55*	*1,16*
5	*710,81*	*669,89*	*1,06*
6	*729,29*	*742,35*	*0,98*
7	*370,34*	*350,64*	*1,06*
8	*378,59*	*382,62*	*0,99*
9	*401,86*	*413,73*	*0,97*
10	*351,59*	*378,16*	*0,93*
11	*335,98*	*336,85*	*1,00*
12	*372,18*	*407,55*	*0,91*
13	*227,11*	*273,29*	*0,83*
14	*277,36*	*360,29*	*0,77*
15	*453,52*	*559,89*	*0,81*
16	*501,38*	*589,87*	*0,85*
		AVG	*0,97*
		COV	*0,13*

Table 8.7. Effective stress after installation - CEM vs UL formulation *(pile half-length)*

Test no	$\sigma_h'^{UL}$	c_u	*M*	$\sigma_h'^{CEM}$	$\sigma_h'^{UL}/\sigma_h'^{CEM}$
	kPa	*kPa*	-	*kPa*	-
1	*935,77*	*300*	*0,941*	*852,19*	*0,91*
2	*822,54*	*300*	*0,941*	*852,19*	*1,04*
3	*859,57*	*300*	*0,941*	*852,19*	*0,99*
4	*567,55*	*200*	*0,941*	*568,13*	*1,00*
5	*607,90*	*200*	*0,941*	*568,13*	*0,93*
6	*646,10*	*200*	*0,941*	*568,13*	*0,88*
7	*302,82*	*100*	*0,941*	*284,06*	*0,94*
8	*316,85*	*100*	*0,941*	*284,06*	*0,90*
9	*324,71*	*100*	*0,941*	*284,06*	*0,87*
10	*287,58*	*80*	*0,835*	*245,94*	*0,83*
11	*276,71*	*80*	*0,835*	*245,94*	*0,89*
12	*294,63*	*80*	*0,835*	*245,94*	*0,83*
13	*245,01*	*75*	*0,877*	*223,12*	*0,91*
14	*281,37*	*75*	*0,877*	*223,12*	*0,79*
15	*391,87*	*120*	*0,877*	*357,00*	*0,91*
16	*463,38*	*110*	*0,601*	*427,01*	*0,92*
				AVG	*0,91*
				COV	*0,07*

distributions are only shown for normalized L/D distances for which ALE and UL solutions in terms of total stress differs no more than 20%. The radial total stress plots obtained from ALE

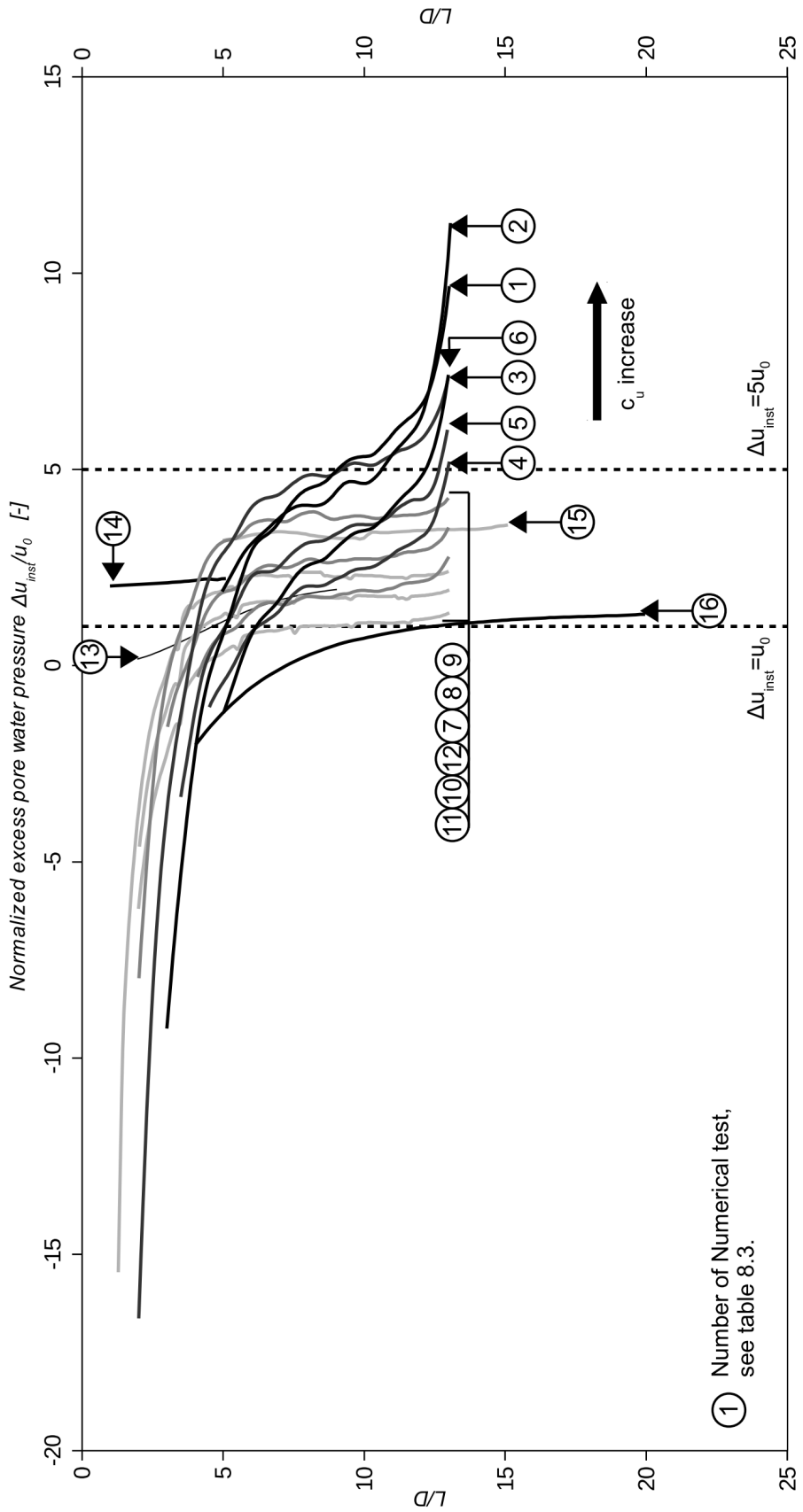

Figure 8.4. Normalized excess pore water pressure distributions after installation phase

Table 8.8. Pore water pressure and total stress after installation - CEM vs UL formulation (pile half-length)

Test no	u^{UL}	c_u	G	p_0'	p_c'	κ	λ	p_f'	u_{oct}	u_{shear}	u_0	u^{CEM}
	kPa	kPa	kPa	kPa	kPa	-	-	kPa	kPa	kPa	kPa	kPa
1	75,78	300	15000	41,25	2529	0,1220	0,6100	637,6	1173,6	-596,37	22,5	599,74
2	72,61	300	15000	16,50	3180	0,1220	0,6100	637,6	1173,6	-621,12	22,5	574,99
3	37,54	300	15000	24,75	2873	0,1220	0,6100	637,6	1173,6	-612,87	22,5	583,24
4	36,00	200	10000	41,25	1915	0,1220	0,6100	425,1	782,6	-408,58	22,5	396,33
5	61,99	200	10000	16,50	1731	0,1220	0,6100	425,1	782,6	-400,33	22,5	404,57
6	96,25	200	10000	24,75	1523	0,1220	0,6100	425,1	782,6	-383,38	22,5	421,08
7	47,82	100	5000	41,25	805	0,1220	0,6100	212,5	391,2	-196,04	22,5	217,66
8	65,78	100	5000	16,50	728	0,1220	0,6100	212,5	391,2	-187,79	22,5	225,91
9	89,02	100	5000	24,75	640	0,1220	0,6100	212,5	391,2	-171,29	22,5	242,41
10	90,59	80	3355,7	48,00	432	0,0800	1,0000	191,6	298,9	-143,61	40,0	195,30
11	60,14	80	3355,7	33,92	446	0,0800	1,0000	191,6	298,9	-157,69	40,0	181,22
12	112,92	80	3355,7	62,08	423	0,0800	1,0000	191,6	298,9	-129,53	40,0	209,38
13	28,28	75	5000	30,00	412	0,0894	0,9210	171,0	315,0	-140,98	15,0	189,00
14	78,92	75	5000	65,60	379	0,0894	0,9210	171,0	315,0	-105,38	25,0	234,60
15	168,02	120	8000	101,47	609	0,0894	0,9210	273,5	504,0	-172,07	40,0	371,89
16	126,49	110	17800	135,20	1217	0,0250	0,0740	366,1	559,5	-230,86	60,0	388,66

and UL models are summarized in Appendix D. A significant increase in radial effective stress with undrained shear strength can be observed. The influence of initial stress state represented by lateral earth et rest coefficient can be also noticed, but generally it can be neglected as a minor factor, especially for lower values of undrained shear strength. This observation is generally consistent with numerical analysis performed by Randolph (1979a). As plastic zone around the pile is created, the initial stress state should not affect the resulting stress distributions. The differences in radial effective stress distributions along the normalized length in some tests are affected by mesh distortions and "trial and errors" method during the mesh generation for successful jacking modelling. Additionally, the numerical solution for c_u of 200 and 300kPa seems to be less reliable, probably due to large dimensions of initial yield surface. As it was mentioned in chapter 5 the CEM solution for effective stress calculation after installation provides good approximation of numerical studies. In CEM method the constant value of radial effective stress along the pile wall is calculated, see equation (5.3). The results are summarized in table 8.7 and the value of radial effective stress corresponding to the pile half-length is assumed as the referential one from numerical analysis. As can be seen, the CEM solution underestimates the UL results and COV for $\sigma_h'^{UL}/\sigma_h'^{CEM}$ ratio is about 7%. Due to the fact that UL gives higher values than ALE, the CEM approximation can be treated as a safe and conservative assessment.

The excess pore water pressures distributions after installation normalized by hydrostatic value are shown in figure 8.4. As can be seen, due to different initial pore water pressure condition the excess pore water pressures are slightly different in each numerical test. However, some common trends can be noted. Firstly, the suction in the upper part of the pile shaft can be observed and it is related to the shear component of excess pore water pressures (e.g., Randolph and Wroth, 1979). Also the significant increase in pore water pressure can be seen near shaft-toe transition, which was already commented in chapter 5, section 5.2.2.1. The average value of excess pore water pressure is between 1 and 5 times the hydrostatic value and the safe assumption is that average excess pore water pressure is about u_0.

The analytical methods based on cylindrical cavity expansion propose the following formula for pore water pressure after installation (e.g, Burns and Mayne, 1998; Randolph et al., 1979a):

$$u_{inst} = \Delta u_{oct} + \Delta u_{shear} + u_0 \tag{8.7}$$

where: u_{inst} – pore water pressure after installation, Δu_{oct} – octahedral component of excess pore water pressure, Δu_{shear} – shear component of excess pore water pressure, u_0 – hydrostatic pore water pressure.

The octahedral component of excess pore water pressure can be calculated from CEM solution as (Randolph et al., 1979a):

$$u_{oct} = c_u \ln\left(\frac{G}{c_u}\right) \tag{8.8}$$

where: Δu_{oct} – octahedral component of excess pore water pressure, c_u – undrained shear

strength of soil, G – shear modulus.
The shear component of excess pore water pressure can be derived from MCC model and it is provided as (e.g., Chen and Mayne, 1994; Randolph et al., 1979a):

$$u_{shear} = p_0' - p_f' = p_0' \left(1 - \left(\frac{p_c'}{2\,p_0'} \right)^{\Lambda} \right) \tag{8.9}$$

where: Δu_{shear} – shear component of excess pore water pressure, p_0' – initial mean pressure, p_f' - mean pressure at failure, Λ – plastic volumetric strain ratio.

The comparison between analytical solution given by CEM and numerical ones obtained by UL is summarized in table 8.8. In the first part of the table the analytical method for ideal undrained conditions is compared with UL results and, as can be seen, the analytical method returns completely different values of u_{inst}. Table 8.9 shows the total stress obtained from UL, ALE and analytical method. Here, the curious aspect can be observed as the total stress in CEM is overestimated by 12-51% with medium value of 38% (COV=11%) in comparison to UL formulation and even higher in comparison to the ALE method (21-81% with medium value of 42% and COV=12%). Consequently, in terms of UL and ALE applicability presented in chapters 6 and 7, the analytical methods such as CEM provide poor reliability of total stress and pore water pressure predictions around pile shaft. This conclusions has been also verified in previous years by field and laboratory tests (e.g., Bond and Jardine, 1991).

Table 8.9. Total stress after pile installation - CEM vs UL vs ALE (pile half-length)

Test no	σ_h^{UL}	σ_h^{ALE}	σ_h^{CEM}	$\sigma_h^{CEM}/\sigma_h^{UL}$	$\sigma_h^{ALE}/\sigma_h^{CEM}$
	kPa	*kPa*	*kPa*	-	-
1	*1011,55*	*1067,93*	*1451,93*	*1,44*	*1,36*
2	*895,15*	*1038,76*	*1427,18*	*1,59*	*1,37*
3	*897,11*	*1040,57*	*1435,43*	*1,60*	*1,38*
4	*603,55*	*698,74*	*964,46*	*1,60*	*1,38*
5	*669,89*	*710,81*	*972,7*	*1,45*	*1,37*
6	*742,35*	*729,29*	*989,21*	*1,33*	*1,36*
7	*350,64*	*370,34*	*501,73*	*1,43*	*1,35*
8	*382,62*	*378,59*	*509,98*	*1,33*	*1,35*
9	*413,73*	*401,86*	*526,48*	*1,27*	*1,31*
10	*378,16*	*351,59*	*441,25*	*1,17*	*1,26*
11	*336,85*	*335,98*	*427,16*	*1,27*	*1,27*
12	*407,55*	*372,18*	*455,33*	*1,12*	*1,22*
13	*273,29*	*227,11*	*412,12*	*1,51*	*1,81*
14	*360,29*	*277,36*	*457,72*	*1,27*	*1,65*
15	*559,89*	*453,52*	*728,89*	*1,30*	*1,61*
16	*589,87*	*501,38*	*815,67*	*1,38*	*1,63*
			AVG	*1,38*	*1,42*
			COV	*0,11*	*0,12*

Table 8.10. Total cone resistance and pore water pressure beneath the cone - CEM vs UL formulation

Test no	q_f^{ALE}	q_f^{UL}	u_{max}^{UL}	q_f^{ALE}/q_f^{UL}	c_u	N_c	G	p_0'	u_{oct}	u_{shear}	u_0	u^{CEM}	u^{CEM}/u_{max}^{UL}
	kPa	*kPa*	*kPa*	-	*kPa*	-	*kPa*	*kPa*	*kPa*	*kPa*	*kPa*	*kPa*	-
1	*2790,67*	*2506,28*	*1852*	*1,11*	*300*	*9,16*	*15000*	*82,5*	*1565*	*165*	*45*	*1775*	*0,96*
2	*2714,00*	*2031,41*	*1631*	*1,34*	*300*	*8,33*	*15000*	*33*	*1565*	*66*	*45*	*1676*	*1,03*
3	*2740,61*	*2361,17*	*1748*	*1,16*	*300*	*8,04*	*15000*	*49,5*	*1565*	*99*	*45*	*1709*	*0,98*
4	*1831,14*	*1586,14*	*1176*	*1,15*	*200*	*8,51*	*10000*	*33*	*1043*	*66*	*45*	*1154*	*0,80*
5	*1860,93*	*1655,31*	*1246*	*1,12*	*200*	*9,37*	*10000*	*49,5*	*1043*	*99*	*45*	*1187*	*0,95*
6	*1908,31*	*1763,48*	*1330*	*1,08*	*200*	*9,15*	*10000*	*82,5*	*1043*	*165*	*45*	*1253*	*0,94*
7	*937,46*	*900,13*	*662,9*	*1,04*	*100*	*9,63*	*5000*	*33*	*522*	*66*	*45*	*633*	*0,95*
8	*979,19*	*946,23*	*704,1*	*1,03*	*100*	*9,92*	*5000*	*49,5*	*522*	*99*	*45*	*666*	*0,95*
9	*1024,83*	*1042,37*	*772,3*	*0,98*	*100*	*9,46*	*5000*	*82,5*	*522*	*165*	*45*	*732*	*0,95*
10	*833,40*	*825,31*	*620,2*	*1,01*	*80*	*10,32*	*3355,7*	*96*	*399*	*192*	*80*	*671*	*1,08*
11	*787,07*	*767,92*	*567,2*	*1,02*	*80*	*9,6*	*3355,7*	*67,84*	*399*	*136*	*80*	*614*	*1,08*
12	*964,77*	*874,81*	*671,4*	*0,99*	*80*	*10,94*	*3355,7*	*124,16*	*399*	*248*	*80*	*727*	*1,08*
13	*805,32*	*780,62*	*507,8*	*1,03*	*75*	*10,41*	*5000*	*41*	*420*	*82*	*20*	*522*	*1,03*
14	*941,45*	*916,36*	*649,6*	*1,03*	*75*	*12,22*	*5000*	*83,2*	*420*	*166*	*30*	*66*	*0,95*
15	*1367,15*	*1333,97*	*984,5*	*1,02*	*120*	*11,12*	*8000*	*130,73*	*672*	*261*	*50*	*983*	*1,00*
16	*1621,96*	*1677,99*	*1085*	*0,97*	*110*	*15,25*	*17800*	*143,67*	*746*	*287*	*65*	*1098*	*1,01*
			AVG	*1,07*								*AVG*	*1,00*
			COV	*0,09*								*COV*	*0,05*

8.3.1.2 Pile toe

The compatibility of ALE and UL solutions is presented in terms of cone resistance ratio at the end of installation, see table 8.10. As can be seen in chapter 5, section 5.2.2.1, this criterion can be also successfully used to ensure ALE and UL compatibility. The N_c coefficient has been calculated using the formula for the pile toe capacity in undrained conditions (e.g., Tomlinson and Woodward, 2015):

$$N_c = \frac{q_f}{c_u} \tag{8.10}$$

where: N_c – bearing capacity coefficient, q_f – ultimate pile toe resistance, c_u – undrained shear strength of soil.

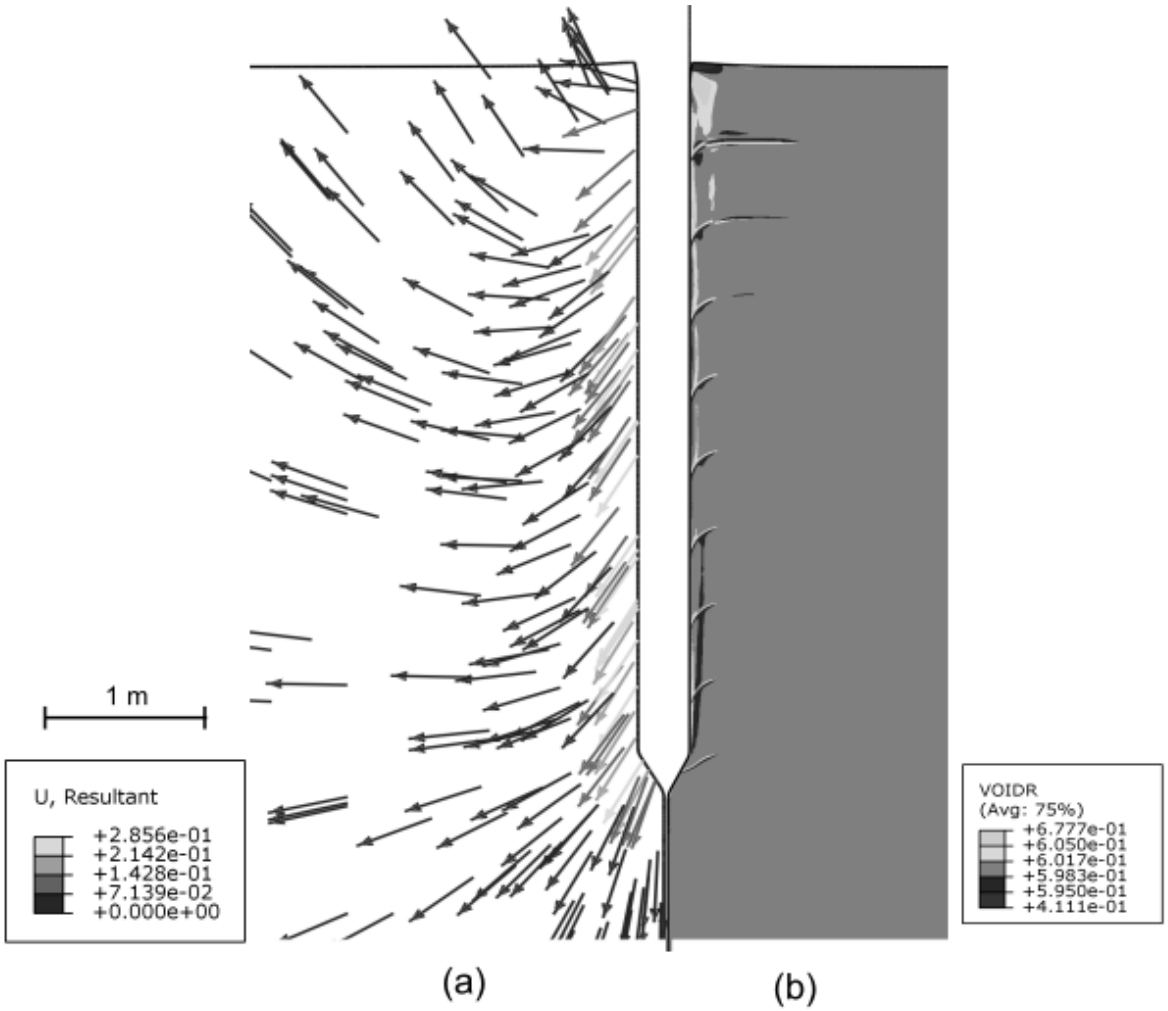

Figure 8.5. Physical change around the pile after installation: (a) deformation and (b) void ratio

As can be seen in table 8.10, for most of tests the obtained N_c factor is close to 9 which induces the classical theorem (e.g., Yu et al., 2007). In some cases, N_c is significantly higher

which is related to high G modulus, see chapter 5 section 5.2.3.1. As it was explained, the applied numerical formulation does not allow for the scale effects consideration, so this high N_c value is only induced by applied elastic modulus ratio. The maximum pore water pressure registered in UL solutions has been compared with analytical method based on spherical cavity expansion. The pore water pressure based on spherical CEM is described with formula (Burns and Mayne, 1998):

$$u_{inst} = \Delta u_{oct} + \Delta u_{shear} + u_0 \tag{8.11}$$

where:

$$u_{oct} = \frac{4}{3} c_u \ln\left(\frac{G}{c_u}\right) \tag{8.12}$$

$$u_{shear} = 2\, p_0' \tag{8.13}$$

where: u_{int} – pore water pressure after installation, Δu_{oct} – octahedral component of excess pore water pressure, Δu_{shear} – shear component of excess pore water pressure, u_0 – hydrostatic pore water pressure, c_u – undrained shear strength of soil, G – shear modulus, p_0' – initial mean pressure.

The comparison presented in table 8.10 shows that very satisfactory agreement has been achieved. Hence, the same conclusion can be drawn like in previous chapters: both numerical and analytical methods provides reliable estimation of soil behaviour under the pile toe.

8.3.1.3 Physical changes

The test number 9 has been selected as the reference one to present the physical changes around the pile. Figure 8.5 shows the soil deformation and void ratio after installation. As can be seen, the soil movement around the pile is a combination of vertical and horizontal displacements. This is the main advantage of UL formulation in comparison to the cylindrical CEM method. Consequently, this is the reason why cylindrical CEM cannot provide proper solution for pile installation and why spherical CEM gives good results for cone penetration. The void ratio change after installation is rather small, so even if almost undrained conditions are modelled, there is always possibility that a small amount of consolidation has taken place, especially in layer borders and on the pile wall, see figure 8.5.

8.3.2 Post-consolidation state

The analysis of post-consolidation state will be concentrated on the same aspects as in post-installation phase i.e.: pile shaft, pile toe and physical changes around the pile. The analysis, similar as in post-installation phase, concerns middle part of pile.

8.3.2.1 Pile shaft

The radial effective stress distribution along the pile is presented in figure 8.6 for the same normalized depth as in post-installation phase. The formula for horizontal stress component after installation and consolidation is usually expressed as (Randolph et al., 1979a):

$$\sigma'_{rr,eq} = \sigma'_{rr,inst} + \Delta u_{inst} \tag{8.14}$$

where: $\sigma'_{rr,eq}$ – radial effective stress after consolidation, $\sigma'_{rr,inst}$ – radial effective stress after installation, Δu_{inst} – excess pore water pressure generated after installation.
The aim of this thesis is to provide some general formula for radial stresses after installation. It has to fulfil two conditions: it has to be safe and as simple as possible. The numerical tests conducted in this thesis generally show that the effective stress distribution $\sigma'_{rr,eq}$ can be assumed as in CEM method (Randolph et al., 1979a):

$$\sigma'_{rr,inst} = \left(\frac{\sqrt{3}}{M} + 1 \right) c_u \tag{8.15}$$

where: $\sigma'_{rr,inst}$ – radial effective stress after installation, M – stress ratio, c_u – undrained shear strength.

The problem arises with proper estimation of excess pore water pressures. In chapter 6 it has been shown that UL formulation provides overestimated pore water pressures. The second problem is the applied constitutive law. The high suction in the upper part of the pile shaft after pile installation is rather unrealistic. As the numerical solution for pile shaft is disturbed in near surface area, the halfway value is chosen as the more appropriate and similar to the real in-situ conditions. This assumption is also verified by relatively good results from numerical models of instrumented piles, see chapter 6. The excess pore water pressure calculated in previous section suggests that the safe value is $\Delta u_{inst} \approx u_0$, see figure 8.4. However, application of this formula is troublesome for saturated clays above the water table level and for offshore structures and piles installed at the high depths below sea level. As in numerical studies presented here, the water table was always close to the surface level and density of soil ρ' is close to the density of water, the following revision can be made to provide hydrostatic pressure independence:

$$\Delta u_{inst} \approx u_0^{(\text{for water table level = surface level})} \approx \sigma'_{v,0} \tag{8.16}$$

where: Δu_{inst} – excess pore water pressure generated after installation, u_0 – hydrostatic pressure when water table is near the surface level, $\sigma'_{v,0}$ – initial geostatic stress.
The figure 8.7 shows that excess pore water pressure normalized by initial vertical effective stress can be successfully used as a good approximation of the Δu_{inst}. Similar observations about excess pore water pressures after installation can be observed in field tests performed or summarized by Karlsrud (2012) in West Delta, Onsoy, Lierstranda, Pentre and Tilbrooke and Pestana (2002) at Islais Creek, California. The second possible and very conservative approach is to assume that:

$$\Delta u_{inst} = 0 \tag{8.17}$$

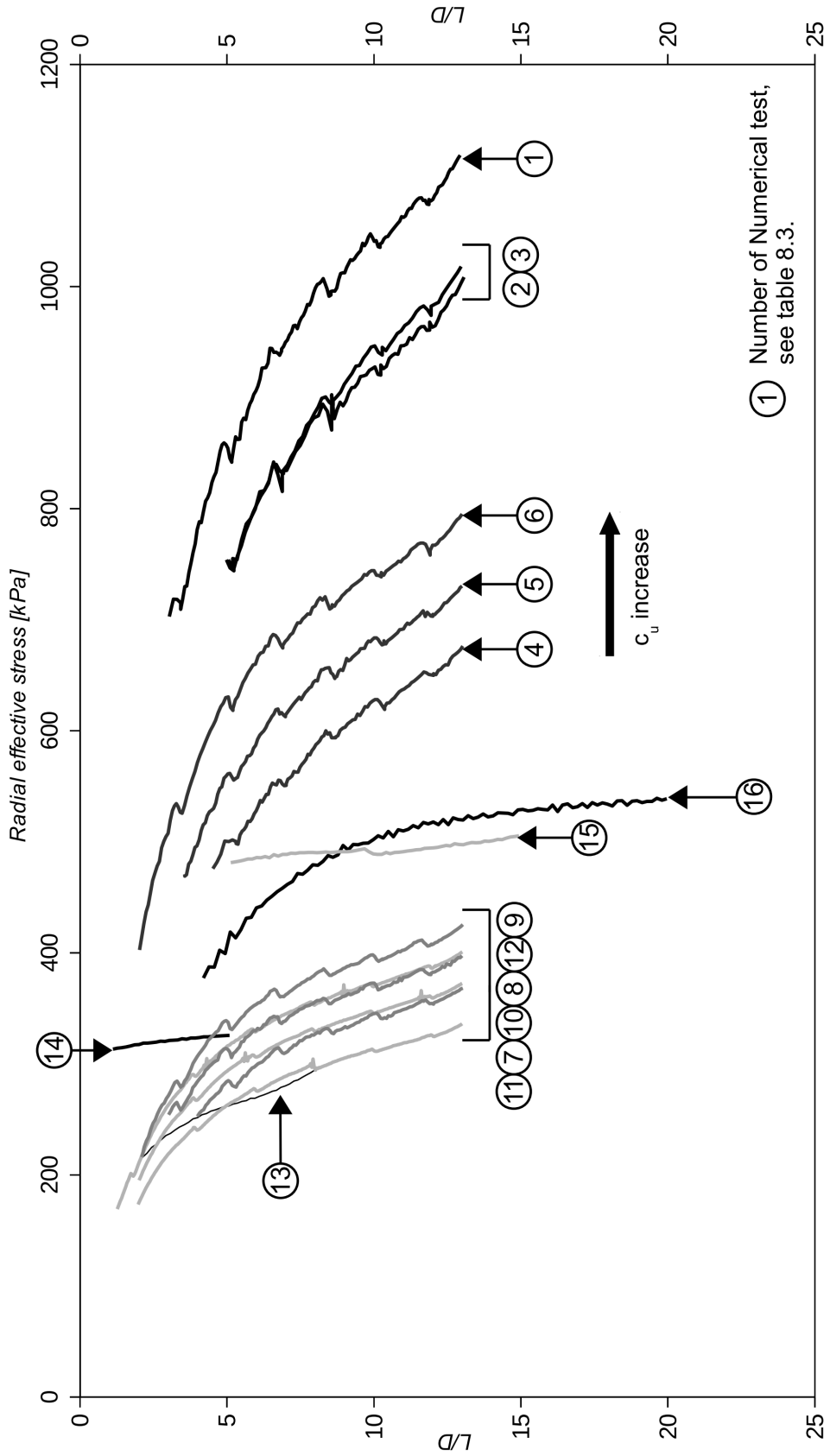

Figure 8.6. Effective stress distributions after consolidation phase

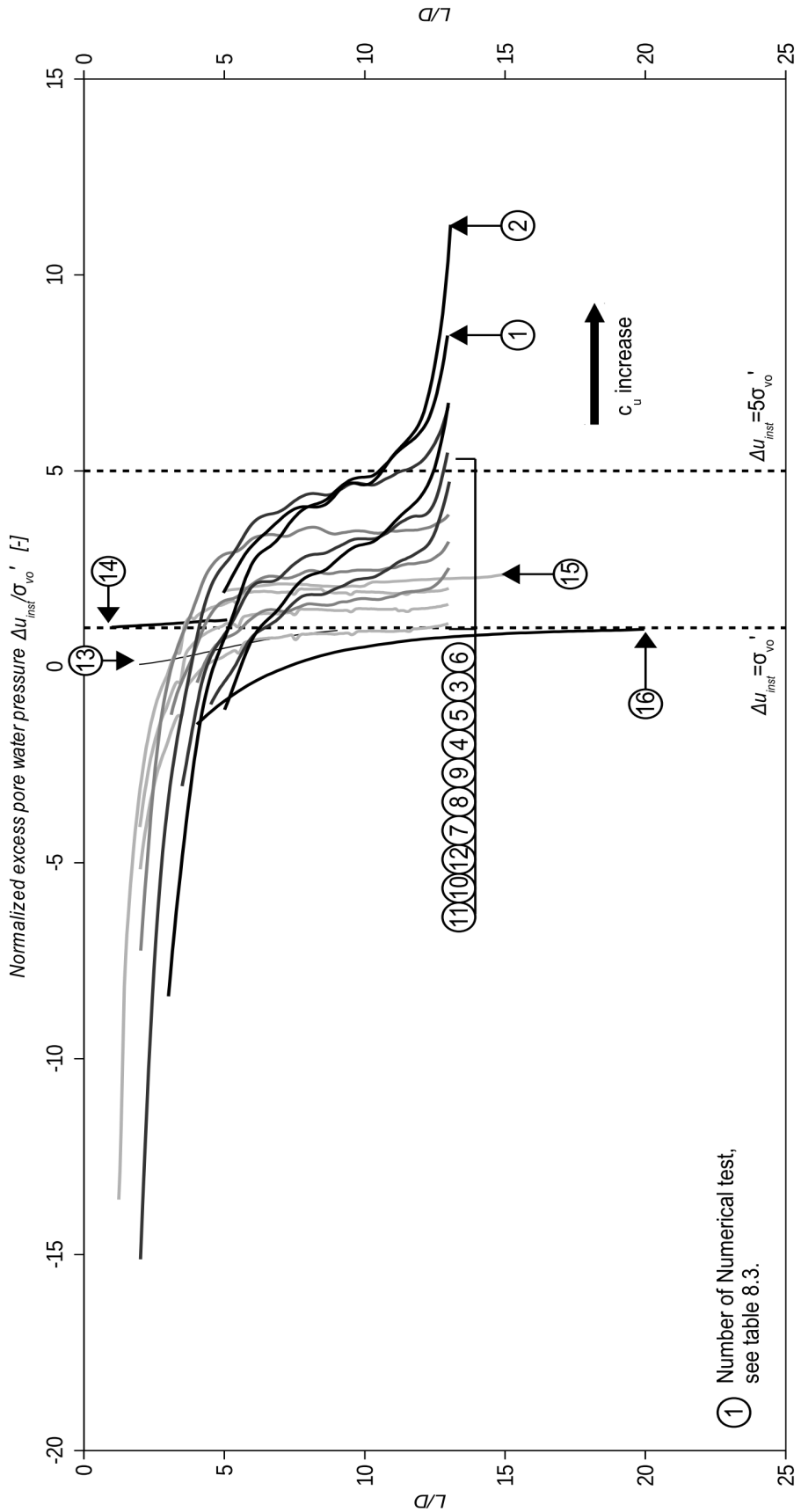

Figure 8.7. Normalized excess pore water pressure distributions after installation phase

where: Δu_{inst} -excess pore water pressure generated after installation.
Consequently, the effective radial stress after consolidation can be express as:

$$\sigma'_{rr,eq} = \left(\frac{\sqrt{3}}{M} + 1 \right) c_u \tag{8.18}$$

or:

$$\sigma'_{rr,eq} = \left(\frac{\sqrt{3}}{M} + 1 \right) c_u + \sigma'_{v,0} \tag{8.19}$$

where: $\sigma'_{rr,eq}$ – radial effective stress after consolidation, M – stress ratio, c_u – undrained shear strength, $\sigma'_{v,0}$ – initial geostatic stress.

The comparison between $\sigma'_{rr,eq}$ using equations (8.18) and (8.19) is presented in table 8.11. As the proposed formulas are intended to present general and average radial effective stresses, the effective stress acting on the pile wall obtained from UL models is averaged for each test and then, it is compared with formulas (8.18) and (8.19). As can be seen from table 8.12, the equations (8.18) and (8.19) provide a good estimation of the radial effective stress. However, the best results are achieved with equation (8.19). Results provided by equation (8.18) are more conservative while equation (8.19) gives more closer results to the average radial effective stress acting on the pile wall. Both propositions are calibrated and verified in chapter 9.

Table 8.11. Effective stress after pile installation – UL vs proposed formulas (calculation on average values)

Test no	$\sigma_{rr,inst}{}'^{UL,Avg}$	$\sigma_{rr,inst}{}'$ *eq. (8.15)*	Δu_{inst} *eq (8.17)*	Δu_{inst} *eq. (8.16)*	$\sigma_{rr,eq}{}'$ *eq. (8.18)*	$\sigma_{rr,eq}{}'$ *eq. (8.19)*		
	kPa	*kPa*	*kPa*	*kPa*	*kPa*	*kPa*	-	-
(1)	*(2)*	*(3)*	*(4)*	*(5)*	*(7)*	*(8)*	*(7)/(2)*	*(8)/(2)*
1	*957,58*	*852,19*	*0*	*24,75*	*852,19*	*876,94*	*0,88*	*0,91*
2	*848,17*	*852,19*	*0*	*24,75*	*852,19*	*876,94*	*0,94*	*0,97*
3	*845,33*	*852,19*	*0*	*24,75*	*852,19*	*876,94*	*0,95*	*0,98*
4	*560,41*	*568,13*	*0*	*24,75*	*568,13*	*592,88*	*0,96*	*1,00*
5	*624,58*	*568,13*	*0*	*24,75*	*568,13*	*592,88*	*0,90*	*0,94*
6	*686,51*	*568,13*	*0*	*24,75*	*568,13*	*592,88*	*0,85*	*0,89*
7	*313,74*	*284,06*	*0*	*24,75*	*284,06*	*308,81*	*0,88*	*0,95*
8	*341,22*	*284,06*	*0*	*24,75*	*284,06*	*308,81*	*0,83*	*0,90*
9	*363,35*	*284,06*	*0*	*24,75*	*284,06*	*308,81*	*0,79*	*0,86*
10	*321,34*	*245,94*	*0*	*48*	*245,94*	*293,94*	*0,78*	*0,93*
11	*289,45*	*245,94*	*0*	*48*	*245,94*	*293,94*	*0,87*	*1,04*
12	*257,70*	*245,94*	*0*	*48*	*245,94*	*293,94*	*0,74*	*0,89*
13	*345,61*	*223,12*	*0*	*41*	*223,12*	*264,12*	*0,84*	*0,99*
14	*324,50*	*223,12*	*0*	*52*	*223,12*	*275,12*	*0,69*	*0,86*
15	*492,20*	*357,00*	*0*	*63*	*357,00*	*420,00*	*0,72*	*0,85*
16	*523,34*	*427,01*	*0*	*86,1*	*427,01*	*513,11*	*0,85*	*1,03*
						AVG	*0,84*	*0,94*
						COV	*0,09*	*0,06*

Table 8.12. Reduction in q_t during equalization period

Test no	q_f^{ULinst}	$q_f^{UL\ eq}$	N_c	$q_f^{UL\ eq}/q_f^{ULinst}$
	kPa	*kPa*	-	-
1	*2506,28*	*1606,91*	*5,36*	*0,64*
2	*2031,41*	*1393,97*	*4,65*	*0,69*
3	*2361,17*	*1512,35*	*5,04*	*0,64*
4	*1586,14*	*1020,44*	*5,1*	*0,64*
5	*1655,31*	*1072,65*	*5,36*	*0,65*
6	*1763,48*	*1129,89*	*5,65*	*0,64*
7	*900,13*	*577,13*	*5,77*	*0,64*
8	*946,23*	*597,83*	*5,98*	*0,63*
9	*1042,37*	*623,47*	*6,23*	*0,60*
10	*825,31*	*556,25*	*6,95*	*0,67*
11	*767,92*	*536,81*	*6,71*	*0,70*
12	*874,81*	*570,23*	*7,13*	*0,65*
13	*780,62*	-	-	-
14	*916,36*	-	-	-
15	*1333,97*	*736,72*	*6,14*	*0,55*
16	*1677,99*	*1133,69*	*10,31*	*0,68*
			AVG	*0,64*
			COV	*0,05*

8.3.2.2 Pile toe

The cone resistances calculated at the end of equalization are presented in table 8.12. The values for tests no. 13 and no. 14 were omitted as the penetration occurred in layered soil, see notes in section 8.3.3.1. In table 8.12 the reduction in cone resistance during consolidation have been calculated. As can be seen, the average cone resistance after consolidation is about 0,64 time lower than the cone resistance after installation. As no size effects are considered in this thesis, the toe resistance obtained after installation can be assumed as equal to the CPT cone resistance. The pile base resistance equal to 0,6 of cone resistance is assumed in many pile design guidelines (e.g., Almeida et al., 1996; Bustamante and Gianeselli, 1982) This observation in also close to the Jardine et al. (2005) proposition for close-ended piles in cohesive soils. Jardine et al. suggest that pile toe resistance is 0,8 times the cone resistance obtained during CPT probing. Thus, Jardine et. al. proposition can be a reasonable estimation of pile toe resistance that is supportted by numerical studies presented in this chapter. While 0,64 reduction obtained from numerical studies requires entire time of consolidation, the value of 0,8 can be treated as a typical number for loading conditions at the site.

8.3.2.3 Physical changes

The total deformations and change in void ratio are shown in figure 8.8. The largest decrease in void ratio and consequently the soil densification is observed near the pile toe, while the most loosest soil appears near the pile surface. Also small movement of soil towards

the pile during consolidation is observed.

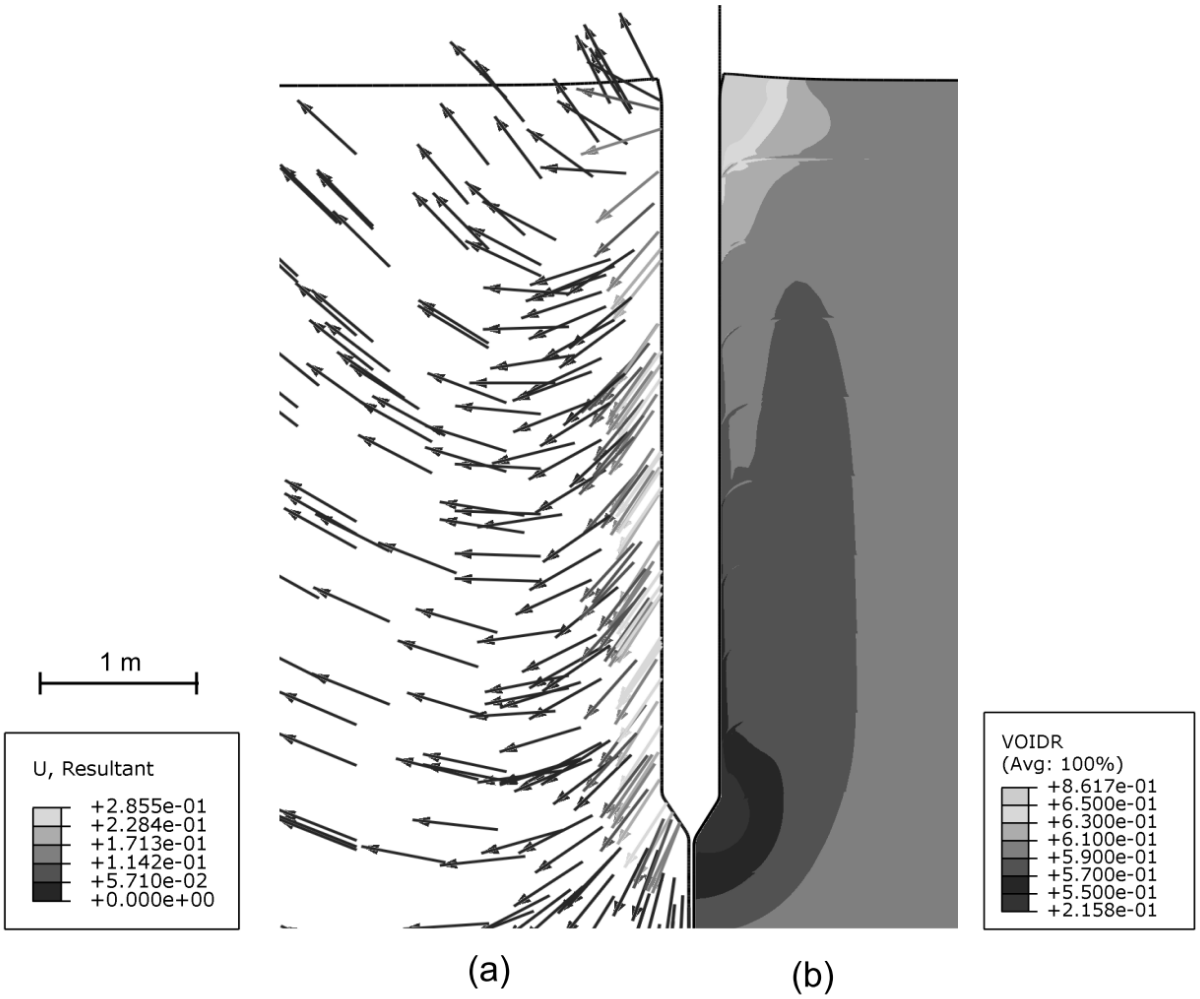

Figure 8.8. Physical change around the pile after installation and subsequent consolidation: (a) deformation and (b) void ratio

8.4 Conclusions

UL models are not fully compatible with corresponding ALE models and some revisions of UL models are often required. This has been encountered by author many times during this research. Hence, the proposed methodology (see chapter 3) helps to ensure if state of the soil after installation is acceptable for further calculations. The research conducted in this chapter shows that UL formulation can provide specific solution for pile jacking problem. The generalisation of those solutions has leaded to formulation of two equations which describe the average value of radial effective stress acting on the pile shaft. Randolph et al. (1979a) suggest that radial effective stress after installation is around $5c_{u0}$. Numerical studies conducted in this thesis indicate that this value is about $3c_{u0}$. The calculated pile base resistance for rigidity index of 40 leads to well-known formulas for pile bearing capacity with coefficient N_c ranging between 6 and 9, for end of consolidation and installation phase,

respectively. Further, as the consolidation takes place during large amount of time the Jardine et al. (2005) proposition that base resistance is equal to the 0,8 of cone resistance can be treated as a reasonable estimation of pile base resistance at the site.

Chapter 9

Installation effects – calibration and verification

In this chapter the empirical formulas (8.18) and (8.19) for installation effects description are calibrated with available databases. The datasets include pile static loading tests (SLT) for tension or compression performed all around the world. In the next part of the chapter, the radial effective stress increase according to the author's proposition will be verified on the basis of static pile loading tests conducted in Poznań, Poland. The author's method will be also compared with other widely used analytical methods of pile design in cohesive soils, e.g., API-2000 design standards. Finally, the load-settlement curves for the representative pile of Poznań static loading tests will be determined and two possible approaches to achieve this goal will be shown.

The aim of this chapter is to present the reliability and applicability of empirical formulas derived and stated in chapter 8. Finally, the possible use of empirical equations in pile design is described and discussed.

9.1 Soil state after installation

Numerical studies conducted in this thesis have shown that the installation of jacked displacement pile induces significant void ratio changes and soil deformations around the pile, see figure 8.9. Consequently, the stress state after installation and subsequent consolidation phase will strongly affect the pile behaviour during static loading test.

9.1.1 Horizontal effective stress

The radial effective stress described with equations (8.18) and (8.19) can be rewritten to the following forms:

$$\sigma'_{rr,eq} = IEC\left[\left(\frac{\sqrt{3}}{M}+1\right)c_u\right] \tag{9.1}$$

and

$$\sigma'_{rr,eq} = IEC\left[\left(\frac{\sqrt{3}}{M}+1\right)c_u+\sigma'_{v,0}\right] \tag{9.2}$$

where: *IEC* – installation effects coefficient, $\sigma'_{rr,eq}$ – radial effective stress after consolidation, M – stress ratio, c_u – undrained shear strength, $\sigma'_{v,0}$'– initial vertical geostatic stress.

The Installation Effects Coefficient (*IEC*) is introduced for the purpose of calibration. Tests conducted in chapters 6 and 7, where instrumented piles and CPT probing have been modelled, show that radial effective stress provided by numerical methods are generally a little underestimated for high OCR clays and overestimated for low OCR or disturbed clays (see sections 6.4.1). Hence, *IEC* will be strongest related with OCR. However, *IEC* can also include the influence of pile type and installation method. However, these factors will be omitted in analysis in this thesis and only IEC with relation to the OCR will be shown.

9.1.2 Vertical effective stress

The numerical studies performed in this thesis generally confirmed the traditional formula for pile base resistance after installation expressed as follows (e.g., Tomlinson and Woodward, 2015):

$$q_b = 9\,c_u \tag{9.3}$$

where: q_b – base resistance, c_u – undrained shear strength.
Although after installation the base resistance has been calculated as closer to the $9c_u$, the pile toe resistance after consolidation seems to be expressed by value of $6c_u$. As effective stress concept is used to calculate the pile shaft resistance the proposition of Jardine et al. (2005) in which the pile toe resistance is equal to the 0,8 of corrected cone resistance is chosen as a most reasonable value for calculation pile base resistance after consolidation.

9.2 Soil state after installation

The calibration of the empirical formulas in terms of *IEC* is based on literature database. The data are divided into two sets. The first one contains high quality data which enables detailed analysis of pile behaviour during installation, consolidation and static loading tests. This dataset is used for calibration of the proposed method. The second set contains some limited data which still can be used as a supplementary source. Consequently, the proposed equations are calibrated with high quality data from the first dataset but the general performance of proposed method is shown in the light of all available data.

9.2.1 Calibration procedure

The static loading tests (STL) are performed as a compression or tension tests. During compression test the total measured axial force can be divided into following components (Tomlinson and Woodward, 2015):

$$Q_{SLT} = Q_{base} + Q_{shaft} \tag{9.4}$$

where: Q_{STL} – pile capacity measured during static load test, Q_{base} – force carried by pile base (toe), Q_{shaft} – force carried by pile shaft.

During tension test, the axial force is equal to the shaft capacity and influence of the pile base or pile self-weight (Tomlinson and Woodward, 2015):

$$Q_{SLT} = Q_{shaft} + Q_{add} \tag{9.5}$$

where: Q_{STL} – pile capacity measured during static load test, Q_{shaft} – force carried by pile shaft, Q_{add} – additional force arising from pile self weight and influence of the pile base.
As the installation effects investigated in this thesis are focused on the pile shaft, only the pile shaft capacity will be taken into account. In SLTs where determination of the pile shaft is hampered, but the *L/D* ratio is high, the Q_{base} or Q_{add} will be omitted as insignificant. The overall radial effective stress mobilized during pile STL can be expressed then as:

$$\sigma'_{rr,STL} = \frac{Q_{shaft}}{\pi D L \tan(\delta_f)} \tag{9.6}$$

where: $\sigma'_{rr,STL}$ – radial effective stress mobilized during SLT, D – pile diameter, L – embedded pile length, δ_f – friction angle at failure on pile-soil interface.
The most crucial part in equation (9.6) is the proper choice of δ_f value. As it has been mentioned in chapter 3, section 3, the interface friction angle at failure is related to the slow shearing following the fast one. The two-part interface testing conducted simultaneously with mechanical properties of soil around the pile is relatively rare and hence, the appropriate assessment of δ_f is often difficult. In high quality database used in this study, the δ_f is always tested.

The radial effective stress acting on the pile wall mobilized during SLT can be identified with radial effective stress described by equations (8.18) or (8.19). Hence, the IEC can be calculated as:

$$IEC = \frac{\sigma'_{rr,STL}}{\sigma'_{rr,eq}} \tag{9.7}$$

where:

$$\sigma'_{rr,eq} = \left(\frac{\sqrt{3}}{M} + 1\right)\overline{c_u} \tag{9.8}$$

or

$$\sigma'_{rr,eq} = \left(\frac{\sqrt{3}}{M} + 1\right)\overline{c_u} + \overline{\sigma'_{v,0}} \tag{9.9}$$

where: *IEC* – installation effect coefficient, $\sigma'_{rr,STL}$ – radial effective stress during SLT, $\sigma'_{rr,eq}$ – radial effective stress after consolidation, M – stress ratio, $\overline{c_u}$ – average undrained shear strength along embedded length, $\overline{\sigma'_{v,0}}$ – average value of vertical initial geostatic stress along embedded length.
The undrained shear strength of soil influences the $\sigma'_{rr,eq}$ to the greatest extend. However, the c_u is strongly affected by OCR (e.g., Saye et al., 2016) and determination of c_u in laboratory

test can be problematic, especially for NC clays. In high quality databases the c_u is averaged along the pile embedded length and it is usually based on UU triaxial tests. The stress ratio M in high quality database is usually somewhere between 0,8÷1,5, hence the term $(\sqrt{3}/M+1)$ is between 2 and 3 with mean value of 2,5. Thus, the influence of stress ratio M is rather predictable.

Summing up, the most influential factors on the proper calibration of the proposed method are the undrained shear strength and the interface friction angle at failure.

9.2.2 High quality database

The high quality database consists of field and laboratory tests performed on seven sites. These are Aquatic Park, Pentre, Tilbrook, Canons Park, Cowden, Bothkennar and Belfast. Key references and general information about gathered high quality data are given in table 9.1. The following comments refer to presented database:

1. Aquatic Park – total axial force has been calculated as the sum of pile tension capacityweight given by authors .
2. Pentre – Clarke and Lambson (1993) reported peak and residual total axial force for LDP pile. In table 9.1 the peak value is used. The pile testes given by Chow (1997) are recovered from databases provided by Lehane et al. (2013) and Karlsrud (2012).
3. Tilbrook – the cyclic tests have been performed in Tilbrook (Karlsrud, 2012, 2014). The Q_{SLT} is provided for the first static loading test. The total axial force for LDP piles is a peak value (Clarke et al., 1993).
4. Canons Park – the data concerning the tests performed by Bond (1989) and Wardle et. al. (1992) are recovered from Lehane et al. (2013).
5. Cowden – pile data are based on Lehane and Jardine (1994a) paper and supplemented after Lehane et al. (2013).
6. Bothkennar – pile data are based on Lehane and Jardine (1994b) data and supplemented after Lehane et al. (2013).
7. Belfast - pile data are based on MaCabe and Lehane (2006), Doherty and Gavin (2011) papers and supplemented after Lehane et al. (2013).

9.2.3 Supplementary database

The supplementary database is divided into two sets. In the first one the lack or unreliable value of interface angle is the reason for a significantly lower quality of data. Consequently, as a practical workaround the estimation of this parameter will be made and this dataset is presented in table 9.2. In the second database the interface friction angle and stress ratio M are not determined from laboratory tests. In this case, some assessment will also be necessary. Those data are summarized in table 9.3. The following comments are made to presented database in table 9.2:

1. The numbering of piles is continued from table 9.1.
2. At Haga site, totally 27 SLT have been performed during 10-36 days after pile installation. Karlsrud (2012) reported that equalization time is about 10 days, The typical initial Q_{STL} is between 60kN and 75kN depending on time after installation. In

Table 9.1. High quality pile dataset

Site	*Reference*	*Year of STL*	*No*	*Pile test*	*Pile type*	*C/T*	$z_{borehole}$	z_{toe}	*L*	*D*	D_i	*L/D*	t_{eq}	Q_{SLT}
	-	-	-	-	-	-	*m*	*m*	*m*	*m*	*m*	-	*days*	*kN*
Aquatic Park, USA	*Pelletier and Doyle (1982)*	*1980*	*1*	*2-1*	*S,O,Dr*	*T*	*57,9*	*80,5*	*22,6*	*0,760*	*0,690*	*29,74*	*60*	*11040*
Pentre, UK	*Karlsrud (1993,2012,2014)*	*1987*	*2*	*A5*	*S,C,Dr*	*T*	*15,0*	*25,0*	*10,0*	*0,219*	-	*45,66*	*27*	*180*
			3	*A6*	*S,C,Dr*	*T*	*22,5*	*32,5*	*10,0*	*0,219*	-	*45,66*	*28*	*460*
	Clarke (1993)	*80s*	*4*	*LDP*	*S,O,Dr*	*C*	*15,0*	*55,0*	*40,0*	*0,762*	*0,650*	*52,49*	*44*	*6031*
	Chow (1996), Karlsrud (2012)	*Mid 90s*	*5*	*PT1*	*S,C,J*	*C*	*10,5*	*14,8*	*4,3*	*0,102*	-	*42,16*	*1*	*40*
			6	*PT2*	*S,C,J*	*C*	*10,5*	*19*	*8,5*	*0,102*	-	*83,33*	*1*	*88*
			7	*PT3*	*S,C,J*	*T*	*12*	*17,5*	*5,5*	*0,102*	-	*53,92*	*1*	*72*
			8	*PT4*	*S,C,J*	*C*	*8,14*	*14,0*	*5,86*	*0,102*	-	*57,45*	*1*	*72*
			9	*PT5*	*S,C,J*	*T*	*8,14*	*18,7*	*10,56*	*0,102*	-	*104*	*1*	*122*
			10	*PT6*	*S,C,J*	*C*	*10,3*	*14*	*3,7*	*0,102*	-	*36,27*	*1*	*51*
			11	*PT7*	*S,C,J*	*C*	*10,3*	*19*	*8,7*	*0,102*	-	*85,29*	*1*	*94*
Tilbrook, UK	*Karlsrud (1993,2012,2014)*	*1989*	*12*	*A*	*S,C,Dr*	*T*	*3,0*	*12,5*	*9,5*	*0,219*	-	*43,38*	*61*	*1236*
			13	*B*	*S,C,Dr*	*T*	*17,5*	*27,5*	*10,0*	*0,219*	-	*45,66*	*59*	*1670*
			14	*C*	*S,C,Dr*	*T*	*3,0*	*19,5*	*16,5*	*0,219*	-	*75,34*	*60*	*1993*
			15	*D*	*S,C,Dr*	*T*	*3,0*	*17,5*	*14,5*	*0,219*	-	*66,21*	*68*	*1888*
	Clarke (1993)	*1987-88*	*16*	*LDP*	*S,O,Dr*	*C*	*0,0*	*30,0*	*30*	*0,762*	*0,620*	*39,37*	*134*	*16130*
			17	*LDP*	*S,O,Dr*	*T*	*0,0*	*31,0*	*31*	*0,762*	*0,690*	*40,68*	*350*	*16280*

Table 9.1. High quality pile dataset, cd.

Site	Reference	Year of STL	No	Pile test	Pile type	C/T	$z_{borehole}$	z_{toe}	L	D	D_i	L/D	t_{eq}	Q_{SLT}
	-	-	-	-	-	-	m	m	m	m	m	-	days	kN
Canons Park, UK	Bond and Jardine (1991)	1989	18	CP07	S,C,J	T	2	5,2	3,2	0,102	-	31,37	109	90
			19	CP1s	S,C,J	C	2	5,28	3,28	0,102	-	32,16	79	68,1
			20	CP2f	S,C,J	C	2	5,95	3,95	0,102	-	38,73	63	110,1
			21	CP4f	S,C,J	T	2	6,16	4,16	0,102	-	40,78	20	118,9
			22	CP5f	S,C,J	T	2	5,92	3,92	0,102	-	38,43	2	105,4
			23	CP6d	S,C,Dr	T	2	5,80	3,8	0,102	-	37,25	2	104,6
			24	CP7do	S,O,Dr	T	2	5,70	3,7	0,102	0,09	36,27	2	93,5
	Bond (1989)	Mid 80s	25	CP7	S,O,Dr	T	2,1	5,7	3,6	0,100	0,08	36,0	-	92
	Wardle et al. (1992)	Early 80s	26	B	S,C,J	C	2	6,5	4,5	0,168	-	26,79	-	194
Cowden, UK	Lehane and Jardine (1994a)	1992	27	CW2	S,C,J	C	2,7	6,36	3,66	0,102	-	35,88	4	124
Bothkennar, UK	Lehane and Jardine (1994b)	1992	28	BK2	S,C,J	C	1,2	6,0	4,8	0,102	-	47,06	4	27
Belfast, NIR	McCabe and Lehane (2006)	Early 00s	29	S2/T	Cr,Sq,Dr	T	0,0	6,0	6	0,250	-	24	99	69
	Doherty and Gavin (2011)	2003-08	30	OE1	S,O,J	T	2,03	4,04	2,01	0,168	0,15	11,96	5	12

Note: STL – Static loading test, C – compression test, T – tension test, $z_{borehole}$ – borehole depth, z_{toe} – toe depth, L – embedded pile length, D – pile external diameter, D_i – pile internal diameter, t_{eq} – pore water pressure equalization time, Q_{STL} – axial force measured during static loading test, S – steel, O – open-ended, C – close-ended, Dr – driven, J – jacked, Cr – concrete, Sq – square

Table 9.2. Medium quality pile dataset

Site	Reference	Year of STL	No	Pile test	Pile type	C/T	$z_{borehole}$	z_{toe}	L	D	D_i	L/D	t_{eq}	Q_{SLT}
	-	-	-	-	-	-	m	m	m	m	m	m	days	kN
Haga, NOR	Karlsrud (2012,2014)	1983	31	B-Pile	S,C,J	T	0	4,85	4,85	0,153	-	31,7	35	75
West Delta. USA	Matlock et al. (1998)	1984-86	32	LP	S,O,Dr	T	0	71,3	71,3	0,762	-	93,57	500	4293
Onsoy, NOR	Karlsrud (1993,2012,2014)	1985-86	33	A1	S,C,Dr	T	5	15	10	0,219	-	45,66	26	98
			34	A2	S,C,Dr	T	12,5	22,5	10	0,219	-	45,66	27	136
			35	A3	S,C,Dr	T	20	30	10	0,219	-	45,66	55	235
			36	A4	S,C,Dr	T	27,5	37,5	10	0,219	-	45,66	35	262
			37	B1	S,O,Dr	T	5	15	10	0,809	0,790	12,36	80	455
			38	C1	S,C,Dr	T	5	37,5	32,5	0,219	-	148,4	37	440
			39	C2	S,C,Dr	T	5	37,5	32,5	0,219	-	148,4	51	535
	Karlsrud (2012)	-	40	O1-1	S,O,Dr	T	1,4	19.1	17,7	0,508	0,502	34,84	78	595
			41	O2-1	S,O,Dr	T	1,4	19.1	17,7	0,508	0,502	34,84	164	680
Lierstranda, NOR	Karlsrud (2012,2014)	1987	42	A7	S,C,Dr	T	5	15	10	0,219	-	45,66	26	82
			43	A8	S,C,Dr	T	12,5	22,5	10	0,219	-	45,66	27	88
			44	A9	S,C,Dr	T	20	30	10	0,219	-	45,66	55	113
			45	A10	S,C,Dr	T	27,5	37,5	10	0,219	-	45,66	34	95
			46	B2	S,O,Dr	T	5	15	10	0,809	0,790	45,66	80	400
Cowden, UK	Gallagher and St John (1980),	80s	47	$457A_0$	S,O,Dr	T	0	9,2	9,2	0,460	0,420	20	-	861
	Ove Arup and Partners (1986)		48	458B	S,C,Dr	T	0	9,22	9,22	0,460	-	20,04	-	975
			49	$305B_0$	S,O,Dr	T	0	9,49	9,49	0,310	0,270	30,61	-	391

Table 9.2. Medium quality pile dataset, cd.

Site	Reference	Year of STL	No	Pile test	Pile type	C/T	$z_{borehole}$	z_{toe}	L	D	D_i	L/D	t_{eq}	Q_{SLT}
	-	-	-	-	-	-	m	m	m	m	m	m	days	kN
			50	305D	S,C,Dr	T	0	9,49	9,49	0,310	-	30,61	-	400
			51	203Go	S,O,Dr	T	0	9,53	9,53	0,220	0,180	47,65	-	306
			52	203I	S,C,Dr	T	0	9,47	9,47	0,200	-	47,65	-	290
	Ponniah (1989)	80s	53	193o	S,C,J	T	0	9,9	9,9	0,220	-	47,35	-	491
	Karlsrud (2012)	-	54	C1-1	S,O,Dr	T	1	10	9	0,457	0,445	19,69	48	1010
			55	C-1-2	S,O,Dr	T	1	10	9	0,457	0,445	19,69	119	1030
Mortaiolo, IT	Totani et al. (1994)	Early 90s	56	L2C	S,C,Dr	C	0	50	50	0,460	-	108,7	19	2400
Mexico City, MEX	Salvadir and Jardine (2005)	-	57	CNT	Cr,Dr	C	0	24,3	24,3	0,350	-	69,43	59	1316
Dublin, IRL	Farrel et al. (1998)	Mid 90s	58	3C	Cr,,Ci,Dr	C	2,9	6,4	3,5	0,273	-	12,82	17	2200
			59	4T	Cr,,Ci,Dr	T	2,9	6,4	3,5	0,273	-	12,82	24	450

Note: STL – Static loading test, C – compression test, T – tension test, $z_{borehole}$ – borehole depth, z_{toe} – toe depth, L – embedded pile length, D – pile external diameter, D_i – pile internal diameter, t_{eq} – pore water pressure equalization time, Q_{STL} – axial force measured during static loading test, S – steel, O – open-ended, C – close-ended, Dr – driven, J – jacked, Cr – concrete, Sq – square

Table 9.3. Low quality pile dataset

Site	Reference	Year of STL	No	Pile test	Pile type	C/T	$z_{borehole}$	z_{toe}	L	D	D_i	L/D	t_{eq}	Q_{SLT}
	-	-	-	-	-	-	m	m	m	m	m	m	days	kN
Hamilton, USA	Kraft et al. (1981)	Late 70s	60	TP1	S,C,Dr	C	0	12,19	12,19	0,112	-	108,84	-	74,8
			61	TP2	S,C,Dr	C	0	12,19	12,19	0,112	-	108,84	-	48
			62	TP3	S,O,Dr	C	0	12,19	12,19	0,112	0,102	108,84	-	45,8
			63	TP4	S,O,Dr	C	0	12,19	12,19	0,112	0,102	108,84	-	61,5
St Alban, CAN	Konrad and Roy (1987)	Mid 80s	64	Pile B	S,C,J	C	0	7,6	7,6	0,219	-	34,55	730	87
Noetsu Bridge, JPN	Matsumoto et al. (1995)	1991	65	T2	S,O,Dr	C	1,8	10,1	8,3	0,800	0,776	10,38	11	3700
Golden Ears Bridge, CAN	Amini et al. (2008)	2006-07	66	BP	Cr,Dr	C	2,4	34,4	32	2,500	-	12,8	96	18400
			67	SC	Cr,Dr	C	0	26	36	0,357	-	100,84	120	3000
Sandpoint, USA	Fellenius et al. (2004)	2001	68	p	S,C,Dr	C	0	45	45	0,406	-	110,84	48	1915
University Houston, USA	O'Neil et al. (1982a,b)	Early 80s	69	1/C	S,C,Dr	C	3	13,1	10,1	0,273	-	37	-	792
			70	1/T	S,C,Dr	T	3	13,1	10,1	0,273	-	37	-	460
Sarapui, BRA	Alves et al. (2009)	Mid 00s	71	P	S,C,Dr	C	0	4,5	4,5	0,102	-	44,12	36	7
Stjordal, NOR	Karlsrud (2012)	-	72	S1-1	S,O,Dr	T	1	23,6	22,6	0,508	0,502	44,49	50	480
			73	S2-1	S,O,Dr	T	1	23,6	22,6	0,508	0,502	44,49	111	700
Femerrn, DEN,-GER	Karlsrud (2012)	-	74	F1-1	S,O,Dr	T	0	25	25	0,508	0,486	49,21	48	3150
			75	F2-1	S,O,Dr	T	0	25	25	0,508	0,486	49,21	119	3200

Note: STL – Static loading test, C – compression test, T – tension test, $z_{borehole}$ – borehole depth, z_{toe} – toe depth, L – embedded pile length, D – pile external diameter, D_i – pile internal diameter, t_{eq} – pore water pressure equalization time, Q_{STL} – axial force measured during static loading test, S – steel, O – open-ended, C – close-ended, Dr – driven, J – jacked, Cr – concrete, Sq – square

Table 9.2. the last SLT conduced 36 days after installation have been used.

3. The West delta data (Matlock et al., 1998) are recovered from Karlsrud (2012) thesis.
4. The data from Cowden reported by Gallagher and St. John (1980), Ove Arup and Partners (1986) and Ponniah (1989) (piles denoted from no. 46 to no. 52) are recovered from Lehane et al. (2013) database.
5. The SLT data from Mortaiolo pile is related to the first SLT at the depth of 50m. After this test the pile was redriven to the sand layer at the depth of 57m and then the second SLT took place (Totani et al., 1994).
6. In Mexico city totally 26 pile have been tested (Saldivar and Jardine, 2005). As the reference pile the CNT pile (the only pile without pre-boring) has been used after Lehane et. al. (2013). This is done due to unknown effect of pre-boring of pile on the axial capacity and shaft capacity in particular (Saldivar and Jardine, 2005).

In terms of table 9.3 data, the following notes are made:

1. The numbering of piles is continued from table 9.2
2. Data for Hamilton site are recovered from Karlsrud (2012) and Lehane et al. (2013) data.
3. Data for St Alban site are recovered from Karlsrud (2012) thesis.
4. University Houston Campus – data recovered from Karlsrud (2012) thesis.
5. Femern site is located on the border between Denmark and Germany.

9.2.4 Calibration of equation (8.18)

The high quality pile data are used to calibrate equation (8.18). The required soil and pile data with average radial effective stresses calculated by equation (9.8) and *IEC* calculated by equation (9.7) are presented in table 9.4. The following notes are made:

1. The pile numbers are consistent with these presented in table 9.1.
2. Aquatic Park – all data are cited after Pelletier and Doyle (1982). The value of geostatic vertical stress is a slightly different than reported by Lehane et. al. (2013).
3. Pentre – σ_{vo}' is used after Karlsrud (2012) and it is lower than provided in Lehane et al. (2013) database. In piles tested by Chow (1997) the undrained shear strength has been calculated from average corrected cone resistance q_t and cone factor 15 after Lehane et al. (2013). The OCR has been estimated on Karlsrud (2012) data. The base capacity for close ended piles has been calculated from Jardine et al. (2005) proposition:

$$Q_b = 0{,}8\, q_t\, A_b \tag{9.10}$$

where: Q_b – pile base bearing capacity, q_t – corrected cone resistance, A_b – pile base area.

The value of interface friction angle at failure have been assumed as 16,5° being a little lower than Lehane et al. (2013) report, but this value is obtained from ring shear apparatus (Karlsrud, 2012) and it is believed as more accurate.

4. Tilbrooke – Average values have been adopted after Karlsrud (2012) and they are consistent with his database. In Tilbrooke two different clay deposits have been

recognised and they are called Lowestoft and Oxford clays. For piles no. 16 and no. 17 which were driven in both clay layers, the average values from two clay deposits have been assumed.

5. The OCR from Canons Park deposit is refered after Karlsrud (2012) as value given by Bond and Jardine (1991) and determined from oedometer tests seems to be overestimated. The undrained shear strength is averaged from disturbed and undisturbed clay layers. Pile base capacity is cited after Bond and Jardine (1995), and where no information is given, the zero value is used.
6. Bothenkennar and Cowden – data are based directly on Lehane and Jardine papers (1994a, 1994b) and they are slightly different than used in Karlsrud (2012) database.
7. Belfast – data are consistent with those provided by Lehane et al. (2013).

The *IEC* coefficients for equation (8.18) obtained from high quality database are plotted versus OCR in figure 9.1. As can be seen very poor results have been achieved and direct relation hardly can be build. Some trend can be noticed, but low value of *IEC* coefficient makes this approximation unacceptable. Consequently, equation (8.18) is rejected as an approximation for radial effective stress determination after pile installation and soil consolidation.

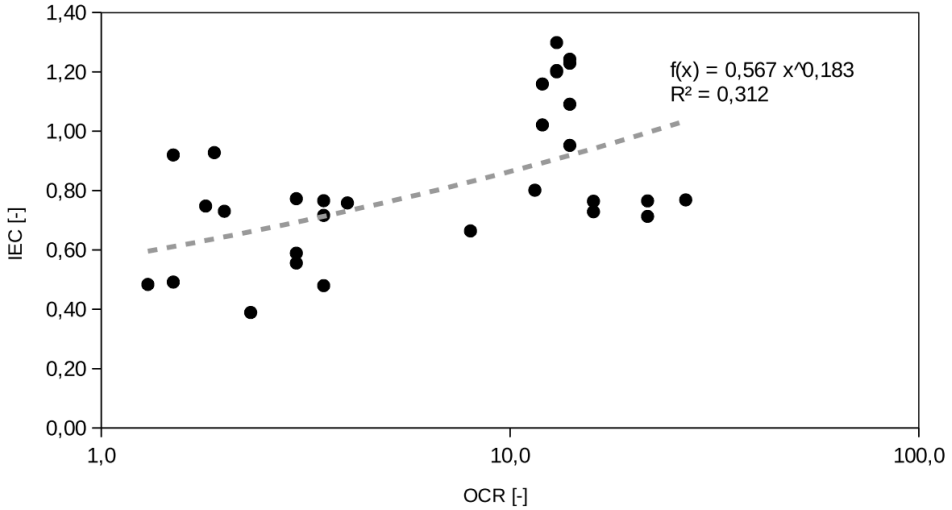

Figure 9.1. IEC obtained from calibration of equation (8.18)

9.2.5 Calibration of equation (8.19)

The same high quality pile database is used to calibrate equation (8.19). Similarly, like in 9.2.6. section, the average radial effective stress calculated by equation (9.9) and *IEC* calculated by equation (9.7) are presented in table 9.5. The same notes concerning database as given in previous section are valid.

The IEC plotted against the OCR for equation (8.19) is shown in figure 9.2. Here, significantly better results are achieved than for calibration of equation (8.18). The coefficient of variation of 0,67 gives a visible trend of IEC described by equation:

$$IEC = 0{,}26\, OCR^{0{,}41} \tag{9.11}$$

where: *IEC* – installation effects coefficient, OCR – overconsolidation ratio.

Table 9.4. Calibration of equation (8.18)

No	Q_{SLT}	Q_{base} or Q_{add}	Q_{shaft}	*D*	*L*	*Average*					δ_f	$\sigma'_{rr,eq}$ eq. (9.8)	$\sigma'_{rr,SLT}$ eq. (9.6)	*IEC* eq. (9.7)
						c_u	σ'_{v0}	*OCR*	ϕ'_{cs}	*M*				
-	*kN*	*kN*	*kN*	*m*	*m*	*kPa*	*kPa*	-	*o*	-	*o*	*kPa*	*kPa*	-
1	*11040*	*640*	*10400*	*0,760*	*22,6*	*294*	*675*	*2*	*35*	*1,42*	*22*	*653,0*	*477,0*	*0,73*
2	*180*	*20*	*160*	*0,219*	*10,0*	*70*	*182*	*2,3*	*23,5*	*0,92*	*16,5*	*201,8*	*78,5*	*0,39*
3	*460*	*21*	*439*	*0,219*	*10,0*	*80,5*	*247*	*1,9*	*23,5*	*0,92*	*16,5*	*232,1*	*215,4*	*0,93*
4	*6031*	*850*	*5181*	*0,762*	*40,0*	*92*	*320*	*1,5*	*23,5*	*0,92*	*12,5*	*265,3*	*244,1*	*0,92*
5	*40*	*7,32*	*32,7*	*0,102*	*4,3*	*58*	*125*	*3,5*	*23,5*	*0,92*	*16,5*	*166,9*	*80,1*	*0,48*
6	*88*	*7,98*	*80*	*0,102*	*8,5*	*62*	*144*	*3*	*23,5*	*0,92*	*16,5*	*178,5*	*99,2*	*0,56*
7	*72*	*0*	*72*	*0,102*	*5,5*	*62*	*144*	*3*	*23,5*	*0,92*	*16,5*	*178,5*	*137,9*	*0,77*
8	*72*	*6,7*	*65,3*	*0,102*	*5,86*	*54*	*109*	*4*	*23,5*	*0,92*	*16,5*	*154,8*	*117,4*	*0,76*
9	*122*	*0*	*122*	*0,102*	*10,56*	*59*	*132*	*3,5*	*23,5*	*0,92*	*16,5*	*169,9*	*121,7*	*0,72*
10	*51*	*7,13*	*43,9*	*0,102*	*3,7*	*57*	*120*	*3,5*	*23,5*	*0,92*	*16,5*	*163,1*	*124,9*	*0,77*
11	*94*	*7,19*	*86,1*	*0,102*	*8,7*	*61*	*143*	*4*	*23,5*	*0,92*	*16,5*	*176,9*	*104,3*	*0,59*
12	*1236*	*6*	*1230*	*0,219*	*9,5*	*330*	*115*	*26,9*	*27,5*	*1,09*	*16*	*951,4*	*656,3*	*0,77*
13	*1670*	*13*	*1657*	*0,219*	*10,0*	*440*	*291*	*11,5*	*18,0*	*0,69*	*11*	*1546,1*	*1239,0*	*0,80*
14	*1993*	*11*	*1982*	*0,219*	*16,5*	*330*	*147*	*21,7*	*27,5*	*1,09*	*16*	*951,4*	*608,9*	*0,71*
15	*1888*	*19*	*1869*	*0,219*	*14,5*	*330*	*147*	*21,7*	*27,5*	*1,09*	*16*	*951,4*	*653,4*	*0,77*
16	*16130*	*1450*	*14681*	*0,762*	*30*	*380*	*209*	*16*	*21,5*	*0,84*	*13,5*	*1168,2*	*851,5*	*0,73*
17	*16280*	*375*	*15905*	*0,762*	*31*	*380*	*209*	*16*	*21,5*	*0,84*	*13,5*	*1168,2*	*892,7*	*0,76*

Table 9.4. Calibration of equation (8.18), cd.

No	Q_{SLT}	Q_{base} or Q_{add}	Q_{shaft}	*D*	*L*	*Average*					δ_f	$\sigma'_{rr,eq}$ eq.(9.8)	$\sigma'_{rr,SLT}$ eq.(9.6)	*IEC* eq.(9.7)
						c_u	σ'_{v0}	*OCR*	ϕ'_{cs}	*M*				
-	*kN*	*kN*	*kN*	*m*	*m*	*kPa*	*kPa*	-	*o*	-	*o*	*kPa*	*kPa*	-
18	*90*	*15*	*75,0*	*0,102*	*3,2*	*92*	*44*	*12*	*22,5*	*0,88*	*13*	*273,3*	*316,8*	*1,16*
19	*68,1*	*0*	*68,1*	*0,102*	*3,28*	*93*	*44*	*12*	*22,5*	*0,88*	*13*	*275,2*	*281,1*	*1,02*
20	*110,1*	*17,9*	*92,2*	*0,102*	*3,95*	*97*	*48*	*14*	*22,5*	*0,88*	*13*	*289,2*	*315,5*	*1,09*
21	*118,9*	*7*	*111,9*	*0,102*	*4,16*	*98*	*49*	*14*	*22,5*	*0,88*	*13*	*292,6*	*363,6*	*1,24*
22	*105,4*	*2,5*	*102,9*	*0,102*	*3,92*	*97*	*48*	*14*	*22,5*	*0,88*	*13*	*288,6*	*354,8*	*1,23*
23	*104,6*	*0*	*104,6*	*0,102*	*3,8*	*96*	*47*	*13*	*22,5*	*0,88*	*13*	*286,5*	*372,1*	*1,30*
24	*93,5*	*0*	*93,5*	*0,102*	*3,7*	*96*	*46*	*13*	*22,5*	*0,88*	*13*	*284,6*	*341,6*	*1,20*
25	*92*	*0*	*92,0*	*0,100*	*3,6*	*98*	*46*	*13*	*22,5*	*0,88*	*13*	*292,5*	*352,3*	*1,20*
26	*194*	*38,66*	*155,3*	*0,168*	*4,5*	*100*	*51*	*14*	*22,5*	*0,88*	*13*	*297,4*	*283,3*	*0,95*
27	*124*	*17,39*	*106,6*	*0,102*	*3,66*	*120*	*53*	*8*	*26*	*1,03*	*23*	*322,4*	*214,2*	*0,66*
28	*27*	*2,03*	*25,0*	*0,102*	*4,8*	*18,3*	*34*	*1,8*	*36*	*1,46*	*28,5*	*40*	*29,9*	*0,75*
29	*69*	*0*	*69,0*	*0,250*	*6*	*22*	*32*	*1,5*	*33,5*	*1,35*	*25*	*50,2*	*24,7*	*0,49*
30	*12*	*0*	*12,0*	*0,168*	*2,01*	*22*	*33*	*1,3*	*33,5*	*1,35*	*25*	*50,2*	*24,3*	*0,48*

Note: Q_{STL} – axial force measured during static load test, Q_b – pile base capacity, Q_{shaft} – pile shaft capacity, D – pile diameter, L – embedded length, c_u – undrained shear strength, σ_{v0}' – vertical geostatic stress, OCR – overconsolidation ratio, ϕ_{cs}' – critical angle of friction, M – stress ratio, δ_f – interface friction angle, $\sigma_{rr,eq}'$ – radial effective stress after equalization, σ_{rrSLT}' – radial effective stress estimated from SLT, IEC – installation effects coefficient

Table 9.5. Calibration of equation (8.19)

No	Q_{SLT}	Q_{base} or Q_{add}	Q_{shaft}	*D*	*L*	*Average*					δ_f	$\sigma'_{rr,eq}$ eq. (9.9)	$\sigma'_{rr,SLT}$ eq. (9.6)	*IEC* eq. (9.7)
						c_u	σ'_{v0}	*OCR*	ϕ'_{cs}	*M*				
-	*kN*	*kN*	*kN*	*m*	*m*	*kPa*	*kPa*	-	*o*	-	*o*	*kPa*	*kPa*	-
1	*11040*	*640*	*10400*	*0,760*	*22,6*	*294*	*675*	*2*	*35*	*1,42*	*22*	*1328,0*	*477,0*	*0,36*
2	*180*	*20*	*160*	*0,219*	*10,0*	*70*	*182*	*2,3*	*23,5*	*0,92*	*16,5*	*328,0*	*78,5*	*0,20*
3	*460*	*21*	*439*	*0,219*	*10,0*	*80,5*	*247*	*1,9*	*23,5*	*0,92*	*16,5*	*479,1*	*215,4*	*0,45*
4	*6031*	*850*	*5181*	*0,762*	*40,0*	*92*	*320*	*1,5*	*23,5*	*0,92*	*12,5*	*585,3*	*244,1*	*0,42*
5	*40*	*7,32*	*32,7*	*0,102*	*4,3*	*58*	*125*	*3,5*	*23,5*	*0,92*	*16,5*	*291,9*	*80,1*	*0,27*
6	*88*	*7,98*	*80*	*0,102*	*8,5*	*62*	*144*	*3*	*23,5*	*0,92*	*16,5*	*322,5*	*99,2*	*0,31*
7	*72*	*0*	*72*	*0,102*	*5,5*	*62*	*144*	*3*	*23,5*	*0,92*	*16,5*	*322,5*	*137,9*	*0,43*
8	*72*	*6,7*	*65,3*	*0,102*	*5,86*	*54*	*109*	*4*	*23,5*	*0,92*	*16,5*	*263,8*	*117,4*	*0,45*
9	*122*	*0*	*122*	*0,102*	*10,56*	*59*	*132*	*3,5*	*23,5*	*0,92*	*16,5*	*301,9*	*121,7*	*0,40*
10	*51*	*7,13*	*43,9*	*0,102*	*3,7*	*57*	*120*	*3,5*	*23,5*	*0,92*	*16,5*	*283,1*	*124,9*	*0,44*
11	*94*	*7,19*	*86,1*	*0,102*	*8,7*	*61*	*143*	*4*	*23,5*	*0,92*	*16,5*	*319,9*	*104,3*	*0,33*
12	*1236*	*6*	*1230*	*0,219*	*9,5*	*330*	*115*	*26,9*	*27,5*	*1,09*	*16*	*968,7*	*656,3*	*0,68*
13	*1670*	*13*	*1657*	*0,219*	*10,0*	*440*	*291*	*11,5*	*18,0*	*0,69*	*11*	*1837,1*	*1239,0*	*0,67*
14	*1993*	*11*	*1982*	*0,219*	*16,5*	*330*	*147*	*21,7*	*27,5*	*1,09*	*16*	*1000,7*	*608,9*	*0,61*
15	*1888*	*19*	*1869*	*0,219*	*14,5*	*330*	*147*	*21,7*	*27,5*	*1,09*	*16*	*1007,7*	*653,4*	*0,65*
16	*16130*	*1450*	*14681*	*0,762*	*30*	*380*	*209*	*16*	*21,5*	*0,84*	*13,5*	*1337,2*	*851,5*	*0,62*
17	*16280*	*375*	*15905*	*0,762*	*31*	*380*	*209*	*16*	*21,5*	*0,84*	*13,5*	*1337,2*	*892,7*	*0,65*

Table 9.5. Calibration of equation (8.19), cd.

No	Q_{SLT}	Q_{base} or Q_{add}	Q_{shaft}	D	L	Average					δ_f	$\sigma'_{rr,eq}$ eq. (9.9)	$\sigma'_{rr,SLT}$ eq.(9.8)	IEC eq. (9.7)
						c_u	σ'_{v0}	OCR	ϕ'_{cs}	M				
-	kN	kN	kN	m	m	kPa	kPa	-	^{o}	-	^{o}	kPa	kPa	-
18	90	15	75,0	0,102	3,2	92	44	12	22,5	0,88	13	316,9	316,8	1,00
19	68,1	0	68,1	0,102	3,28	93	44	12	22,5	0,88	13	319,2	281,1	0,88
20	110,1	17,9	92,2	0,102	3,95	97	48	14	22,5	0,88	13	336,9	315,5	0,94
21	118,9	7	111,9	0,102	4,16	98	49	14	22,5	0,88	13	341,5	363,6	1,06
22	105,4	2,5	102,9	0,102	3,92	97	48	14	22,5	0,88	13	336,2	354,8	1,06
23	104,6	0	104,6	0,102	3,8	96	47	13	22,5	0,88	13	333,4	372,1	1,12
24	93,5	0	93,5	0,102	3,7	96	46	13	22,5	0,88	13	330,9	341,6	1,03
25	92	0	92,0	0,100	3,6	98	46	13	22,5	0,88	13	338,8	352,3	1,04
26	194	38,66	155,3	0,168	4,5	100	51	14	22,5	0,88	13	348,2	283,3	0,81
27	124	17,39	106,6	0,102	3,66	120	53	8	26	1,03	23	375,4	214,2	0,57
28	27	2,03	25,0	0,102	4,8	18,3	34	1,8	36	1,46	28,5	74,0	29,9	0,40
29	69	0	69,0	0,250	6	22	32	1,5	33,5	1,35	25	82,2	24,7	0,30
30	12	0	12,0	0,168	2,01	22	33	1,3	33,5	1,35	25	82,2	24,3	0,29

Note: Q_{STL} – axial force measured during static load test, Q_b – pile base capacity, Q_{shaft} – pile shaft capacity, D – pile diameter, L – embedded length, c_u – undrained shear strength, σ_{v0}' – vertical geostatic stress, OCR – overconsolidation ratio, ϕ_{cs}' – critical angle of friction, M – stress ratio, δ_f – interface friction angle, $\sigma_{rr,eq}'$ – radial effective stress after equalization, σ_{rrSLT}' – radial effective stress estimated from SLT, IEC – installation effects coefficient

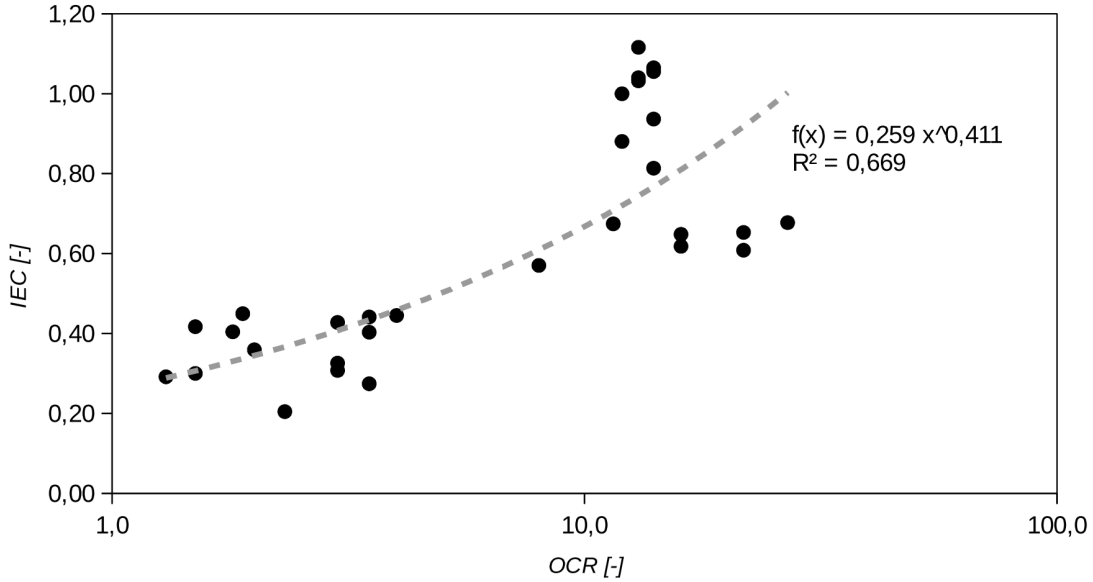

Figure 9.2. IEC calibrated from equation (8.19)

The next step is the prediction of total pile capacity with *IEC* described by equation (9.11) and radial effective stress given by equation (9.9). This will be done using all 75 piles in collected database. The following assumptions are made for calculation:

1. IEC coefficient is calculated using equation (9.7).
2. The radial total stress is calculated using equation (9.9).
3. Pile shaft capacity is given by equation (Tomlinson and Woodward, 2015):

$$Q_{shaft} = \tau_f A_s = \sigma'_{rr,eq} \pi D L \tan(\delta_f) \tag{9.12}$$

where: Q_{shaft} – pile shaft capacity, τ_f – unit skin friction, A_s – shaft area, $\sigma'_{rr,eq}$ – radial effective stress after equalization, D – pile diameter, L – embedded pile length, δ_f – interface friction angle at failure.

4. Pile base capacity is calculated using formula (Tomlinson and Woodward, 2015):

$$Q_{base} = 9 c_u \cdot \pi R^2 \tag{9.13}$$

where: Q_{base} – pile base capacity, c_u – undrained shear strength, R – pile radius.
This is done due to lack of CPT data in some part of the tests and consequently the inability of Jardine et al. (2005) formula application (see equation 9.10).

5. c_u for base resistance calculation is an average value from 1,5D above and below pile base.
6. For compression tests Q_c is equal to the sum of Q_{shaft} and Q_{base}. For tension test Q_c is equal to the Q_{shaft}.
7. When tension SLT have been performed the influence of the pile base and pile self weight represented by Q_{add} is often provided. Hence, as Q_m the estimated or measured shaft capacity Q_{shaft} is used.

In piles denoted by numbers from no. 31 to no. 59 no or ambiguous information about interface angle at failure has been given. Consequently, the values provided by Lehane et al. (2013) or estimated with relation $\delta_f = \frac{2}{3}\phi'_{cs}$ (e.g., Tsubakihara et al., 1993) have been used. The other notes to this data set are as follows:

1. Haga, West Delta, Lierstranda and Onsoy – all data are adopted after Karlsrud (2012) database.
2. Cowden – undrained shear strength is taken from Lehane and Jardine (1994a) data and Karlsrud (2012) uses similar values. However, OCR values seem to be overestimated in Karlsrud's database, so Lehane and Jardine (1994a) OCRs are used.
3. Mortaiolo – data taken from Totani et al. (1994) and supplemented by Lehane et al. (2013) database.
4. Mexico city – the interface angle of 36º is a post-peak value after initial fast shearing stage. However, the laboratory tests shows residual values also close to 30º (Saldivar and Jardine, 2005).
5. Dublin – the interface angle of 32º is a peak value (Farrel et al., 1998). The high differences are encountered in pile shaft capacity during tension and compression test. Also extremely high pile toe capacity is recorded. Thus, reliability of those data is limited.

Pile denoted by numbers from no. 60 to no. 75 are a group of poor quality data where no information is given about interface behaviour and effective angle of friction. Thus, the $(\sqrt{(3)}/M+1)$ is assumed to be equal to 2,5 which is a medium value from previously reported piles. Consequently, corresponding stress ratio M is equal to 1,15. The following notes are made to this part of dataset:

1. Hamilton – data are adopted from Karlsrud (2012) thesis and they slightly different than in Lehane et al. (2013) database.
2. St. Alban – data are consistent with Karlsrud's (2012) database.
3. Noetsu Bridge – data are consistent with Lehane at al. (2013) paper. The undrained shear strength is estimated from CPT sounding.
4. Golden Ears Bridge – data are directly taken from Amimi et al. (2008) report and they are slightly different than reported by Lehane et al. (2013).
5. Sandpoint – data are consistent with Lehane (2013) database.
6. Houston – data are adopted after Karlsrud (2012) thesis and they slightly differ from those reported by Lehane et al. (2013).
7. Sarapui – data are consistent with Lehane et al. (2013) paper.
8. Stjordal, Femern – data are taken from Karlsrud (2012) database.

The calculated capacity versus measured pile capacity for collected data is presented in figure 9.3. The general observation is that a good agreement is achieved and most of data sets in 50% range from perfect fit. This is confirmed with average Q_c/Q_m of 1,02 and COV of 0,29. The satisfactory agreement have been also achieved for pile shaft capacity calculation (AVG=1,03 and COV=0,32). Two piles has been removed from analysis (pile no. 59 and no. 45) due to significant scatter from the rest database. The histogram with Gauss curve for the data presented in table 9.6 is shown in figure 9.4 and, as one can see, relatively good results

Table 9.6. Reliability of proposed method

				Pile Shaft								Pile base			SLT			
				Average								Avg.						
No	T/C	D	L	c_u	σ'_{v0}	OCR	ϕ'_{cs}	M	δ_f	$\sigma'_{rr,eq}$	Q_{shaft}	c_u	Q_{base}	Q_c	Q_{base}	Q_{shaft}	Q_m	Q_c/Q_m
								eq. (8.3)		eq. (9.2)	eq. (9.12)		eq.(9.13)	eq. (9.4)	or Q_{add}			
-	-	m	m	kPa	kPa	-	o	-	o	kPa	kN	kPa	kN	kN	kN	kN	kN	-
1	T	0,760	22,6	294	675	2	35	1,42	22	458,8	10003,1	-	-	10003,1	640	10400	10400	0,96
2	T	0,219	10,0	70	182	2,3	23,5	0,92	16,5	140,9	287,2	-	-	287,2	20	160	160	1,80
3	T	0,219	10,0	80,5	247	1,9	23,5	0,92	16,5	161,7	329,6	-	-	329,6	21	439	439	0,75
4	C	0,762	40,0	92	320	1,5	23,5	0,92	12,5	179,7	3814,9	120	1080	4307,4	850	5181	6031	0,71
5	C	0,102	4,3	58	125	3,5	23,5	0,92	16,5	126,9	51,8	60	4,4	56,2	7,32	32,7	40	1,40
6	C	0,102	8,5	62	144	3	23,5	0,92	16,5	131,5	106,1	70	5,1	111,3	7,98	80	88	1,26
7	T	0,102	5,5	62	144	3	23,5	0,92	16,5	131,5	68,7	-	-	68,7	0	72	72	0,95
8	C	0,102	5,86	54	109	4	23,5	0,92	16,5	121,1	67,4	60	4,4	71,8	6,7	65,3	72	1,00
9	T	0,102	10,56	59	132	3,5	23,5	0,92	16,5	131,2	131,5	-	-	131,5	0	122	122	1,08
10	C	0,102	3,7	57	120	3,5	23,5	0,92	16,5	123,0	43,2	60	4,4	47,6	7,13	43,9	51	0,93
11	C	0,102	8,7	61	143	4	23,5	0,92	16,5	130,5	107,8	70	5,1	112,9	7,19	86,1	94	1,20
12	T	0,219	9,5	330	115	26,9	27,5	0,92	16	971,3	1820,6	-	-	1820,6	6	1230	1230	1,48
13	T	0,219	10,0	440	291	11,5	18,0	0,69	11	1300,1	1738,9	-	-	1738,9	13	1657	1657	1,05
14	T	0,219	16,5	330	147	21,7	27,5	0,92	16	918,8	2991,1	-	-	2991,1	11	1982	1982	1,51
15	T	0,219	14,5	330	147	21,7	27,5	0,92	16	918,8	2628,5	-	-	2628,5	19	1869	1869	1,41
16	C	0,762	30	380	209	16	21,5	0,84	13,5	1116,0	19243,9	460	1888,0	21131,8	1450	14681	16131	1,31
17	T	0,762	31	380	209	16	21,5	0,84	13,5	116,0	19885,3	-	-	19885,3	375	15905	15905	1,25
18	T	0,102	3,2	92	44	12	22,5	0,88	13	228,2	54,0	-	-	54,0	15,0	90,0	75,0	0,72
19	C	0,102	3,28	93	44	12	22,5	0,88	13	229,9	55,7	120	8,8	64,5	0	68,1	68,1	0,95

Table 9.6. Reliability of proposed method, cd.

				Pile Shaft								Pile base				SLT			
				Average								Avg.							
No	T/C	D	L	c_u	σ'_{v0}	OCR	ϕ'_{cs}	M	δ_f	$\sigma'_{rr,eq}$	Q_{shaft}	c_u	Q_{base}	Q_c	Q_{base}	Q_{shaft}	Q_m	Q_c/Q_m
								eq. (8.3)		eq. (9..2)	eq. (9.12)		eq. (9.13)	eq. (9.4)	or Q_{add}			
-	-	m	m	kPa	kPa	-	o	-	o	kPa	kN	kPa	kN	kN	kN	kN	kN	-
20	C	0,102	3,95	97	48	14	22,5	0,88	13	258,4	75,5	120	8,8	84,4	17,9	92,2	110,1	0,77
21	T	0,102	4,16	98	49	14	22,5	0,88	13	261,9	80,6	-	-	80,6	7	111,9	111,9	0,72
22	T	0,102	3,92	97	48	14	22,5	0,88	13	257,9	74,8	-	-	74,8	2,5	102,9	102,9	0,73
23	T	0,102	3,8	96	47	13	22,5	0,88	13	248,1	69,8	-	-	69,8	0	104,6	104,6	0,67
24	T	0,102	3,7	96	46	13	22,5	0,88	13	246,3	67,4	-	-	67,4	0	93,5	93,5	0,72
25	T	0,100	3,6	98	46	13	22,5	0,88	13	252,2	65,8	-	-	65,8	0	92,0	92,0	0,72
26	C	0,168	4,5	100	51	14	22,5	0,88	13	267,1	146,5	120	23,9	170,4	38,66	155,3	194,0	0,88
27	C	0,102	3,66	120	53	8	26	1,03	23	229,0	114,0	120	8,8	122,8	17,39	106,6	124,0	0,99
28	C	0,102	4,8	18,3	34	1,8	36	1,46	28,5	24,5	20,4	120	8,8	29,3	2,03	25,0	27,0	1,08
29	T	0,250	6	22	32	1,5	33,5	1,35	25	25,2	55,4	-	-	55,4	0	69,0	69,0	0,80
30	T	0,168	2,01	22	33	1,3	33,5	1,35	25	24,1	11,9	-	-	11,9	0	12,0	12,0	0,99
31	T	0,153	4,85	42	54	5,5	34,5	1,4	(18)	77,5	58,7	-	-	58,7	0	75,0	75,0	0,78
32	T	0,762	71,3	37,6	132	1,2	31	1,24	(20)	62,2	3861,9	-	-	3861,9	-50	3559,0	3559,0	1,09
33	T	0,219	10	17	64	1,3	29,5	1,18	(18)	30,7	68,6	-	-	68,6	5	91,0	91,0	0,75
34	T	0,219	10	24	100	1,3	29,5	1,18	(18)	46,1	103,1	-	-	103,1	8	128,0	128,0	0,81
35	T	0,219	10	35	139	1,3	29,5	1,18	(18)	65,3	145,9	-	-	145,9	10	225,0	225,0	0,65
36	T	0,219	10	45	180	1,3	29,5	1,18	(18)	84,3	188,5	-	-	188,5	12	250,0	250,0	0,75
37	T	0,809	10	17	64	1,3	29,5	1,18	(18)	30,7	253,4	-	-	253,4	30	425,0	425,0	0,60
38	T	0,219	32,5	30	142	1,3	29,5	1,18	(18)	62,6	454,6	-	-	454,6	11	429,0	429,0	1,06

Table 9.6. Reliability of proposed method, cd.

				Pile Shaft								Pile base			SLT			
				Average								Avg.						
No	T/C	D	L	c_u	σ'_{v0}	OCR	ϕ'_{cs}	M	δ_f	$\sigma'_{rr,eq}$	Q_{shaft}	c_u	Q_{base}	Q_c	Q_{base}	Q_{shaft}	Q_m	Q_c/Q_m
								eq. (8.3)		eq. (9.2)	eq. (9.12)		eq. (9.13)	eq. (9.4)	or Q_{add}			
-	-	m	m	kPa	kPa	-	o	-	o	kPa	kN	kPa	kN	kN	kN	kN	kN	-
39	T	0,219	32,5	30	142	1,3	29,5	1,18	(18)	62,6	454,6	-	-	454,6	11	524	524	0,87
40	T	0,508	17,7	23,5	68	1,5	29,5	1,18	(18)	37,8	347,1	-	-	347,1	0	549	549	0,63
41	T	0,508	17,7	23,5	68	1,5	29,5	1,18	(18)	37,8	347,1	-	-	347,1	0	634	634	0,55
42	T	0,219	10	23	70,5	2,5	35	1,42	(18)	46,0	102,9	-	-	102,9	7	75	75	1,37
43	T	0,219	10	33,8	120	1,4	35	1,42	(18)	57,3	128,2	-	-	128,2	10	78	78	1,64
44	T	0,219	10	42,8	173	1	35	1,42	(18)	69,7	155,8	-	-	155,8	13	100	100	1,56
45	T	0,219	10	53,2	229	1	35	1,42	(18)	90,2	201,7	-	-	201,7	16	79	79	~~2,55~~
46	T	0,809	10	26,9	71	2,5	35	1,42	(18)	49,5	408,8	-	-	408,8	110	290	290	1,41
47	T	0,460	9,2	120	59	7	26	1,03	(23)	220,2	1243,0	-	-	1243,0	0	861	861	1,44
48	T	0,460	9,22	120	60	7	26	1,03	(23)	220,8	1249,0	-	-	1249,0	0	975	975	1,28
49	T	0,310	9,49	120	64	7	26	1,03	(18)	223,1	552,6	-	-	552,6	0	391	391	1,41
50	T	0,310	9,49	120	64	7	26	1,03	(18)	223,1	552,6	-	-	552,6	0	400	400	1,38
51	T	0,220	9,53	120	66	7	26	1,03	(18)	224,3	359,9	-	-	359,9	0	306	306	1,18
52	T	0,200	9,47	120	63	7	26	1,03	(18)	222,5	354,8	-	-	354,8	0	290	290	1,22
53	T	0,220	9,9	120	68	7	26	1,03	(18)	225,4	413,3	-	-	413,3	0	491	491	0,84
54	T	0,457	9	125	53	10	26	1,03	(18)	259,9	899,9	-	-	899,9	148	862	862	1,04
55	T	0,457	9	125	53	10	26	1,03	(18)	259,9	899,9	-	-	899,9	148	882	882	1,02
56	C	0,460	50	40	308	1	33	1,33	(22)	104,0	3036,9	70	104,7	3141,6	0	2400	2400	1,31
57	C	0,350	24,3	37,7	82,4	1,5	40	1,64	(36)	49,1	759,9	30	26,0	783,9	0	1316	1316	0,74

Table 9.6. Reliability of proposed method, cd.

				Pile Shaft							Pile base			SLT			
				Average							Avg.						
No	T/C	D	L	c_u	σ'_{v0}	OCR	ϕ'_{cs}	M	δ_f	$\sigma'_{rr,eq}$	Q_{shaft}	c_u	Q_{base}	Q_c	Q_{base}	Q_{shaft}	Q_m	Q_c/Q_m
								eq. (8.3)		eq. (9.2)	eq. (9.12)		eq. (9.13)	eq. (9.4)	or Q_{add}			
-	-	m	m	kPa	kPa	-	°	-	°	kPa	kN	kPa	kN	kN	kN	kN	kN	-
58	C	0,273	3,5	450	72	16	37	2,15	(32)	842,5	1580,4	450	237,1	1817,5	1450	750,0	2200	0,83
59	T	0,273	3,5	450	72	16	37	2,15	(32)	842,5	1580,4	-	0	1580,4	0	450,0	450	~~3,51~~
60	C	0,112	12,19	21,3	45	1,8	-	(1,15)	(20)	32,5	32,5	21,3	1,9	52,6	2	72,8	74,8	0,60
61	C	0,112	12,19	21,3	45	1,8	-	(1,15)	(20)	32,5	32,5	21,3	1,9	52,6	2	46,0	48	0,93
62	C	0,112	12,19	21,3	45	1,8	-	(1,15)	(20)	32,5	32,5	21,3	1,9	52,6	2	43,8	45,8	0,97
63	C	0,112	12,19	21,3	45	1,8	-	(1,15)	(20)	32,5	32,5	21,3	1,9	52,6	2	59,4	61,4	0,73
64	C	0,219	7,6	19,5	33	2	-	(1,15)	(25)	28,5	69,6	28	9,5	79,1	10,3	76,7	87	0,91
65	C	0,800	8,3	179	83	10	-	(1,15)	(15)	317,9	1777,1	180	814,3	2591,4	0	3700	3700	0,70
66	C	2,500	32	64	161	2,3	-	(1,15)	(25)	117,4	13764,1	95	4197,0	17961,1	2600	15800	18400	0,98
67	C	0,357	36	70	175	2,6	-	(1,15)	(25)	134,6	2535,3	95	85,6	2620,8	100	2900	3000	0,87
68	C	0,406	45	50	204	1,5	-	(1,15)	(18)	101,0	1884,0	70	81,6	1965,5	0	1915	1915	1,03
69	C	0,273	10,1	106	111	9,6	-	(1,15)	(20)	247,1	779,2	180	94,8	874,0	0	792	792	1,10
70	T	0,273	10,1	106	111	9,6	-	(1,15)	(15)	247,1	573,6	-	0	573,6	0	460	460	1,25
71	C	0,102	4,5	8	11	2,5	-	(1,15)	(25)	11,7	7,9	8	0,6	8,5	0	7	7	1,21
72	T	0,508	22,6	32,7	136	1,4	-	(1,15)	(15)	65,2	630	-	-	630,0	0	402	402	1,57
73	T	0,508	22,6	32,7	136	1,4	-	(1,15)	(15)	65,2	630	-	-	630,0	0	622	622	1,01
74	T	0,508	25	100	104	6	-	(1,15)	(15)	191,9	2051,5	-	-	2051,5	0	3030	3030	0,68
75	T	0,508	25	100	104	6	-	(1,15)	(15)	191,9	2051,5	-	-	2051,5	0	3080	3080	0,67
																	AVG	1,02
																	COV	0,29

Note: C – compression test, T – tension test, D – pile diameter, L – embedded pile length, c_u – undrained shear strength, σ_{v0}' – vertical geostatic stress, OCR – overconsolidation ratio, ϕ_{cs}' – critical angle of friction, M – stress ratio, δ_f – interface friction angle, $\sigma_{rr,eq}'$ – radial effective stress after equalization, Q_{shaft} – pile shaft capacity, Q_{base} – pile base capacity, Q_c – calculated axial pile capacity, Q_m – axial force measured during static load test

are achieved.

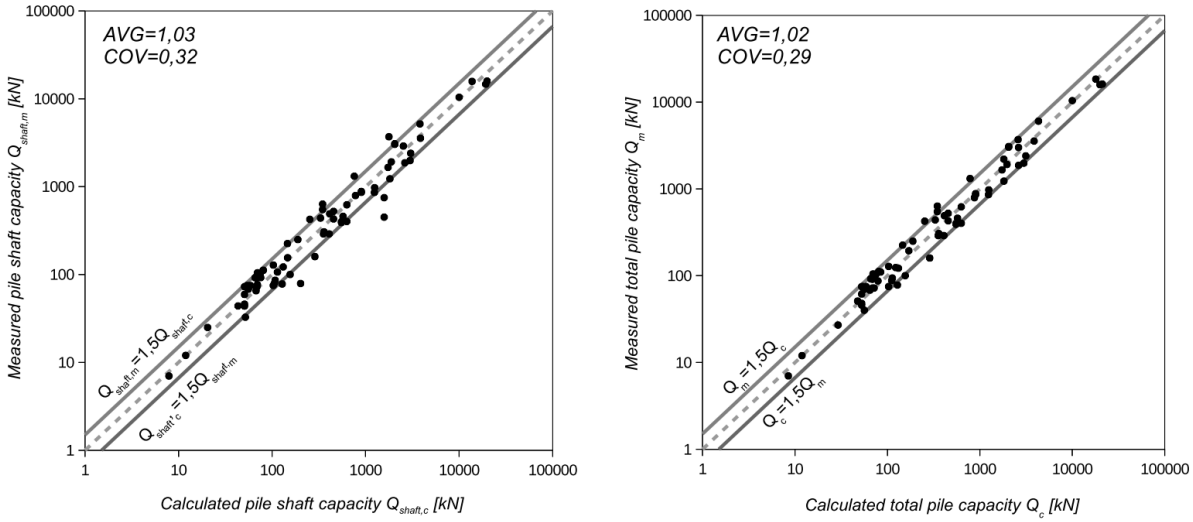

Figure 9.3. Calculated pile shaft capacity and total pile capacity versus measured values

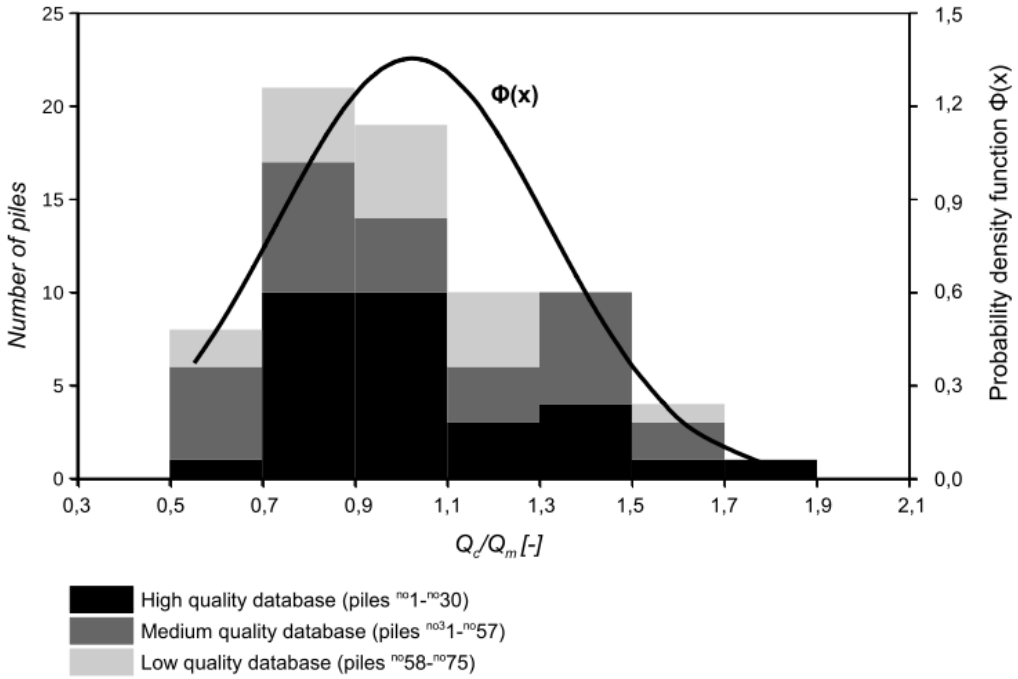

Figure 9.4. Histogram for Q_c/Q_m ratio

9.3 Incorporation of installation effects in pile design

The necessity of reliable and efficient pile design method is major issue for researchers and designers. In this section the possibility of more precise pile calculation using proposed formula for radial effective stress is shown. Firstly, the pile static test program in Poznań Łacina Commercial Centre is introduced. The validation of proposed method is presented using Poznań SLTs. Next, the author's formula will be compared with others, currently used methods in pile design. Furthermore, the representative pile form Poznań site will be

modelled numerically with two different approaches. In the first one, the full large deformation finite element methods are used. In the second one, the application of author's equations in pile settlement calculations using standard FEM approach is presented.

9.3.1 Pile static load tests in Poznań

The three geotechnical reports have been done for Poznań Łacina Commercial Centre located in Poznań, Polska as it has been already reported in chapter 7. Totally, the in-situ investigation consists of 106 boreholes, 86 CPT/CPT-u with 22 dissipation tests, 5 dilatometer tests (DMT) and 10 Dynamic Light Probe (DPL) tests. Laboratory tests include 6 series of consolidated undrained (CU) tests, 6 oedometer tests, grain size analysis and basic physical properties determination. The building is founded on footings with Controlled Modulus Columns (CMC) drilled with Full Displacement Pile (FDP) auger. The 16 CMC piles in different parts of building have been selected for SLTs, but only 10 piles are considered for validation purposes in this thesis. All piles have been summarized in table 9.7 with comment regarding validation. The ultimate axial load Q_{SLT} is considered as corresponding the settlement equal 10% of pile diameter (Tomlinson and Woodward, 2015) and it is obtained directly from SLT or Chin (1970) approximation. The Q_{SLT} is shown in table 9.7 while the load-settlement curves are presented in Appendix E.

9.3.2 Verification of proposed method

The soil stress state after installation and following consolidation phase is represented by radial effective stress described by equation (9.9) and *IEC* expressed with formula (9.11). The pile bearing capacity has been calculated using standard approach. The pile toe capacity is equal to $0{,}8q_tA_b$ as it is presented by equation (9.10). The Q_{shaft} is calculated with accordance to equation (9.12) with assumption that radial effective stresses are equal to the author's proposition. The bearing capacity for 10 piles from Poznań site is calculated in table 9.8 and it is compared with SLT results. The following assumption are made for analytical calculations:

1. Average undrained shear strength is estimated from CPT-u tests using cone factor N_{kt}=20 which has been confirmed with laboratory data.
2. Vertical geostatic stresses are calculated with accordance to in-situ conditions and laboratory determination of soil density.
3. The *M* is the same for all Poznań site and it is determinated from CU triaxial testing.
4. Interface angle of friction for concrete-soil interface is usually assumed as 0,7-1,0ϕ' (e.g., Chen et al., 2015; Tsubakihara et al., 1993). As no laboratory data have been provided for interface testing, the δ=0,85ϕ' is used with possible ±0,15ϕ' variation.
5. OCR is assessed with CPT and DMT sounding.
6. *IEC* coefficient is calculated using equation (9.11).
7. The average radial effective stress is calculated using equation (9.9).
8. Pile base and pile shaft capacity are calculated using equations (9.10) and (9.12), respectively.
9. Corrected cone resistance for pile base capacity calculation is averaged from distance ±1,5D from pile toe.

Table 9.7. Poznań static loading test program

No	*CMC pile*	*C/T*	z_{head}	z_{toe}	*D*	*L*	*L/D*	*Time to SLT*	Q_{SLT}	*Notes*	*For validation*
	-	-	m	m	m	m	-	days	kN	-	-
1	*SD3*	*C*	*0,0*	*9,52*	*0,36*	*9,52*	*26,4*	*20*	*982*	*-*	*Yes*
2	*A2*	*T*	*0,0*	*7,64*	*0,36*	*7,64*	*21,2*	*26*	*761*	*-*	*Yes*
3	*SD4*	*C*	*0,0*	*7,67*	*0,36*	*7,67*	*21,3*	*21*	*980*	*-*	*Yes*
4	*137*	*C*	*0,0*	*6,1*	*0,36*	*6,1*	*16,9*	*51*	*768*	*Damaged pile head*	*Yes*
5	*E407*	*C*	*0,0*	*7,0*	*0,36*	*7,0*	*19,4*	*31*	*937*	*-*	*Yes*
6	*H151*	*C*	*0,0*	*7,3*	*0,36*	*7,3*	*20,3*	*43*	*1081*	*Damaged pile head*	*Yes*
7	*G415*	*C*	*0,0*	*7,2*	*0,36*	*7,2*	*20,0*	*28*	*987*	*-*	*Yes*
8	*100*	*C*	*0,0*	*7,0*	*0,36*	*7,0*	*19,4*	*42*	*718*	*-*	*Yes*
9	*359*	*C*	*0,0*	*6,0*	*0,36*	*6,0*	*16,7*	*17*	*581*	*-*	*Yes*
10	*D689*	*C*	*0,0*	*7,0*	*0,36*	*7,0*	*19,4*	*41*	*684*	*Pile embedded in loam/clay mixture*	*Yes*
11	*SD1*	*C*	*0,0*	*8,63*	*0,36*	*8,63*	*24,0*	*23*	*(283)*	*Unreliable data, damaged pile head*	*No*
12	*SD2*	*C*	*0,0*	*6,65*	*0,36*	*6,65*	*18,5*	*27*	*(357)*	*Unreliable data, servomotor malfunction*	*No*
13	*A5*	*T*	*0,0*	*11,52*	*0,36*	*11,52*	*32,0*	*19*	*(467)*	*Unreliable data, excessive support settlement*	*No*
14	*H291*	*C*	*0,0*	*8,0*	*0,36*	*8,0*	*22,2*	*43*	*1345*	*Pile partially in sand deposit*	*No*
15	*545*	*C*	*0,0*	*6,23*	*0,36*	*6,23*	*17,3*	*41*	*-*	*Unreliable data, test unfinished*	*No*
16	*G373*	*C*	*0,0*	*7,0*	*0,36*	*7,0*	*19,4*	*44*	*1566*	*Pile partially in sand deposit*	*No*

Note: CMC – Controlled Modulus Column, SLT- Static Load Test, C – compression test, T – tension test, z_{head} –pile head depth, z_{toe} – toe depth, L – embedded pile length, D – pile diameter, Q_{STL} – axial force measured during static load test, values in brackets refers to unreliable measured pile axial force

Table 9.8. Validation of author's proposition with Poznań SLTs

				Pile Shaft							Pile base			SLT	
				Average							Avg.				
No	T/C	D	L	c_u	σ'_{v0}	OCR	ϕ'_{cs}	M	δ_f	$\sigma'_{rr,eq}$	Q_{shaft}	q_t	Q_{base}	Q_c	Q_m	Q_c/Q_m
								eq.(8.3)		eq.(9.9)	eq.(9.12)		eq.(9.10)	eq.(9.4)		
-	-	m	m	kPa	kPa	-	^{o}	-	^{o}	kPa	kN	MPa	kN	kN	kN	-
1	C	0,36	9,52	102	97,1	10	16	0,601	13,5 (±2,5)	330	768 (±148)	2,2	262	1030 (±148)	982	1,05 (±0,15)
2	T	0,36	7,64	100	77,9	11	16	0,601	13,5 (±2,5)	324	616 (±118)	-	-	616 (±118)	761	0,81 (±0,16)
3	C	0,36	7,67	100	78,2	11	16	0,601	13,5 (±2,5)	324	618 (±119)	2,12	240	859 (±119)	980	0,88 (±0,12)
4	C	0,36	6,1	90	62,2	10	16	0,601	13,5 (±2,5)	275	421 (±81)	1,91	187	608 (±81)	768	0,79 (±0,11)
5	C	0,36	7,0	110	71,4	14	16	0,601	13,5 (±2,5)	382	675 (±130)	2,23	232	907 (±130)	937	0,97 (±0,14)
6	C	0,36	7,3	125	74,5	12	16	0,601	13,5 (±2,5)	403	746 (±144)	2,55	239	985 (±144)	1081	0,91 (±0,13)
7	C	0,36	7,2	131	73,4	9	16	0,601	13,5 (±2,5)	372	682 (±132)	2,77	355	1037 (±132)	987	1,05 (±0,13)
8	C	0,36	7,0	77	71,4	14	16	0,601	13,5 (±2,5)	284	488 (±94)	1,41	189	677 (±94)	718	0,94 (±0,13)
9	C	0,36	6,0	83	71,4	7,5	16	0,601	13,5 (±2,5)	234	404 (±78)	1,79	189	593 (±78)	581	0,87 (±0,11)
10	C	0,36	7,0	90	61,2	8	16	0,601	13,5 (±2,5)	250	378 (±73)	1,94	186	563 (±73)	684	0,97 (±0,12)
															AVG	0,92 (±0,13)
															COV	0,10

Note: C – compression test, T – tension test, D – pile diameter, L – embedded pile length, c_u – undrained shear strength, σ_{v0}' – vertical geostatic stress, OCR – overconsolidation ratio, ϕ_{cs}' – critical angle of friction, M – stress ratio, δ_f – interface friction angle, $\sigma_{rr,eq}'$ – radial effective stress after equalization, Q_{shaft} – pile shaft capacity, Q_{base} – pile base capacity, Q_c – calculated axial pile capacity, Q_m – pile bearing capacity determined from SLT

A very satisfactory results have been achieved (table 9.8) with average coincidence of 0,92 between calculated and measured capacities with very low COV of 0,10. However, the applied friction coefficient on pile-soil interface can strongly affect the empirical solution. In Poznań site this can differ the Q_c/Q_m ratio about 13%. The knowledge of δ_f determined from interface direct shear tests would substantially improve the shaft resistance prediction. In particular, the knowledge about the dilative or contractive interface (Bałachowski, 2006b) during SLT can be crucial for successful calculation.

9.3.3 Confrontation of proposed approach with other design methods

The author's proposition for improvement in pile design will be compared with others, widely used design methods which will be described in section below. The aim of such action is to check if author's proposition can be contributed to pile designing and if it can be competitive approach in comparison to well-established methods.

9.3.3.1 Other pile design methods overview

In this section the brief overview of selected empirical methods for pile designing is provided.

API-2000

API-2000 was originally applied as a design method for steel piles. In recent years it was extended to another pile types and installation techniques. The API-2000 is total stress method where adhesion factor is used and the pile shaft unit resistance is related to undrained shear strength as follows (American Petroleum Institute, 2000):

$$\tau_f = \alpha\, c_u \tag{9.14}$$

where: α – adhesion coefficient, τ_f – pile shaft friction (pile shaft unit resistance), c_u – undrained shear strength.
The adhesion coefficient for driven piles can be estimated from Randolph and Murphy work (1985):

$$\alpha = 0{,}5\left(c_u/\sigma'_{v0}\right)^{-0{,}5} \qquad for \qquad c_u/\sigma'_{v0} \le 1 \tag{9.15}$$

$$\alpha = 0{,}5\left(c_u/\sigma'_{v0}\right)^{-0{,}25} \qquad for \qquad c_u/\sigma'_{v0} > 1 \tag{9.16}$$

where: α – adhesion coefficient, c_u – undrained shear strength., σ'_{v0} – vertical geostatic stress.
For bored concrete pile the FHWA (Brown et al., 2010) guidelines can be applied to estimate the adhesion coefficient:

$$\alpha = 0{,}55 \qquad for \qquad c_u/p_a \le 1{,}5 \tag{9.17}$$

$$\alpha = 0{,}55 - 0{,}1\left(\frac{c_u}{p_a} - 1{,}5\right) \qquad for \qquad 1{,}5 \le c_u/p_a \le 2{,}5 \tag{9.18}$$

where: α – adhesion coefficient, c_u – undrained shear strength., p_a – atmospheric pressure

equal 100kPa.
For Poznań site the c_u ranges around the 110kPa, thus the adhesion coefficient obtained from FHWA guidelines is 0,55. Values about 0,4 are obtained from equation (9.16), see table F.1 in Appendix F. In this thesis, the FHWA adhesion factor is used. The pile base resistance is calculated using equation (9.13).

β Method

FHWA gudelines (Brown et al., 2010) allow to use the effective stress approach for cohesive soils with OCR>8. This condition is fulfilled for Poznań site where average OCR is equal to 12. In β method the pile base unit resistance is calculated using Terzaghi bearing capacity equation (Terzaghi, 1943):

$$q_b = \sigma'_{v,b} N_q + c_b' N_c \tag{9.19}$$

where: $\sigma'_{v,b}$ – vertical effective stress at the pile base, c'_b – soil cohesion, N_c and N_q – bearing capacity factors.
The bearing capacity factors can be calculated as follows (Janbu, 1976):

$$N_q = \left(\tan\phi' + \sqrt{1+\tan^2\phi'}\right)^2 \exp\left(2\eta\tan\phi'\right) \tag{9.20}$$

$$N_c = \left(N_q - 1\right)\cot\phi' \tag{9.21}$$

where: N_c and N_q – bearing capacity factors, ϕ' – effective angle of internal friction, η – angle which defines the shear surface under pile toe, here $\eta=\pi/3$.
Consequently, the skin friction in β method can be expressed as (Fleming et al., 2009):

$$\tau_f = \beta \sigma'_{v,0} \tag{9.22}$$

where: τ_f – pile shaft friction (pile shaft unit resistance), β – beta coefficient, $\sigma'_{v,0}$ – vertical effective stress.
The beta coefficient β can be calculated by equations (Fleming et al., 2009):

$$\beta = \tan\delta_f K_c \tag{9.23}$$

where: β – beta coefficient, δ_f – friction angle at failure on pile-soil interface, K_c – coefficient of horizontal stress, The FHWA guidelines (Brown et al., 2010) for concrete bored piles in clays suggest that for clays the $K_c=K_0$. Here, the lateral earth pressure is assumed after Meyerhof (1976): $K_c = 1{,}5\left(1-\sin\phi'\right)OCR^{0,5}$.

NGI-05

Norwegian Geotechnical Intitute (NGI) method for pile design is rather dedicated for steel driven or jacked piles but it will be also applied to Poznań site case. The reason is that Poznań CMC drilled piles are also displacement type piles and that pile capacity calculated by NGI-05 approach corresponds to time of 100 days after driving (Karlsrud et al., 2005). NGI-05 is

an alpha-based method where the adhesion coefficient is defined as (Karlsrud et al., 2005):

$$\alpha = 0{,}32\left(I_p - 10\right)^{-0{,}3} \qquad for \qquad c_u/\sigma'_{v0} < 0{,}25 \tag{9.24}$$

$$\alpha = 0{,}5\left(c_u/\sigma'_{v0}\right)^{-0{,}3} \qquad for \qquad c_u/\sigma'_{v0} > 1 \tag{9.25}$$

where: α – adhesion coefficient, I_p – plasticity index, c_u – undrained shear strength, σ'_{v0} – vertical geostatic stress.
The adhesion coefficient in range $0{,}25 \le c_u/\sigma'_{v0} \le 1$ is interpolated. The shaft capacity is calculated using equation (9.12) while the pile base is calculated using equation (9.13).

Almeida-1996

Almeida (1996) proposed the CPT-based correlation for skin friction on the basis of jacked and driven piles in clay. The skin friction is estimated as follows:

$$\tau_f = \left(q_t - \sigma_{v,0}\right)/k_1 \tag{9.26}$$

where:

$$k_1 = 12 + 14{,}9\log\left(q_n/\sigma'_{v0}\right) \qquad for \qquad I_p < 20\,\% \tag{9.27}$$

$$k_1 = 11{,}8 + 14\log\left(q_n/\sigma'_{v0}\right) \qquad for \qquad I_p \ge 20\,\% \tag{9.28}$$

where: τ_f – skin friction (pile shaft unit resistance), q_t – average corrected cone resistance, $\sigma'_{v,0}$ – vertical total stress, k_1 – correction coefficient. In this research the $I_p > 20\%$ is assumed.
The pile base capacity is calculated using Almeida et al. proposition (1996), where pile toe resistance is equal $0{,}6q_t$.

LCPC

The Laboratoire Central des Ponts et Chaussées (LCPC) proposition (Bustamante and Gianeselli, 1982) for pile shaft unit resistance for concrete piles in clay is described by equations:

$$\tau_f = q_c/30 \qquad where \qquad \tau_{f,max} = 15\,kPa \qquad for \qquad q_c \le 1\,MPa \tag{9.29}$$

$$\tau_f = q_c/40 \qquad where \qquad \tau_{f,max} = 80\,kPa \qquad for \qquad 1\,MPa \le q_c \le 5\,MPa \tag{9.30}$$

where: q_c – cone resistance, $\tau_{f,max}$ – maximum skin friction.
The pile base resistance is equal to $0{,}35q_t$ (Bustamante and Gianeselli, 1982).

ICP-05

Jardine et al. (2005) have summarized the research conducted at Imperial Collaege London and proposed the formula for unit shaft resistance for driven piles in clays and friction concrete piles. The skin friction is based on effective stress approach:

$$\tau_f = \sigma'_{rf}\tan\delta_f \tag{9.31}$$

Table 9.9. Predictions of Poznań piles bearing capacity using different approaches

	SLT	Author's prop.		API-2000		Beta Method		NGI-05		Almeida-1996		LCPC		ICP-05		Lehane-2013			
No	Q_m	Q_c	Q_c/Q_m	Q_c	Q_c/Q_m	Q_c	Q_c/Q_m	Q_c	Q_c/Q_m	Q_c	Q_c/Q_m	Q_c	Q_c/Q_m	Q_c	Q_c/Q_m	Q_c eq.(9.33)	Q_c/Q_m	Q_c eq.(9.34)	Q_c/Q_m
-	kN	kN	-	kN	-	kN	-	kN	-	kN	-	kN	-	kN	-	kN	-	kN	-
1	982	1030	1,05	756	0,77	501	0,51	592	0,60	849	0,86	707	0,72	632	0,64	939	0,96	646	0,66
2	761	616	0,81	475	0,62	305	0,40	326	0,43	492	0,65	458	0,60	259	0,34	547	0,72	301	0,40
3	980	859	0,88	570	0,58	352	0,36	420	0,43	674	0,69	565	0,58	501	0,51	789	0,80	543	0,55
4	768	608	0,79	467	0,61	225	0,29	351	0,46	489	0,64	411	0,54	355	0,46	599	0,78	410	0,53
5	937	907	0,97	607	0,65	331	0,35	439	0,47	639	0,68	543	0,58	472	0,50	768	0,82	522	0,56
6	1081	985	0,91	693	0,64	334	0,31	484	0,45	727	0,67	631	0,58	485	0,45	874	0,81	577	0,53
7	987	1037	1,05	777	0,79	288	0,29	555	0,56	845	0,86	719	0,73	558	0,57	1036	1,05	713	0,72
8	718	677	0,94	432	0,60	331	0,46	339	0,47	455	0,63	362	0,50	451	0,63	528	0,74	385	0,54
9	581	593	0,87	459	0,67	254	0,37	352	0,51	527	0,77	437	0,64	380	0,56	619	0,90	429	0,63
10	684	563	0,97	432	0,74	200	0,34	317	0,54	485	0,83	410	0,70	336	0,58	598	1,03	408	0,70
AVG			0,92		0,67		0,37		0,49		0,73		0,62		0,52		0,86		0,58
COV			0,10		0,11		0,19		0,12		0,13		0,13		0,17		0,14		0,17

Note:SLT – Static Loading Test, Q_c – calculated axial pile capacity, Q_m – axial force determined in static load test

where:

$$\sigma'_{rf} = (2 - 0{,}625\, I_{vr})\, \sigma'_{v0}\, YSR^{0{,}42} [max(h/R, 8)]^{-0{,}2} \tag{9.32}$$

where: τ_f – pile shaft friction (pile shaft unit resistance), σ'_{rf} – radial effective stress acting on pile shaft after installation and consolidation phases, δ_f – friction angle at failure on pile-soil interface, $\sigma'_{v,0}$ – vertical geostatic effective stress, I_{vr} – measure of clay sensitivity, $I_{vr} = \log(S_t)$ where S_t – soil sensitivity, YSR – equivalent of OCR, h – height above pile tip, R – pile radius. As friction fatigue occurrence in FDP concrete pile is ambiguous, the term $[max(h/R, 8)]^{-0{,}2}$ in equation (9.31) is reduced to $[max(h/R)]^{-0{,}2}$, where h is equal to the half of embedded pile length. The pile base capacity is calculated with Jardine et al. (2005) proposition, see equation (9.10).

Lehane-2013

Lehane et al. (2013) formulate two equations for skin friction dedicated for displacement piles in clay:

$$\tau_f = 0{,}055\, q_t [max(h/R, 1)]^{-0{,}2} \tag{9.33}$$

$$\tau_f = \frac{0{,}23\, q_t [max(h/R, 1)]^{-0{,}2}}{(q_t/\sigma'_{v0})^{0{,}15}} \tan \delta_f \tag{9.34}$$

where: τ_f – pile shaft friction, q_t – corrected cone resistance, h – height above pile tip, R – pile radius, $\sigma'_{v,0}$ – vertical geostatic effective stress, δ_f – interface friction angle at failure.
The influence of friction fatigue is ambiguous and similar as in ICP-05 the $[max(h/R, 1)]^{-0{,}2}$ is reduced to $[max(h/R)]^{-0{,}2}$ where h=0,5L. The base is calculated using equation (9.10).

9.3.3.2 Reliability of the proposed method

The author's method is compared with eight pile design approaches in table 9.9. The detailed calculation procedure with pile design methods presented in section 9.3.3.1 is shown in Appendix F.

The following assumption are made in calculations:

1. The average values of undrained shear strength, vertical stresses and corrected cone resistance along pile shaft are used.
2. c_u is estimated from CPT-u test using cone factor N_{kt}=20.
3. Interface friction angle is assumed as $0{,}85\phi'_{cs}$ =13,5°.
4. The average OCR is assessed with CPT sounding.
5. Undrained shear strength and corrected cone resistance q_t for pile base capacity calculation is averaged from distance ±1,5D from pile toe.
6. In beta method the peak failure envelope have been used with ϕ' and c' determined in TX tests, see Appendix G.

As one can see, proposition presented in this thesis can be satisfactory applied in pile design as a competitive design method for well-established approaches. Further, a very low coefficient of variation have been achieved for tested piles calculated with author's

proposition and the obtained results are conservative. Only the Lehane-2013:eq.(9.33) method shows similar reliability in pile capacity prediction for Poznań site.

9.3.3.3 Conclusions

In this section the author's contribution for pile design methods has been compared with eight design methods. The proposed method forms safe solution and it is competitive to other design methods. Consequently, it can be used as an additional approach for pile calculation improvement and more efficient design.

9.3.4 FEM calculation of representative pile

The pile number 5 (E407 CMC pile) is selected as the reference pile for FEM calculations. The E407 column is 7m long, drilled from the working platform located about 3m below the ground level, with pile toe buried at the depth of 10m. The E407 pile has been selected due to very homogeneous soil deposit and satisfactory set of in-situ and laboratory investigation. The reference pile localization is presented in figure 9.5. The in-situ investigation has been already presented in chapter 7, figure 7.8. The same location as in CPT modelling is used. The Poznań clay parameters have been previously summarized in table 7.5 in chapter 7.

In this section two possible approaches of FEM calculation with installation effects incorporation will be shown. These include full large deformation model and FEM model where post-consolidation stress state described with author's proposition is taken into account and it is modelled as an initial condition.

9.3.4.1 Large deformation approach

The full large deformation analysis of E407 pile is provided in author's paper (Konkol and Bałachowski, 2017) and here only brief review of this problem is described.

Assumption to analysis

Modelling of FDP pile is challenging task due to complex installation technique. Grabe et al. (2013) has shown FDP drilling tool installation using CEL method while Jiangtao (2009) has modelled sand compaction pile. In Jingtao approach (2009) the casting tool is jacked on prescribed depth and then it is withdrew with simultaneous lifting of sand injection. The same procedure can be applied to the CMC column, but the influence of the stresses under the pile toe are lost then. Therefore, in this section the similar technique as that presented by Larisch (2014) will be used. Firstly, let us assume that all displacement piles induce the same or at least similar stress change in subsoil during installation. Consequently, the CMC pile can be modelled as jacked pile as long as only the stress state change around the pile is important. This negligence of pile technology facilitates the CMC installation problem and allows for simplification of geometry.

The entire construction process of E407 pile will be modelled with UL formulation and effective stress approach. These include the overlaying soil excavation, installation process, consolidation and SLT. The UL installation phase will be compared to independent CEL model calculated with accordance to total stresses.

The effective stress parameters are the same as presented in table 7.6, section 7.2.2. Only

one exception is made. The shear modulus of 15 MPa is used to provide better correspondence to typical G/c_u ratio for large deformation (e.g., Vardanega and Bolton, 2013). The all parameters are summarized in table 9.10 and their calibration has been shown in section 7.7.2. The preconsolidation pressure distribution for one thick layers is calculated from equation (3.32) and it is shown in figure 9.6 where the assumed c_u distribution is also presented. The undrained shear strength profile is assessed from CPT-u data using N_{kt}=20 which was confirmed with laboratory tests. The total stress parameters are shown in table 9.11 and the undrained elastic modulus have been calculated by equation (3.26).

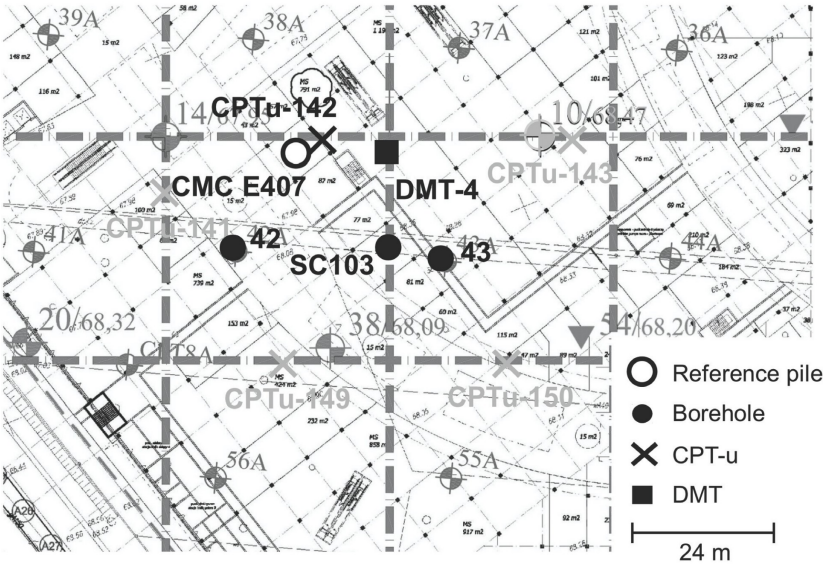

Figure 9.5. Reference CMC pile localization

Table 9.10. Effective stress parameters for LDFEM model

Parameter	*ρ'*	*G'*	*e_0*	*κ*	*λ*	*p_c'*	*M*	*ρ_w*	*K_0*	*k*
	g/cm³	*kPa*	*-*	*-*	*-*	*kPa*	*kPa*	*g/cm³*	*-*	*m/s*
Value	*1,02*	*15000*	*0,70*	*0,025*	*0,074*	*varying*	*0,601*	*1,0*	*2,0*	*$2x10^{-10}$*

Table 9.11. Total stress parameters for LDFEM model

Parameter	*ρ_{sr}*	*E_u*	*υ_u*	*c_u*	*σ_h/σ_v*
	g/cm³	*kPa*	*-*	*kPa*	*-*
Value	*2,02*	*45000*	*0,49*	*60÷140*	*1,5*

The last unknown parameter is the friction coefficient on pile-soil interface. In installation and consolidation phase the frictionless contact between soil and pile is assumed. In SLT the friction behaviour is used with prescribed value of friction coefficient. In section 9.3.3 the interface angle of friction has been presented as varying between 0,7ϕ' and 1,0ϕ' with average value of 0,85ϕ'. For purposes of large deformation modelling the lower bound of angle of internal friction equal to $\delta_f=⅔\phi'$ is used as conservative and safe assumption which is based on soil-concrete interface tests made by Chen et al. (2015). Chen et al. have tested red clay of similar strength parameters to that of Poznań clay (ϕ'=16°) and found that peak interface

friction angles vary from 10° to 15° while the residual ones vary from 9° to 12°. In empirical calculations δ_f=0,85ϕ'=13,5° can be satisfactory used, but in more precise FEM calculations conservative value of δ_f=⅔ϕ'=10,7° seems to be more suitable and accurate.

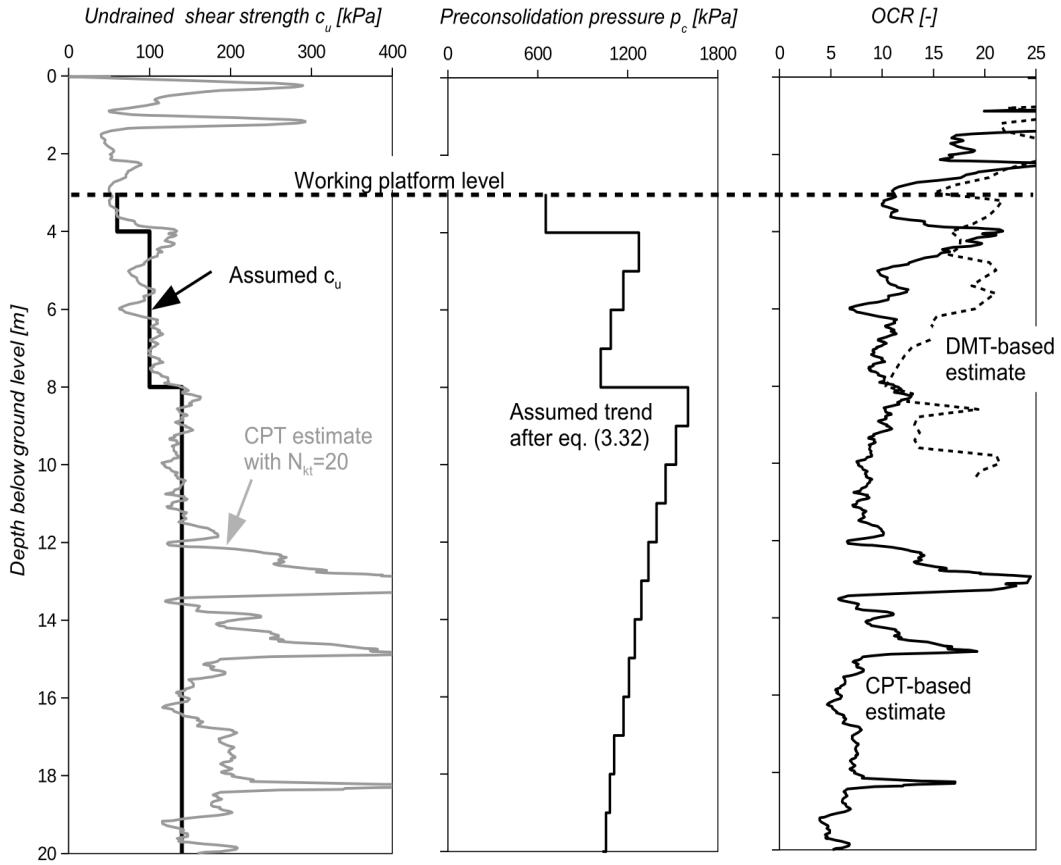

Figure 9.6. Undrained shear strength, OCR assessment and corresponding preconsolidation pressure distributions for CMC pile modelling

UL numerical model

Figure 9.7 shows the UL-LDFEM model geometry for considered problem. The soil domain is 11m wide and 22m height and it is discretized with 5916 C3D8RP elements. The UL model takes into account the entire pile history at Poznań site which includes excavation, pore water pressure equalization, following installation, 31 days of consolidation and static loading test according to programme that has been preformed in field location. The jacking velocity of 7 cm/s is taken from CMC drilling log, see Appendix H. The pile is modelled as a discrete rigid body.

CEL numerical model

The CEL-LDFEM model is presented in figure 9.8. The soil domain contains three layers with different shear strength values. The model consists of 186480 elements discretized with EC3D8R elements. The same assumptions and modelling techniques as in previous CEL models are used.

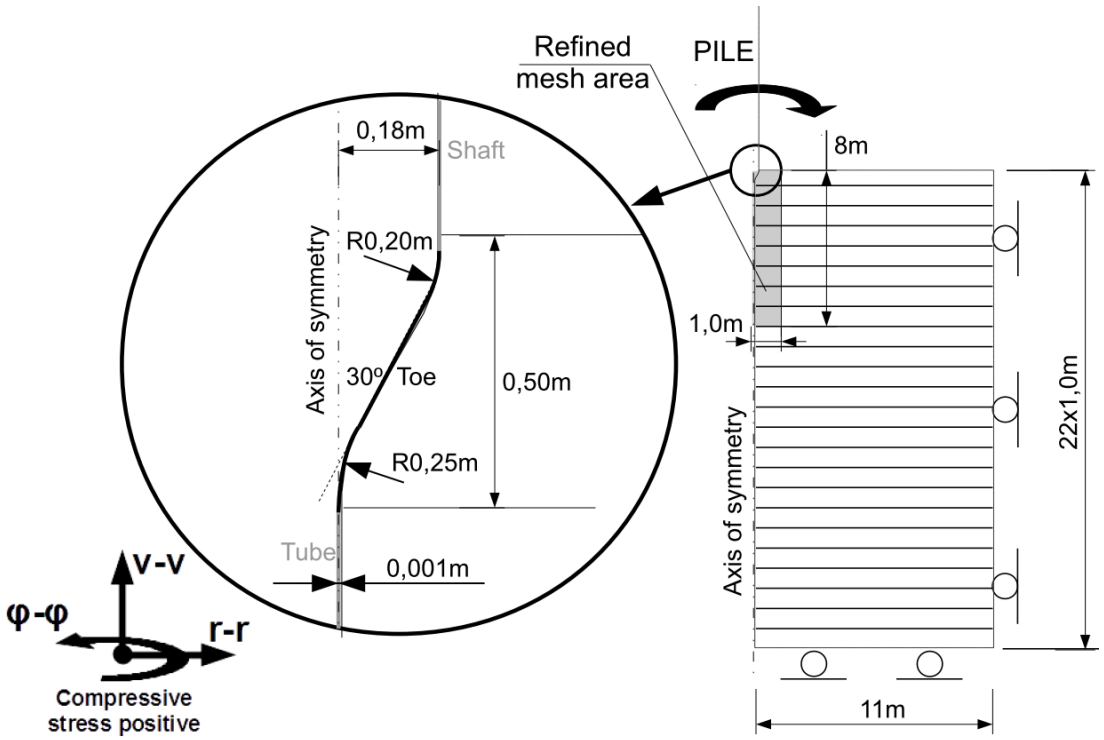

Figure 9.7. UL-LDFEM model for reference CMC pile

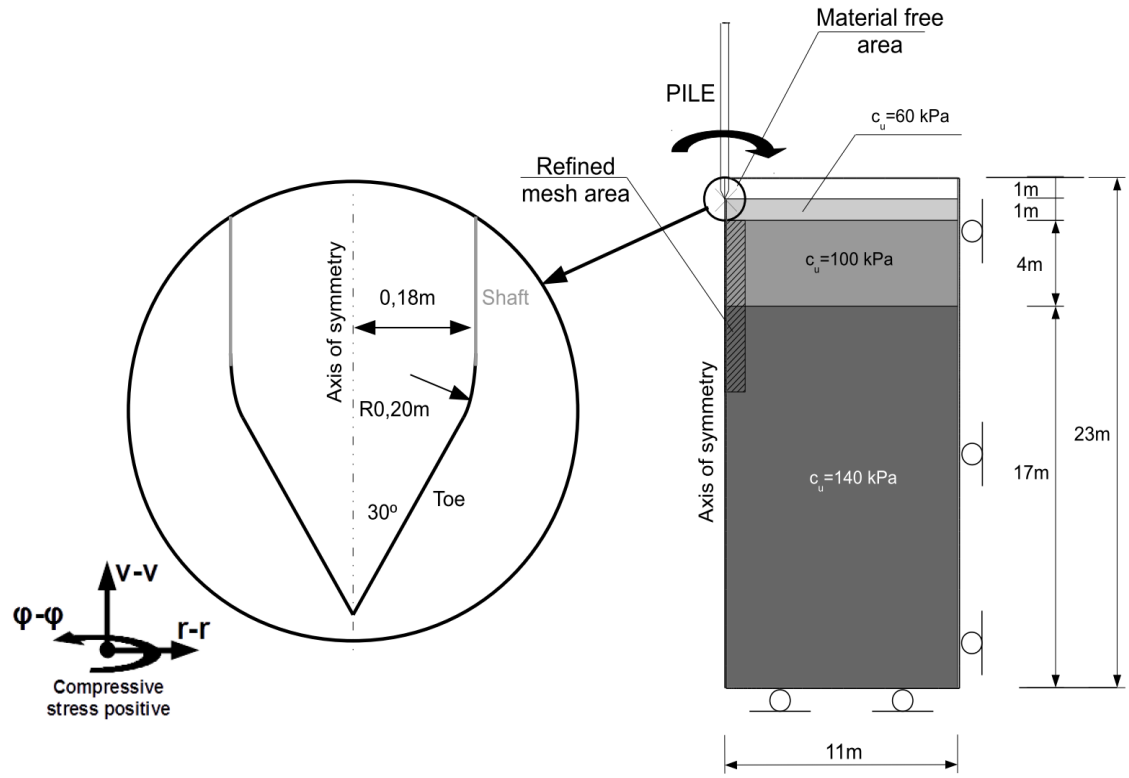

Figure 9.8. CEL-LDFEM model for reference CMC pile

Post-installation state

The UL and CEL models comparison in terms of total stresses is presented in figure 9.9a. The CEL underestimates the radial total stresses, but both formulations provides almost the same response around the pile toe. The pushing forces in both solutions are also similar and they are close to the data obtained from CMC drilling machine, see figure 9.9b. Thus, both formulations can be treated as a good approximation of installation processes which takes place in the soil.

Post-consolidation state

The radial effective stress and pore water pressure distributions after consolidation are presented in figure 9.10. As expected, significant increase in radial effective stress can be seen. However, the pore water dissipation curve reveals that after 31 days the pore water pressures are not equalized yet. The negative pore pressure in the upper part of the pile can be still observed, see figure 9.10.

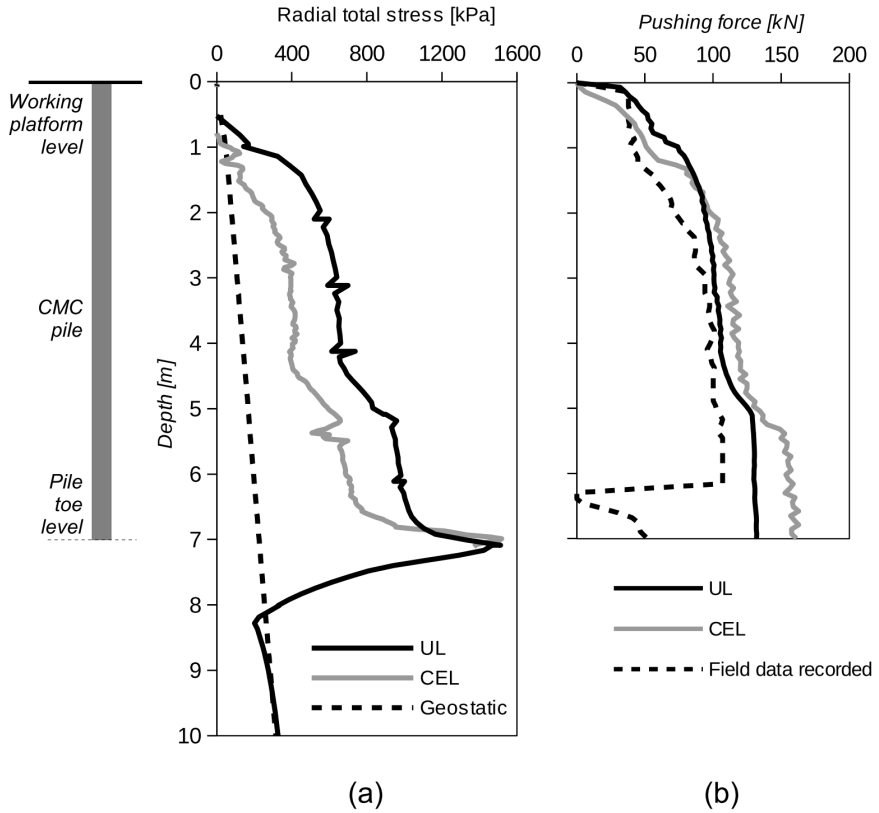

Figure 9.9. (a) Radial total stress acting on the pile wall after installation, (b) total pushing force obtained from numerical analysis and field drilling log.

SLT

The comparison between numerical model and field measurement is presented in figure 9.11, where almost perfect fit has been achieved. The decomposition of numerically obtained

capacity on pile toe and shaft resistance shows that toe capacity is almost equal to the well-known empirical formula which returns value of 128,5 kN, see equation (9.13) (e.g., Tomlinson and Woodward, 2015). Hence, installation effects are related to the shaft capacity

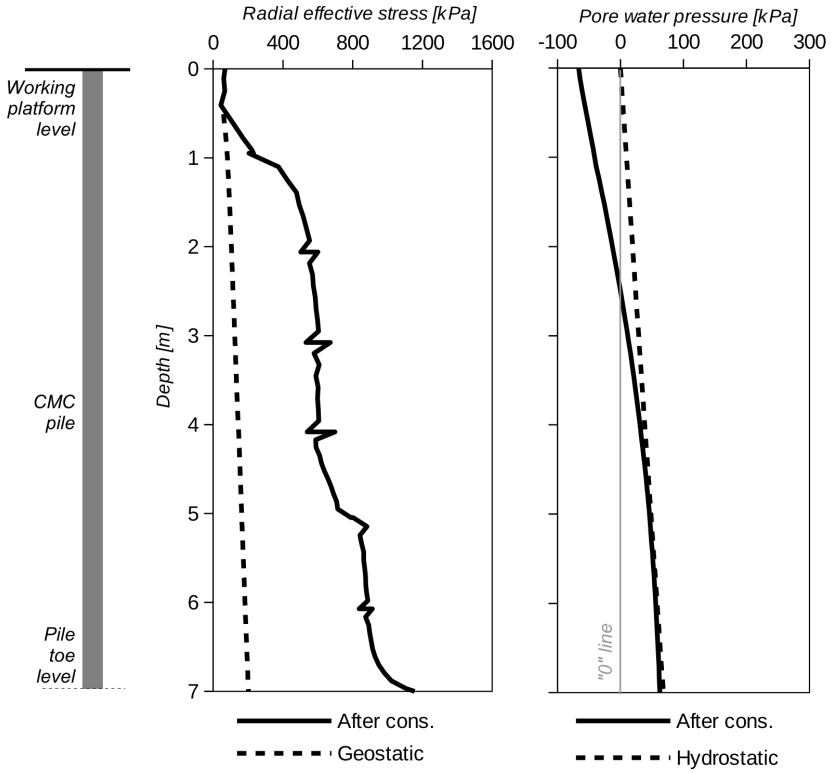

Figure 9.10. Radial effective stress and pore water pressure distributions along pile wall after 31 days of consolidation

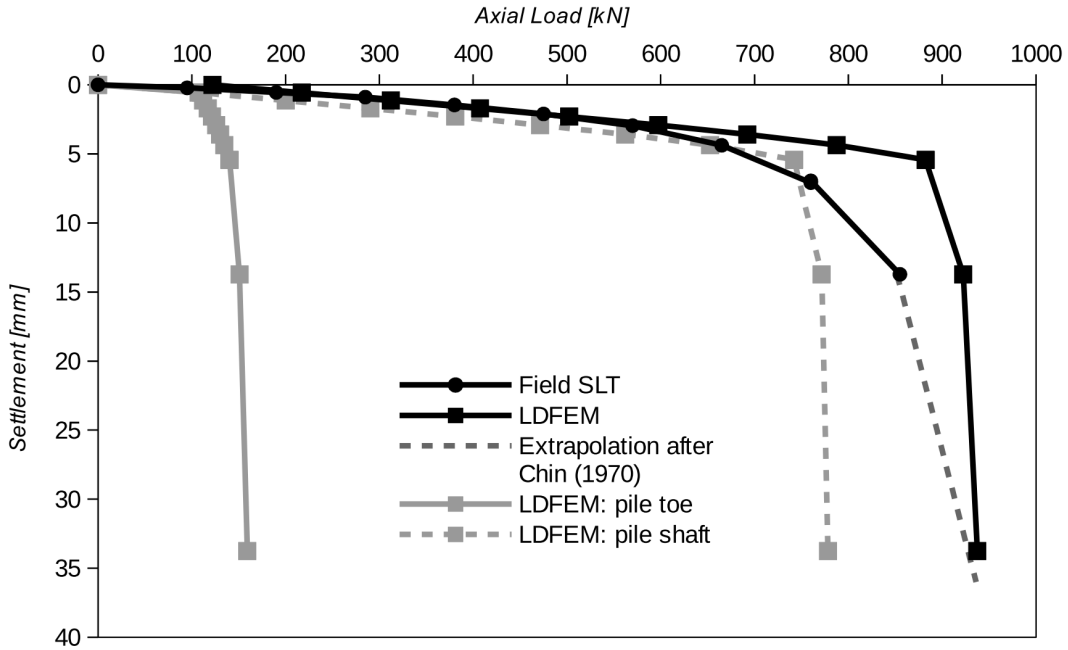

Figure 9.11. Field static loading test versus numerical UL-LDFEM model for CMC reference pile

and significant increase in radial effective stresses along the pile shaft. Thus, the applied coefficient of friction becomes a governing parameter in analysis and a slight difference in interface angle of friction can result in significant change in pile shaft bearing capacity. In E407 CMC pile the initially applied coefficient of friction gives a very good results but this may not be a rule and some interface testing are necessary to confirm this assumption.

9.3.4.2 Combined empirical and FEM approach

There is a different way to obtain the *Q-s* curve than performing the full LDFEM analysis. The idea is to use the empirical equations (9.9) and (9.11) that describe radial effective stress after equalization and then to use these stresses as an initial condition in FEM model. Figure 9.12 shows the radial stress distribution with depth obtained from equations (9.9) and (9.11). The average effective radial stress after consolidation is 342kPa. To implement this value in standard FEM software we can proceed twofold: firstly, we can artificially increase the friction coefficient on pile-soil interface or, secondly, we can modify the lateral earth pressure at rest coefficient. For E407 reference pile in Poznań site the average vertical geostatic stresses which act along the pile shaft are equal to 35,1kPa. The skin friction that should be mobilized during SLT can be expressed as follows:

$$\tau_f = \tan(\delta_f)\,\sigma'_{rr,eq} \tag{9.35}$$

where: τ_f – pile shaft friction, $\sigma'_{rr,eq}$ – radial effective stress after consolidation, δ_f – interface friction angle.

The same pile shaft friction should be obtained using artificial coefficient of friction and initial horizontal stress:

$$\tau_f = \mu\,\sigma'_{h,0} = \mu\,K_0\,\sigma'_{v,0} \tag{9.36}$$

where: τ_f – pile shaft friction, μ – friction coefficient, $\sigma'_{h,0}$ – initial horizontal stresses, K_0 – lateral earth pressure at rest coefficient, $\sigma'_{v,0}$ – initial vertical geostatic stress.

The comparison between equations (9.35) and (9.36) leads to derivation of required coefficient of friction that can be calculated from simple relation:

$$\mu = \frac{\tan(\delta_f)\,\sigma'_{rr,eq}}{K_0\,\sigma'_{v0}} \tag{9.37}$$

where: μ – friction coefficient, $\sigma'_{rr,eq}$ – radial effective stress after consolidation, δ_f – interface friction angle, K_0 – lateral earth pressure at rest coefficient $\sigma'_{v,0}$ – initial vertical geostatic stress.

Substituting the $\sigma'_{rr,eq}$=342kPa, δ_f=11º (acceptable approximation, see section 9.3.2.1), K_0=2 and $\sigma'_{v,0}$=35,1kPa the artificial friction coefficient is equal to 0,94 which is extremely high value. Consequently, the "friction" approach can introduce convergence problems in numerical model using implicit solver and so it has been observed in author's attempts where no success has been achieved. The second possible way to incorporate the equalization

stresses is to use artificially higher earth et rest pressure coefficient. For reference pile this can be written as:

$$K_c = \frac{\sigma'_{rr,eq}}{\sigma'_{v0}} \tag{9.38}$$

where: K_c – artificial effective stress ratio, $\sigma'_{rr,eq}$ – radial effective stress after consolidation, $\sigma'_{v,0}$ – initial vertical geostatic stress.

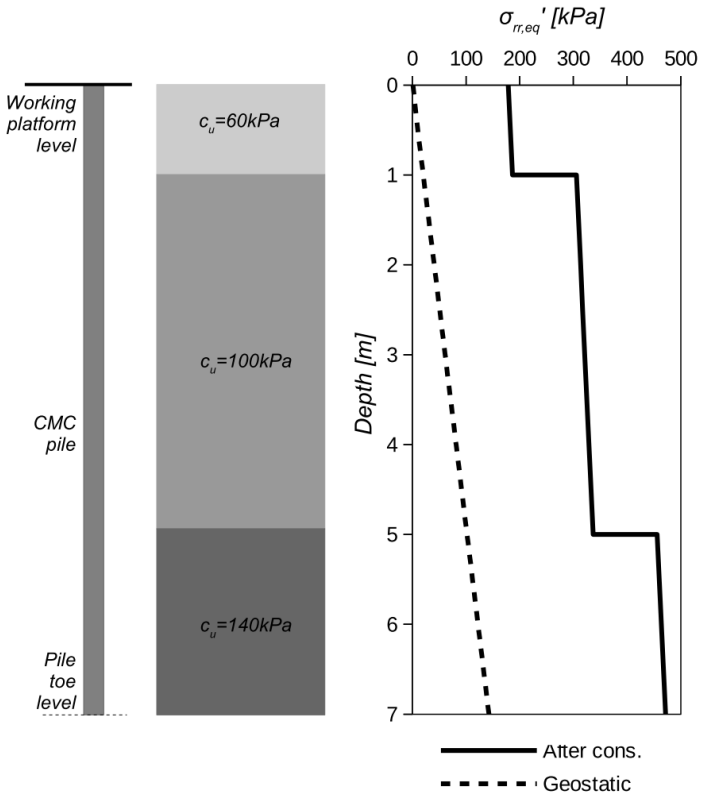

Figure 9.12. Radial effective stress distribution after author's method

Substituting the average values of $\sigma'_{rr,eq}$ =342kPa and $\sigma'_{v,0}$=35,1kPa, equation (9.38) returns the effective stress ratio K_c equal to 9,8. Here, some simplification is used as the horizontal stress distribution in numerical model using artificial K_c is different than actual one, see figure 9.12. Only the average values are the same, but this is still acceptable as long as total force acting on pile shaft is considered. The more actual radial stress distribution can be modelled only when overburden pressure is applied on the top of soil surface. However, this approach also requires several simplifications and as the result, the vertical stress state in whole model is changed. This can be also acceptable approach which has been tested by author and which also proved its applicability. However, the use of one, global K_c is simpler and it affects only the shaft area where the largest increase of stress is seen. Using this “stress” approach the only problem is to check if the initial mean stress is lower than preconsolidation pressure. For the numerical model as it is presented in figure 9.13 and the same material properties as in

LDFEM model (see table 9.10), the preconsolidation pressure in every layer is higher than initial mean stresses. The soil domain is discretized with 2722 C3D8RP elements and pile is modelled as a rigid discrete body. To show the influence of friction behaviour on pile-soil interface the two interface friction angles have been used: 10,8º and 13,5º which corresponds to interface friction coefficients 0,188 and 0,240, respectively.

The results of numerical SLT compared with field measurements are shown in figure 9.14. As one can see, a good agreement between field measurements and numerical solutions is achieved. The interface angle has strong impact on ultimate bearing capacity, but the load-settelement behaviour in the range of low and medium axial loads from FEM models are very similar to the field tests. Hence, the simplified “stress” approach can be easily applied to the standard FEM codes used in pile design industry.

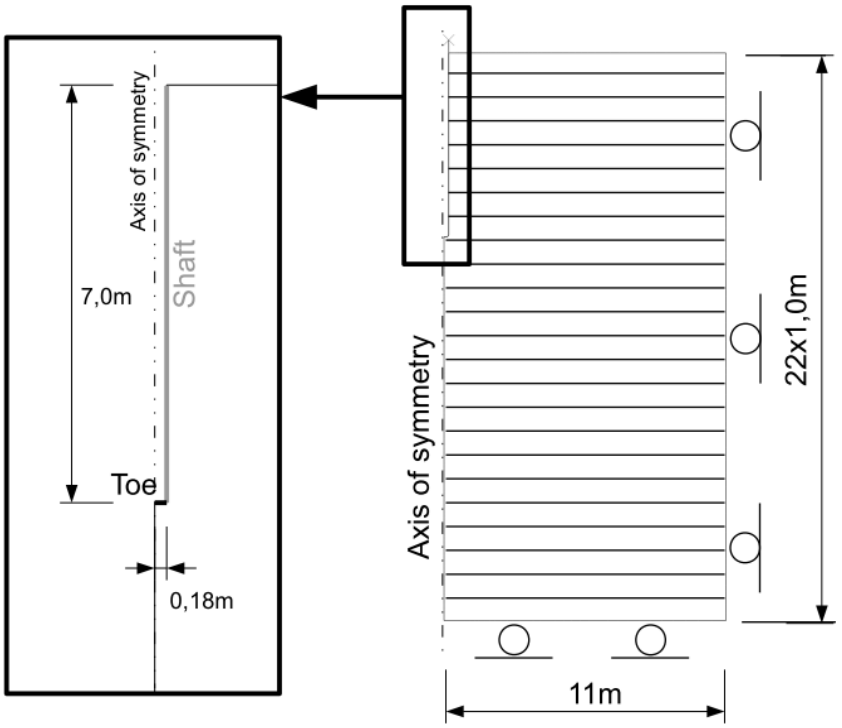

Figure 9.13. CMC reference pile FEM model for combined empirical and FEM approach

9.4 Summary

In this chapter the calibration of equation (8.19) using dataset of 30 piles has been made. The reliability and safety of the author's method has been verified using database of 75 piles. The proposition has been validated with SLTs results from Poznań site and compared with other pile design methods. The LDFEM analysis of reference CMC pile and its compatibility with field measurements shows capabilities of recent numerical codes. Further, the simplified FEM

approach, where author's proposition has been used, also presents the satisfactory agreement with in-situ SLTs.

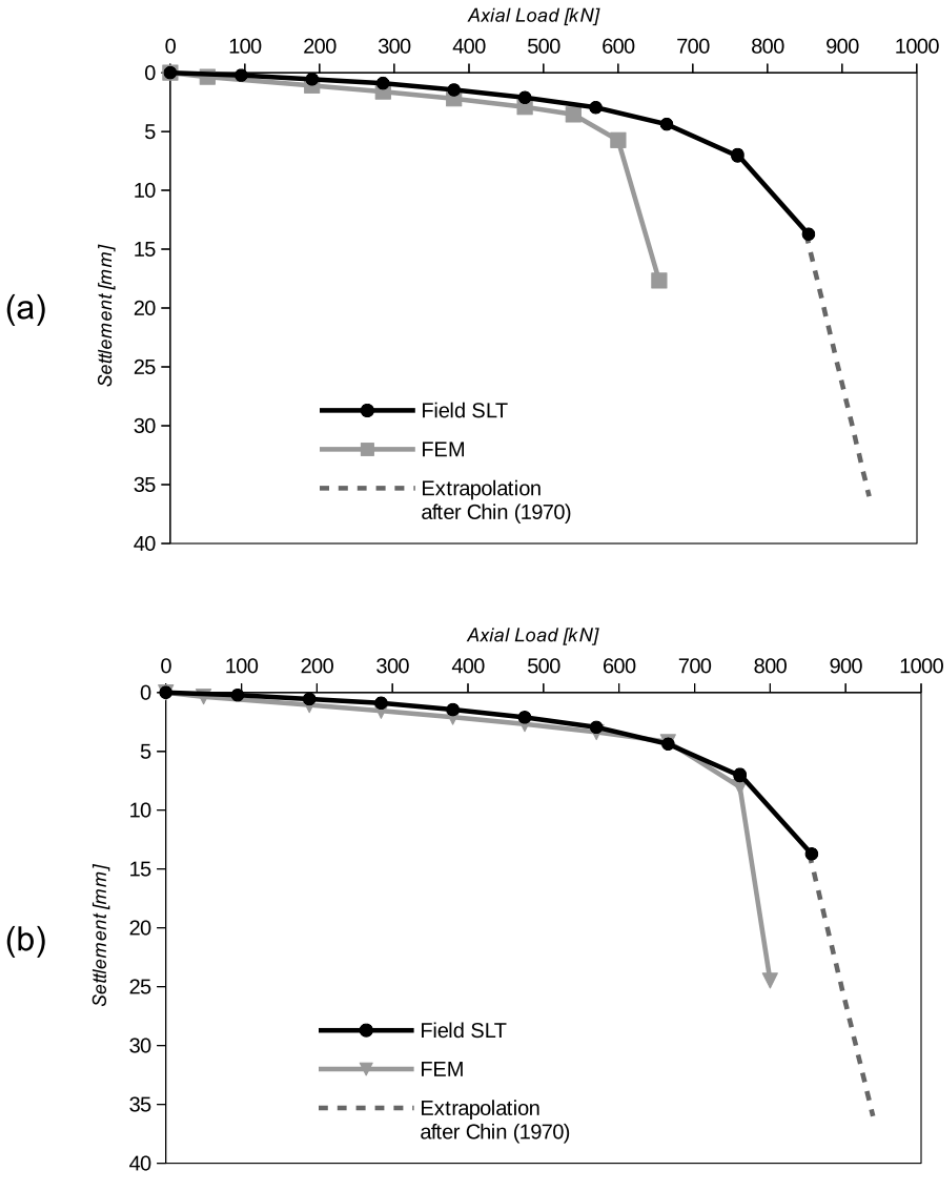

Figure 9.14. Field Static loading test versus combined empirical and FEM approach for interface friction angle: (a) 10,8° and (b) 13,5°

Chapter 10
Conclusions

This thesis focused on numerical large deformation analysis of pile installation and subsequent soil consolidation with emphasis on radial stress development. Many issues have been discussed including constitutive modelling of soil, reliability of Large Deformation Finite Element Method and development of empirical formula for radial effective stress distribution. Some final remarks from this research are drawn in this chapter.

10.1 Reliability of Large Deformation Finite Element Methods in installation problems

In this study, the historical review of Large Deformation Finite Element Method with its origin and current implementation in numerical codes has been described. The research presented in this thesis shows that large deformation formulations such as Updated Lagrangian (UL), Arbitrary Larangian-Eulerian (ALE) and Coupled Eulerian-Lagrangian (CEL) implemented in Finite Element Method software can provide satisfactory solutions for pile installation problem. However, each method has advantages, disadvantages and limitations. ALE and CEL which are based on explicit solver are suitable methods for modelling pile installation, but the following soil consolidation has to be calculated in UL formulation and implicit solver. It has been found that field variables such as stress, strain etc. for Eulerian soil domain in CEL formulation can be less accurate near the interface between Lagrangian and Eulerian parts. In UL formulation the “trial and error” method (Sheng et al., 2014) has to be used. On the other hand, the compatibility between ALE method in total stresses and UL method in effective stresses has been shown. The Vermeer and Verruijt (1981) formula for minimum time step in UL formulation does not to be fulfilled but it is highly recommended. Practical informations and remarks about numerical models development were summarized in chapter 5.

The numerical study performed in chapter 6 has shown that ALE, UL and CEL methods can provide accurate and consistent results in terms of radial total stresses distributions along the pile shaft at the end of installation. It was also observed that UL formulation overestimates the pore water pressure near pile toe after installation, but provides acceptable distributions

for effective stress along the pile shaft. In chapter 7, the satisfactory agreement in cone resistance between numerical methods and field measurements has been presented. Further, the rapid change in pore water pressures distributions between cone and sleeve has been observed and it is in coincidence with field measurements databases (e.g., Robertson et al., 1986). However, the accuracy of sleeve prediction depends highly on the applied interface parameters. Thus, the importance of proper contact modelling on both cone-soil and sleeve-soil interfaces has been pointed out.

Chapter 8 shows the detailed insight into the radial stress and pore water pressure distributions along the pile shaft after installation and consolidation. The studies reveal the compatibility between radial effective stress after installation obtained from UL solutions and the cylindrical Cavity Expansion Method (CEM). On the other hand, it was found that pore water pressure calculated with accordance to CEM is highly overestimated in comparison to UL. This aspect is considered to be a reason for radial effective stress overestimation in CEM in relation to corresponding in-situ measurement (e.g., Bond and Jardine, 1991). However, the Large Deformation Finite Element Methods such as UL and ALE present high accuracy in comparison with Spherical Cavity Expansion method (SCEM) in terms of cone resistance and pore water pressures in the vicinity and below the cone/pile base. Finally, it has been shown that soil movement during installation consist of horizontal and vertical deformations and it should not be simplified to merely horizontal displacement as it is in pure CEM method.

10.2 Empirical formula for installation effects calculation in cohesive soils

The findings obtained from numerical analyses presented in chapters 6,7, and 8 have been extended and calibrated with high quality database of 30 piles. It has been found that pile installation induces the change in radial effective stresses which can be described by empirical formula:

$$\sigma'_{rr,eq} = IEC\left[\left(\frac{\sqrt{3}}{M}+1\right)c_u + \sigma'_{v,0}\right] \tag{10.1}$$

where:

$$IEC = 0{,}26\,OCR^{0{,}41} \tag{10.2}$$

where: IEC – installation effect coefficient, $\sigma'_{rr,eq}$ – radial effective stress after consolidation, M – stress ratio (slope of p-q plane), c_u – undrained shear strength, $\sigma'_{v,0}$ – initial vertical geostatic stress, OCR – overconsolidation ratio.

According to database of 75 piles, where typical value of M is equal to 1,15, the equation (10.1) can be simplified to:

$$\sigma_{rr,eq}' = IEC\left(2{,}5\,c_u + \sigma_{v,0}'\right) \tag{10.3}$$

where: *IEC* – installation effect coefficient, $\sigma_{rr,eq}'$ – radial effective stress after consolidation, c_u – undrained shear strength, $\sigma_{v,0}'$ – initial geostatic stress.

Radial effective stress after installation and the following consolidation expressed by equation (10.1) or (10.3) can be easy adopted in pile design due to its simplicity. Further, the formula described by equation (10.1) has been validated with 10 field static loading tests in Poznań site and it has also proved its accuracy in comparison with other pile design approaches (see section 9.3.3). However, the real accuracy of application of equation (10.1) or (10.3) in design depends on interface friction angle, see section 9.3.4. Hence, the interface modelling in reliable installation effects prediction becomes even more crucial.

10.3 Further research possibilities

The first challenge is the further expansion of the coupled soil behaviour in explicit code which allows for more accurate soil modelling with special emphasis on pore water pressure development. Many attempts have been already made in this topic (e.g., Hamann and Grabe, 2013). Secondly, more accurate constitutive laws which facilitates the transition from small to large strains should be introduced in numerical codes. These include for instance the Brick-type models (e.g., Simpson, 1992).

The second branch of possible research is development of more complex constitutive modelling for pile-soil interfaces. As it has been shown in this thesis, the accurate interface model is crucial for reliable field variables prediction. The interface testing should include the shear behaviour on steel-soil and on concrete-soil interfaces from small to large strains. Consequently, the interface shear with different roughness or concrete curing times should be capture in constitutive law. Currently, the progress in this field can also be noticed (e.g., Mašín and Stutz, 2017).

Finally, the presented formula for Installation Effect Coefficient (IEC) calculation can be extended taking into account pile type, pile installation method or other soil parameters. Furthermore, the attempts can be made to include in the proposed equation the effect of friction fatigue which is widely observed in pile installation (e.g., Bond and Jardine, 1991).

Page intentionally left blank

Bibliography

Abu-Farsakh, M., Tumay, M.T., Voyiadis, G.Z., 2003. Numerical parametric study of piezocone penetration test in clays. International Journal of Geomechanics 3, 170–181. doi:10.1061/(ASCE)1532-3641(2003)3:2(170)

Almeida, M.S.S., Danziger, F.A.B., Lunne, T., 1996. Use of the piezocone test to predict the axial capacity of driven and jacked piles in clay. Canadian Geotechnical Journal 33, 23–41. doi:10.1139/t96-022

Alves, A.M.L., Lopes, F.R., Randolph, M.F., 2009. Investigations on the dynamic behavior of a small-diameter pile driven in soft clay. Canadian Geotechnical Journal 46, 1418–1430. doi:10.1139/T09-069

American Petroleum Institute, 2000. Recommended practice of planning, designing and constructing fixed offshore platforms (No. RP2A), 16th edition. Washington, DC.

Amini, A., Fellenius, B.H., Sabbagh, M., Neasgaard, E., Buehler, M., 2008. Pile loading tests at Golden Ears Bridge. Presented at the 61st Canadian Geotechnical Conference, Edmonton, Canada.

Atkinson, J., 2007. The mechanics of soils and foundations. Taylor & Francis Group.

Axelsson, G., 2000. Long-Term Set-up of Driven Piles at Sand, Ph.D.Thesis. ed. Royal Institute of Technology, Stockholm.

Azzouz, A., Morrison, M., 1988. Field Measurements on Model Pile in Two Clay Deposits. Journal of Geotechnical Engineering 114, 104–121. doi:10.1061/(ASCE)0733-9410(1988)114:1(104)

Azzouz, A.S., Krizek, R.J., Corotis, R.B., 1976. Regression analysis of soil compressibility. Soils and Foundations 16, 19–29. doi:10.3208/sandf1972.16.2_19

Bałachowski, L., 2006a. Soft soil overconsolidation and CPTU dissipation test. Archives of Hydroengineering and Environmental Mechanics 53, 155–180.

Bałachowski, L., 2006b. Scale effect in shaft friction from the direct shear interface tests. Archives of Civil and Mechanical Engineering 6, 13–28. doi:10.1016/S1644-9665(12)60238-6

Baligh, M.M., 1985. Strain path method. Journal of Geotechnical Engineering 111, 1108–1136.

Baligh, M.M., 1975. Theory of deep site static cone penetration resistance, Final Report Massachusetts Insitute of Technology. ed. Department of Civil Engineering., Massachusetts Insitute of Technology, Cambridge.

Baligh, M.M., Levadoux, J.N., 1980. Pore pressure dissipation after cone penetration. Department of Civil Engineering, Massachusetts Institute of Technology, Massachusetts.

Baligh, M.M., Scott, R.F., 1976. Analysis of wedge penetration in clay. Geotechnique 26, 185–208. doi:10.1680/geot.1976.26.1.185

Barlov, J., 1976. Optimal stress locations in finite element models. International Journal for Numerical Methods in Engineering 10, 243–251. doi:10.1002/nme.1620100202

Bathe, K.J., 1996. Finite Element Procedures. Prentice Hall, New Jersey.

Bayoumi, A., Bobet, A., Lee, J., 2008. Pullout capacity of a reinforced soil in drained and undrained conditions. Finite Elements in Analysis and Design 44, 525–536. doi:10.1016/j.finel.2008.01.009

Belytschko, T., Chiapetta, R.L., Bartel, H.D., 1976. Efficient large scale non-linear transient analysis by finite elements. International Journal for Numerical Methods in Engineering 10, 579–596. doi:10.1002/nme.1620100308

Benson, C.H., Zhai, H., Rashad, S.M., 1992. Assessment of Construction Quality Control Measurements and Sampling Frequencies For Compacted Soil Liners (No. Environmental Geotechnics Report No. 92-6). University of Wisconsin-Madison, Madison, Wisconsin.

Benson, D.J., 1992. Computational methods in Lagrangian and Eulerian hydrocodes. Computer methods in Applied mechanics and Engineering 99, 235–394. doi:10.1016/0045-7825(92)90042-I

Benson, D.J., Okazawa, S., 2004. Contact in a multi-material Eulerian finite element formulation. Computer methods in applied mechanics and engineering 193, 4277–4298. doi:10.1016/j.cma.2003.12.061

Beuth, L., 2012. Formulation and Application of a Quasi-Static Material Point Method, PhD Thesis. ed. University of Stuttgart, Stuttgart.

Bienen, B., Qiu, G., Pucker, T., 2015. CPT correlation developed from numerical analysis to predict jack-up foundation penetration into sand overlying clay. Ocean Engineering 108, 2016–226. doi:10.1016/j.oceaneng.2015.08.009

Bjorhus, J., 1995. Jonathan Turner, Airplane Engineer. The Seattle Times.

Bond, A.J., 1989. Behaviour of displacement piles in overconsolidated clays, PhD Thesis. ed. Imperial College London, London, UK.

Bond, A.J., Jardine, R.J., 1995. Shaft capacity of displacement piles in a high OCR clay. Geotechnique 45, 3–23. doi:10.1680/geot.1995.45.1.3

Bond, A.J., Jardine, R.J., 1991. Effects of installing displacement piles in a high OCR clay. Geotechnique 41, 341–363.

Brown, D.A., Turner, J.P., Castelli, R.J., 2010. Drilled Shafts: Construction Procedures and LRFD Design Methods (No. FHWA NHI-10-016). National Highway Institute, U.S. Department of Transportation Federal Highway Administration, Washington.

Brown, K.H., Burns, S.P., Christon, M.A., 2002. Coupled Eulerian-Lagrangian methods for earth penetrating weapon applications (No. SAND2002-1014). Sandia National Laboratories, Albuquerque, New Mexico, US.

Burns, S.E., Mayne, P.W., 1998. Monotonic and dilatory pore-pressure decay during piezocone tests in clay. Canadian Geotechnical Journal 35, 1063–1073. doi:10.1139/t98-062

Bustamante, M., Gianeselli, L., 1982. Pile bearing capacity predictions by means of static penetrometer CPT. Presented at the 2nd European Symposium on Penetration Testing, Baklema, Amsterdam, Netherlands, pp. 493–500.

Ceccato, F., Beuth, L., Simonini, P., 2016. Analysis of Piezocone Penetration under Different Drainage Conditions with the Two-Phase Material Point Method. Journal of Geotechnical and Geoenvironmental Engineering 140, 04016066. doi:10.1061/(ASCE)GT.1943-5606.0001550

Chandler, R.J., Leroueil, S., Trenter, N.A., 1990. Measurements of the permeability of London Clay using a self-boring permeameter. Geotechnique 40, 113–124. doi:10.1680/geot.1990.40.1.113

Chen, B.S.Y., Mayne, P.W., 1994. Profiling the overconsolidation ratio of clays by piezocone tests, Internal Report GIT-CEEGEO-94-1. ed. Georgia Institute of Technology, Atlanta.

Chen, C.S., Liew, S.S., Tan, Y.C., 1999. Time Effects on The Bearing Capacity of Driven Piles. Presented at the 11th Asian Regional Conference on Soil Mechanics and Geotechnical Engineering, Balkema, pp. 175–178.

Chen, X., Zhang, J., Xiao, Y., Li, J., 2015. Effect of roughness on shear behavior of red clay–concrete interface in large-scale direct shear tests. Canadian Geotechnical Journal 52, 1122–1135. doi:10.1139/cgj-2014-0399

Chin, F.K., 1970. Estimation of the ultimate load of piles not carried to failure. Presented at the 2nd Southeast Asia Conference on Soil Engineering, Southeast Asian Society of Soil Engineering, Singapore, pp. 81–90.

Chow, F.C., 1997. Investigations into the behaviour of displacement piles for offshore foundations, PdD Thesis. ed. Imperial College London, London.

Clarke, J., Lambson, M.D., 1993. Large diameter pile test program - summary, in: Offshore Site Investigation and Foundation Behaviour. Presented at the Advances in Underwater Technology, Ocean Science and Offshore Engineering, Springer, London, UK, pp. 513–549.

Clarke, J., Long, M.M., Hamilton, J., 1993. The axial tension test of an instrumented pile in overconsolidated clay at Tilbrook Grange, in: Large-Scale Pile Tests in Clay. Presented at the Recent large-scale fully intrumented pile tests in clay, Thomas Telford Ltd., London, UK. doi:10.1680/lptic.19188.0017

Cooke, R.W., Price, G., 1973. Strains and displacements around friction piles. Presented at the 8th International Conference on Soil Mechanics and Foundation Engineering, Moscow, pp. 53–60.

Cooke, R.W., Price, G., Tarr, K., 1979. Jacked piles in London Clay: a study of load transfer and settlement under working conditions. Geotechnique 29, 113–147. doi:10.1680/geot.1979.29.2.113

Coop, M.R., 1987. The axial capacity of driven piles in clay, PhD Thesis. ed. University of

Oxford, Oxford.

Coop, M.R., Wroth, C.P., 1989. Field studies of an instrumented model pile in clay. Geotechnique 39, 679–696. doi:10.1680/geot.1989.39.4.679

Cummings, A.E., Kerkhoff, G.O., Peck, R.B., 1950. Effect of driving piles into soft clay. Transactions of the American Society of Civil Engineers 115, 275–285.

Dai, Z.H., Qin, Z.Z., 2013. Numerical and theoretical verification of modified cam-clay model and discussion on its problems. Journal of Central South University 20, 3305–3313. doi:10.1007/s11771-013-1854-7

Dassault Systèmes, 2013. Abaqus 6.13 Documentation.

Dassault Systémes, 1999. Answers to Common ABAQUS Questions.

DeBorst, R., Vermeer, P.A., 1984. Possibilities and limitations of finite element for limit analysis. Geotechnique 32, 199–210.

Doherty, P., Gavin, K., 2013. Pile Aging in Cohesive Soils. Journal of Geotechnical and Geoenvironmental Engineering 139, 1620–1624. doi:10.1061/(ASCE)GT.1943-5606.0000884

Doherty, P., Gavin, K., 2011. The shaft capacity of displacement piles in clay: a state of the art review. Geotechnical and Geological Engineering 29, 389–410. doi:10.1007/s10706-010-9389-2

Donea, J., Giuliani, S., Halleux, J.P., 1982. An arbitrary Lagrangian-Eulerian finite element method for transient dynamic fluid-structure interactions. Computer methods in applied mechanics and engineering 33, 689–723.

Donea, J., Huerta, A., Ponthot, J.-P., Rodriguez-Ferran, A., 2004. Arbitrary Lagrangian–Eulerian Methods, in: Encyclopedia of Computational Mechanic. John Wiley & Sons, Ltd., pp. 413–437.

Eid, H.T., Amarasinghe, R.S., Rabie, K.H., Wijewickreme, D., 2014. Residual shear strength of fine-grained soils and soil–solid interfaces at low effective normal stresses. Canadian Geotechnical Journal 52, 198–210. doi:10.1139/cgj-2014-0019

Farrel, E.R., Lehane, B.M., Looby, M., 1998. Instrumented driven pile in Dublin boulder clay. Proceedings of the Institution of Civil Engineers - Geotechnical Engineering 131, 233–241. doi:10.1680/igeng.1998.30715

Fedkiw, R.P., Aslam, T., Merriman, B., Osher, S., 1999. A non-oscillatory Eulerian approach to interfaces in multimaterial flows (the ghost fluid method). Journal of computational physics 152, 457–492. doi:10.1006/jcph.1999.6236

Fellenius, B.H., Harris, D., Anderson, D.G., 2004. Static loading test on a 45 m long pipe pile in Sandpoint, Idaho. Canadian Geotechnical Journal 41, 613–628. doi:10.1139/t04-012

Fellenius, B.H., Samson, L., 1976. Testing of drivability of concrete piles and disturbance to sensitive clay. Canadian Geotechnical Journal 13, 139–160. doi:10.1139/t76-015

Fleming, K., Weltman, A., Randolph, M., Elson, K., 2009. Piling Engineering, third. ed. Taylor & Francis Group, New York.

Gallagher, K.A., St. John, H.D., 1980. Field scale model studies of piles as anchorages for buoyant platforms. Presented at the European Offshore Petroleum Conference and Exhibition, London, UK.

Gavin, K., Gallagher, D., Doherty, P., McCabe, B., 2010. Field investigation of the effect of installation method on the shaft resistance of piles in clay. Canadian Geotechnical Journal 47, 730–741. doi:10.1139/T09-146

Gawriuczenkow, I., 2005. Iły poznañskie jako izolacyjne bariery geologiczne składowisk odpadów komunalnych. Przegląd Geologiczny 53, 691–694.

Geotechdata.info, 2013. Angle of Friction [WWW Document]. Geotechdata.info. URL http://geotechdata.info/parameter/angle-of-friction.html (accessed 12.14.13).

Gingold, R.A., Monaghan, J.J., 1977. Smoothed particle hydrodynamics: theory and application to non-spherical stars. Monthly notices of the royal astronomical society 181, 375–389.

Grabe, J., Henke, S., Pucker, T., Hamann, T., 2013. CEL: simulations for soil plugging, screwed pile installation and deep vibration compaction. Presented at the International Conference on Installation Effects in Geotechnical Engineering, CRC Press, Rotterdam, The Netherlands.

Hamann, T., Grabe, J., 2013. A simple dynamic approach for the numerical modelling of soil as a two-phase material. Geotechnik 36, 180–191. doi:10.1002/gete.201200018

Hamann, T., Qiu, G., Grabe, J., 2015. Application of a Coupled Eulerian–Lagrangian approach on pile installation problems under partially drained conditions. Computers and Geotechnics 63, 279–290. doi:10.1016/j.compgeo.2014.10.006

Hara, A., Ohta, T., Niwa, M., Tanaka, S., Banno, T., 1974. Shear modulus and shear strength of cohesive soils. Soils and Foundations 14, 1–12.

Heerema, J.P., 1980. Predicting pile driveability: Heather as an illustration of the friction fatigue theory. Ground Engineering 13, 15–37.

Hirt, C.., Amsden, A.A., Cook, J.L., 1974. An arbitrary Lagrangian-Eulerian computing method for all flow speeds. Journal of Computational Physics 14, 227–253. doi:10.1016/0021-9991(74)90051-5

Holloway, D.M., Beddard, D.L., 1995. Dynamic testing results, indicator pile test program, I-880, Oakland, California. Presented at the 20th Annual Members Conference and Meeting, Deep Foundations Institute, Charleston, South Carolina, pp. 105–126.

Holtz, W.G., Lowitz, C.A., 1965. Effects of driving displacement piles in lean clay. Journal of the Soil Mechanics and Foundations Division 91, 1–14.

Housel, W.S., Burkey, J.R., 1948. Investigation to determine the driving characteristics of piles in soft clay. Presented at the 2nd International Conference on Soil Mechanics and Foundation Engineering, Rotterdam, pp. 146–154.

Huang, S., 1988. Application of Dynamic M easurement on Long H-Pile Driven into Soft Ground in Shanghai. Presented at the 3rd International Conference on the Application of Stress-Wave Theory to Piles, Ottawa, Ontario, Canada, pp. 635–643.

Hunt, C.E., 2000. Effect of pile installation on static and dynamic soil properties, PhD dissertation. ed. University of California, Department of Civil and Environmental Engineering, Berkeley, California.

Introduction to Finite Element Methods, 2015. . University of Colorado, Boulder.

Janbu, N., 1976. Static bearing capacity of friction piles. Presented at the 6th European

Conference on Soil Mechanics and Foundation Engineering, Vienna, Austria, pp. 479–488.

Jardine, R.J., 1985. Investigations of pile-soil behaviour, with special reference to the foundations of offshore structures, PhD Thesis. ed. Imperial College London, London.

Jardine, R.J., Chow, F.C., Overy, R., Standing, J., 2005. ICP design methods for driven piles in sands and clays. Thomas Telford Ltd., London.

Jardine, R.J., Symes, J.M., Burland, J.B., 1984. Measurement of soil stiffness in the triaxial apparatus. Geotechnique 34, 323–340. doi:10.1680/geot.1984.34.3.323

Jiangtao, Y., 2009. Centrifuge and Numerical Modelling of Sand Compaction Pile Installation, Phd Thesis. ed. National University of Singapore, Singapore.

Karlsrud, K., 2014. Ultimate Shaft Friction and Load-Displacement Response of Axially Loaded Piles in Clay Based on Instrumented Pile Tests. Journal of Geotechnical and Geoenvironmental Engineering 140, 04014074. doi:10.1061/(ASCE)GT.1943-5606.0001170

Karlsrud, K., 2012. Prediction of load-displacement behaviour and capacity of axially loaded piles in clay based on analyses and interpretation of pile load test results, PhD Thesis. ed. Norwegian University of Science and Technology, Trondheim.

Karlsrud, K., Clausen, C.J.F., Aas, P.M., 2005. Bearing Capacity of Driven Piles in Clay, the NGI Approach. Presented at the Intenational Symposium on Frontiers in Offshore Geotechnics, Perth, Australia, pp. 775–782.

Karlsrud, K., Haugen, T., 1985. Axial static capacity of steel model piles in overconsolidated clay. Presented at the 11th International Conference on Soil Mechanics and Foundation Engineering, San Francisco, pp. 1401–1406.

Karlsrud, K., Kalsnes, B., Nowacki, F., 1993. Response of piles in soft clay and silt deposits to static and cyclic axial loading based on recent instrumented pile load tests, in: Offshore Site Investigation and Foundation Behaviour. Presented at the Advances in Underwater Technology, Ocean Science and Offshore Engineering, Springer, London, UK, pp. 549–584.

Kennedy, J.M., Belytschko, T.B., 1982. Theory and application of a finite element method for arbitrary Lagrangian-Eulerian fluids and structures. Nuclear engineering and design 68, 129–146. doi:10.1016/0029-5493(82)90026-7

Kiousis, P.D., Voyiadis, G.Z., Tumay, M.T., 1988. A large strain theory and its application in the analysis of the cone penetration mechanism. International Journal for Numerical and Analytical Methods in Geomechanics 12, 45–60.

Knupp, P., Margolin, L.G., Shashkov, M., 2002. Reference Jacobian Optimization-Based Rezone Strategies for Arbitrary Lagrangian Eulerian Methods. Journal of Computational Physics 176, 93–128. doi:10.1006/jcph.2001.6969

Komurka, V.E., Wagner, A.B, Edil, T.B, 2003. A Review of Pile Set-Up. Presented at the 51st Annual Geotechnical Engineering Conference, University of Minnesota, Minnesota, pp. 105–130.

Konkol, J., 2015. Numerical estimation of the pile toe and shaft unit resistances during the installation process in sands. Studia Geotechnica et Mechanica 37, 37–44.

doi:10.1515/sgem-2015-0005

Konkol, J., Bałachowski, L., 2017. Influence of Installation Effects on Pile Bearing Capacity in Cohesive Soils - Large Deformation Analysis Via Finite Element Method. Studia Geotechnica et Mechanica 39, 27–38. doi:10.1515/sgem-2017-0003

Konkol, J., Bałachowski, L., 2016. Large deformation finite element analysis of undrained pile installation. Studia Geotechnica et Mechanica 38, 45–54. doi:10.1515/sgem-2016-0005

Konrad, J.M., Roy, M., 1987. Bearing capacity of friction piles in marine clay. Geotechnique 37, 163–175. doi:10.1680/geot.1987.37.2.163

Krabbenhoft, K., Zhang, X., 2013. Particle Finite Element Method For Extreme Deformation Problems.

Kraft, L.M., Focht, J.A., Amerasinghe, S.F., 1981. Friction Capacity of Piles Driven Into Clay. Journal of the Geotechnical Engineering Division 107, 1521–1541.

Kulhawy, F.H., Mayne, P.W., 1990. Manual on estimating soil properties for foundation design. Electric Power Research Institute, Palo Alto, California, USA.

Larisch, M., 2014. Behaviour of stiff, fine-grained soil during the installation of screw auger displacement piles, PhD Thesis. ed. University of Queensland, Queensland, Australia.

Law, K.T., Holtz, R.D., 1978. A note on Skempton's A parameter with rotation of principal stresses. Geotechnique 28, 57–64. doi:10.1680/geot.1978.28.1.57

Lehane, B.M., 1992. Experimental investigations of pile behaviour using instrumented field piles, PhD Thesis. ed. Imperial College London, London.

Lehane, B.M., Gill, D.R., 2004. Displacement fields induced by penetrometer installation in an artificial soil. International Journal of Physical Modelling in Geotechnics 4, 25–36. doi:10.1680/ijpmg.2004.040103

Lehane, B.M., Jardine, R.J., 1994a. Displacement pile behaviour in glacial clay. Canadian Geotechnical Journal 31, 79–90. doi:10.1139/t94-009

Lehane, B.M., Jardine, R.J., 1994b. Displacement-pile behaviour in a soft marine clay. Canadian Geotechnical Journal 31, 181–191. doi:0.1139/t94-024

Lehane, B.M., Li, Y., Williams, R., 2013. Shaft capacity of displacement piles in clay using the cone penetration test. Journal of Geotechnical and Geoenvironmental Engineering 139, 253–266. doi:10.1061/(ASCE)GT.1943-5606.0000749

Lemos, L.J.L., 1986. The effect of rate on residual strength of soil, PhD Thesis. ed. Imperial College London, London.

Levadoux, J.N., Baligh, M.M., 1986. Consolidation after undrained piezocone penetration. I: Prediction. Journal of Geotechnical Engineering 112, 707–726. doi:10.1061/(ASCE)0733-9410(1986)112:7(707)

Li, Y., Li, J., 2009. Behavior of the Penetration Process of Model Jacked Pile in Layered Soil. The Electronic Journal of Geotechnical Engineering 14P, 1–10.

Lied, E.K.., 2010. A Study of time effects on pile capacity. EYELGIP, Brno, Czech Republic.

Liu, G.R., Quek, S.S., 2013. The Finite Element Method: A Practical Course. Butterworth-Heinemann.

Liyanapathirana, D.S., 2009. Arbitrary Lagrangian Eulerian based finite element analysis of

cone penetration in soft clay. Computers and Geotechnics 36, 851–860. doi:10.1016/j.compgeo.2009.01.006

Long, J., Wysockey, M., Kerrigan, J., 1999. Measured Time Effects for Axial Capacity of Driven Piling. Transportation Research Record Journal of the Transportation Research Board 1663, 8–15. doi:10.3141/1663-02

Mabsout, M.E., Tassoulas, J.L., 1994. A finite element model for the simulation of pile driving. International Journal for Numerical Methods in Engineering 37, 257–278. doi:10.1002/nme.1620370206

Marchetti, S., 1980. In situ tests by flat dilatometer. Journal of Geotechnical and Geoenvironmental Engineering 106, 299–321.

Marchetti, S., Monaco, P., Totani, G., Calabrese, M., 2001. The Flat Dilatometer Test (DMT) in Soil Investigations, in: A Report by the ISSMGE Committee TC16. Presented at the International Conference on In Situ Measurement of Soil Properties and Case Histories, Bali, Indonesia, p. 41pp.

Margolin, L.G., 2013. Arbitrary Lagrangian-Eulerian (ALE) methods a personal perspective.

Mašín, D., Stutz, H., 2017. Hypoplastic interface models for fine-grained soils. International Journal for Numerical and Analytical Methods in Geomechanics 41, 284–303. doi:10.1002/nag.2561

Matlock, H., Bogard, D., McClelland, F., Chan, J.H., 1998. Technical Program-Tension Pile Study. Presented at the Offshore Technology Conference, Houston, USA.

Matsumoto, T., Michi, Y., Hirano, T., 1995. Performance of axially loaded steel pipe piles driven in soft rock. Journal of Geotechnical Engineering 121, 305–315. doi:10.1061/(ASCE)0733-9410(1995)121:4(305)

Mayne, P.W., 2001. Stress-strain-strength-flow parameters from enhanced in-situ tests. Presented at the International Conference on In Situ Measurement of Soil Properties and Case Histories, Graduate Program, Parahyangan Catholic University, Bali, Indonesia, pp. 27–47.

Mayne, P.W., 1991. Determination of OCR in clays by piezocone tests using cavity expansion and critical state concepts. Soils and Foundations 31, 65–76. doi:10.3208/sandf1972.31.2_65

Mayne, P.W., 1988. Determining OCR in clays from laboratory strength. Journal of Geotechnical Engineering 114, 76–92. doi:10.1061/(ASCE)0733-9410(1988)114:1(76)

McCabe, B., Lehane, B.M., 2006. Behavior of axially loaded pile groups driven in clayey silt. Journal of Geotechnical and Geoenvironmental Engineering 132, 401–410. doi:10.1061/(ASCE)1090-0241(2006)132:3(401)

Meyerhof, G.G., 1976. Bearing Capacity and Settlement of Pile Foundations. Journal of the Geotechnical Engineering Division 102, 195–228.

Mittal, R., Iaccarino, G., 2005. Immersed boundary methods. Annual Review of Fluid Mechanics 37, 239–261. doi:10.1146/annurev.fluid.37.061903.175743

Ni, Q., Hird, C.C., Guymer, I., 2010. Physical modelling of pile penetration in clay using transparent soil and particle image velocimetry. Geotechnique 60, 121–132.

doi:10.1680/geot.8.P.052

Noh, W.F., 1963. CEL: a time-dependent, two-space dimensional, coupled Eulerian-Lagrangian code, Lawrence Radiation Lab. ed. University of California, Livermore.

Nonlinear Finite Element Methods, 2016. . University of Colorado, Boulder.

Obrzud, R.F., Truty, A., Vulliet, L., 2011. Numerical modeling and neural networks to identify model parameters from piezocone tests: I. FEM analysis of penetration in two-phase continuum. International Journal for Numerical and Analytical Methods in Geomechanics 35, 1703–1730. doi:10.1002/nag.972

Olovsson, L., 2000. On the Arbitrary Lagrangian-Eulerian Finite Element Method, Dissertation No. 635. ed. Linköping Studies in Technology, Linköping University, Linköping, Sweden.

Oñate, E., Idelsohn, S.R., Del Pin, F., Aubry, R., 2004. The particle finite element method—an overview. International Journal of Computational Methods 1, 267–307.

O'Neill, M.W., Hawkins, R.A., Audibert, J.M., 1982a. Installation of pile group in overconsolidated clay. Journal of the Geotechnical Engineering Division 108, 1369–1385.

O'Neill, M.W., Hawkins, R.A., Mahar, L.J., 1982b. Load transfer mechanism in piles and pile groups. Journal of the Geotechnical Engineering Division 108, 1605–1623.

Ove Arup and Partners, 1986. Research on the behaviour of piles as anchors for buoyant structures (Offshore Technology Report No. OTH 86215). London, UK.

Pelletier, J.H., Doyle, E.H., 1982. Tension capacity in silty clays - Beta pile test. Presented at the 2nd International Conference on Numerical Methods in Offshore Piling, University of Texas, Austin, Texas, pp. 163–181.

Peskin, C.S., 1972. Flow patterns around heart valves: a numerical method. Journal of computational physics 10, 252–271. doi:10.1016/0021-9991(72)90065-4

Pestana, J.M., Hunt, C.E., Bray, J.D., 2002. Soil deformation and excess pore pressure field around a closed-ended pile. Journal of geotechnical and geoenvironmental engineering 128, 1–12. doi:10.1061/(ASCE)1090-0241(2002)128:1(1)

Phuong, N.T.V., van Tol, A.F., Elkadi, A.S.K., Rohe, A., 2014. Modelling of pile installation using the material point method, in: Numerical Methods in Geotechnical Engineering. Presented at the 8th European Conference on Numerical Methods in Geotechnical Engineering, Taylor & Francis Group, Delft, pp. 271–276.

Plaxis Manuals, 2015. Material Models Manual.

Ponniah, D.A., 1989. Instrumentation of a jacked in pile. Presented at the Geotechnical instrumentation in practice: Purpose, performance and interpretation, Thomas Telford Ltd., London, UK. doi:10.1680/giip.15159.0024

Popov, V., 2010. Contact mechanics and friction: physical principles and applications. Springer, Berlin.

Potts, D.M., Zdravković, L., 1999. Finite Element Analysis in Geotechnical Engineering: Theory. Thomas Telford Ltd.

Potyondy, J.G., 1961. Skin Friction between variuos soils and construction materials. Geotechnique 11, 339–353. doi:10.1680/geot.1961.11.4.339

Qiu, G., Grabe, J., 2012. Numerical investigation of bearing capacity due to spudcan penetration in sand overlying clay. Canadian Geotechnical Journal 49, 1393–1407. doi:10.1139/t2012-085

Qiu, G., Henke, S., Grabe, J., 2011. Application of a Coupled Eulerian–Lagrangian approach on geomechanical problems involving large deformations. Computers and Geotechnics 38, 30–39. doi:10.1016/j.compgeo.2010.09.002

Randolph, M.F., 2003. Science and Empiricism in pile foundation design. Geotechnique 53, 847–875. doi:10.1680/geot.53.10.847.37518

Randolph, M.F., 1983. Design considerations for offshore piles. Presented at the Conference on Geotechnical Practice in Offshore Engineering, University of Texas at Austin, Austin, Texas, pp. 422–439.

Randolph, M.F., Carter, J.P., Wroth, C.P., 1979a. Driven piles in clay-the effects of installation and subsequent consolidation. Geotechnique 29, 361–393.

Randolph, M.F., Murphy, B.S., 1985. Shaft capacity of driven piles in clay. Presented at the 17th Annual Offshore Technical Conference, Houston, USA, pp. 371–378.

Randolph, M.F., Steenfelt, J.S., Wroth, C.P., 1979b. The effect of pile type on design parameters for driven piles. Presented at the 7th European Conference on Soil Mechanics and Foundations in Engineering, Brighton, pp. 107–114.

Randolph, M.F., Wroth, C.P., 1979. Randolph, M. F., & Wroth, C. P. (1979). An analytical solution for the consolidation around a driven pile. nternational Journal for Numerical and Analytical Methods in Geomechanics 3, 217–229.

Robertson, P.K., Cabal, K.L., 2010. Guide for cone penetration testing for Geotechnical Engineering, 4th ed. Gregg Drilling and Testing, Inc.

Robertson, P.K., Campanella, R.G., Gillespie, D., Grieg, J., 1986. Use of piezometer cone data. Presented at the Use of in situ tests in geotechnical engineering, American Society of Civil Engineers, New York, Virginia Tech, Blacksburg, Virginia, United States, pp. 1263–1280.

Rosti, F., Abu-Farsakh, M., Jung, J., 2016. Development of Analytical Models to Estimate Pile Setup in Cohesive Soils Based on FE Numerical Analyses. Geotechnical and Geological Engineering 34, 1119–1134. doi:10.1007/s10706-016-0032-8

Roy, M., Blanchet, R., Tavenas, F., La Rochelle, P., 1981. Behaviour of a sensitive clay during pile driving. Canadian Geotechnical Journal 18, 67–85. doi:10.1139/t81-007

Sabetamal, H., Nazem, M., Carter, J.P., Sloan, S.W., 2014. Large deformation dynamic analysis of saturated porous media with applications to penetration problems. Computers and Geotechnics 55, 117–131. doi:10.1016/j.compgeo.2013.08.005

Sagaseta, C., Whittle, A.J., 2001. Prediction of Ground Movements due to Pile Driving in Clay. Journal of Geotechnical and Geoenvironmental Engineering 127, 55–66. doi:10.1061/(ASCE)1090-0241(2001)127:1(55)

Saldivar, E.E., Jardine, R.J., 2005. Application of an effective stress design method to concrete piles driven in Mexico City clay. Canadian Geotechnical Journal 42, 1495–1508. doi:10.1139/t05-062

Samson, L., Authier, J., 1986. Change in pile capacity with time: Case histories. Canadian

Geotechnical Journal 23, 174–180. doi:10.1139/t86-027

Saye, S.R., Lutenegger, A.J., Brown, D.A., Kumm, B.P., 2016. Influence of Sample Disturbance on Estimated Side Resistance of Driven Piles in Cohesive Soils. Journal of Geotechnical and Geoenvironmental Engineering 142. doi:10.1061/(ASCE)GT.1943-5606.0001517

Schmertmann, J.H., 1991. The Mechanical Aging of Soils. Journal of Geotechnical Engineering 117, 1288–1330. doi:10.1061/(ASCE)0733-9410(1991)117:9(1288)

Segall, P., Fitzgerald, S.D., 1998. A note on induced stress changes in hydrocarbon and geothermal reservoirs. Tectonophysics 289, 117–128. doi:10.1016/S0040-1951(97)00311-9

Sheng, D., Axelsson, K., Magnusson, O., 1997. Stress and strain fields around a penetrating cone. Presented at the th International Symposium on Numerical Models in Geomechanics, Balkema, Rotterdam, pp. 456–465.

Sheng, D., Cui, L., Ansari, Y., 2013. Interpretation of cone factor in undrained soils via full-penetration finite-element analysis. International Journal of Geomechanics 13, 745–753. doi:10.1061/(ASCE)GM.1943-5622.0000279

Sheng, D., Eigenbrod, K.D., Wriggers, P., 2005. Finite element analysis of pile installation using large-slip frictional contact. Computers and Geotechnics 32, 17–26. doi:10.1016/j.compgeo.2004.10.004

Sheng, D., Kelly, R., Pineda, J., Bates, L., 2014. Numerical study of rate effects in cone penetration test. Presented at the 3 rd International Symposium on Cone Penetration Testing, Las Vegas, Nevada.

Sheng, D., Nazem, M., Carter, J.P., 2009. Some computational aspects for solving deep penetration problems in geomechanics. Computational Mechanics 44, 549–561. doi:10.1007/s00466-009-0391-6

Simpson, B., 1992. Retaining structures: displacement and design. Geotechnique 42, 541–576. doi:10.1680/geot.1992.42.4.541

Skempton, A.W., 1960. Significance of Terzaghi's concept of effective stress, in: From Theory to Practice in Soil Mechanics. John Wiley & Sons, Ltd., New York.

Skempton, A.W., 1954. The pore-pressure coefficients A and B. Geotechnique 4, 143–147. doi:10.1680/geot.1954.4.4.143

Skov, R., Denver, H., 1988. Time-dependence of bearing capacity of piles. Presented at the Third International Conference on the Application of Stress-Wave Theory to Piles, BiTech Publisher, Ottawa, pp. 879–888.

Som, N.N., 1968. The effect of stress path on the deformation and consolidation of London Clay, PhD Thesis. ed. University of London (Imperial College London), London.

Suleiman, M.T., Ni, L., Davis, C., Lin, H., Xiao, S., 2015. Installation Effects of Controlled Modulus Column Ground Improvement Piles on Surrounding Soil. Journal of Geotechnical and Geoenvironmental Engineering 142, 04015059. doi:10.1061/(ASCE)GT.1943-5606.0001384

Sully, J.P., Robertson, P.K., Campanella, R.G., Woeller, D.J., 1999. An approach to evaluation of field CPTU dissipation data in overconsolidated fine-grained soils. Canadian

Geotechnical Journal 36, 369–381. doi:10.1139/t98-105

Sulsky, D., Schreyer, H.L., 1996. isymmetric form of the material point method with applications to upsetting and Taylor impact problems. Computer Methods in Applied Mechanics and Engineering 139, 409–429.

Terzaghi, K., 1943. Theoretical Soil Mechanics. John Wiley & Sons, Inc., New York.

Terzaghi, K., 1925. Erdbaumechanik auf Bodenphysikalischer Grundlage. Franz Deuticke, Liepzig-Vienna.

Terzaghi, K., Peck, R.B., Mesri, G., 1996. Soil mechanics in engineering practice, 3rd ed. John Wiley & Sons, Inc.

Tho, K.K., Leung, C.F., Chow, Y.K., Swaddiwudhipong, S., 2013. Eulerian finite element simulation of spudcan–pile interaction. Canadian Geotechnical Journal 50, 595–608. doi:10.1139/cgj-2012-0288

Thomsen, L., 1986. Weak elastic anisotropy. Geophysics 51, 1954–1966. doi:10.1190/1.1442051

Tika, T., 1989. The effect of fast shearing on the residual strength of soils, Phd Thesis. ed. Imperial College London, London.

Tomlinson, M., Woodward, J., 2015. Pile Design and Construction Practice, Sixth Edition. ed. CRC Press.

Totani, G., Marchetti, S., Calabrese, M., Monaco, P., 1994. Field studies of an instrumented full-scale pile driven in clay. Presented at the XIII International Conference on Soil Mechanics and Foundation Engineering, CRC Press, New Delhi, India, pp. 695–698.

Tsubakihara, Y., Kishida, H., 1993. Frictional behaviour between normally consolidated clay and steel by two direct shear type apparatuses. Soils and Foundations 33, 1–13.

Tsubakihara, Y., Kishida, H., Nishiyama, T., 1993. Friction between cohesive soils and steel. Soils and foundations 33, 145–156.

Turner, M.J., Clough, R.W., Martin, H.C., Topp, L.J., 1956. Stiffness and Deflection Analysis of Complex Structures. Journal of the Aeronautical Sciences 23, 805–523.

Van Den Berg, P., 1994. Analysis of soil penetration, PhD Thesis. ed. Delft University of Technology, Delft.

Vardanega, P.J., Bolton, M.D., 2013. Stiffness of clays and silts: Normalizing shear modulus and shear strain. Journal of Geotechnical and Geoenvironmental Engineering 139, 1575–1589. doi:10.1061/(ASCE)GT.1943-5606.0000887

Vermeer, P.A., Meier, C., -P., 1998. Standsicherheit und Verformungen bei tiefen Baugruben in bindigem Boden. Presented at the Vorträge der Baugrundtagung 1998 in Stuttgart, Stuttgart, pp. 133–148.

Vermeer, P.A., Verruijt, A., 1981. An accuracy condition for consolidation by finite elements. International Journal for numerical and analytical methods in geomechanics 5, 1–14. doi:10.1002/nag.1610050103

Verruijt, A., 2016. Theory and problems of poroelasticity. Delft University of Technology, Delft.

Walker, J., Yu, H.S., 2006. Adaptive finite element analysis of cone penetration in clay. Acta Geotechnica 1, 43–57. doi:10.1007/s11440-006-0005-9

Walton, P., Borg, S., 1998. Using Dynamic Pile Testing To Evaluate Quality and Verify Capacity of Driven Piles. Transportation Research Record: Journal of the Transportation Research Board 1633, 1–7. doi:10.3141/1633-15

Wang, D., Bienen, B., Nazem, M., Tian, Y., Zheng, J., Pucker, T., Randolph, M.F., 2015. Large deformation finite element analyses in geotechnical engineering. Computers and Geotechnics 65, 104–114. doi:10.1016/j.compgeo.2014.12.005

Wardle, I.F., Price, G., Freeman, T.J., 1992. Effect of Time and Maintained Load on the Ultimate Capacity of Pile in Stiff Clay, in: Piling, European Practice and Worldwide Trends. Presented at the Piling, European Practice and Worldwide Trends, Thomas Telford Ltd., London, UK. doi:10.1680/pepawt.35645.0015

Water Resources Board, 1972. The Hydrogeology of the London Basin.

Wei, L., 2004. Numerical Simulation and Field Verification of Inclined Piezocone Penetration Test in Cohesive Soils, Phd Thesis. ed. Louisiana State University, Louisiana.

Wei, L., Abu-Farsakh, M., Tumay, M.T., 2005. Finite-element analysis of inclined piezocone penetration test in clays. International Journal of Geomechanics 5, 167–178. doi:10.1061/(ASCE)1532-3641(2005)5:3(167)

Wendel, E., 1900. On the test loading of piles and its application to foundation problems in Gothenburg. Tekniska Samfundets Handlingar 3–62.

Whittle, A.J., Sutabutr, T., 1999. Prediction of pile setup in clay. Transportation Research Record: Journal of the Transportation Research Board 1663, 30–34. doi:10.3141/1663-05

Woken, M.D., 2013. Advantages of a Pilot Study.

Wroth, C.P., 1984. Interpretation of in situ soil tests. Geotechnique 34, 449–489. doi:10.1680/geot.1984.34.4.449

Wu, C.H., 2005. Continuum mechanics and plasticity. Chapman and Hall/CRC.

Yi, J.T., Goh, S.H., Lee, F.H., Randolph, M.F., 2012. A numerical study of cone penetration in fine-grained soils allowing for consolidation effects. Geotechnique 62, 707–719. doi:10.1680/geot.8.P.155

Yi, J.T., Zhao, B., Li, Y.P., Yang, Y., Lee, F.H., Goh, S.H., Zhang, X.Y., Wu, J.F., 2014. Post-installation pore-pressure changes around spudcan and long-term spudcan behaviour in soft clay. Computers and Geotechnics 56, 133–147. doi:10.1016/j.compgeo.2013.11.007

Yu, H.-M., Ma, G.-W., Qiang, H.-F., Zhang, Y.-Q., 2007. Generalized plasticity. Springer, Berlin.

Yu, H.S., 2000. Cavity expansion methods in geomechanics. Springer Netherlands, Dordrecht, Netherlands.

Yu, H.S., Mitchell, J.K., 1998. Analysis of cone resistance: review of methods. Journal of Geotechnical and Geoenvironmental Engineering 124, 140–149. doi:10.1061/(ASCE)1090-0241(1998)124:2(140)

Zhou, T., Tan, F., Li, C., 2013. Numerical Analysis for Excess Pore Pressure Dissipation Process for Pressed Pile Installation. Applied Mechanics and Materials 405, 133–137. doi:10.4028/www.scientific.net/AMM.405-408.133

Zienkiewicz, O.C., 1995. Origins, milestones and directions of the finite element method - a personal view. Archives of Computational Methods in Engineering 2, 1–48. doi:10.1007/BF02736188

Zienkiewicz, O.C., Cheung, Y.K., 1967. The Finite Element Method in Continuum and Structural Mechanics. McGraw-Hill, New York.

Appendix A

All notations have been submitted at the beginning of this thesis.

In chapter 3, section 3.2.3 the equations (3.7)-(3.10) have been presented as follows:

(A.1) $$\boldsymbol{\sigma} = 2G\,\boldsymbol{e}^{\boldsymbol{el}} + K\,\varepsilon_{vol}^{el}\,\boldsymbol{I}$$

(A.2) $$\boldsymbol{\varepsilon}^{\boldsymbol{el}} = \boldsymbol{e}^{\boldsymbol{el}} + \frac{1}{3}\,\varepsilon_{vol}^{el}\,\boldsymbol{I}$$

(A.3) $$K = \frac{E}{3(1-2\nu)}$$

(A.4) $$G = \frac{E}{2(1+\nu)}$$

The generalised Hooke Law can be derived in following way. Combining (A.1) with (A.3) and (A.4) one can get:

(A.5) $$\boldsymbol{\sigma} = \frac{E}{(1+\nu)}\,\boldsymbol{e}^{\boldsymbol{el}} + \frac{E}{3(1-2\nu)}\,\varepsilon_{vol}^{el}\,\boldsymbol{I}$$

Incorporating $\mathbf{e}^{\mathbf{el}}$ from equation (A.2) into equation (A.5) leads to:

(A.6) $$\boldsymbol{\sigma} = 2\,\frac{E}{2(1+\nu)}\,\boldsymbol{\varepsilon}^{\boldsymbol{el}} + \left(\frac{E\nu}{(1+\nu)(1-2\nu)}\right)\varepsilon_{vol}^{el}\,\boldsymbol{I}$$

The result is the generalised Hooke's law in terms of Lamé constants:

(A.7) $$\boldsymbol{\sigma} = 2\,\bar{\mu}\,\boldsymbol{\varepsilon}^{\boldsymbol{el}} + \bar{\lambda}\,\varepsilon_{vol}^{el}\,\boldsymbol{I}$$

where

(A.8) $$\bar{\lambda} = \frac{E\nu}{(1+\nu)(1-2\nu)}$$

is a Lamé's first parameter and

(A.8) $$\mu = G = \frac{E}{2(1+\nu)}$$

is shear modulus also called Lamé's second parameter.

Appendix B

All notations have been submitted at the beginning of this thesis.

The undrained shearing of the fully saturated soils, because of incompressibility of water, proceeds with constant volume. Thus, initial void ratio e_0 of soil is constant during whole process. According to the critical state theory, the soil can be on the wet or dry site of the

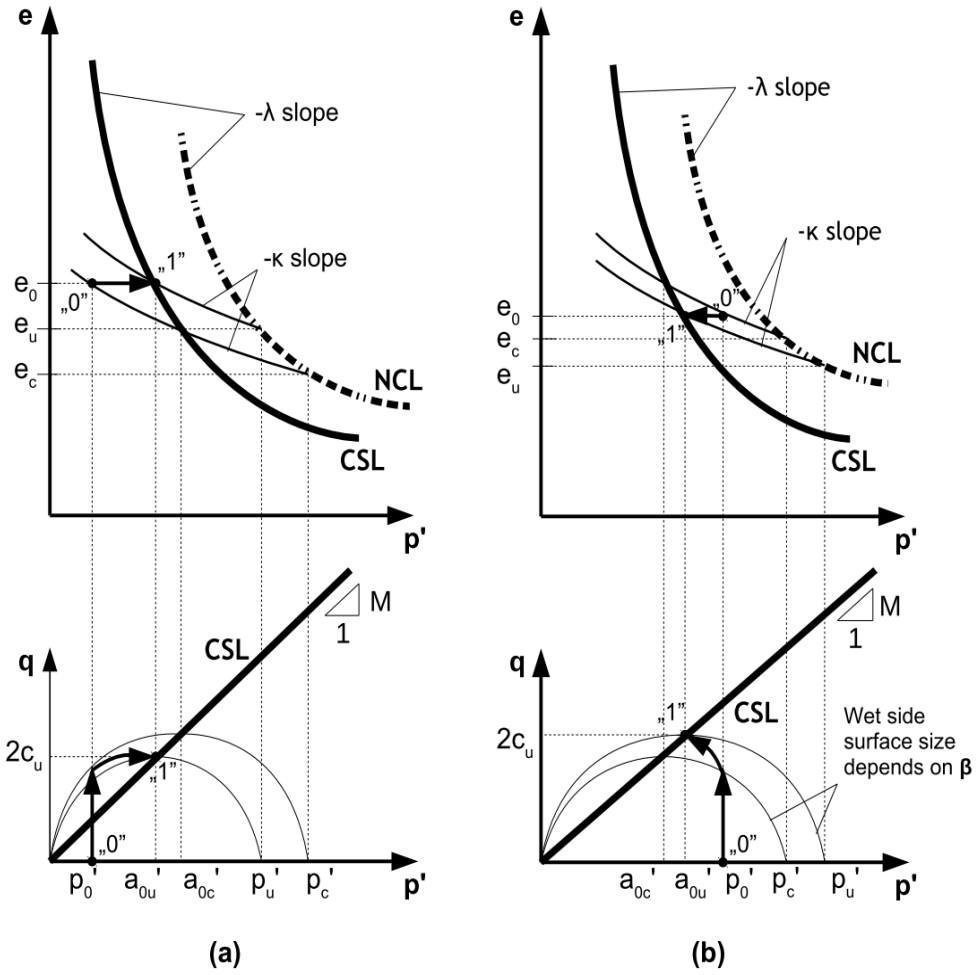

F*igure B.1. Stress paths during undrained shearing when initial state of soil is on (a) dry side of the critical line or (b) on the wet side of the critical line*

critical line (e.g., Atkinson, 2007). Firstly, let us consider dry site of the critical state line. The stress path during this kind of shearing is presented in figure B.1. and it is denoted as „0”-„1”. Hence the following equations can be written for the dry side of the CSL (see figure B.1a):

(B.1) $$e_0 - e_c = \kappa \ln\left(\frac{p_c'}{p_0'}\right)$$

(B.2) $$e_0 - e_u = \kappa \ln\left(\frac{p_u'}{a'_{0u}}\right)$$

(B.3) $$e_u - e_c = \lambda \ln\left(\frac{p_c'}{p_u'}\right)$$

The yield surface size on the dry site of the CSL in the MCC model can be described as:

(B.4) $$a'_{0u} = \frac{1}{2} p_u'$$

Consequently, equation (B.2) can be rewritten as:

(B.5) $$e_0 - e_u = \kappa \ln(2)$$

Combining equations (B.1),(B.3) and (B.5) leads to:

(B.6) $$\kappa \ln\left(\frac{p_c'}{p_0'}\right) = \lambda \ln\left(\frac{p_c'}{p_u'}\right) + \kappa \ln(2)$$

Equation (B.6) can be transform to the following form:

(B.7) $$\left(\frac{p_c'}{2\,p_0'}\right)^{\kappa/\lambda} = \frac{p_c'}{p_u'}$$

Stress ratio M (see figure B.1) can be defined as:

(B.8) $$M = \frac{2c_u}{a'_{ou}}$$

Combining equations (B.4) and (B.8) we get:

(B.9) $$p_u' = \frac{4c_u}{M}$$

Hence, from equations (B.7) and (B.9) the following formula can be derived:

$$p_c' = \left(\frac{4c_u}{M} \cdot (2\,p_0')^{-\kappa/\lambda}\right)^{\frac{\lambda}{\lambda-\kappa}}$$

(B.10)

The similar, general form derivation can be made for the wet side of the CSL with modifiable cap surface. In this case following equations can be written (see figure B.1b):

(B.11) $$e_0 - e_c = \kappa \ln\left(\frac{p_c'}{p_0'}\right)$$

(B.12) $$e_0 - e_u = \kappa \ln\left(\frac{p_u'}{a'_{0u}}\right)$$

(B.13) $$e_c - e_u = \lambda \ln\left(\frac{p_u'}{p_c'}\right)$$

Using power low of logarithm equation (B.13) can be transformed into the following form:

(B.14) $$e_u - e_c = \lambda \ln\left(\frac{p_c'}{p_u'}\right)$$

One can notice, that equations (B.11)-(B.12) are the same as equations (B.1)-(B.2). However, the yield surface size is described as:

(B.15) $$a_{0u}' = \frac{p_u'}{1+\beta}$$

Hence, equation (B.12) can be rewritten as:

(B.16) $$e_0 - e_u = \kappa \ln(1+\beta)$$

Consequently, combining equations (B.11),(B.14) and (B.16) leads to

(B.17) $$\kappa \ln\left(\frac{p_c'}{p_0'}\right) = \lambda \ln\left(\frac{p_c'}{p_u'}\right) + \kappa \ln(1+\beta)$$

and

(B.18) $$\left(\frac{p_c'}{(1+\beta)p_0'}\right)^{\kappa/\lambda} = \frac{p_c'}{p_u'}$$

Stress ratio in this case will be equal to:

(B.19) $$M = \frac{(1+\beta)c_u}{a'_{ou}}$$

Finally, by combining equations (B.18) and we get the following formula:

$$p_c' = \left(\frac{2(1+\beta) c_u}{M} \cdot ((1+\beta) p_0')^{-\kappa/\lambda} \right)^{\frac{\lambda}{\lambda-\kappa}} \tag{B.20}$$

One can see that for β=1,0 we get:

$$p_c' = \left(\frac{4 c_u}{M} \cdot (2 p_0')^{-\kappa/\lambda} \right)^{\frac{\lambda}{\lambda-\kappa}} \tag{B.21}$$

The equations (B.10) and (B.21) can be also derived directly from Wroth (1984) proposition:

$$\frac{c_u}{p_0'} = \frac{M}{2} \left(\frac{p_c'}{2 p_0'} \right)^{(\lambda-\kappa)/\lambda} \tag{B.22}$$

Equation (B.22) after transformation gets form:

$$\frac{2 c_u}{M p_0'} (2 p_0')^{(\lambda-\kappa)/\lambda} = (p_c')^{(\lambda-\kappa)/\lambda} \tag{B.23}$$

then

$$\frac{4 c_u}{M} (2 p_0')^{\frac{(\lambda-\kappa)}{\lambda}-1} = (p_c')^{(\lambda-\kappa)/\lambda} \tag{B.24}$$

and

$$\frac{4 c_u}{M} (2 p_0')^{-\kappa/\lambda} = (p_c')^{(\lambda-\kappa)/\lambda} \tag{B.25}$$

Thus, finally:

$$p_c' = \left(\frac{4 c_u}{M} \cdot (2 p_0')^{-\kappa/\lambda} \right)^{\frac{\lambda}{\lambda-\kappa}} \tag{B.26}$$

Appendix C

All notations have been also submitted at the beginning of this thesis.

In this thesis, when parameters are estimated with CPT-based correlations the formulas provided in this appendix are maintained. The corrected cone resistance can be expressed as (Robertson and Cabal, 2010):

(C.1) $$q_t = q_c + (1+a)u_2$$

where: q_t – corrected cone resistance, q_c – directly measured cone resistance, a – cone area ratio, u_2 – pore pressure measured directly behind the cone.
The undrained shear strength is assessed using empirical formula(Robertson and Cabal, 2010):

(C.2) $$c_u = \frac{q_t - \sigma_{v0}}{N_{kt}}$$

where: q_t – corrected cone resistance, σ_{v0} – total vertical stress, N_{kt} – cone factor.
The soil sensitivity can be estimated as (Robertson and Cabal, 2010):

(C.3) $$S_t = \frac{q_t - \sigma_{v0}}{N_{kt}}(1/f_s)$$

where: S_t – soil sensitivity, q_t – corrected cone resistance, σ_{v0} – total vertical stress, N_{kt} – cone factor, f_s – directly measured sleeve friction.
The overconsolidation ratio (OCR) can be described as (Kulhawy and Mayne, 1990):

(C.4) $$OCR = 0{,}33\left(\frac{q_t - \sigma_{v0}}{\sigma'_{v0}}\right)$$

where: OCR – overconsolidation ratio, q_t – corrected cone resistance, σ_{v0} – total vertical stress,

σ_{v0} '– effective vertical stress.
The earth pressure at rest coefficient is defined as (Kulhawy and Mayne, 1990):

$$K_0 = 0{,}1\left(\frac{q_t - \sigma_{v0}}{\sigma'_{v0}}\right) \tag{C.5}$$

where: K_0 – earth pressure at rest coefficient, q_t – corrected cone resistance, σ_{v0} – total vertical stress, σ'_{v0} – effective vertical stress.
When the DMT-based correlations are refereed the following formulas are used. The Material Index is defined as (Marchetti et al., 2001):

$$I_D = \left(\frac{P_1 - P_0}{P_0 - u_0}\right) \tag{C.6}$$

where: I_D – material index, P_1 – pressure to expand membrane 1mm into soil, P_0 – soil-membrane-contact stress, u_0 – in-situ pore water pressure.
Dilatometr modulus is expressed as (Marchetti et al., 2001):

$$E_D = 34{,}7\left(P_1 - P_0\right) \tag{C.7}$$

where: P_1 – pressure to expand membrane 1mm into soil, P_0 – soil-membrane-contact stress.
The horizontal stress index is calculated as (Marchetti et al., 2001):

$$K_D = \frac{\left(P_0 - u_0\right)}{\sigma'_{v0}} \tag{C.8}$$

where: P_0 – soil-membrane-contact stress, u_0 – in-situ pore water pressure, σ_{v0} '– effective vertical stress.
The OCR can be estimated as (Marchetti et al., 2001):

$$OCR = \left(0{,}5\, K_D\right)^{0{,}47} \tag{C.9}$$

where: OCR – overconsolidation ratio, K_D – horizontal stress index.
The earth pressure at rest coefficient is described with equation (Marchetti, 1980):

$$K_0 = \left(K_D / 1{,}5\right)^{0{,}47} - 0{,}6 \tag{C.10}$$

where: K_0 – earth pressure at rest coefficient, K_D – horizontal stress index.
The undrained shear strength is assessed as (Marchetti, 1980):

(C.11) $$c_u = 0{,}22\,\sigma_{vo}'\,(0{,}5\,K_D)^{1{,}25}$$

where: OCR – overconsolidation ratio, K_D – horizontal stress index, σ_{v0}' – effective vertical stress.
The vertical drained constrained modulus is defined as (Marchetti et al., 2001):

(C.12) $$M_{DMT} = R_m\,E_D$$

where:

(C.13) $$R_m = 0{,}32 + 2{,}18\log K_D \quad for \quad K_D > 10$$

where: M_{DMT} – vertical drained constrained modulus, E_D – Dilatometr modulus, K_D – horizontal stress index.
The effective drained modulus can be written as:

(C.14) $$E' = 0{,}8\,M_{DMT}$$

where: E' – effective elastic drained modulus, M_{DMT} – vertical drained constrained modulus

Page intentionally left blank

Appendix D

All notations have been submitted at the beginning of this thesis.

The radial total stress distribution along the pile shaft obtained with UL and ALE formulations with specified deviation cut-offs which are used in chapter 8 are provided below.

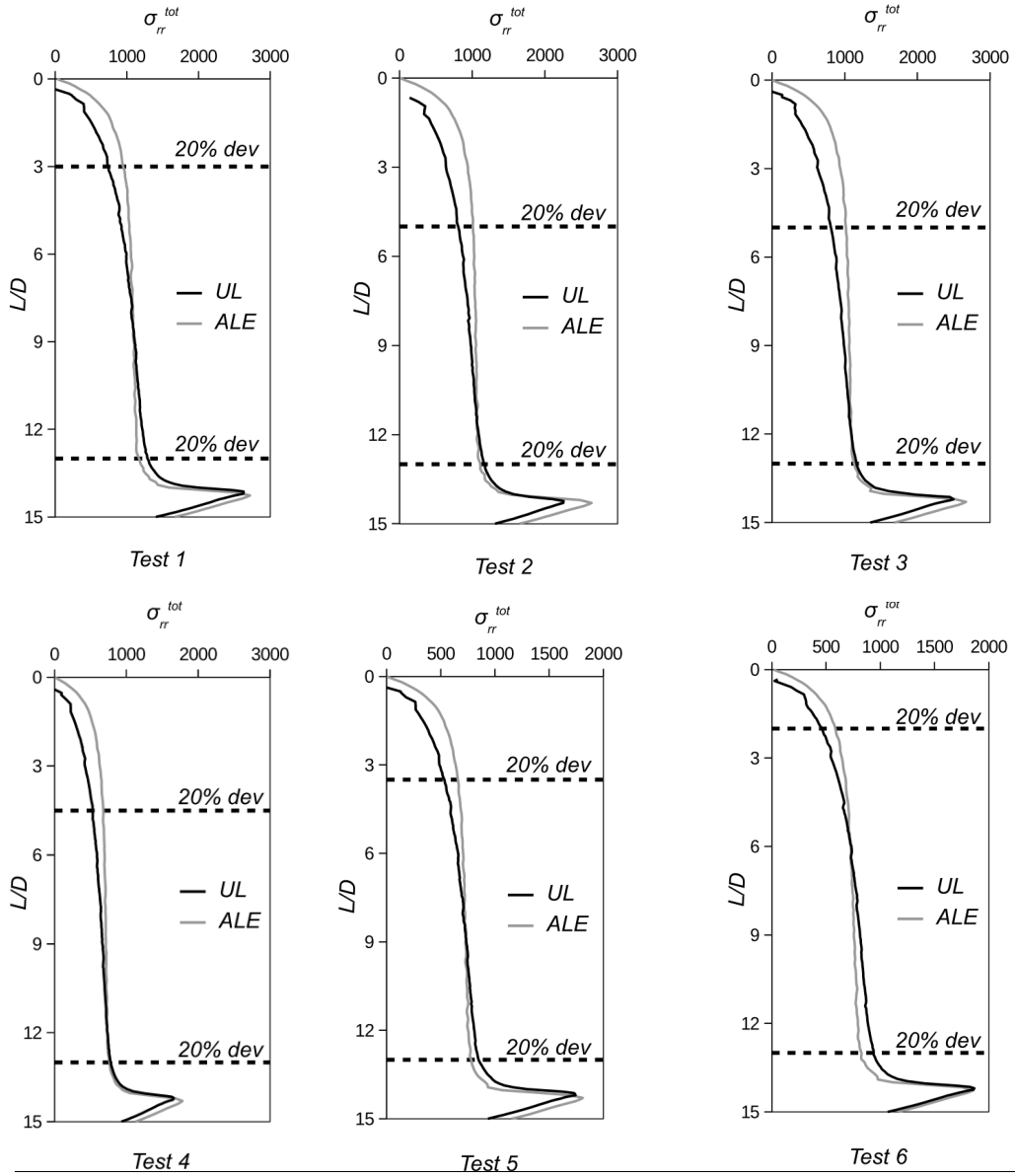

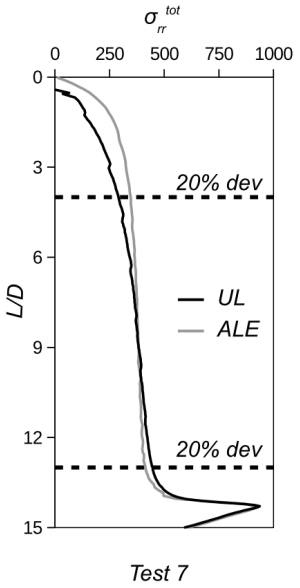

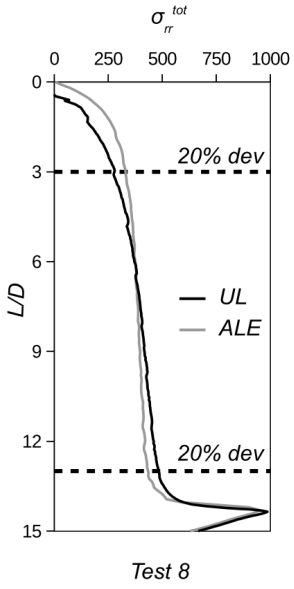

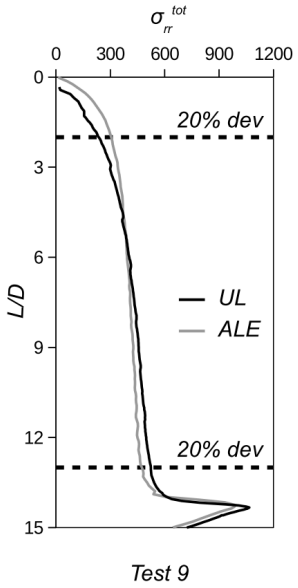

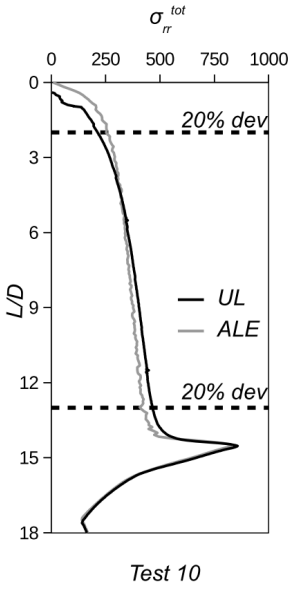

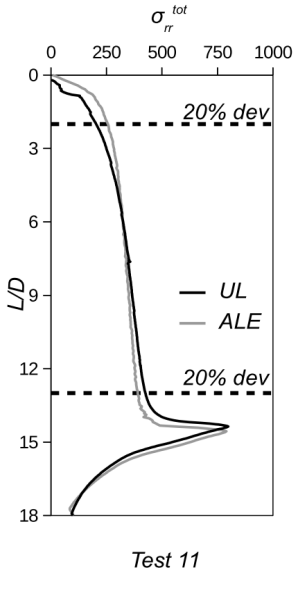

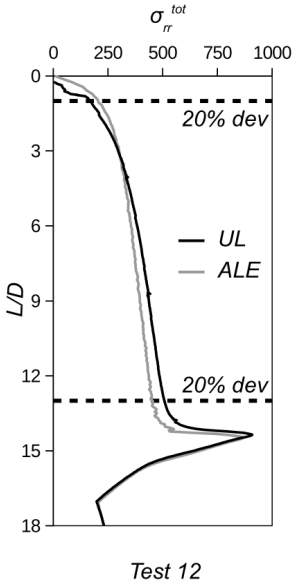

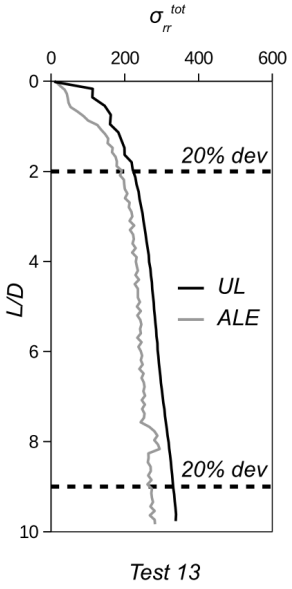

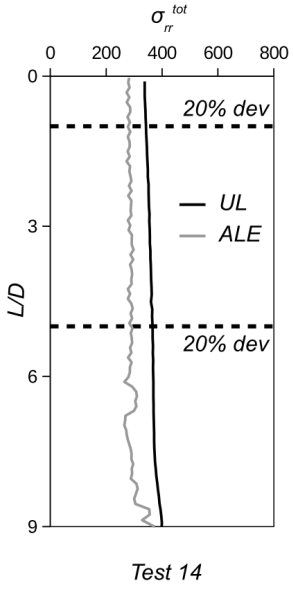

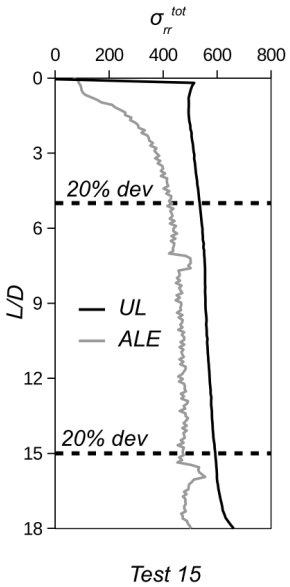

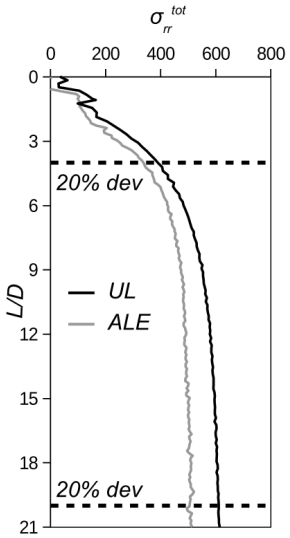

Test 16

Page intentionally left blank

Appendix E

All notations have been submitted at the beginning of this thesis.

The results of in-situ pile static load tests in Poznań site are submitted in figures below.

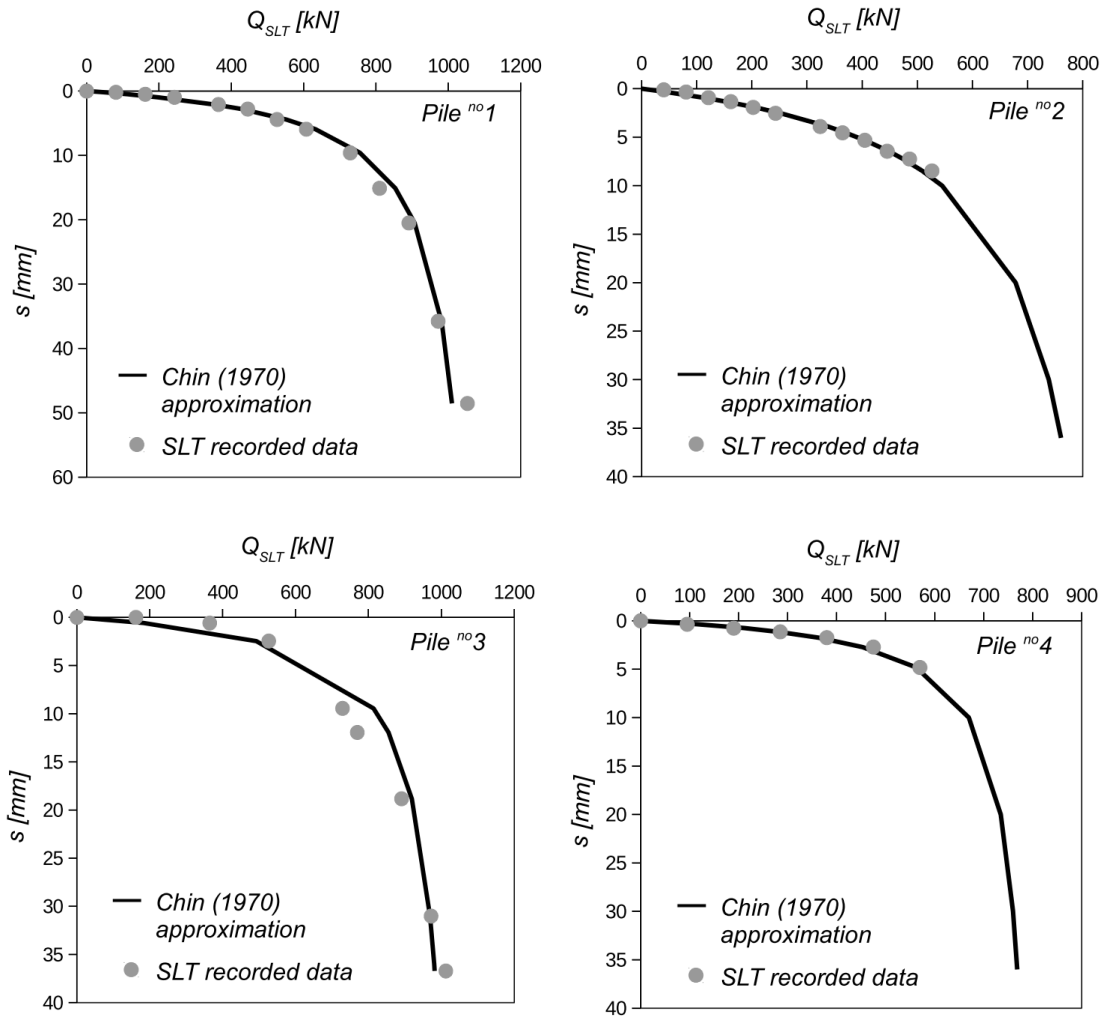

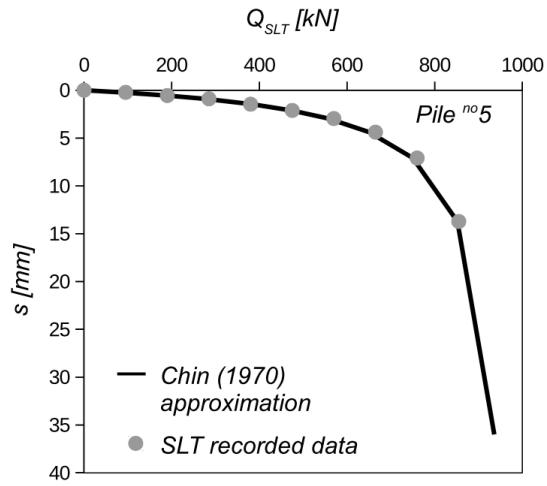

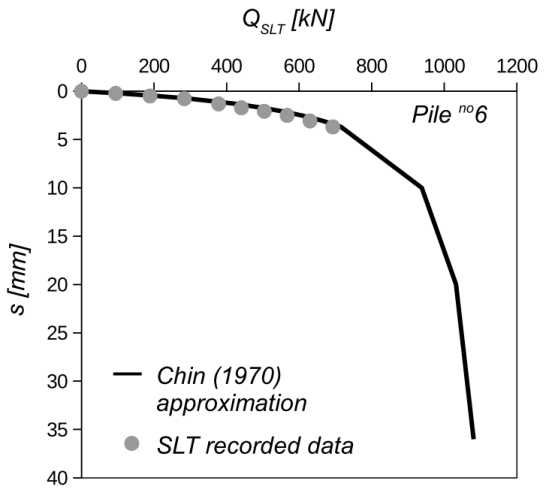

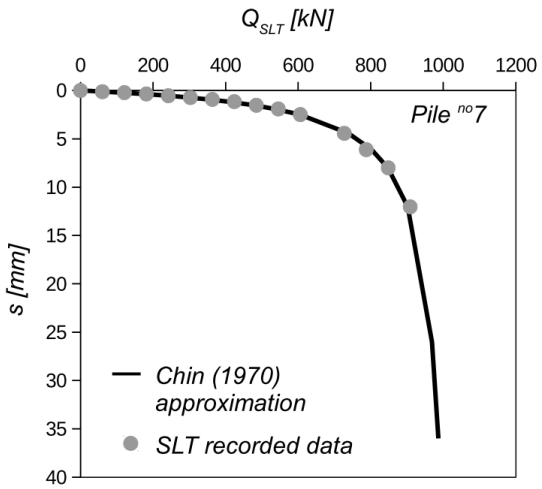

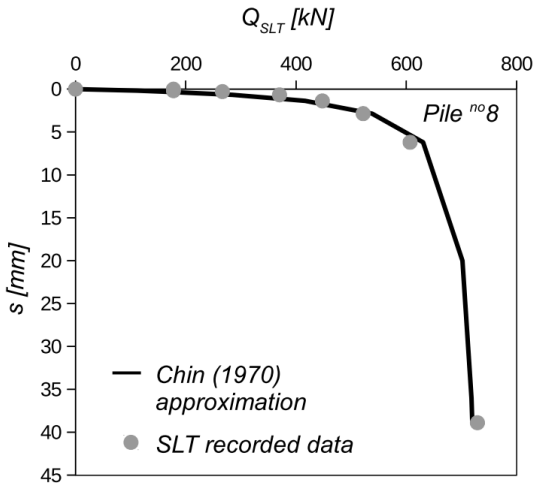

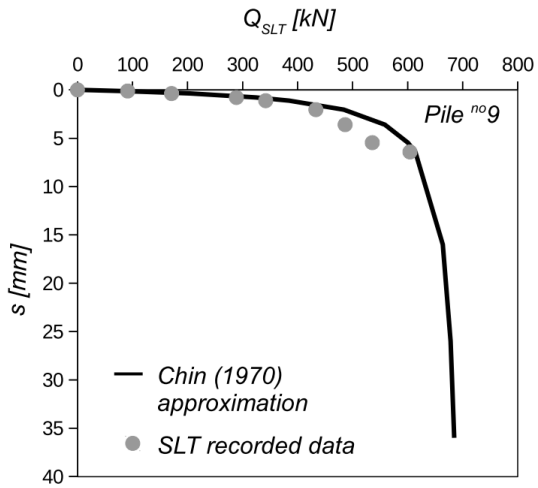

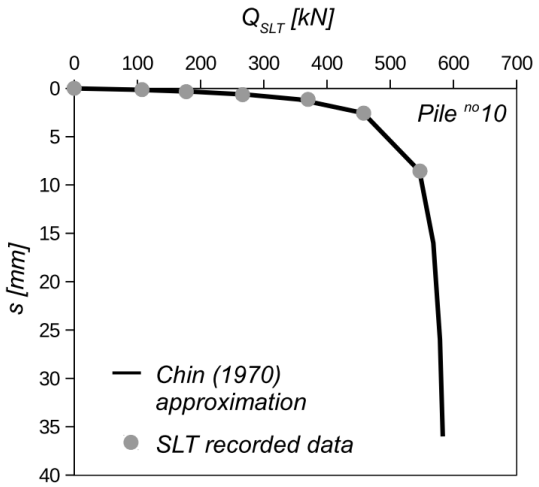

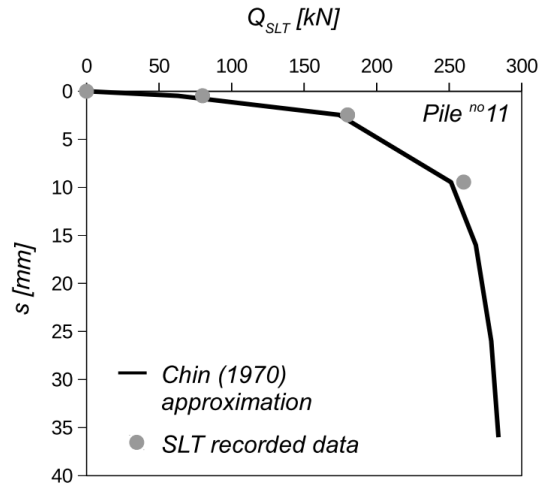

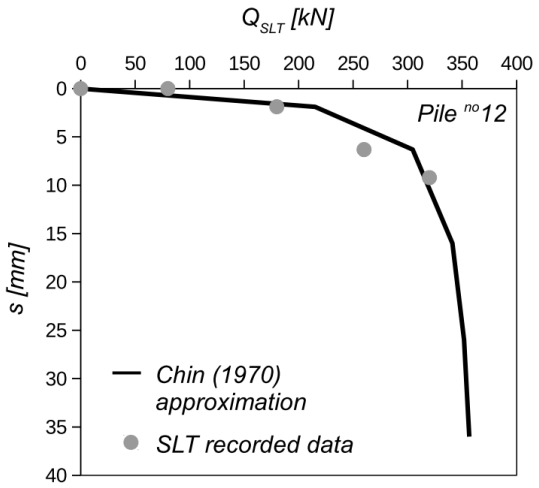

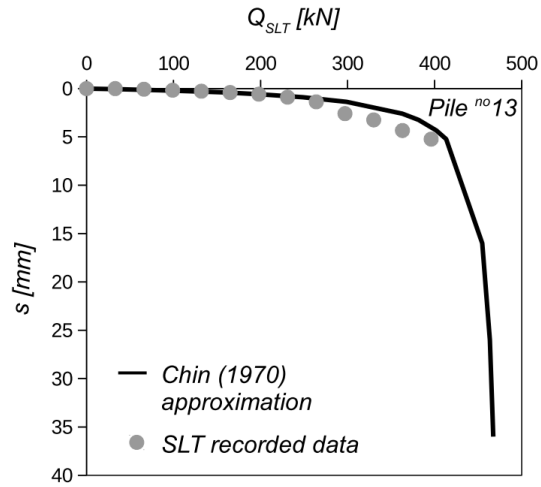

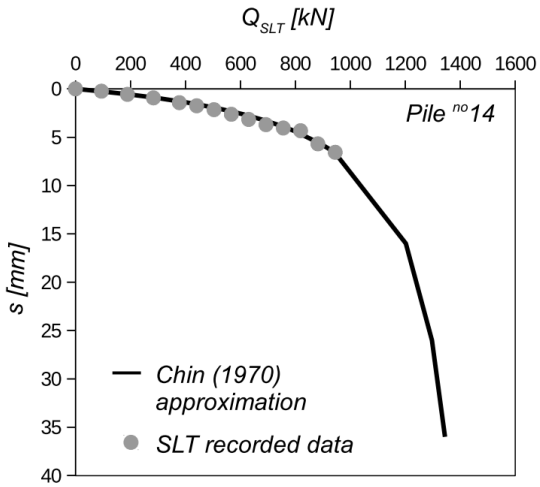

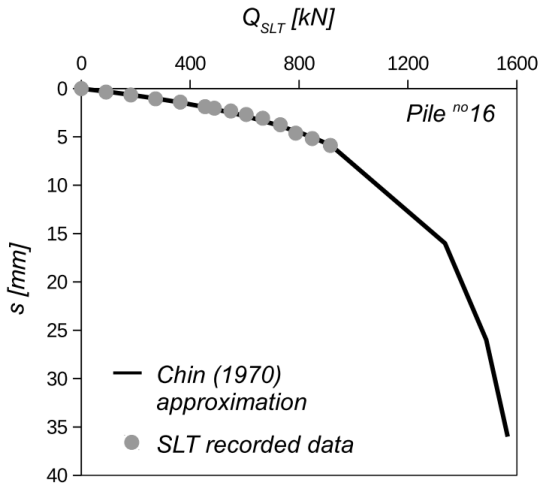

Page intentionally left blank

Appendix F

All notations have been submitted at the beginning of this thesis.

Herein, the detailed calculation of pile bearing capacities for Poznań site are provided.

Table F.1. API-2000

					Pile Shaft							Pile base			
					Average							Avg.			
No	*T/C*	*D*	*L*		c_u	σ'_{v0}	c_u/σ'_{v0}	α	α	τ_f	Q_{shaft}	c_u	Q_{base}	Q_c
								eq.(9.16)	*eq.(9.17)*	*eq.(9.14)*	*eq.(9.12)*		*eq.(9.13)*	*eq.(9.4)*
-	-	*m*	*m*		*kPa*	*kPa*	-	-	-	*kPa*	*kN*	*kPa*	*kN*	*kN*
1	*C*	*0,36*	*9,52*		*102*	*48,6*	*2,10*	*0,42*	*0,55*	*56,1*	*604*	*166*	*152*	*756*
2	*T*	*0,36*	*7,64*		*100*	*39,0*	*2,57*	*0,40*	*0,55*	*55,0*	*475*	-	-	*475*
3	*C*	*0,36*	*7,67*		*100*	*39,1*	*2,56*	*0,40*	*0,55*	*55,0*	*477*	*101*	*93*	*570*
4	*C*	*0,36*	*6,1*		*90*	*31,1*	*2,89*	*0,38*	*0,55*	*49,5*	*341*	*137*	*126*	*467*
5	*C*	*0,36*	*7,0*		*110*	*35,7*	*3,08*	*0,38*	*0,55*	*60,5*	*479*	*140*	*128*	*607*
6	*C*	*0,36*	*7,3*		*125*	*37,2*	*3,36*	*0,37*	*0,55*	*68,8*	*568*	*137*	*126*	*693*
7	*C*	*0,36*	*7,2*		*131*	*36,7*	*3,57*	*0,36*	*0,55*	*72,1*	*587*	*208*	*191*	*777*
8	*C*	*0,36*	*7,0*		*77*	*35,7*	*2,16*	*0,41*	*0,55*	*42,4*	*335*	*106*	*97*	*432*
9	*C*	*0,36*	*6,0*		*83*	*35,7*	*2,32*	*0,40*	*0,55*	*45,7*	*361*	*106*	*97*	*459*
10	*C*	*0,36*	*7,0*		*90*	*30,6*	*2,94*	*0,38*	*0,55*	*49,5*	*336*	*105*	*96*	*432*

Table F.2. Beta method

						Pile Shaft							Pile base					
						Average									Avg.			
No	T/C	D	L	ϕ'	c'	σ'_{v0}	OCR	K_c	δ_f	β	τ_f	Q_{shaft}	N_q	N_c	σ'_{v0}	q_b	Q_{base}	Q_c
										eq. (9.23)	eq.(9.22)	eq.(9.12)	eq.(9.20)	eq.(9.21)		eq.(9.19)	eq.(9.13)	eq.(9.4)
-	-	m	m	°	kPa	kPa	-	-	°	-	kPa	kN			kPa	kPa	kN	kN
1	C	0,36	9,52	14	31	48,6	10	3,60	13,5	0,86	41,9	451	2,76	7,07	97,1	487	50	501
2	T	0,36	7,64	14	31	39,0	11	3,77	13,5	0,91	35,3	305	-	-	-	-	-	305
3	C	0,36	7,67	14	31	39,1	11	3,77	13,5	0,91	35,4	307	2,76	7,07	78,2	435	44	352
4	C	0,36	6,1	14	31	31,1	10	3,60	13,5	0,86	26,9	185	2,76	7,07	62,2	391	40	225
5	C	0,36	7,0	14	31	35,7	14	4,25	13,5	1,02	36,5	289	2,76	7,07	71,4	416	42	331
6	C	0,36	7,3	14	31	37,2	12	3,94	13,5	0,95	35,2	291	2,76	7,07	74,5	425	43	334
7	C	0,36	7,2	14	31	36,7	9	3,41	13,5	0,82	30,1	245	2,76	7,07	73,4	422	43	288
8	C	0,36	7,0	14	31	35,7	14	4,25	13,5	1,02	36,5	289	2,76	7,07	71,4	416	42	331
9	C	0,36	6,0	14	31	35,7	7,5	3,11	13,5	0,75	26,7	211	2,76	7,07	71,4	416	42	254
10	C	0,36	7,0	14	31	30,6	8	3,22	13,5	0,77	23,6	160	2,76	7,07	61,2	388	39	200

Table F.3. NGI-05

				Pile Shaft						Pile base		
				Average						Avg.		
No	T/C	D	L	c_u	σ'_{v0}	c_u/σ_{v0}'	α eq.(9.25)	τ_f eq.(9.14)	Q_{shaft} eq.(9.12)	c_u	Q_{base} eq.(9.13)	Q_c eq.(9.4)
-	-	m	m	kPa	kPa	-	-	kPa	kN	kPa	kN	kN
1	C	0,36	9,52	102	48,6	2,10	0,40	40,8	439	166	152	592
2	T	0,36	7,64	100	39,0	2,57	0,38	37,7	326	-	-	326
3	C	0,36	7,67	100	39,1	2,56	0,38	37,7	327	101	93	420
4	C	0,36	6,1	90	31,1	2,89	0,36	32,7	226	137	126	351
5	C	0,36	7,0	110	35,7	3,08	0,36	39,2	311	140	128	439
6	C	0,36	7,3	125	37,2	3,36	0,35	43,5	359	137	126	484
7	C	0,36	7,2	131	36,7	3,57	0,34	44,7	364	208	191	555
8	C	0,36	7,0	77	35,7	2,16	0,40	30,6	242	106	97	339
9	C	0,36	7,0	83	35,7	2,32	0,39	32,2	255	106	97	352
10	C	0,36	6,0	90	30,6	2,94	0,36	32,6	221	105	96	317

Table F.4. Almeida-1996

				Pile Shaft						Pile base		
				Average						Avg.		
No	T/C	D	L	σ_{v0}	σ'_{v0}	q_t	k_1 eq.(9.28)	τ_f eq.(9.26)	Q_{shaft} eq.(9.12)	q_t	Q_{base} eq.(9.13)	Q_c eq.(9.4)
-	-	m	m	kPa	kPa	MPa	-	kPa	kN	kPa	kN	kN
1	C	0,36	9,52	96,2	48,6	2,20	34,7	60,6	653	3,22	197	849
2	T	0,36	7,64	77,2	39,0	2,12	35,9	56,9	492	-	-	492
3	C	0,36	7,67	77,5	39,1	2,12	35,8	57,0	494	2,95	180	674
4	C	0,36	6,1	61,6	31,1	1,91	36,6	50,5	348	2,30	140	489
5	C	0,36	7,0	70,7	35,7	2,23	36,7	58,8	465	2,85	174	639
6	C	0,36	7,3	73,7	37,2	2,55	37,3	66,4	548	2,94	180	727
7	C	0,36	7,2	72,7	36,7	2,77	37,9	71,1	579	4,36	266	845
8	C	0,36	7,0	70,7	35,7	1,41	33,8	39,6	313	2,32	142	455
9	C	0,36	7,0	70,7	35,7	1,79	35,4	48,6	385	2,32	142	527
10	C	0,36	6,0	60,6	30,6	1,94	36,8	51,0	346	2,28	139	485

Table F.5. LCPC

				Pile Shaft			Pile base		
				Average			Avg.		
No	*T/C*	*D*	*L*	q_t	τ_f *eq.(9.30)*	Q_{shaft} *eq.(9.12)*	q_t	Q_{base} *eq.(9.13)*	Q_c *eq.(9.4)*
-	-	*m*	*m*	*MPa*	*kPa*	*kN*	*kPa*	*kN*	*kN*
1	*C*	*0,36*	*9,52*	*2,20*	*55,0*	*592*	*3,22*	*115*	*707*
2	*T*	*0,36*	*7,64*	*2,12*	*53,0*	*458*	*-*	*-*	*458*
3	*C*	*0,36*	*7,67*	*2,12*	*53,0*	*460*	*2,95*	*105*	*565*
4	*C*	*0,36*	*6,1*	*1,91*	*478*	*329*	*2,30*	*82*	*411*
5	*C*	*0,36*	*7,0*	*2,23*	*55,8*	*441*	*2,85*	*102*	*543*
6	*C*	*0,36*	*7,3*	*2,55*	*63,8*	*526*	*2,94*	*105*	*631*
7	*C*	*0,36*	*7,2*	*2,77*	*69,3*	*564*	*4,36*	*155*	*719*
8	*C*	*0,36*	*7,0*	*1,41*	*35,3*	*279*	*2,32*	*83*	*362*
9	*C*	*0,36*	*7,0*	*1,79*	*44,8*	*354*	*2,32*	*83*	*437*
10	*C*	*0,36*	*6,0*	*1,94*	*48,5*	*329*	*2,28*	*81*	*410*

Table F.7. ICP-05

				Pile Shaft								Pile base		
				Average								Avg.		
No	*T/C*	*D*	*L*	q_t	δ_f	$max(h/R)^{-0,2}$	*OCR*	S_t	I_{vr}	τ_f *eq.(9.31)*	Q_{shaft} *eq.(9.13)*	q_t	Q_{base} *eq.(9.13)*	Q_c *eq.(9.4)*
-	-	*m*	*m*	*MPa*	*°*	-	-	-	-	*kPa*	*kN*	*MPa*	*kN*	*kN*
1	*C*	*0,36*	*9,52*	*2,20*	*13,5*	*0,52*	*10*	*0,56*	*-0,25*	*34,4*	*370*	*3,22*	*262*	*632*
2	*T*	*0,36*	*7,64*	*2,12*	*13,5*	*0,54*	*11*	*0,56*	*-0,25*	*30,0*	*259*	*-*	*-*	*259*
3	*C*	*0,36*	*7,67*	*2,12*	*13,5*	*0,54*	*11*	*0,56*	*-0,25*	*30,1*	*261*	*2,95*	*240*	*501*
4	*C*	*0,36*	*6,1*	*1,91*	*13,5*	*0,57*	*10*	*0,52*	*-0,28*	*24,3*	*168*	*2,30*	*187*	*355*
5	*C*	*0,36*	*7,0*	*2,23*	*13,5*	*0,55*	*14*	*0,65*	*-0,19*	*30,4*	*240*	*2,85*	*232*	*472*
6	*C*	*0,36*	*7,3*	*2,55*	*13,5*	*0,55*	*12*	*0,59*	*-0,23*	*29,8*	*246*	*2,94*	*239*	*485*
7	*C*	*0,36*	*7,2*	*2,77*	*13,5*	*0,55*	*9*	*0,85*	*-0,07*	*24,9*	*203*	*4,36*	*355*	*558*
8	*C*	*0,36*	*7,0*	*1,41*	*13,5*	*0,55*	*14*	*0,32*	*-0,49*	*33,1*	*262*	*2,32*	*189*	*451*
9	*C*	*0,36*	*7,0*	*1,79*	*13,5*	*0,55*	*7,5*	*0,50*	*-0,30*	*24,1*	*191*	*2,32*	*189*	*380*
10	*C*	*0,36*	*6,0*	*1,94*	*13,5*	*0,57*	*8*	*0,45*	*-0,35*	*22,2*	*151*	*2,28*	*186*	*336*

Table F.8. Lehane-2013:eq.(32)

				Pile Shaft				Pile base		
				Average				Avg.		
No	T/C	D	L	q_t	$max(h/R)^{-0,2}$	τ_f eq.(9.33)	Q_{shaft} eq.(9.12)	q_t	Q_{base} eq.(9.13)	Q_c eq.(9.4)
-	-	m	m	MPa	-	kPa	kN	MPa	kN	kN
1	C	0,36	9,52	2,20	0,52	62,9	677	3,22	262	939
2	T	0,36	7,64	2,12	0,54	63,3	547	-	-	547
3	C	0,36	7,67	2,12	0,54	63,2	549	2,95	240	789
4	C	0,36	6,1	1,91	0,57	59,6	412	2,30	187	599
5	C	0,36	7,0	2,23	0,55	67,7	536	2,85	232	768
6	C	0,36	7,3	2,55	0,55	76,8	634	2,94	239	874
7	C	0,36	7,2	2,77	0,55	83,7	681	4,36	355	1036
8	C	0,36	7,0	1,41	0,55	42,8	339	2,32	189	528
9	C	0,36	7,0	1,79	0,55	54,4	431	2,32	189	619
10	C	0,36	6,0	1,94	0,57	60,8	412	2,28	186	598

Table F.9. Lehane-2013:eq.(9.33)

				Pile Shaft					Pile base			
				Average					Avg.			
No	T/C	D	L	q_t	σ'_{v0}	δ_f	$max(h/R;1)$	τ_f eq.(9.34)	Q_{shaft} eq.(9.12)	q_t	Q_{base} eq.(9.13)	Q_c eq.(9.4)
-	-	m	m	MPa	kPa	o	-	kPa	kN	MPa	kN	kN
1	C	0,36	9,52	2,20	48,6	13,5	0,52	35,6	383	3,22	262	646
2	T	0,36	7,64	2,12	39,0	13,5	0,54	34,9	301	-	-	301
3	C	0,36	7,67	2,12	39,1	13,5	0,54	34,9	303	2,95	240	543
4	C	0,36	6,1	1,91	31,1	13,5	0,57	32,3	223	2,30	187	410
5	C	0,36	7,0	2,23	35,7	13,5	0,55	36,6	290	2,85	232	522
6	C	0,36	7,3	2,55	37,2	13,5	0,55	40,9	338	2,94	239	577
7	C	0,36	7,2	2,77	36,7	13,5	0,55	43,9	358	4,36	355	713
8	C	0,36	7,0	1,41	35,7	13,5	0,55	24,8	196	2,32	189	385
9	C	0,36	7,0	1,79	35,7	13,5	0,55	30,3	240	2,32	189	429
10	C	0,36	6,0	1,94	30,6	13,5	0,57	32,7	222	2,28	186	408

Page intentionally left blank

Appendix G

All notations have been submitted at the beginning of this thesis.

Below, the peak strength envelope for Poznań clay is presented.

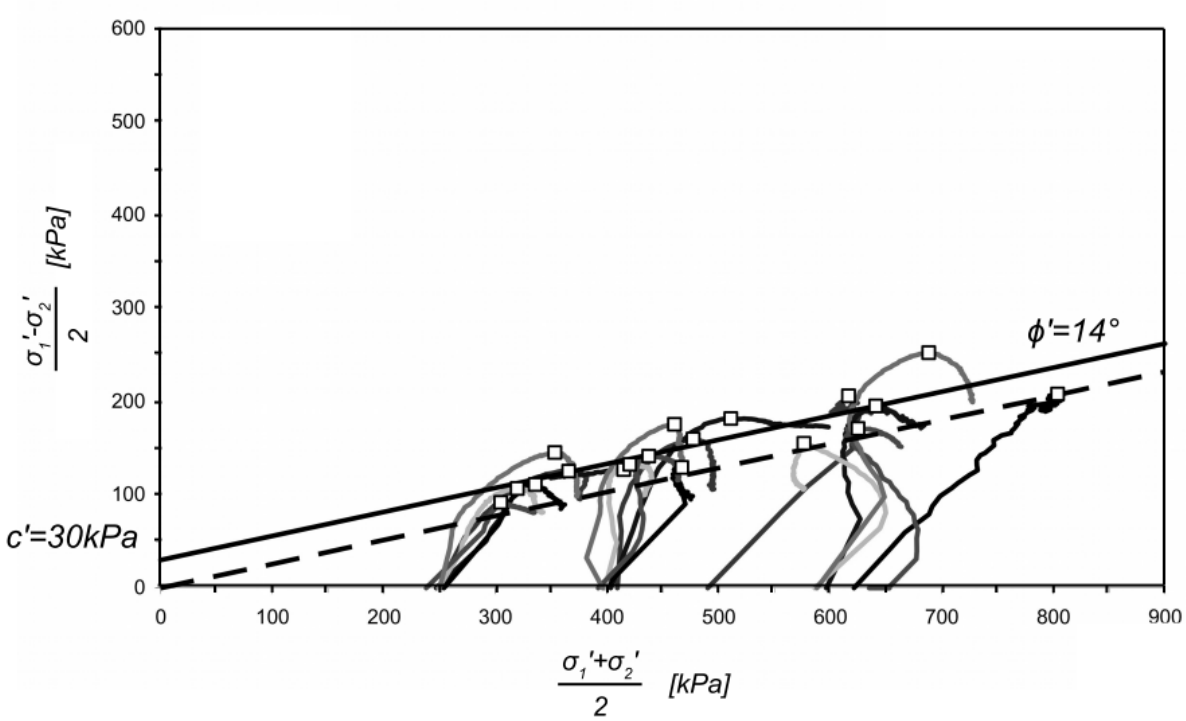

F*igure G.1. Peak and residual envelope for CU triaxial tests on samples from Poznań site*

Page intentionally left blank

Appendix H

All notations have been submitted at the beginning of this thesis.

Below, the drilling log for E407 pile is presented.

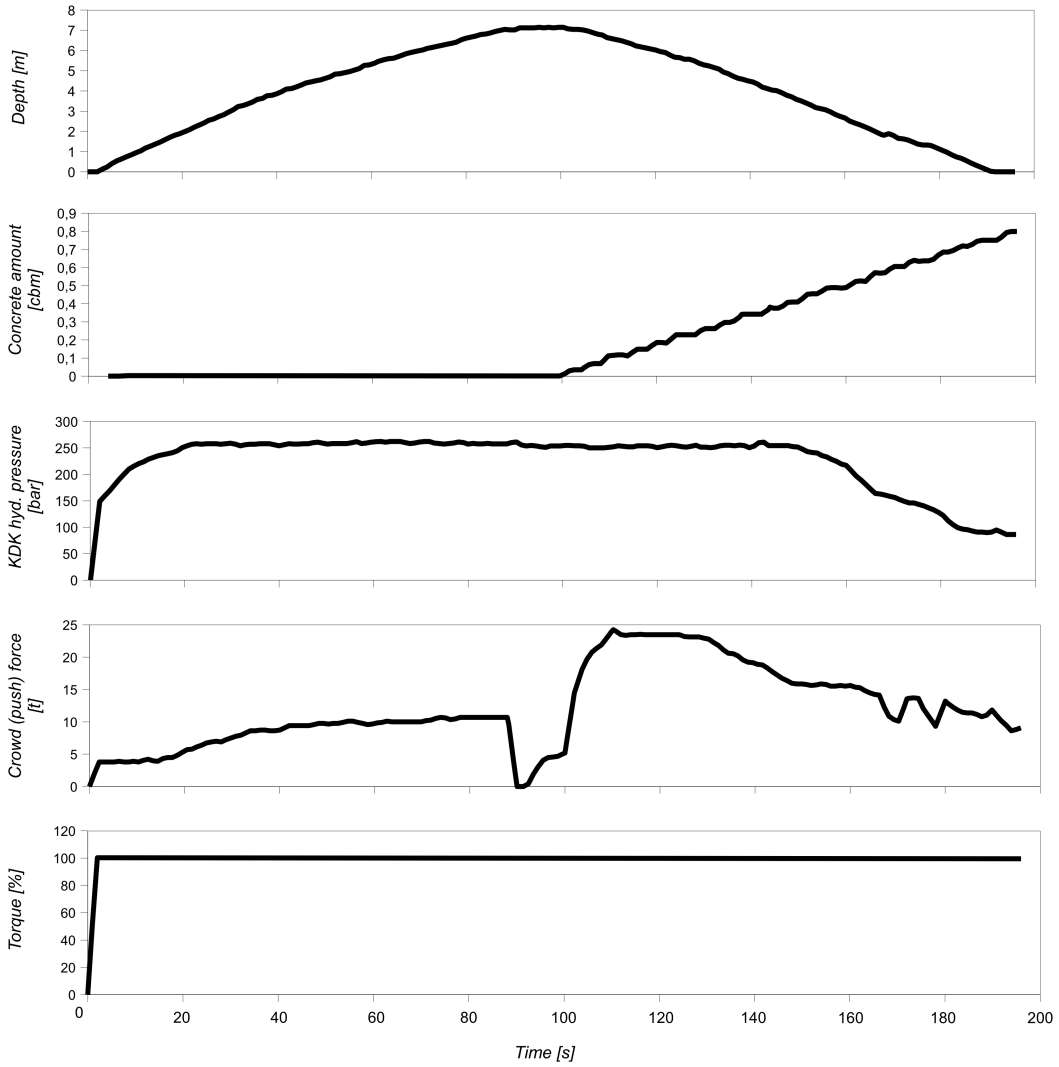

F*igure H.1. CMC pile E407 drilling log*

Page intentionally left blank
Last page